Tracing Excited-State Photochemistry by Multidimensional Electronic Spectroscopy

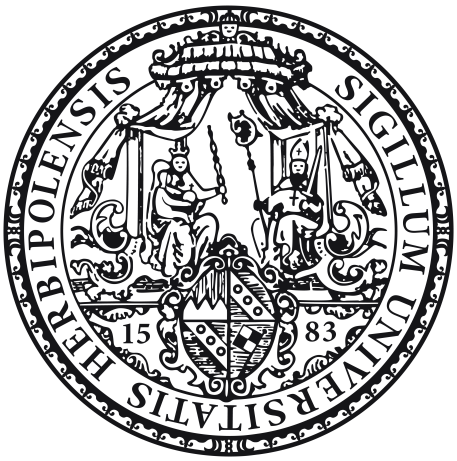

Dissertation zur Erlangung
des naturwissenschaftlichen Doktorgrades
der Julius-Maximilians-Universität Würzburg

vorgelegt von

Martin Armin Kullmann
aus Aschaffenburg

Würzburg 2013

Eingereicht am: _____
bei der Fakultät für Chemie und Pharmazie

1. Gutachter: Prof. Dr. T. Brixner
2. Gutachter:

der schriftlichen Arbeit

1. Prüfer: Prof. Dr. T. Brixner
2. Prüfer:
3. Prüfer:
des öffentlichen Promotionskolloquiums

Datum des öffentlichen Promotionskolloquiums: _____

Doktorurkunde ausgehändigt am: _____

List of Publications

J. Buback, M. Kullmann, F. Langhojer, P. Nuernberger, R. Schmidt, F. Würthner, and T. Brixner,
Ultrafast Bidirectional Photoswitching of a Spiropyran,
J. Am. Chem. Soc. **132**, 16510–16519 (2010).

D. Reizenstein, T. Quast, F. Kanal, M. Kullmann, S. Ruetzel, M. S. Hammer, C. Deibel, V. Dyakonov, T. Brixner, and C. Lambert,
Synthesis and Electron Transfer Characteristics of a Neutral Low Band Gap Mixed-Valence Polyradical,
Chem. Mater. **22**, 6641–6655 (2010).

J. Buback, M. Kullmann, P. Nuernberger, R. Schmidt, F. Würthner, and T. Brixner,
Photoswitching Cycle of a Nitro-Substituted Spiropyran: Ring-Opening and Ring-Closure Dynamics,
Ultrafast Phenomena XVII, 379–391 (2011).

J. Buback, P. Nuernberger, M. Kullmann, F. Langhojer, R. Schmidt, F. Würthner, and T. Brixner,
Ring-Closure and Isomerization Capabilities of Spiropyran-Derived Merocyanine Isomers,
J. Phys. Chem. A **115**, 3924–3935 (2011).

M. Kullmann, S. Ruetzel, J. Buback, P. Nuernberger, and T. Brixner,
Reaction Dynamics of a Molecular Switch Unveiled by Coherent Two-Dimensional Electronic Spectroscopy,
J. Am. Chem. Soc. **133**, 13074–13080 (2011).

M. Kullmann, A. Hipke, P. Nuernberger, T. Bruhn, D. C. G. Götz, M. Sekita, D. M. Guldi, G. Bringmann, and T. Brixner,
Ultrafast exciton dynamics after Soret- or Q-band excitation of a directly β,β'-linked bisporphyrin,
Phys. Chem. Chem. Phys. **14**, 8038–8050 (2012).

F. Koch, M. Kullmann, U. Selig, P. Nuernberger, D. C. G. Götz, G. Bringmann, and T. Brixner,
Coherent two-dimensional electronic spectroscopy in the Soret band of a chiral porphyrin dimer,
New J. Phys. **15**, 25006-01–25006-12 (2013).

S. Ruetzel, M. Kullmann, J. Buback, P. Nuernberger, and T. Brixner,
Exploring Higher-Lying Electronic States of a Molecular Switch by Coherent Triggered-Exchange 2D Electronic Spectroscopy,
Ultrafast Phenomena XVIII, 05001-01–05001-03 (2013).

S. Ruetzel, M. Kullmann, J. Buback, P. Nuernberger, and T. Brixner,
Tracing the Steps of Photoinduced Chemical Reactions in Organic Molecules by Coherent Two-Dimensional Electronic Spectroscopy Using Triggered Exchange,
Phys. Rev. Lett. **110**, 148305-01–148305-05 (2013).

Table of Contents

Chapter 1

Introduction

The synthesis of many (artificial) chemical compounds created a huge industrial sector, which has steadily increased over the last century. By using the Haber-Bosch process invented at the beginning of the 20th century, for example, millions of tons of ammonia, a natural fertilizer, are produced annually [1]. In geographical and economic circles this up-scaled chemical process is even considered the most important invention of the former century. Resulting from the fact that chemical reactions often branch, meaning that one reactant can result in multiple products, exact setting of the experimental parameters is required. Depending on the specific reaction, these parameters can possibly be temperature, pressure, illumination, and/or an addition of substances working as catalysts (G. Ertl, Nobel Price in Chemistry in 2007 [2]).

The final reaction product is easy to identify by using methods like mass spectrometry, nuclear magnetic resonance and liquid chromatography. However, the reaction mechanism itself, often consisting of multiple steps, is usually only inferred by using chemical intuition. Nevertheless, by knowing the exact sequence, fine tuning of reaction parameters and the transfer of knowledge to similar systems is made possible. Hence, directly resolving the mechanism is an essential part of basic research in chemistry (predominantly in the liquid phase) and physics (mainly solid-state based research). Since reaction mechanisms often proceed over multiple excited molecular states, tracing excited-state behavior is an important goal in chemistry, especially in photochemistry. For example, 5-diazo Meldrum's acid, a photoresist compound in ultraviolet (UV) photolithography [3], reacts to an ester following 267 nm excitation, whereas 330 nm illumination generates Meldrum's acid [4] — a fact that illustrates the influence of the illumination wavelength.

As explained above, understanding the behavior of electronically excited states enables tailoring of a reaction outcome into the desired product. Unraveling the relaxation mechanisms of photoexcited molecules requires both speed and skill. Speed is necessary, because an event in time can only be resolved by an even faster event [5] and light-induced reactions typically proceed within a time range of femtoseconds to microseconds [6]. Therefore, femtosecond laser pulses [7] are utilized to study reactions on their fundamental time-scales [8,9], providing the required speed. Now-

adays, clever combinations of femtosecond laser pulses are used. First of all there was the pump–probe or transient-absorption technique (A. Zewail, Nobel Price in Chemistry, 1999 [10]), where one ultrashort laser pulse induces a chemical reaction, followed by a subsequent pulse probing the unfolding dynamics in real time. Although pump–probe spectroscopy is still the most common ultrafast time-resolved spectroscopy method, this seminal technique has been extended and generalized in past years. For example, by spectrally resolving the pump pulse, the concept of two-dimensional (2D) spectroscopy, very common for nuclear magnetic resonance measurements [11,12], was transferred into the optical regime [13,14]. The additional frequency axis can be used to track photophysical transport mechanisms like energy distribution [15] and photochemical processes like isomerization [16]. Furthermore, using a sequence of pump pulses before the probe pulse interacts with the sample, the so-called pump–repump–probe method, allows time-resolved excited-state photochemistry to be within grasp [17].

Within this thesis, the above mentioned experimental techniques were either used (pump–probe and 2D spectroscopy) or adapted (two-color 2D and pump–repump–probe spectroscopy) to meet the requirements of the multiple systems under investigation. Furthermore, in a novel approach for assessing electronic transitions, pump–repump–probe and two-color 2D spectroscopy were combined into electronic triggered-exchange 2D spectroscopy (TE2D). Since this method links information about reactants, intermediates and products, excited-state photochemistry is elucidated in a unique way. All these techniques are demonstrated on two intriguing photosystems, a metalated bisporphyrin and a dinitro-substituted merocyanine. Thus, not only proof-of-principle experiments are presented, but also two comprehensive reaction schematics are unraveled by subsequent experiments with increasing complexity.

The necessary theoretical background for understanding both the techniques and photochemistry, is presented in the following chapter (Chapter 2). There, the properties of femtosecond laser pulses, nonlinear frequency conversion processes, and, lastly, light-induced transitions in molecules are summarized.

In Chapter 3, the principles of time-resolved spectroscopy in liquid phase are explained, both for transient-absorption and 2D spectroscopy. In addition, the experimental implementations, including the used laser system are described. Both setups are optimized for electronic spectroscopy, which means that the corresponding vibronic transitions are induced with photons possessing visible or ultraviolet wavelengths.

Porphyrins, the so-called colors of life [18], are the focus of Chapter 4. Natural porphyrinoid systems possess excellent energy transport mechanisms which are important in photosynthesis and can be resolved by time-resolved methods [15]. Another curious detail about porphyrins is the strong contribution of the second electronically excited singlet state, called “Soret band” for these molecules, to the photophysical behavior. Completely artificial light-harvesting complexes are part of current research, but it is still a long way to go. Thus, to gain further knowledge about this molecular class, a directly β,β'-linked bisporphyrin with zinc metalation is analy-

zed using both pump–probe and 2D spectroscopic measurements. Additionally, the dimer is compared to its monomeric building block. In this study, pump–probe measurements provide a general overview of the photodynamics, while 2D spectroscopy visualizes especially the Soret-band chemistry. By combining all this the excited-state energy transport mechanisms are unraveled, both on a femtosecond and on a nanosecond time-scale.

The properties of a molecular photoswitching device [19] are analyzed in Chapter 5 with similar spectroscopic means as in the chapter about the time-resolved properties of a porphyrin. The molecular class of spiropyran/merocyanine is an electrocylic photosystem, which enables light-induced switching between two stable isomers, either spiropyran or merocyanine, on an ultrafast time-scale [20]. In addition to assessing the switching by pump–probe and pump–repump–probe spectroscopy directly, possible loss channels are analyzed using a novel two-color 2D setup in pump–probe geometry with a continuum probe. This new setup enables monitoring of the potential energy surfaces belonging to the ground state and the first excited singlet state, so that merocyanine, which absorbs strongly in the visible, can be analyzed in detail. The latter surface is scanned afterwards with the newly developed method of electronic TE2D spectroscopy, thus, tracking intermediate states in the photochemistry of this molecule.

The thesis is concluded with a summary of the most important results (Chapter 6). Insight is provided, both from an experimental point of view, stressing the transferability of the new techniques to other challenges, as well as from a photochemical angle, assessing the potentials of both the bisporphyrin and the spiropyran–merocyanine photosystem.

Chapter 2

Theoretical Background

Chemical reactions often occur within picoseconds. Time-resolved spectroscopy offers a possibility to investigate these processes if two conditions are fulfilled. On the one hand, an event in time is needed to start a reaction. On the other hand, additional events, which are shorter than the duration of the mechanism itself, are needed to observe the temporal evolution. Since ultrashort laser pulses are highly sensitive tools, which satisfy these requirements [8–10], photochromic [21] reactions are well suited to be studied in a time-resolved fashion. Therefore, the temporal and spatial properties of laser pulses are explained in Sec. 2.1, followed by an introduction to nonlinear optics (Sec. 2.2). The latter is necessary to understand the generation of ultrashort laser pulses with tunable frequencies as well as the signals in time-resolved spectroscopy. Finally, light-induced transitions, the Born-Oppenheimer approximation and relaxation mechanisms are elucidated (Sec. 2.3).

2.1 Mathematical Description of Ultrashort Laser Pulses

Ultrashort laser pulses are the main tool in most experiments performed in this thesis. A common representation of these pulses are superpositions of electromagnetic waves with different frequencies, which interfere constructively. This approach is well documented in literature, e.g., in Refs. [22–24], and is presented in the following in a compressed way, introducing the physical parameters of laser pulses.

These superimposed plane waves or spatially and temporally changing electrical fields $\vec{E}(t,\vec{r})$ have to satisfy the inhomogeneous wave equation

$$-\nabla \times \left[\nabla \times \vec{E}(t,\vec{r})\right] - \frac{1}{c^2}\frac{\partial^2}{\partial t^2}\vec{E}(t,\vec{r}) = \mu_0 \frac{\partial^2}{\partial t^2}\vec{P}(t,\vec{r}) \ , \tag{2.1}$$

where $c = 1/\sqrt{\epsilon_0 \mu_0}$ is the speed of light, μ_0 the magnetic permeability, and ϵ_0 the dielectric constant, all in vacuum. On the one hand, polarization $\vec{P}(t,\vec{r})$ is the generator of an electrical field. On the other hand, it is also the response of matter

to an applied electrical field. Therefore, spatial and temporal behavior is coupled via the wave equation. Equation 2.1 is only valid for homogeneous and non-magnetic materials. The most significant bulk materials used, fused silica, nonlinear crystals, and organic solvents, can be treated within this approximation.

The beam propagation itself can be described via the homogeneous wave equation, i.e., linear polarization of the electrical field and propagation along an arbitrarily chosen z-axis as a plane wave. Accordingly, the solutions $\vec{E}(t,\vec{r})$ of Equation 2.1 can be separated into the form

$$\vec{E}(t,\vec{r}) \propto u(\vec{r})\vec{E}(t,z), \tag{2.2}$$

with $u(\vec{r})$ as the spatial beam profile and $\vec{E}(t,z)$ as the time-dependent polarization state along the z-Axis. Both parts will be treated separately in the following sections.

2.1.1 The Electrical Field in Time and Frequency Domain

As time and frequency domains are equivalent, from a pure mathematical point of view it is sufficient to describe the pulses in only one of the two domains and transform the solution if necessary. Furthermore, since it is sufficient to neglect the vectorial attributes and to consider only one spatial point, $\vec{E}(t,z)$ is treated as $E(t)$. Hence, the initial real-valued temporal electrical field can be simplified to

$$E(t) = 2A(t)\cos\left[\Phi(t)\right] = A(t)e^{i\Phi(t)} + c.c. = E^{+}(t) + E^{-}(t), \tag{2.3}$$

where $A(t)$ denotes the real-valued amplitude and $\Phi(t)$ the corresponding temporal phase. Since the complex-valued electrical field $E^{+}(t)$ contains all contributions originating from positive frequencies, it is termed as the signal. By contrast, $E^{-}(t)$ contains the contributions originating from negative frequencies. The Phase $\Phi(t)$ itself can be separated into different factors

$$\Phi(t) = a_0 + \omega_0\, t + \varphi(t). \tag{2.4}$$

A constant phase offset is denoted by a_0. The phase contribution, which is linearly proportional to the time t with ω_0 being the center frequency of the electrical field, is described by $\omega_0\, t$. A nonlinear part $\varphi(t)$ sums up all higher order contributions.

Using Equation 2.4 the complex-valued temporal electric field $E^{+}(t)$ is expressed as

$$E^{+}(t) = A(t)e^{ia_0}\, e^{i\omega_0 t}\, e^{i\varphi(t)} = E_c(t)e^{ia_0}\, e^{i\omega_0 t}, \tag{2.5}$$

with $E_c(t)$ as the complex-valued envelope function without the absolute phase and $\omega_0\, t$ describing the oscillations of the electrical field within this envelope function [25]. If rapidly oscillating carrier-frequency phase factors are neglected, meaning $E_c(t)$ does not change much within one optical cycle $T = 2\pi/\omega_0$, this separation is called slowly-varying envelope approximation (SVEA). The SVEA is valid for all used laser pulses in the presented work.

The corresponding electrical field in the frequency domain $E(\omega)$ is obtained after Fourier transformation (FT) of $E(t)$:

$$E(\omega) = \frac{1}{\sqrt{2\pi}} \int_{-\infty}^{\infty} E(t) e^{-i\omega t} = \mathcal{F}\Big\{E(t)\Big\}. \tag{2.6}$$

The electrical field $E(t)$, resulting from the back-transformation,

$$E(t) = \frac{1}{\sqrt{2\pi}} \int_{-\infty}^{\infty} E(\omega) e^{i\omega t} = \mathcal{F}^{-1}\Big\{E(\omega)\Big\} \tag{2.7}$$

has to be equal to Equation 2.3. Even though $E(\omega)$ has contributions originating from positive and negative frequencies it suffices to use

$$E^{+}(\omega) = \begin{cases} E(\omega) & \text{if } \omega \geq 0 \ , \\ 0 & \text{if } \omega < 0 \ , \end{cases} \tag{2.8}$$

since for real-valued $E(t)$ the following relation

$$E(\omega) = E^{*}(-\omega) \tag{2.9}$$

is valid where the asterisk denotes complex conjugation.

Analogously to the mathematical treatment in the time domain, a separation of $E^{+}(\omega)$ into a real-valued amplitude $A(\omega)$ and a spectral phase $\Phi(\omega)$ is possible:

$$E^{+}(\omega) = A(\omega) e^{-i\Phi(\omega)}. \tag{2.10}$$

In order to better understand the importance of the phase and the resulting effects on the laser pulses used, both the temporal and spectral phase will be expanded into a Taylor series. The power series is centered around time zero for $\Phi(t)$ and, accordingly, around the center frequency ω_0 for $\Phi(\omega)$, resulting in

$$\Phi(t) = \sum_{j=0}^{\infty} \frac{a_j}{j!} t^j \quad \text{with} \quad a_j = \frac{\partial^j \Phi(t)}{\partial t^j}\Big|_{t=0}, \tag{2.11}$$

$$\Phi(\omega) = \sum_{j=0}^{\infty} \frac{b_j}{j!} (\omega - \omega_0)^j \quad \text{with} \quad b_j = \frac{\partial^j \Phi(\omega)}{\partial \omega^j}\Big|_{\omega=\omega_0}. \tag{2.12}$$

The individual Taylor coefficients correspond to different properties of laser pulses. In both domains the coefficients of zero order a_0 and b_0, the absolute phase, describe the shift of the maximum of the electrical field compared to the maximum of the envelope. The temporal coefficient of the first order a_1 describes the center frequency ω_0, while the higher order coefficients a_j are combined into $\varphi(t)$, which characterizes the chirp of the pulse. This term describes a change in frequency over time as observed in the chirping of birds, explaining the name. If the change is positive ($d\omega/dt > 0$) it is denoted up-chirp and $d\omega/dt < 0$ is called down-chirp. In the frequency domain, the influence of the phase is not as intuitive. The following

explanations are valid for the common Gaussian-shaped spectrum. The coefficient b_1 describes a simple shift of the entire pulse in time. Higher order coefficients lead to different behavior. Contributions of even order lead to chirped pulses whereas contributions of odd order generate pulse sequences.

The spectral phase is affected by materials like glass and solvents, when the corresponding pulse passes through them. Therefore, the phase

$$\Phi(\omega) = k(\omega)L = \frac{\omega}{c} n(\omega) L, \tag{2.13}$$

is accumulated, where L is the length of the medium and $n(\omega)$ the real-valued index of refraction in a material without any loss [25]. The value of the latter is strongly frequency dependent. Additional absorption effects are added with an imaginary part in the index of refraction. The first derivative of the spectral phase

$$T_g = \frac{\partial \Phi(\omega)}{\partial \omega} = L\Big(\frac{\partial \omega}{\partial k}\Big)^{-1} = \frac{L}{v_g} \tag{2.14}$$

describes the delay of the maximum of the envelope with v_g as the group velocity of the wave packet. A second important effect when an optical wave passes through material is an increasing dispersion, resulting from the frequency dependence of the refractive index. Hence, pulse broadening is observed. This group delay dispersion (GDD) is described by the second derivative of the spectral phase normalized to the length of the material, depending on the wavelength $\lambda = 2\pi c/\omega$, resulting in

$$\mathrm{GDD} = \frac{\partial^2 \Phi(\omega)}{\partial \omega^2} = \frac{\lambda^3}{2\pi c^2} \frac{d^2 n}{d\lambda^2}. \tag{2.15}$$

2.1.2 Optical Observables

The electrical fields $E(t)/E(\omega)$ and the respective phases $\Phi(\omega)/\Phi(t)$, all introduced in section 2.1.1, are sufficient for a theoretical description of laser pulse phenomena. Since these quantities are not directly measurable, observables are needed that can be detected without further data analysis. They are introduced in the following.

The average of E^2 over a complete optical cycle multiplied by proportionality factors is called intensity and is measured by most common detectors, like, e.g., CCD-cameras or photodiodes. Within the slowly-varying envelope approximation the intensity as a function of time is

$$I(t) = c\epsilon_0 n \frac{1}{T} \int_{t-T/2}^{t+T/2} E^2(t')dt' = 2c\epsilon_0 n A(t)^2, \tag{2.16}$$

with n as the index of refraction of the medium in which the intensity is measured. Analogously, the spectral intensity is

$$I(\omega) = 2c\epsilon_0 n A(\omega)^2. \tag{2.17}$$

While theoretical descriptions often use the angular frequency ω, experimentalists commonly use the wavelength $\lambda = 2\pi c/\omega$. A frequency-to-wavelength conversion with a Jacobi-transformation, which is necessary because $\lambda \propto \omega^{-1}$, results in

$$I(\omega)d\omega = I[\omega(\lambda)]\left|\frac{d\omega}{d\lambda}\right| \propto I\Big(\frac{1}{\lambda}\Big)\frac{1}{\lambda^2}. \tag{2.18}$$

In addition to the transmission $\mathrm{Tr} = I(\lambda)/I_0(\lambda)$ corresponding to the percentage of intensity passing through a certain sample, spectroscopic measurements often detect the absorbance $\mathrm{Abs}(\lambda)$ of a sample corresponding to an intensity change in a logarithmic way, defined as

$$\mathrm{Abs}(\lambda) = -\lg\Big[\frac{I(\lambda)}{I_0(\lambda)}\Big] = \epsilon(\lambda)cd. \tag{2.19}$$

The absorption coefficient $\epsilon(\lambda)$ is wavelength dependent, c corresponds to the concentration and d to the thickness of the sample, while lg denotes the decadic logarithm ($\log_{10}$). This linear dependence of absorbance on c and d is called Lambert–Beer law and it describes the observed intensity by an exponential decay.

In time-resolved experiments the detected response is often not the absolute absorbance but the change in comparison to a reference beam that passes the sample under fixed conditions. Because both pulses are compared to the same intensity I_0, the absorption change $\Delta\mathrm{Abs}(\lambda, T)$ can be measured for a specific wavelength λ and a fixed time delay T between pulse and reference pulse, resulting in

$$\Delta\mathrm{Abs}(\lambda, T) = \mathrm{Abs}(\lambda, T) - \mathrm{Abs}(\lambda)_{\mathrm{ref}} = -\lg\Big[\frac{I(\lambda, T)}{I(\lambda)_{\mathrm{ref}}}\Big]. \tag{2.20}$$

An equivalent representation of the Lambert–Beer law but in dependence of the number of absorbing molecules $N(T)$ instead of the concentration is

$$I(\lambda, T) = I_0(\lambda)e^{-\gamma(\lambda)N(T)d}, \tag{2.21}$$

with $\gamma(\lambda) = \ln(10^{\epsilon})$.This results in an absorption change of

$$\Delta\mathrm{Abs}(\lambda, T) = \frac{1}{\ln(10)}\gamma(\lambda)(N(T) - N_0)d, \tag{2.22}$$

where N_0 denotes the maximal number of excitable molecules. Hence, an absorption change is directly linked to a photochemical or photophysical process in the measured sample. As ΔAbs is calculated by using the quotient of two quantities possessing the same units, it should not possess a real physical unit. However, the unit OD (short for "optical density", which is a synonym for absorbance) is used from now on, as it is a common convention in literature [26, 27].

For better characterization of the laser pulses used beyond the integrated intensity or energy, information about the pulse length (time domain) or spectral width (frequency domain) is necessary. For simple pulses without any pre- or post-pulses, for

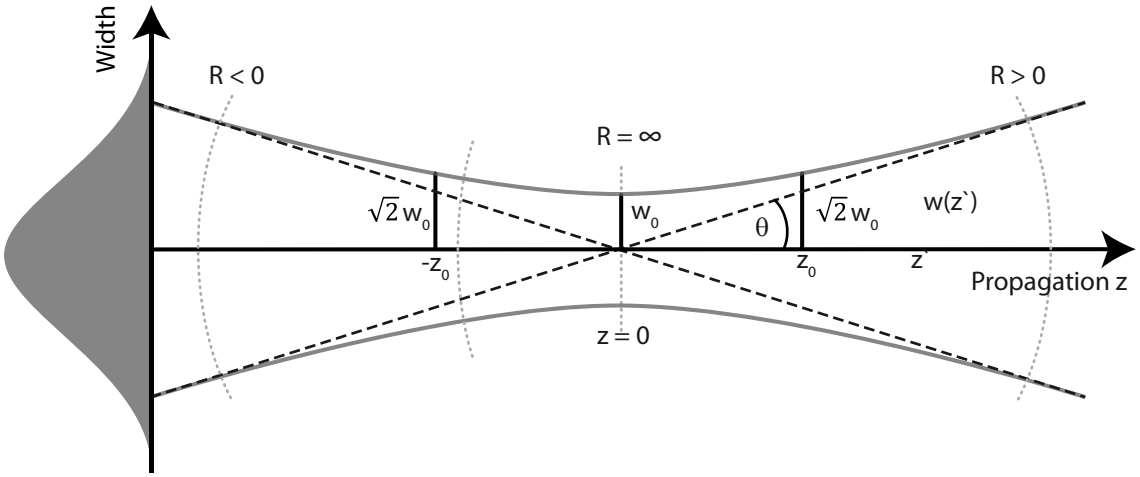

Figure 2.1: Spatial propagation of a Gaussian beam. The intensity profile is shown on the left, while the right side describes the paraxial beam propagation around the beam waist $w_0(z = 0)$. The red lines follow the beam width, the black lines at $|z| = z_0$ denote the Rayleigh length, and dashed black lines represent the beam propagation of a geometrical beam defining the divergence angle θ. The gray dashed lines describe the curvature.

example Gaussian-shaped ones, the full width at half maximum (FWHM) for the measured intensity is used. The FWHM denotes the time or frequency difference if the values are measured at half of the maximal signal strength on both sides of the intensity peak. Hence, the spectral width $\Delta\omega$ and the pulse length Δt is defined as

$$\Delta\omega = \mathrm{FWHM}[I(\omega)], \text{ and} \tag{2.23}$$

$$\Delta t = \mathrm{FWHM}[I(t)]. \tag{2.24}$$

It is important to keep in mind that these two values are not independent from each other but are linked by a Fourier transform. Thus, the time-bandwidth product

$$\Delta t \Delta\omega \geq 2\pi c_B \tag{2.25}$$

is valid for all (laser) pulses. The magnitude of the coefficient c_B is of the order of unity and depends on the overall pulse shape. For the most common pulse shape, the Gaussian pulse, $c_B = 4\ln(2)/(2\pi) = 0.441$ is valid. If expression 2.25 changes from an inequation to an equation, the associated laser pulse is called bandwidth-limited and it is as short as possible, the pulse is perfectly compressed.

2.1.3 Spatial Beam Propagation

While the former section dealt with the behavior of $\vec{E}(t, z)$, i.e., the propagation in time, the properties of the spatial directions have been neglected. The properties of $\mathrm{u}(\vec{r})$, describing the spatial behavior will be explained now [24, 28].

While a laser pulse itself consists of many modes in longitudinal or z-direction there are also transversal modes that define the spatial profile of the beam in the x-y-plane.

For all laser pulses used in this thesis the approximation holds that only the simplest possible spatial mode, the pure Gaussian mode (called TEM_{00}-mode), is sufficient to solve the wave equation (Equation 2.1). The corresponding spatial profile is

$$u(\vec{r}) = u_0 \frac{1}{\sqrt{1+z^2/z_0^2}} e^{-i\theta(z)} e^{ik(x^2+y^2)/[2R(z)]} e^{-(x^2+y^2)/w^2(z)}, \tag{2.26}$$

and this solution represents the optimal behavior of a laser beam. Every deviation from this mode leads to an increase in divergence and focus spot size [28]. Hence, even a Gaussian beam has a finite focus size $w_0 \neq 0$ at $z = 0$, the so-called beam waist, in contrast to plane waves, where $w_0 = \infty$. No point-sized focus is possible for real pulses. Figure 2.1 visualizes the propagation properties of a Gaussian beam. These are

$$w(z) = w_0 \sqrt{1+z^2/z_0^2}, \tag{2.27}$$

$$z_0 = \frac{n\pi w_0^2}{\lambda}, \tag{2.28}$$

$$R(z) = z + \frac{z_0^2}{z}, \tag{2.29}$$

$$\theta(z) = \arctan(z/z_0), \tag{2.30}$$

$$\theta(z \gg z_0) = \frac{\lambda}{n\pi w_0} = \frac{w_0}{z_0}. \tag{2.31}$$

The beam radius $w(z)$ and the divergence angle $\theta(z)$ define the propagation. The wave front is described by the radius of curvature $R(z)$, which is ∞ at the beam waist. Within the Rayleigh length z_0, the part of the laser beam where the width has not yet reached $\sqrt{2}w_0$, the wave front can be treated as approximately planar. This part of the beam used in all following experiments, because the beam spot is as small as possible and the pulse can be treated within the framework of plane waves.

2.2 Nonlinear Optics

So far the polarization $\vec{P}(t, \vec{r})$ was treated as a purely linear response of matter to the applied electrical field. In this case, as shown in section 2.1.2, the real part of the proportionality constant ϵ describes the phase, the dispersion and the group velocity while the imaginary part describes a gain or a loss of intensity in the medium [24]. For higher intensities, this assumption of a linear response is not sufficient any more and the polarization $\vec{P}(\omega)$ has to be treated as a series of polarization contributions, depending on different powers of the electrical field. Hereby, the polarization can be written as a combination of linear and nonlinear contributions

$$\vec{P}(\omega) = \vec{P}^{(1)}(\omega) + \vec{P}_{\mathrm{NL}}(\omega) = \vec{P}^{(1)}(\omega) + \vec{P}^{(2)}(\omega) + \vec{P}^{(3)}(\omega) + \dots . \tag{2.32}$$

As a result, new processes have to be taken into consideration when laser pulses are used, which possess high intensities in a short amount of time.

2.2.1 Nonlinear Processes

Polarization is of special importance as a source of new electrical fields. Hence, it is possible to generate electrical fields which satisfy the unique requirements of each experiment. Further separation of Equation 2.32 results in

$$P_i(\omega_q) = \epsilon_0 \Big(\sum_j \chi^{(1)}_{ij}(-\omega_q, \omega_m) E_j(\omega_m) + \sum_{j,k} \chi^{(2)}_{ijk}(-\omega_q, \omega_m, \omega_n) E_j(\omega_m) E_k(\omega_n) + ... \Big) \ , \tag{2.33}$$

where the subscripts i, j, k denote the spatial directions, the susceptibility $\chi^{(n)}$ is the n-th order answer of the medium in regards to the applied number n of electrical field(s). The emitted frequency ω_q is determined by

$$\omega_q = \omega_m + \omega_n + \ ... \ . \tag{2.34}$$

Within this work, the most important nonlinearities are the polarization components of second and third order. In isotropic media $\chi^{(2)} = 0$ is valid and the next remaining higher order is $\chi^{(3)}$. Most non-crystallized media, like solutions, are isotropic. Therefore, the remaining nonlinear contribution is the measured signal response in time-resolved measurements, like transient-absorption, transient-grating and two-dimensional spectroscopy. Often a corresponding change in absorption is detected.

For the generation of the laser pulses used non-isotropic crystals like β-barium-borat (BBO) or Ti:sapphire are employed, possessing large susceptibilities $\chi^{(2)}$. These can be exploited for frequency conversion processes, generating tailored frequencies. Some of the most important conversions are visualized in Fig. 2.2, with colors denoting the frequencies. A conversion of incoming frequencies is evident, when considering the example of an electrical field

$$E = E_m e^{-i\omega_m t} + E_n e^{-i\omega_n t} + c.c. \tag{2.35}$$

consisting of two frequencies ω_m and ω_n propagating in the same direction. This field results in a polarization response of second order:

$$\begin{aligned} P^{(2)} =& 2\epsilon_0 \chi^{(2)} (E_m E_m^* + E_n E_n^*) \\ &+ \epsilon_0 \chi^{(2)} (E_m^2 e^{-2i\omega_m t} + E_n^2 e^{-2i\omega_n t} + c.c. \\ &+ \epsilon_0 \chi^{(2)} (2E_m E_n e^{-i(\omega_m+\omega_n)t} + 2E_m E_n^* e^{-i(\omega_m-\omega_n)t} + c.c.). \end{aligned} \tag{2.36}$$

Equation 2.36 can be separated into three parts, each describing a different class of conversion processes. The first line describes a static field that is generated by the two time-dependent electrical fields. The second line describes a frequency doubling of each incoming wave, called second harmonic generation (SHG). The third line describes new electrical fields, either oscillating with the sum $\omega_{\text{sum}} = (\omega_m + \omega_n)$ [sum frequency generation, SFG, Fig. 2.2a)] or the difference frequency $\omega_{\text{diff}} = (\omega_m - \omega_n)$ [difference frequency generation, DFG, Fig. 2.2b)] of the two source field frequencies.

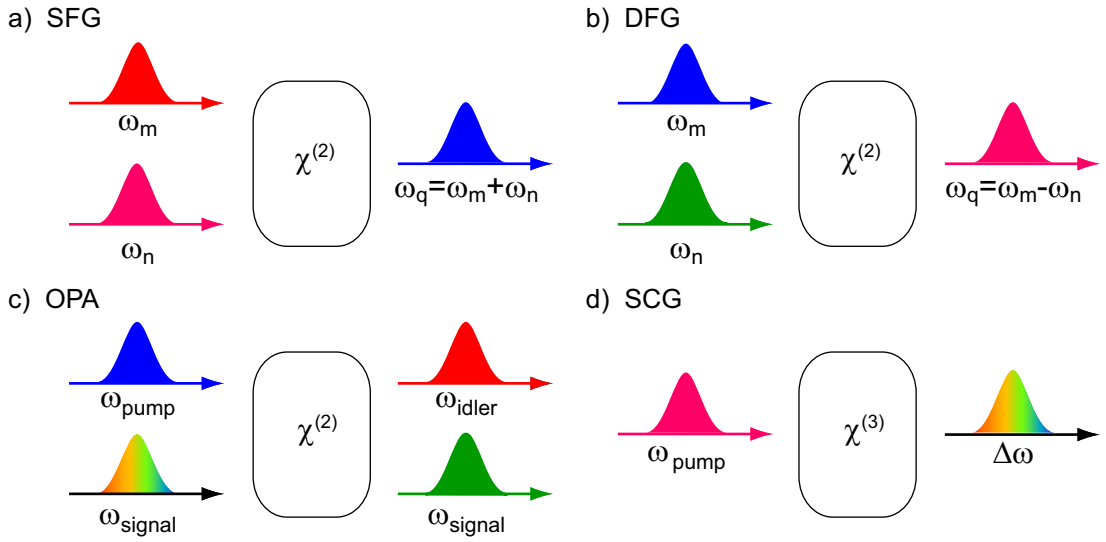

Figure 2.2: Schemes of the most common nonlinear frequency conversion methods: a) Sum frequency generation (SFG) b) Difference frequency generation (DFG) c) optical parametric amplification (OPA) d) Supercontinuum generation (SCG). Colored pulses denote the frequencies before and after the conversion processes take place.

Experimentally, often the case $\omega_m = \omega_n$ is used resulting in only one new time-dependent field $E(2 \cdot \omega_m)$. Hence, a stronger second harmonic signal is obtained [29].

These nonlinear conversion processes are optimized by using phase matching between all participating beams. This is necessary to minimize destructive interference between the incoming and outgoing waves inside the bulk material. Most processes lead to the use of three different waves. Therefore, the following phase matching condition for the combined wave vectors $\vec{k}$ has to be fulfilled:

$$0 = \vec{k}_m + \vec{k}_n - \vec{k}_q \tag{2.37}$$

If the assumption $\omega_q > \omega_m > \omega_n$ with $|\vec{k}_i| = n_i \omega_i / c$ holds and normal dispersion, i.e., an increase of refraction with increasing frequency, is present, this equation cannot be fulfilled in isotropic media. A solution is offered by birefringent crystals, because the polarization can be chosen such that the dispersion differs for ordinary and extraordinary directions, thus, Equation 2.37 can be fulfilled. However, optimal phase matching is only possible for one specific frequency and for neighboring frequencies to a certain degree. Therefore, the thinner the crystal, the larger is the potential bandwidth as less dispersion has to be corrected. A compromise has to be found as the efficiency of the frequency conversion process scales with the thickness.

Another important frequency conversion is optical parametric amplification [OPA, Fig. 2.2c)]. A narrow part of a weak but broadband seed pulse is strongly intensified, generating the signal pulse. Energy conservation is fulfilled by depleting a collinear intense pump pulse. Momentum and energy conversation laws lead to the generation of a third pulse, the idler pulse, at a frequency of $\omega_{\text{idler}} = \omega_{\text{pump}} - \omega_{\text{signal}}$. OPA is used to generate pulses ranging from the ultraviolet into the mid-infrared

regime. Often an improved approach is used, called non-collinear optical parametric amplification (NOPA). Here, the pump and seed pulses overlap under a certain angle (nonzero), which enables phase-matching for a wider spectral width of the seed pulse. This results in pulses with a higher spectral bandwidth, thus, they can be compressed down to shorter durations (compare Equation 2.25). However, the efficiency is reduced comparing the NOPA process to collinear OPA [30].

In addition to $\chi^{(2)}$-conversion processes, white-light or supercontinuum generation [SCG, Fig. 2.2d)] is often used in time-resolved spectroscopy [31]. Here, a narrowband, high-intensity pulse is focused into a nonlinear medium, like water or calciumfluoride (CaF_2), resulting in a spectrally broadened pulse. Broadening is observed on both sides of the pump. Generally considered and treated as a $\chi^{(3)}$-process SCG is not understood completely theoretically, but self-phase-modulation and Raman-scattering are important contributions [32]. These SCG pulses normally cover the complete visible spectral range in the case of a 800 nm pump pulse. If special materials like photonic crystal fibers are used the bandwidth can even exceed one octave. Accordingly, the spectrum covers parts of the ultraviolet, the entire visible and parts of the infrared spectral range [33]. Continua in the deep UV are also possible by combining nonlinear processes. In a first step, a UV pump pulse is generated by SFG. In a second step, this pulse is frequency broadened with SCG [34].

2.2.2 Laser Pulse Characterization

In order to understand the results of a photochemical study, it is necessary to know exactly which kind of laser pulses are employed to separate the chemical results from the properties of the pulses themselves. For example, if isomerization happens within a few tens or hundreds of femtoseconds but the exciting pulse has a duration of 200 fs the measured duration of the isomerization process will be 200 fs, since there is an uncertainty at which moment in time the photon initiates the photoreaction. A very simple way to estimate pulse durations is to measure the spectrum and then to approximate the duration with a Fourier transformation assuming a flat spectral phase or to use the time-bandwidth product (Equation 2.25) to estimate the duration (Sec. 2.1.2). But these two possibilities, using purely spectral information, yield the shortest possible pulse instead of the real one. The latter is possibly broadened by material dispersion, and, thus, the properties resulting from the phase contributions are completely neglected.

The nonlinear processes previously described (Sec. 2.2.1) cannot only be used to generate electric fields for the experiment but also to characterize them. There is a large variety of methods, which use purely time-domain data like intensity autocorrelation, or frequency-domain data like spectral interferometry [5, 25, 35–38]. A very popular pulse characterizing method is frequency resolved optical gating (FROG), which uses a mixed time-frequency approach to characterize the laser pulse [35]. Pulse duration, spectrum, time-bandwidth product, and the value of all phase contributions are determined while — depending on the specific method used — a few ambiguities remain.

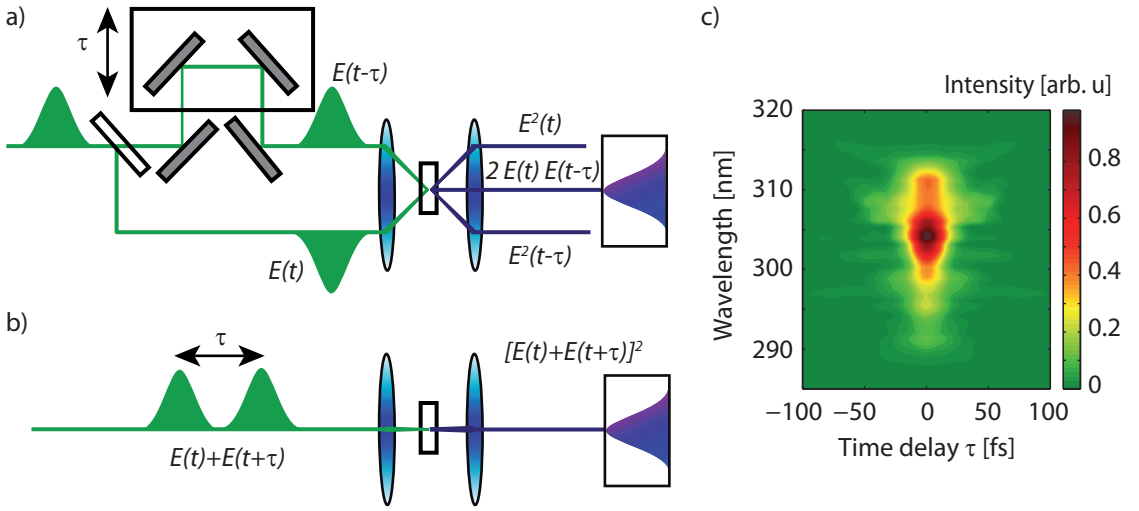

Figure 2.3: Schematics of two SHG-FROG techniques. The incoming pulse (green) is frequency doubled in a BBO crystal (violet) and the signal is measured in a spectrally-resolved manner. a) Noncollinear approach: After splitting the pulse by using an interferometer, one part is delayed via a stage. Only the signal response from the overlap of both pulses $2 \cdot E(t) \cdot E(t-\tau)$ is detected, exploiting phase-matching conditions. b) Collinear approach: Intrinsic phase stability is guaranteed by generating the pulse pair completely in-line. However, the SHG-signal has to be extracted from $[E(t)+E(t+\tau)]^2$. c) Measured FROG trace of an uncompressed NOPA pulse in the visible spectral range.

Due to the similarity of a FROG measurement to an intensity autocorrelation, it is also called a spectrally-resolved autocorrelation. Commonly, a FROG setup is implemented by spatially and temporally overlapping the unknown pulse with a copy of itself noncollinearly identical to an autocorrelation. At the intersection a nonlinear medium is placed. By detecting the corresponding nonlinear signal, often the second harmonic, a frequency-resolved and phase-sensitive feedback is gained. This frequency-resolved detection is the difference between a FROG and an autocorrelation measurement. Essentially, the pulse serves as a time gate for its copy by shifting one pulse continuously with respect to the other, e.g., by a linear stage. The noncollinear geometry results in a background free signal because the conservation of momentum leads to emission in the direction of $\vec{k}_S = \vec{k}_1 + \vec{k}_2 \neq \vec{k}_1 \neq \vec{k}_2$. With a stepwise variation of the relative delay τ between the two pulses the FROG-trace

$$I_{\mathrm{FROG}}^{\mathrm{SHG}}(\omega,\tau) = \left| \int_{-\infty}^{\infty} \tilde{E}(t) + \tilde{E}(t-\tau) e^{-i\omega t}\, \mathrm{d}t \right|^2 \tag{2.38}$$

is measured by resolving the signal as a function of frequency or wavelength and time delay. A schematic experimental implementation is shown in Fig. 2.3a). After the measurement, the pulse is reconstructed by different algorithms allowing identification of the electrical field, which generates the trace. The calculation of $I_{\mathrm{FROG}}^{\mathrm{SHG}}$ is repeated for various fields until calculated and observed traces agree within a chosen convergence criteria. Whereas convergence of these algorithms has not been proven theoretically so far [35], for all pulses in this work convergence was observed.

Moreover, while the generation of a pulse copy is easily achievable in theory, experimental limitations may force a collinear approach (abbreviated cFROG) sketched in Fig. 2.3b) [39]. While the obtained signal is no longer background free, because SHG contributions resulting from only one electrical field are emitted into the same direction, a cFROG can be measured in a lot of different setups, resulting in

$$I_{\mathrm{cFROG}}^{\mathrm{SHG}}(\omega,\tau) = \left| \int_{-\infty}^{\infty} \left[\tilde{E}(t) + \tilde{E}(t+\tau)\right]^2 e^{(-i\omega t)}\,\mathrm{d}t \right|^2 . \tag{2.39}$$

Only the generation of double pulses with a shiftable delay, e.g., by using a pulse shaper is required [40]. The pulse reconstruction is done by the same algorithms as for the FROG after the cFROG trace is reduced to expression 2.38. Therefore, low pass Fourier filtering is performed and the permanent offset for long delay times subtracted, resulting in a FROG trace similar to the one shown in Fig. 2.3c).

2.3 Molecular Transitions

The previous sections introduced the properties of laser pulses used to induce or detect atomic or molecular reaction dynamics. The underlying molecular transitions are explained in the following section.

A photochemical molecular reaction is the interaction of a photon with a molecule, often resulting in the absorption of the former. As a result, the molecular state changes from its initial configuration with the wave function Ψ_i and energy E_i (most probably the ground state) into a final one with Ψ_f and energy E_f, also called an excited state in the case of a resonant excitation. The energy separation between the initial state Ψ_i and the final state Ψ_f is equal to the photon energy $\hbar\omega$ with $\hbar$ as Planck's reduced constant, hence $\hbar\omega = E_f - E_i$. This energy difference is covered by rotational, vibrational, and electronic transitions with an increasing amount of energy. The energy of the states is obtained by solving the Schrödinger equation

$$H|\Psi_{\mathrm{mol}}(r,R)\rangle = E|\Psi_{\mathrm{mol}}(r,R)\rangle \tag{2.40}$$

for the corresponding molecular wave function $|\Psi_{\mathrm{mol}}(r,R)\rangle$ where r denotes the coordinates of the electrons and R the coordinates of the nuclei. In the following spin contributions are neglected for simplicity. An exact solution for this equation is very challenging and only systems of three or less particles, e.g., the hydrogen ion H_2^+ consisting of two protons and one electron, are analytically solvable. Using the Born-Oppenheimer approximation often allows numerical solutions for larger molecular systems, which help to estimate properties like transition energies or corresponding wave functions [41].

The Born-Oppenheimer approximation is applied after taking a closer look at the Hamiltonian of a molecular system, consisting of

$$H = T_e + T_N + V_{ee} + V_{eN} + V_{NN}, \tag{2.41}$$

with $T_e = \sum_i \frac{p_i^2}{2m_e}$ and $T_N = \sum_K \frac{P_K^2}{2m_K}$ as the kinetic energy of the electrons (e) or nuclei (N) and the interaction potentials V_{xy}. In addition, the wave function is separated into

$$|\Psi_{\mathrm{mol}}(r,R)\rangle = \sum_e |\Psi_e(r,R)\rangle|\Phi(R)\rangle. \tag{2.42}$$

$|\Psi_e(r,R)\rangle$ denotes the electronic wave function that only depends parametrically on the coordinates of the nuclei R and $|\Phi(R)\rangle$ denotes the wave function of the nuclei, which is completely independent from the electron dynamics. The Born-Oppenheimer approximation is to first solve the electronic parts of the Schrödinger equation at fixed coordinates R:

$$(T_e + V_{ee} + V_{eN})|\Psi_e(r,R)\rangle = E^e|\Psi_e(r,R)\rangle. \tag{2.43}$$

This has to be repeated for many different sets of coordinates R. Thereafter, the equation for the nuclei

$$(T_N + V_{NN} + E^e)|\Phi(R)\rangle = E|\Phi(R)\rangle, \tag{2.44}$$

is solved, using the previous results as parametric parameters. This corresponds to a complete separation of the electronic movement from the kinetics of the nuclei, thereby neglecting all contributions of the kinetic energy that result from coupling between nuclei and electrons. Coupling terms are present because the kinetic energy operator of the electrons is applied to the wave functions of the nuclei and vice versa, generating non-zero terms. The approximation is often valid because the mass difference between electrons and nuclei exceeds three orders of magnitude, which results in different velocities and inertias. Hence, the electrons react nearly instantaneously to any changes of the nuclei (adiabatic approximation). The total energy of a molecular state depends on the possible movements of all atoms, which basically lead to multidimensional potential energy surfaces describing a certain electronic state. Within this state there are vibrational sublevels, which describe the movements of the electronic wave packet. Hence, one potential energy surface corresponds to one electronic molecular state with the spin used as the characteristic distinction, for example singlet (S) with the effective spin $\sum_i s_i = 0$ and triplet states (T) with $\sum_i s_i = 1$. In addition to this separation electronic states can be divided into two other categories. There are bound states where the electron remains within the system after excitation. The second category are unbound states. In the latter, the electron leaves the molecular system, resulting in a positive ion and a free electron. Fig. 2.4a) visualizes transitions between two bound states (black, solid lines) also containing vibrational states (gray, dashed lines). Absorption of a photon (green arrow) from the ground state is followed by fluorescence after the molecule has internally relaxed (orange arrow).

The probability of an optical transition between two potential energy surfaces is described by Fermy's golden rule

$$k_{i-f} \propto |M_{if}^e|^2 \cdot FC, \tag{2.45}$$

where the probability k_{i-f} is proportional to the vibrational Franck–Condon factor FC defined by the initial and final states, which denotes the overlap integral of the vibrational wave functions in both state. Therefore, the greater the vibrational overlap of the wave functions belonging to the initial and final states is, the larger is the transition probability. Furthermore, k_{i-f} is proportional to the transition matrix of the electronic wave function

$$M_{if}^{e} = \langle \Psi_{e,i}(r,R) | \mu_e | \Psi_{e,f}(r,R) \rangle, \tag{2.46}$$

which depends on the overlap and symmetries of the electronic wave functions and their corresponding transition dipole moments

$$\mu_e = -e \sum_i r_i + e \sum_K Z_K R_K, \tag{2.47}$$

defined by the amount and position of the charges of both electrons (first term) and nuclei (second term) [42, 43]. Transitions often occur at the turning point of the excited-state wave functions belonging to a certain vibrational state, as a result from the statistical higher probability density there. In each vibrational ground-state level, however, the highest probability density is in the middle. Furthermore, transitions are (within the adiabatic Born-Oppenheimer approximation) always vertical because the nuclei coordinates R do not change during an electronic excitation. These electronic transitions proceed mostly in the visible or ultraviolet spectral range. Purely vibrational transitions, however, depend on the transition dipole moment of the wave function describing the nuclei. Thus, they are at lower energies, often in the mid-infrared regime. Within this thesis, photons with wavelengths ranging from 267 nm to 1000 nm are used. They induce primarily electronic transitions, often coupled to higher vibrational levels. Thus, they are called vibronic transitions and both absorption (green) and emission (orange) are visualized in Fig. 2.4a) combined with the corresponding vibrational wave functions (blue).

After photoexcitation, the excited molecule relaxes back to the ground state. Certain deactivation processes exist, all possessing characteristic time-scales. Thus, by determination of the time-scale using time-resolved spectroscopic methods, the relaxation can be analyzed. In addition, one has to distinguish between non-radiative and radiative processes [44]. Both transitions and molecular states can be combined in a so-called Jablonski diagramm. The molecular states are visualized by horizontal lines marking the lowest energy. Additionally, the spin multiplicity is used as the abscissa. Transitions are marked by arrows with the direction denoting excitation (upwards) and relaxation (downwards) [45]. Fig. 2.4b) shows an exemplary Jablonski diagram with four different electronic states (black, solid) and corresponding vibrational levels (gray, dashed). Possible transitions are named by their abbreviations visualizing the multitude of possibly competing relaxation channels.

Relaxation from a vibrationally hot state proceeds via vibrational cooling (VC) until the vibrational ground state of the same electronic state is reached. The lost excess energy is either transported to solvent molecules, used as a thermal bath, or distributed over the entire molecule. The former is called intermolecular vibrational

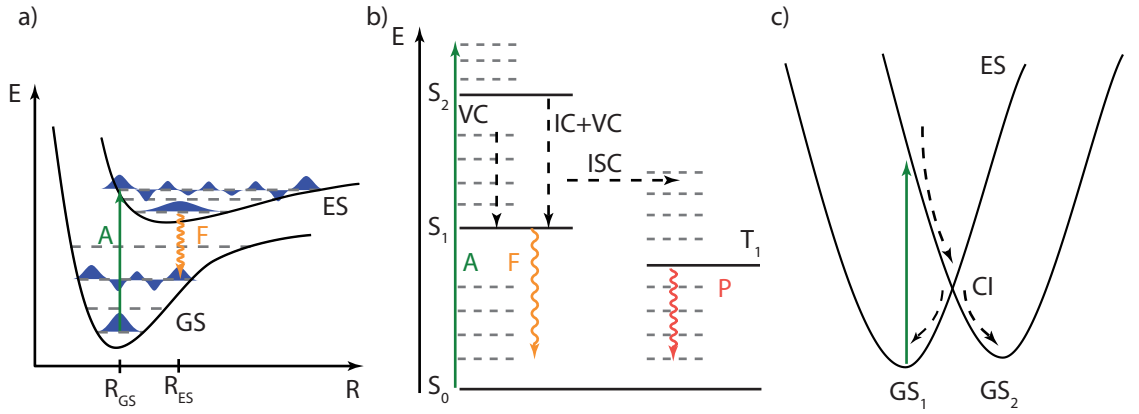

Figure 2.4: a) Two exemplary one-dimensional potential energy surfaces, belonging to the ground state (GS) and an excited state (ES) (black, solid). Vibrational states are drawn as vertical lines (grey, dashed) together with corresponding wave functions (blue). Two vertical radiative transitions (arrows), absorption (green) and emission (orange), proceed between states possessing strong vibrational overlap (Franck–Condon transition). b) Jablonski diagramm, describing the energetic ordering of molecular states (indicated by vertical lines) with regard to their spin. Exemplarily, three singlet (S_0, S_1, and S_2) and one triplet state (T_1) are drawn (black), vibrational sublevels are marked in gray. Possible non-radiative relaxation processes (IC, VC, ISC) are marked by black, dashed arrows and the radiative processes, fluorescence (F, orange) and phosphorescence (P, red), are shown as undulated arrows. c) Isomerization process occurring via a conical intersection (CI) connecting a common excited state and two different ground-state minima. After photoexcitation (green), non-radiative vibrational relaxation occurs until the wave packet reaches the CI. There, an ultrafast transition into each GS may take place.

energy transfer (VET) and proceeds typically within picoseconds. The latter faster process, is called intramolecular vibrational relaxation (IVR), constituting distribution of vibrational energy contained in one hot mode into many of the $3N-6$ different vibrational modes in existence (or $3N-5$ for linear molecules), typically on a femtosecond time-scale. These time-scales are valid for electronically excited states, while in the ground state vibrational relaxation is much slower.

Relaxation from one electronically excited state into another only requires strong electronic coupling if states of the same spin multiplicity participate. An isoenergetic horizontal transition takes place on an ultrafast time-scale (< 1 ps) called internal conversion (IC). Subsequently, vibrational cooling in the new state leads to further relaxation. If states of different multiplicity intersect (often S_1 and T_1) and no other relaxation pathway exists, intersystem crossing (ISC) can take place. There, in addition to electronic coupling like in IC, spin-orbit coupling must also be strong to permit changes of the total spin. Typical lifetimes are in the fast ns domain, when going from S to T and up to milliseconds if the direction is reversed (T to S).

In addition to this non-radiative transition, both fluorescence (F) and phosphorescence (P) are possible. In accordance to Kasha's rule, fluorescence is often the dominating relaxation pathway connecting S_1 and S_0. This leads to relaxation via

emission of a photon, usually red-shifted compared to the absorption wavelength. Picoseconds are the typical time-scale while IC between these two states would proceed on a nanosecond time-scale, resulting from the large energy shift when compared to the energy separation of excited states. A similar luminescent process connecting T_1 and S_0 is called phosphorescence, however, typical time-scales can reach milliseconds. ISC between these two states is also highly unlikely (up to seconds).

Experimentally, using time-resolved spectroscopy, it was shown that non-radiative transitions between two different molecular geometries are possible resulting in isomerization. These reactions were explained via a common excited state [46–48]. Hence, the Born-Oppenheimer approximation fails when two potential energy surfaces come close. Often potential surfaces are not allowed to intersect, especially for two-atomic atoms. By avoiding degeneracy of different states, an "avoided crossing" occurs and the potential energy surfaces deform. Thus, a non-radiative transition between two different electronic states should happen via internal conversion followed by vibrational relaxation within picoseconds, which does not match the observed femtosecond time-scale. Furthermore, for larger molecular systems intersections of potential energy surfaces are very common, which therefore require a non-adiabative approach where electronic and nuclei movements are no longer uncoupled. They often possess a conical shape, thus, are called conical intersections (CI), which enable ultrafast transitions between electronic states [43, 49]. A possible visualization of the corresponding potential energy surfaces is given in Fig. 2.4c). Within a single vibrational period, the wave function crosses the CI and relaxes from a higher excited state into a lower one. Often, S_1-S_0 relaxation is observed. One famous example is the isomerization in bacteriorhodopsin, where an ultrafast (< 1 ps) transition and strong coherent oscillations connecting the two states are observed [50]. A complex theoretical description of conical intersections and their behavior within the Born-Huang theory is given in Ref. [51].

Chapter 3

Experimental Methods

In the following chapter several time-resolved measurement techniques and the corresponding experimental implementations are explained. While within this thesis new methods have been developed, all implementations described here were largely already present in the laboratories used. Therefore, references are added, when additional information about the construction or capabilities are available in literature. The first section shortly describes the employed femtosecond laser system and the available frequency-conversion setups (Sec. 3.1). Afterwards, after a short introduction of transient-absorption spectroscopy, the data analysis is summarized, and the actual implementation discussed (Sec. 3.2). Finally, two-dimensional spectroscopy is introduced. A short summary of the theoretical requirements is given, followed by an explanation of the box geometry. This section is concluded by the description of the miniaturized setup, which is capable of using ultraviolet pulses (Sec. 3.3).

3.1 Laser System

All laser pulses used over the course of this thesis were generated by a femtosecond laser system based on a Ti:Sapphire oscillator combined with a regenerative amplifier. The commercial Solstice setup (Spectra Physics) was predominantly used. The integrated Ti:Sapphire oscillator (MaiTai) generates the seed pulses (800 nm, 14 nm width, < 100 fs) at an 80 MHz repetition rate. These pulses are afterwards amplified by "chirped pulse amplification" [52]. Hence, the oscillator pulses are stretched, amplified, and compressed again. The necessary energy for the amplification process is provided by a 527 nm Nd:YLF pump laser operating at 1 kHz (Empower) pumping a second Ti:Sapphire crystal, serving as the gain medium. Afterwards, pulses at 800 nm with 100 fs duration and 3 mJ at a repetition rate of 1 kHz are available for subsequent frequency conversion processes. Therefor, the output is split into three beams using beam splitters; each beam possessing roughly one third of the laser power. While one beam can be used in various ways, depending on the actual performed experiment, the remaining two are directly converted into frequencies required for the experiments using different NOPA setups.

One of the two beams is used to seed a commercial NOPA with two amplification stages (TOPAS White, LightConversion), generating pulses between 250 and 1000 nm. These are compressed afterwards by an internal prism pair down to 20 fs. Pulses below 450 nm are generated via frequency doubling, while contributions above 850 nm are available by using the near-infrared part of the continuum seed pulse. The visible pulses possess energies between 20 and 50 nJ, by contrast the ultraviolet and infrared pulses are about one order of magnitude weaker [53].

The second beam line is used to seed another NOPA. However, the input energy is reduced below $E_{\mathrm{pump}} \approx 400\ \mu\mathrm{J}$, which corresponds to $E_{\mathrm{pump,\,SHG}} \approx 80$ µJ of 400 nm pump power, in order not to damage the crystals. This homebuilt system is described in greater detail in Ref. [54], including details about the construction. In short, pulses covering large parts of the visible spectral range — up to a bandwidth of 200 nm and down to a pulse duration of 10 fs — are generated. These short pulse durations are achieved by combining two processes. First, the seed continuum is compressed with an internal prism compressor, reducing the effective pulse length. Second, the pump pulse is stretched by a 10 cm fused silica rod in the beam path of the 400 nm light. Therefore, both seed and pump overlap more favorably in two different amplification stages, generating the broadband pulses. The output energy is ≈ 8 nJ, when using a broadband pulse, and is reduced to ≈ 2 nJ when the NOPA is optimized for a specific wavelength and operated in a narrower capacity.

While the commercial system is completely computer controlled and provides comparable pulses with a fast adjustable center wavelength on a day-to-day basis, the homebuilt system has to be tuned manually but results in shorter pulses. Therefore, the actual system used depends on the specific requirements of the experiment. Spectroscopic experiments are performed with pulse energies in the nJ regime, thus, both systems are efficient enough.

3.2 Transient-Absorption Spectroscopy

Since electronic methods like streak cameras or time-correlated single photon counting employ one laser pulse and detect the signal response using electronic means only, are limited to a time resolution of a few picoseconds, a completely different approach is necessary for an increase in time resolution [25, 55]. By using two different femtosecond laser pulses, spatially overlapping at one defined sample point the limitations of purely electronic-based detection devices are circumvented. Hence, these femtosecond laser pulses provide an alternative spectroscopic approach with improved time resolution. Pump–probe or transient-absorption spectroscopy is the most common time-resolved spectroscopy method, using femtosecond laser pulses. There, one pulse is exciting the sample and the second one probes the light-induced differences over time. On the one hand, this technique enables the study of many light-induced electronic and/or vibrational transitions. On the other hand, pump–probe is conceptionally simple, the experimental implementation and data analysis is straightforward. All of this taken together, the wide-spread use is explained.

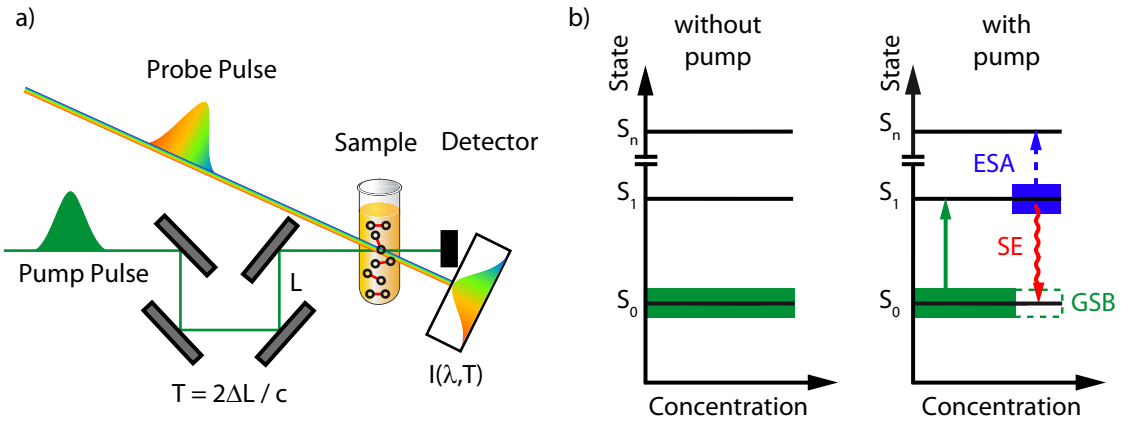

Figure 3.1: a) Schematic noncollinear pump–probe setup with a pump having an adjustable delay T (green) and a continuum probe with spectrally-dispersed detection spatially overlapping in the sample cell. b) Energy level diagram with population shown in bars (colors represent absorption maxima). Without a pump pulse all molecules are in S_0, after pump pulse interaction a small percentage is excited into S_1. When calculating ΔAbs four signal contributions can be observed: Negative valued GSB, corresponding to missing molecules in the ground state (green) and SE, caused by a probe photon stimulating emission in S_1 (red), and positive ESA, where a probe photon is resonantly absorbed into higher-lying states S_n (blue). Positive product absorption (PA) is not shown.

3.2.1 Observable Signal Contributions

For many measurements performed in this thesis, the transient-absorption approach visualized in Fig. 3.1a) is used. The first laser pulse, the intense pump pulse (green), excites the sample into higher-lying electronic states. Afterwards, the second one, the probe pulse (continuum), probes the changes induced by the pump pulse in the sample (mostly solutions or thin films). This possesses different absorption properties in the ground and excited states. Hence, the name pump–probe spectroscopy. The two pulses possess an adjustable relative time delay T, called waiting time, which allows measurements in a time-resolved manner by step-wise scanning of T. Comparing the spectrally-resolved intensity changes with $[I_{\mathrm{PPr}}(\lambda, T)]$ and without $[I_{\mathrm{Pr}}(\lambda)]$ presence of the pump pulse, Equation 2.20 can be used to detect the changes in absorbance, slightly rewritten as:

$$\Delta\mathrm{Abs}_{\mathrm{PPr}}(\lambda, T) = -\lg\left(\frac{I_{\mathrm{PPr}}(\lambda, T)}{I_{\mathrm{Pr}}(\lambda)}\right). \tag{3.1}$$

This change in absorption is time-dependent because transitions between vibrational or electronic levels occur with time as covered in Sec. 2.3, resulting in differing absorption and transmission properties subjected to the probe pulse. The absorption change $\Delta\mathrm{Abs}_{\mathrm{PPr}}$ alongside one specific wavelength for different waiting times is called a transient and enables identification of relaxation time-scales. Furthermore, spectrally-resolved data, covering different transitions, for one time delay T is a so-called difference spectrum. These difference spectra visualize, which different signal contributions are dominant at a certain waiting time.

In principle, there are four different signal contributions as visualized in Fig. 3.1b), which cause changes in $\Delta\mathrm{Abs}_{\mathrm{PPr}}$. They can all be traced back to effective concentration changes (represented by horizontal bars) induced by the pump pulse. First, after excitation of a sample, the number of molecules in the ground state is reduced. Hence, less intensity of the probe pulse is absorbed at wavelengths where ground-state absorption (GSA) occurs. This negative signal, occurring (nearly) immediately after photoexcitation, is called a ground-state bleach (GSB), which can be (partially) recovered over time, as molecules relax back into the ground state. A second, also negative signal, is caused by stimulated emission (SE). There, often occurring at wavelengths known from fluorescence measurements, probe photons induce the emission of additional photons with identical energy and momentum. Hence, the detected probe intensity increases after photoexcitation of the sample by the pump, resulting in a negative signal. It is often red-shifted compared to the GSA wavelength because of vibrational cooling and more effective Franck–Condon overlap with higher vibrational levels in the ground state. The difference of SE and GSB in regards to I_{PPr} is that the intensity belonging to GSB is increased because less photons are absorbed, while in the SE signal additional photons are emitted, increasing the probe intensity I_{PPr}.

The third possible signal is positive excited-state absorption (ESA). There, resulting from the population transfer into excited states, different transitions show a resonant absorption. Hence, additional probe photons are absorbed. If a permanent product is formed, e.g., by bond breaking, isomerization or ionization, this also corresponds to positive changes in $\Delta\mathrm{Abs}(\lambda, T)$ and it is called product absorption (PA). The reasoning is identical to ESA. Separation of product absorption and ESA is possible when comparing their behavior to corresponding SE signals, e.g., using two difference spectra. If both bands decay, the positive signal originates from ESA; if only the SE decays the new positive band corresponds to a permanent product absorption. Summarizing, the following changes in intensity cause the corresponding positive and negative absorption changes:

$$\mathrm{GSB}: \; I_{\mathrm{PPr}} > I_{\mathrm{Pr}} \Rightarrow \Delta\mathrm{Abs}_{\mathrm{PPr}} < 0 \tag{3.2}$$

$$\mathrm{SE}: \; I_{\mathrm{PPr}} > I_{\mathrm{Pr}} \Rightarrow \Delta\mathrm{Abs}_{\mathrm{PPr}} < 0 \tag{3.3}$$

$$\mathrm{ESA}: \; I_{\mathrm{PPr}} < I_{\mathrm{Pr}} \Rightarrow \Delta\mathrm{Abs}_{\mathrm{PPr}} > 0 \tag{3.4}$$

$$\mathrm{PA}: \; I_{\mathrm{PPr}} < I_{\mathrm{Pr}} \Rightarrow \Delta\mathrm{Abs}_{\mathrm{PPr}} > 0 \tag{3.5}$$

In addition to temporal relaxation, also rotational diffusion can be measured. Using linearly polarized laser pulses for both pump and probe, a subensemble of an isotropic sample is excited whose transition dipole moment is parallel to the laser polarization. With time, often on a fast picosecond, or even a femtosecond [56] time-scale, this anisotropic behavior relaxes back into a homogeneous distribution because of rotational relaxation and collisions of the sample with the solvent. By choosing a relative angle, called "magic angle", of 54.7° (resulting from $\tan^2\phi = 2$) between respective pump and probe polarization, the anisotropic effects are mostly avoided, because the absorption changes alongside the perpendicular contributions

are two times the parallel contributions relative to the polarization axis [57]. For a detailed theoretical study about anisotropic effects influencing transient-absorption spectroscopy, see Ref. [58].

Furthermore, time-resolved spectroscopy in the liquid phase is aggravated at the time of simultaneous arrival of both pump and probe ($T \approx 0$) by unwanted signal contributions. These short-lived absorption changes are caused by the temporal overlap of the laser pulses inside the flow cell and the solvent. The, so-called, "coherent artifact" is mostly a signal contribution of third order and theoretically fairly well understood [59–61]. It can even be used for experimental determination of time zero via cross correlation [62]. The largest signal contribution is caused by cross phase modulation, which describes the interaction of the intense pump pulse with the weak probe pulse via the media where they intersect. Basically, the refraction indices of all nonlinear media, where the pulses intersect, are modulated with time, similar to self phase modulation. The weak probe pulse is subjected to a frequency shift of

$$\Delta\omega(t) = -2\frac{n\omega_0 d}{c}\frac{\partial}{\partial t}|A(t)|^2, \tag{3.6}$$

where n denotes the effective refractive index, ω_0 the central probe pulse frequency, d the intersection length, and $A(t)$ the envelope function within the SVEA. Looking at Equation 3.1 it is clear that a frequency shift changes the spectral intensity. Thus, by comparing the probe pulse intensity with and without the pump pulse present, necessary for calculating $\Delta\mathrm{Abs}_{\mathrm{PPr}}$, the cross phase modulation is detected as an unwanted signal. The shorter the used pulses are, the shorter-living is the coherent artifact, stressing the need to use compressed pulses for the experiments in order to obtain the best possible time resolution. The coherent artifact is basically masking the sample response, effectively blinding the measurement. The minimal possible time-resolution, even in the optimal case without a coherent artifact, is a convolution of the temporal profiles of both pump and probe pulses. Therefore, a shorter pulse length corresponds to a higher time resolution. Since by measuring the pure solvent the coherent artifact is obtained, which strongly depends on the pulse overlap, this convolution of pump and probe is achieved experimentally. Furthermore, the longest possible probe time-scale corresponds to the length of the linear stage used.

3.2.2 Signal Evolution and Data Analysis

After describing the principal signal contributions in the previous sections, changes in the temporal behavior are assessed in the following. Some of the detected signals can be permanent, most probably new product bands or GSB, showing no temporal behavior. Other signals change with time, e.g., stimulated emission signals if a radiative relaxation channel (fluorescence) is possible and, accordingly, ESA, which monitors the concentration of a specific excited state. Hence, if the system is excited into S_2 and relaxes into S_1, the ESA and SE signals originating from S_2 or S_1 decrease/increase with increasing time delay. Therefore, these relaxation dynamics have to be assessed in order to analyze and understand the measured data.

One possible way to access the temporal behavior is the use of rate equations. They describe photochemical changes using sets of differential equations of first order. For example, recovery of the ground-state concentration $c(S_0)$ after excitation into S_1 can be described as:

$$\frac{d\ c(S_1)(t)}{dt} = -\frac{1}{\tau_{S1}} c(S_1)(t), \tag{3.7}$$

$$\frac{d\ c(S_0)(t)}{dt} = \frac{1}{\tau_{S1}} c(S_1)(t). \tag{3.8}$$

The first equation describes how S_1 is emptied, while the second equation describes the replenishment of S_0. The time constant τ_{S1} simultaneously describes the lifetime of S_1 and the replenishment of the ground state because no additional states are considered [63]. The characteristic solutions of differential equations like these are exponential rise and decay functions

$$c(T) = c_0 \exp(-\frac{T}{\tau}), \tag{3.9}$$

depending on the waiting time T, the effective lifetime τ, and the concentration c. One possibility for evaluating the data is to generate a set of rate equations and compare them afterwards to the results. However, if multiple states and relaxation channels participate in the reaction scheme of the detected sample this is a challenging task.

Thus, the data obtained in this thesis was analyzed by global fitting routines based on the mechanisms reviewed by van Stokkum *et al.* and by using the graphical interface Glotaran accessing the statistical fitting package TIMP [64–66]. The basic idea of a global fit in pump–probe spectroscopy is to use a sum of exponential functions, each representing the lifetime of a certain state or a cooling dynamic. Each of these time constants is fixed over the entire bandwidth, and multiplied by a wavelength-dependent amplitude. It is important to assess the minimal number of time constants needed to adequately fit the data, because if the amount is overestimated the fit quality will increase. In addition to these exponential functions, the fit function is convoluted with a Gaussian shaped instrument response function (IRF), modeling the coherent artifact and estimating the time resolution. A chirp in the pump pulse, resulting in slightly varying zero times for different wavelengths, is considered by using a polynomial function, shifting time zero with increasing wavelength. This separation into exponential decays and a spectral amplitude is possible when considering the Lambert–Beer law in Equation 2.19 and combining it with the exponential decays obtained from using an ansatz of first order differential equations (Equation. 3.7). Accordingly, the Lambert–Beer law can be rewritten into a sum of n differently absorbing coefficients, depending on the wavelength and concentration, exponentially changing with time,

$$\mathrm{Abs}(t, \lambda) \propto \sum_{i=0}^{n-1} \epsilon_i(\lambda) \cdot c_i(t). \tag{3.10}$$

No spectral correlation is assumed in the fitting procedure, every wavelength is treated independently, only the time constants remain the same. For further discussion, the concepts of evolution-associated difference spectrum/spectra (EADS) and decay-associated difference spectrum/spectra (DADS) are exploited, which are both weighting the wavelength-dependent parameter differently [64].

Both, EADS and DADS, represent the spectral fitting parameters when a transient-absorption map, consisting of a set of difference spectra for different waiting times T, is globally fitted with a parallel rate model (DADS) or a sequential rate model (EADS). In a sequential model, the excited photosystem relaxes n-times from an excited state into an energetically favorable state, thus, until the number of estimated time constants is reached and the ground state is replenished. No branching is possible. By contrast, in a parallel model the photosystem is excited into a series of states, from where independent relaxation directly into the ground state sets in, so that the branching is maximal, while no two-step reactions are assumed. Here, the number n of exponential functions represents the number of excited states. Accordingly, the corresponding time-dependent change of concentration and connected change of absorption is

$$c_i^{\text{para}}(t) = e^{-\frac{t}{\tau_i}} \times \text{IRF}, \tag{3.11}$$

$$\Delta\text{Abs}^{\text{para}}(t,\lambda) = \sum_{i=1}^{n-1} \text{DADS}_i(\lambda) \cdot c_i^{\text{para}}(t), \tag{3.12}$$

in the parallel model. The parallel model is very similar to Equation 3.10, no weighing parameters are necessary. In the sequential rate model (EADS), time-dependent change of concentration and absorption

$$c_i^{\text{seq}}(t) = \sum_{j=1}^{i} b_{ij} e^{-\frac{t}{\tau_j}} \times \text{IRF}, \tag{3.13}$$

$$\Delta\text{Abs}^{\text{seq}}(t,\lambda) = \sum_{i=1}^{n-1} \text{EADS}_i(\lambda) \cdot c_i^{\text{seq}}(t), \tag{3.14}$$

is fitted again. However, the concentration is weighted with the parameter b_{ij}

$$b_{ij} = \frac{\prod_{m=1}^{i-1} k_m}{\prod_{n=1,n\neq j}(k_n - k_j)}, \tag{3.15}$$

where instead of a time constant τ_i the corresponding rate $k_i = 1/\tau_i$ is used out of simplicity. This parameter is needed, because not every transition is treated independently, but step-wise relaxation from one state into the next is assumed.

In both models each rate represents a photochemical transition. The advantage of using a sequential fit model is that the corresponding parallel model can be calculated, while the reverse transformation is not possible. Basically, multiplication of the difference spectra with the associated concentration profiles results in a three-dimensional fit of the data. In short, the EADS represent the difference spectra

at different time delays and specify how these evolve with time. DADS show the wavelength-dependent amplitude, which is associated with one time constant. It contains the same overall information as EADS. While EADS provide an overview on and insight into spectral dynamics, DADS place more emphasis on the structure of the change. In particular, a DADS sheds light onto a specific time constant and corresponding relaxation processes, and how the latter are connected to each other. Introducing the behavior of a system with the help of EADS and discussing details with the support of DADS is therefore aimed at combining their strengths. However, DADS are more commonly used for the discussion of time-resolved data, as well as in pump–probe [27], fluorescence upconversion [48], and even 2D spectroscopy [67–69].

If the exact relaxation mechanism is known, a species associated rate model (also called target model) can be fitted allowing a combination of branched and multi-step reactions. The benefit is that the spectral behavior reflects the real absorption and emission properties of the molecule. However, the fit quality is not increased when compared to purely parallel or sequential models. An exemplary study can be found in Ref. [70], however, the additional benefits are marginal in most cases so that this approach is not further commented on.

3.2.3 Transient-Absorption Spectrometer

Nearly all experiments in this thesis were performed using the transient-absorption setup in the following as the basis, only the degenerate pump–probe and four-wave mixing experiments in Sec. 4.6 were performed in a different lab. However, the specifications were very similar. The pump–probe setup was developed as part of a former dissertation [58] and is described there in full detail.

The setup was developed with the goal of being adaptable to a number of different experiments, thus, possessing three different beam lines instead of just two. The principal layout is shown in Fig. 3.2. The primary probe pulses are obtained by super continuum generation (black line), while the primary pump pulses are the output pulses of a NOPA (green line). The third pulse can either be used as a pump or a monochromatic probe pulse (blue line), depending on the experiment. All pulses are spatially overlapped at the sample position. All elements placed there can be positioned by linear stages in order to adjust the optimal position and the effective angles between pump and probe pulses were minimized to achieve the best possible overlap and to come as close to a completely collinear configuration as possible. The entire setup is placed on a $(90 \cdot 60)$ cm large breadboard and inside a nontransparent box for dust protection, to reduce temporal fluctuations and room-light illumination.

The pump pulse (green) inside the setup is guided via silver-coated (Ag-coated) mirrors in an all-reflective manner, avoiding as much dispersive media as possible, and providing achromatic usability. Only the adjustable neutral-density (ND) wheel, controlling the pump intensity, and the broadband $\lambda/2$-wave plate, adjusting the polarization plane, remain. With a focal length of 200 mm a spot size of ≈ 50 µm is achieved, the position of which can be adjusted by the focusing mirror, placed

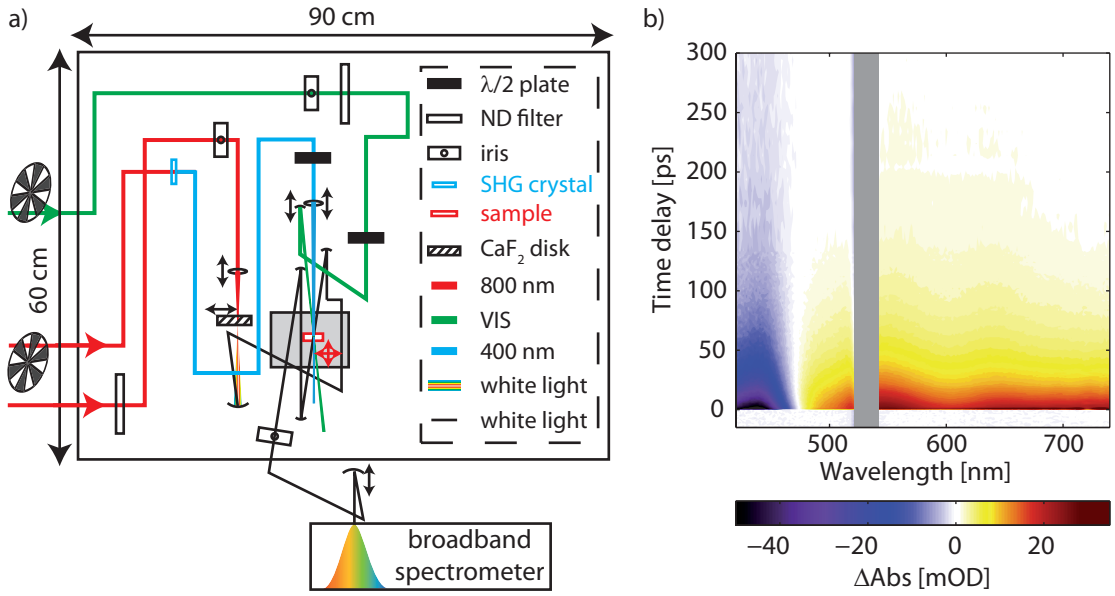

Figure 3.2: a) Layout of the transient-absorption setup including breadboard dimensions: Colored lines represent pump or probe beams. The continuum probe beam is detected spectrally resolved and the other two can be independently chopped with half of the laser's repetition rate. Pulse intensities are adjustable via neutral density (ND) filter wheels and focusing optics are adjustable by delay stages. Schematics adapted from Ref. [58]. b) Exemplary transient-absorption map of a mixed-valence polyradical measured with this setup. Changes in ΔAbs are color coded, with bluish colors denoting negative and reddish colors positive signals. For negative time delays $\Delta\text{Abs} = 0$ is valid because the pump arrives before the probe. For $T > 0$ there are a strong GSB (450 nm) and two ESA bands identified (550 nm, 650 nm). No permanent product formation is observed and all signals approach zero for long waiting times.

on a linear stage. The most common pump pulses are used from one of two NOPA systems, allowing a custom adaption of both bandwidth and center frequency.

The variable pulse (blue) was changed in contrast to Ref. [58] from a pure 267 nm usability to a wider usage, by using Al-coated optics, instead of dielectric high-reflective mirrors. Hence, both 800 nm, 400 nm, 267 nm pulses are possible as light sources in addition to the second NOPA. Depending on the wavelength the focusing lens has to be adjusted and the beam size exceeded the first pump pulse by ≈ 2 times. Both pulses can be independently moved by computer-controlled mechanized delay stages of 600 mm length with Al- or Ag-coated retroreflectors (corresponding to $T_{\text{max}} \approx 3.4$ ns) placed outside the protective box.

Finally, the probe pulses (black), fixed in time, are obtained by focusing ≈ 1 mW of the 800 nm fundamental into a, constantly linearly moving, 5 mm thick CaF_2 window. Thus, continuum pulses, covering the entire visible spectral range instead of possessing a sharp cutoff at 450 nm, as the previously used Sapphire plate, were obtained [26, 71]. The strong contribution of the 800 nm seed pulse was eliminated by inserting a custom made hot mirror (Laser Components), designed for high

transmission between 400 and 750 nm, while 800 nm is blocked, before the beam is focused into the sample. The beam line is also all-reflective using Ag-coated optics. Scatter is reduced by inserting a reflective, focusing telescope after the sample and placing an aperture in the focus. Thus, the beam profile is cleaned and only pure probe light remains. Broadband, shot-to-shot detection is used by focusing the probe light after passing of the sample into a spectrometer (Acton SpectraPro2500i), possessing a $2048 \cdot 512$ pixel wide, cooled CCD camera (Pixis 2K) as the detector unit. The signal noise is limited by calculating ΔAbs via shot-to-shot measurements. Thus, every second pump pulse is blocked using an optical chopper wheel operating at 500 Hz (half of the laser's repetition rate of 1 kHz).

An exemplary measurement is shown as a contour plot in Fig. 3.2b). Excitation at 525 nm is used (gray box) and the entire visible spectral range is probed for waiting times up to $T = 300$ ps. Bluish colors denote negative and reddish colors positive contributions. A negative GSB (450 nm) and a broadband ESA, possibly splitted into two separate bands is clearly visible (550 nm, 650 nm). All the signal contributions decay parallely and after 250 ps no time-resolved signal is left, thus, the entire excited population has relaxed. For these long waiting times and for $T < 0$ the low noise of the setup is seen. For a more in-depth study of the time-resolved data measured for a neutral, low-band-gap, mixed-valence polyradical, which exceeds demonstrating the capabilities of the system used, it is referred to Refs. [72, 73].

3.3 Coherent Two-Dimensional Spectroscopy

Coherent two-dimensional (2D) spectroscopy [8,74–77] provides a more versatile and illustrative approach compared to transient absorption (Sec. 3.2), as it directly relates the excitation dependence and the spectral response of a system within a single measurement. In addition to signal contributions known from transient-absorption experiments (ESA, SE, GSB, PA), coupling or energy or population transfer between different states can be intuitively extracted. The additional frequency axis, providing a specific spectral response for every excitation frequency, also separates the behavior of different absorbing contributions, like isomers [78] or chromophores within a light-harvesting complex [15], and visualizes the interconnection of participating states.

The result of such a measurement is a contour plot, the so-called 2D spectrum, containing two frequency axes. In Fig. 3.3 a cartoon-like 2D spectrum of a photosystem absorbing at two different pump frequencies (ω_1, ω_2) is visualized. Both states show an elliptical diagonal contribution, where ω_{Pump} corresponds to ω_{Probe}. Reddish circular contributions describe direct coupling between the two states via off-diagonal signals. The coupling is evident because a system which is excited at one frequency, for example ω_2, absorbs at the frequency of the second state ω_1. Thus, a transfer of population from state two into one must have occurred. In addition, the state absorbing at ω_1 possesses another contribution (bluish circle) which is not coupled to the second state because the emission frequency is not identical with ω_2.

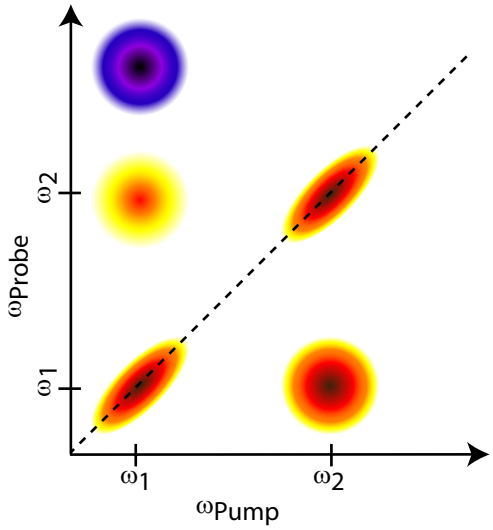

Figure 3.3: Schematic 2D spectrum, where a spectrally-resolved emission (ω_{Probe}) is combined with an axis relating to excitation (ω_{Pump}). As a result, contributions are resolved which are hidden in a pump–probe experiment, e.g., the two circular reddish off-diagonal peaks for both ω_1 and ω_2. By contrast, the bluish peak denotes a signal originating from ω_1 that is not coupled with ω_2. A 2D spectrum is related to a difference spectra in transient absorption via integration over the pump axis while the probe axis is retained.

Coherent 2D spectroscopy has been implemented in different wavelength regimes. 2D spectroscopy using pulses in the infrared spectral range (2DIR) enables analysis of the electronic ground-state behavior and tracks coupling between different vibrational states [79, 80]. For electronic correlations 2D spectroscopy was realized in the visible [13, 81–83] and recently in the ultraviolet (UV) [84–86] spectral range. The necessary theoretical background is briefly summarized in the following section (Sec. 3.3.1). The interested reader is referred to the Refs. [8, 74–76, 87, 88] as far as a deeper insight is concerned, especially regarding perturbation theory, nonlinear optics and the density matrix formalism. After understanding how third-order polarization is connected to a 2D spectrum (Sec. 3.3.1), Sec. 3.3.2 describes how a 2D spectrum is obtained from the measured data. The relationship of transient-absorption, transient-grating, and 2D spectroscopy is covered in Sec. 3.3.3, while the actually used experimental implementation is described in Sec. 3.3.4.

3.3.1 Theoretical Description of $\vec{P}^{(3)}(t, r)$

In time-resolved spectroscopic measurements within this thesis the detected signal depends most of the times on the third-order polarization $\vec{P}^{(3)}(t, r)$. Multicolor-excitation experiments are the exception. For transient-absorption, transient-grating and two-dimensional spectroscopy this polarization coefficient depends upon interaction of three electric fields, each one arriving at its own moment in time, with a quantum mechanical system, the sample. $\vec{P}^{(3)}(t, r)$, related to the signal response, can be calculated by combining perturbation theory and the density formalism in

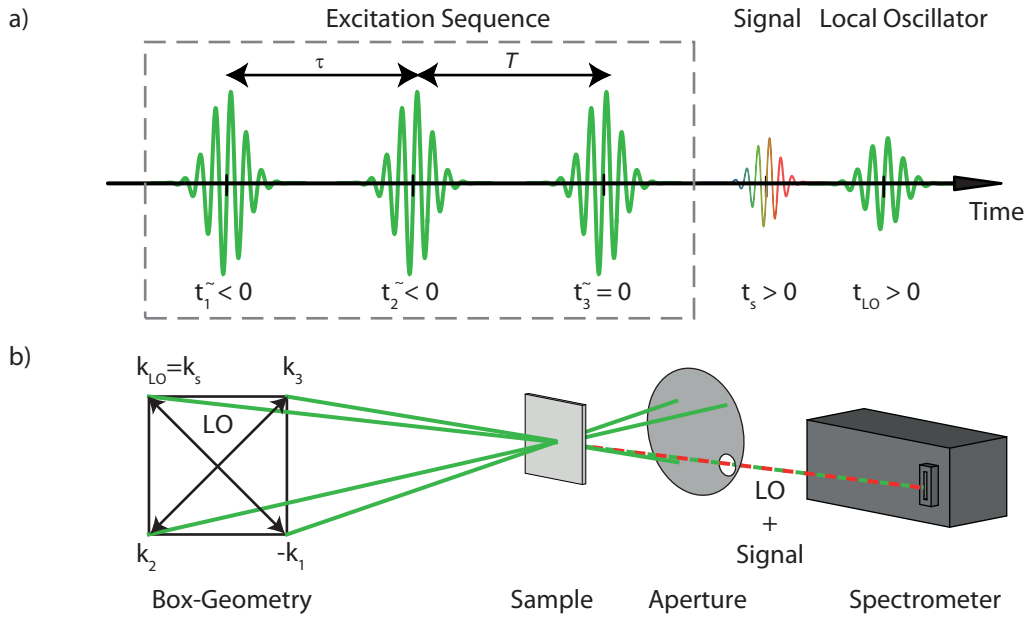

Figure 3.4: a) Pulse sequence of a four-wave mixing experiment with heterodyne detection. The first three pulses (green) at $\tilde{t}_i$, separated by coherence time τ or population time T, respectively, excite the sample. The emitted response (continuum) is detected via spectral interferometry using a local oscillator (green) arriving after the pump-pulse interaction. b) Schematic implementation of a 2D experiment in box geometry. By adding up the wave vectors $(-\vec{k}_1 + \vec{k}_2 + \vec{k}_3)$ it is evident that the signal direction $\vec{k}_S$ is in line with the LO direction $\vec{k}_{LO}$. Other signal contributions are blocked by an aperture before detection the spectrally-resolved interference pattern caused by signal and LO is detected.

the Liouville space [8], resulting in

$$\vec{P}^{(3)}(t,r) = \int_0^\infty dt_3 \int_0^\infty dt_2 \int_0^\infty dt_1 \vec{S}^{(3)}(t_3,t_2,t_1) \\ \vec{E}(t-t_3)\vec{E}(t-t_3-t_2)\vec{E}(t-t_3-t_2-t_1). \tag{3.16}$$

Here, the third order response function $\vec{S}^{(3)}(t_3,t_2,t_1)$ contains every information about the measured system itself, while the interaction with the electrical fields at a certain time is treated by $\vec{E}(t')$. The detection of the resulting signal is called a four-wave mixing experiment because three incident beams generate a coherent signal response with the emission direction defined by phase matching [8]. In the following, the most general case of a four-wave mixing experiment, 2D spectroscopy, is treated theoretically. The other two methods used, transient-absorption and transient-grating spectroscopy can be considered as a higher degenerate case of the former and can be derived from the formalism describing 2D measurements as will be explained in Sec. 3.3.3. If all excitation pulses share the spectral and temporal profile it is a one-color measurement [81]. If pulses one and two (which need to be identical) are different from pulse three it is a so-called two-color 2D measurement [89].

For a 2D experiment the pulse sequence shown in Fig. 3.4 is used. The three excitation fields, each with its one phase ϕ_i and wave vector $\vec{k}_i$ denoting the direction of the corresponding electrical field, are located in time at $\tilde{t}_1$, $\tilde{t}_2$, and $\tilde{t}_3$. The difference $\tau = \tilde{t_2} - \tilde{t_1}$ is called coherence time because the corresponding density matrix is in a state of coherence, i.e., off-diagonal elements are nonzero. The time delay $T = \tilde{t_3} - \tilde{t_2} = -\tilde{t_2}$ is the population or waiting time. After interaction of the corresponding fields only diagonal elements in the density matrix are nonzero in a two-level system while in a three-level system double coherence contributions are possible. The (often very weak) signal is measured with the help of a fourth pulse, called the local oscillator (LO) pulse, using so-called heterodyne detection. By detection of the spectral interference pattern caused by signal response and local oscillator, data extraction becomes possible. However, only the first three pulses are used for excitation. The LO is strictly used for detection purposes.

In order to obtain the complete third-order response function the phase-sensitivity of the measured signal is exploited. For a single 2D spectrum the population time T is fixed and the coherence time τ between the first two pulses is systematically scanned from $-\tau_{\max}$ to $+\tau_{\max}$. The maximal value of τ has to be large enough that no coherence is observed any more. After two Fourier transformations, one along τ and one for t, the response function can be plotted in a contour plot with the frequencies axes ω_τ, denoting the excitation axis, and ω_t, denoting the emission axis. The latter axis is in principle the same as in a transient-absorption experiment while the former information cannot (easily) be obtained there.

The electrical field $\vec{E}(t)$ necessary for a 2D experiment is described by

$$\begin{aligned}\vec{E}(t) = \quad & \tilde{A}(t-\tilde{t}_1)\exp(-i\omega_0(t-\tilde{t}_1)+i\vec{k}_1\vec{r}) + \tilde{A}(t-\tilde{t}_2)\exp(-i\omega_0(t-\tilde{t}_2)+i\vec{k}_2\vec{r}) \\ + \quad & \tilde{A}(t-\tilde{t}_3)+i\vec{k}_3\vec{r}) + c.c.\ , \end{aligned} \tag{3.17}$$

where $\tilde{A}(t) = A(t)\exp[-i\phi(t)]$ denotes the complex-valued envelope function and ω_0 the frequency of the laser pulses [81]. Using this expression to solve Equation 3.16 the experimental and theoretical challenges become evident. Every electrical field contains 6 different contributions. Therefore, the complete expression $\vec{P}^{(3)}(r,t)$ consists of up to $6 \cdot 6 \cdot 6 = 216$ signal contributions, which can overlap in space and/or time. Using phase-cycling mechanisms [90], described in more detail in Sec. 5.5.1, or phase matching, used in the following, the amount of detected terms can be greatly reduced. Using the box geometry, i.e., the three identical excitation pulses and the local oscillator travel alongside the edges of a perfect square, as visualized in Fig. 3.4b), before they are focused into the sample, the signal is emitted in the direction $\vec{k}_S = -\vec{k}_1 + \vec{k}_2 + \vec{k}_3 = \vec{k}_{LO}$ and only 6 terms contribute in signal direction.

A second simplification is the "rotating wave approximation", which can be used if the excitation frequency is approximately the monitored transition frequency of the system under investigation. On the one hand, there are fast oscillating phase terms, depending on τ. These can be neglected in the data evaluation because positive and negative contributions cancel each other. On the other hand, also a constant signal offset or a very slowly oscillating contribution in the integral is observed, which corresponds to the effective signal.

Using all this, the polarization vector $\vec{P}^{(3)}_{rw}$ is obtained. Similar to transient-absorption data there are signal contributions in the 2D spectra corresponding to stimulated emission, ground-state bleaching, or excited-state absorption. However, the sign convention is commonly inverted. Advantageous is that the homogeneous (diagonal width) and inhomogeneous (anti-diagonal width) line width of a diagonal absorption can be obtained. Off-diagonal peaks visualize direct couplings between the connect states like transport processes. Monitoring the changes over different waiting times describe how energy transport proceeds within a photosystem.

3.3.2 Extraction of a Two-Dimensional Spectrum

Theoretically, the third-order polarization is the desired signal, however, experimentally only the signal field $\vec{E}_S(\tau, T, \omega_t)$, or even more precise the signal intensity, is measured in an optical experiment and not the polarization itself. Therefore, the relation

$$\vec{E}_S(\tau, T, \omega_t) \sim \frac{i\omega_t}{n(\omega_t)} \vec{P}^{(3)}(\tau, T, \omega_t) \tag{3.18}$$

has to be used to generate a 2D spectrum. The fact, that the probe or emission axis is already detected spectrally resolved by the spectrometer after the signal time t and no additional Fourier transformation has to be performed is already considered in this expression. The 2D spectrum itself is obtained after a second Fourier transformation, this time alongside τ, resulting in

$$\vec{S}_{2D}(\omega_\tau, T, \omega_t) = \int_{-\infty}^{\infty} i\vec{P}^{(3)}(\tau, T, \omega_t) \exp(i\omega_\tau \tau) d\tau. \tag{3.19}$$

The obtained signal field $\vec{S}_{2D}(\omega_\tau, T, \omega_t)$ is a complex-valued function depending on two frequencies [75]. By plotting the real-valued contributions, the change in absorbance is visualized. While, by plotting the imaginary parts, the change in the refraction index becomes evident. In photochemistry, the change of absorbance is commonly of higher interest, since it can easily be connected to a concentration change using the Lambert–Beer law (compare Sec. 3.2.1). Finally, the signal field also depends on the population time T. Hence, experimentally often a series of 2D spectra for different waiting times is measured. This enables tracking of photochemical relaxation both in frequency as well in time.

In principle, the electrical field of the signal response $\vec{E}_S(\tau, T, \omega_t)$ in direction $\vec{k}_S$ has to be measured directly, resulting in the absolute value and the signal phase. This is for example done in degenerate four-wave mixing measurements [91]. However, this signal is very small, aggravating the detection. The signal can effectively be amplified by using heterodyne detection. Hence, a fourth pulse is employed, the so-called local oscillator, which spatially overlaps with the emitted signal but shares no temporal overlap. Afterwards, spectral interference between the signal field $\vec{E}_S$ and the electrical field of the local oscillator $\vec{E}_{LO}$ is detected. Commonly the local

oscillator is either a pulse copy of the third pulse delayed by t_{LO} or the third pulse itself. The spectrally-resolved intensity is determined as

$$\begin{aligned} I_{SI}(\omega_t) &= \left|\vec{E}_S(\omega_t)e^{i\phi_S(\omega_t)} + \vec{E}_{LO}(\omega_t)e^{i\phi_{LO}(\omega_t)}\right|^2 \\ &= I_S(\omega_t) + I_{LO}(\omega_t) + 2\sqrt{I_S(\omega_t)I_{LO}(\omega_t)}\cos[\phi_S(\omega_t) - \phi_{LO}(\omega_t)], \end{aligned} \tag{3.20}$$

where the signal amplitude $\vec{E}_S(\omega_t)$ and phase $e^{i\phi_S(\omega_t)}$ can be extracted, while the corresponding values of the local oscillator are already known.

The extraction of the signal field from the measured data proceeds in four steps. First, a Fourier transformation of Equation 3.20, experimentally a spectrum with strong modulations, from the frequency into the time domain leads to three signal contributions: one around time zero and one each at $\pm t_{LO}$. Second, by using a rectangular Fourier window around t_{LO} the contributions from the signal field are separated by setting all other values equal to zero. This is only possible if the signal at time zero and the one centered at t_{LO} are clearly separated. Accordingly, a minimal possible delay for t_{LO} is determined. Third, an inverse Fourier transform retrieves the signal field, still overlaid with contributions from the local oscillator. In a last step, by dividing the spectrum after the Fourier transform by the LO spectrum and subtracting effects of the LO phase, the pure signal field $\vec{E}_S(\omega_t)e^{i\phi_S(\omega_t)}$ is retrieved.

The signal intensification in a heterodyned scheme is attributed to the adjustable intensity of the local oscillator while the signal intensity is always fixed for a certain pump intensity. Therefore, the detected signal without heterodyne detection is proportional to $I_S(\omega_t)$. Using the local oscillator the detected oscillating phase-sensitive term is proportional to $\sqrt{I_S(\omega_t)I_{LO}(\omega_t)}$. Hence, by increasing the intensity of the local oscillator the signal intensity also increases. As a result, in experiments with heterodyne detection often pulse intensities with ≈ 1 nJ are used compared to roughly 10 times higher intensities in pump–probe geometry based experiments without heterodyned schemes.

However, the signal extraction is aggravated by experimental challenges. Equation 3.20 represents the ideal case, while in reality the signal pulse is overlaid by scattered light. The heterodyne detection scheme not only intensifies weak signals, but also scatter, resulting in the measured intensity I_{123LO} [88, 92]. However, by setting the Fourier windows around the time of the local oscillator only coherent scatter within this time window has to be considered. By measuring the signal response with only the third pulse and the LO present (I_{3LO}) and the response with pulses one and two and the LO present (I_{12LO}) and subtracting them from I_{123LO}

$$I_{SI}(\omega_t) = I_{123LO}(\omega_t) - I_{3LO}(\omega_t) - I_{12LO}(\omega_t) \tag{3.21}$$

the signal intensity $I_{SI}(\omega_t)$ is obtained and data evaluation can proceed as described. A drawback is the necessity to perform additional measurements, which do not contribute to an increased signal-to-noise ratio. Only scatter is effectively reduced.

The signal is not only weak but also depends strongly on the phases of the excitation pulses. If one beam path is deranged, e.g., by a loose optical element, an unknown

temporal shift occurs, leading to uncertainties between the measured and the calculated time delays. As a result, the corresponding 2D spectra are distorted because not every element is attributed to the right time. Thus, phase stability between the pulses is necessary. Whereas for 2D measurements in the infrared actively stabilized possibilities exist [93], passive solutions are preferred for electronic 2D spectroscopy employing visible or ultraviolet pulses because of the shorter wavelengths. One solution is pairwise beam manipulation, where optical elements always influence two beams [82]. While this passive technique does not provide perfect phase stability, a satisfactory precision of $\lambda/100$ is commonly observed [83, 85].

As previously explained, a full 2D data set has a real-valued (called absorptive) and a complex-valued (called dispersive) contribution, which are plotted in separate spectra. However, this separation requires knowledge about the absolute phase, but often only the phase difference between two or more pulses is controllable. However, the absolute phase can be determined by comparing phase-insensitive transient-absorption data for a specific waiting time with 2D data for the same population time T. The spectrally resolved pump–probe amplitude, divided by the square root of the probe pulse intensity, is related via the projection-slice theorem to the real-valued 2D spectrum [13, 75]. More precisely, the projection of the real-valued 2D spectrum onto the ω_t-axis has to be identical to the pump–probe data, thus:

$$\vec{S}_{TA} \overset{!}{\propto} \mathrm{Re}\left(\frac{\omega_t}{n(\omega_t)}\vec{E}_{Pr}(\omega_t)\int_{-\infty}^{\infty}\vec{S}_{2D}(\omega_\tau, T, \omega_t)e^{i\phi_c + i(\omega_t-\omega_0)t_c}d\omega_\tau\right). \tag{3.22}$$

By numerically varying different values for ϕ_c, the absolute phase, and t_c, a timing offset between pulse 3 and the local oscillator, different real-valued 2D spectra are generated, which all possess the same absolute value. The corresponding projections are compared with the pump–probe data S_{TA}, which does not depend on the absolute phase at all, until sufficient convergence is obtained. This process of determining and correcting the phase offset in a 2D spectrum is called "phasing". Without this process a separation of the 2D spectrum into real and imaginary parts is not allowed, only a plot of the absolute value is possible. This signal correction is important to extract the information, which can directly be attributed to the absorbance change.

3.3.3 Relationship of Time-Resolved Spectroscopic Techniques

While coherent 2D spectroscopy allows extraction of the complete third-order signal field $\vec{S}_{2D}(\omega_\tau, T, \omega_t)$ also other, related techniques exist. They often retrieve only a small part of the latter signal but have lower requirements. Two other spectroscopic techniques, transient grating and transient absorption, are also used in this thesis and their relation to 2D spectroscopy is now explained.

One possibility is transient-grating spectroscopy in box geometry. This measurement is performed similar to a 2D experiment, but pulses one and two arrive always at the same time ($\tau = 0$) while the population time T is scanned. Therefore, transient

grating is a degenerate 2D measurement. The first two pulses interfere with each other generating a spatial modulation, which possess the wave vector $(-\vec{k}_1 + \vec{k}_2)$. Using the Bragg condition the signal field is emitted in $\vec{k}_S = (-\vec{k}_1 + \vec{k}_2 + \vec{k}_3)$. By using heterodyne detection, very low excitation densities are possible. The retrieved signal field contains information about the lifetime of the excited-state population. In principle, ESA, SE, and GSB can be detected on the probe axis and no influence of the excitation frequency is resolved. The information content is similar but not identical to a transient-absorption measurement introduced in Sec. 3.2. Often, a transient-grating experiment is performed before a 2D measurement to obtain information about photostability and basic photochemistry of a sample.

Transient-absorption spectroscopy is also a four-wave mixing experiment. The pump pulse used there has to be treated as a pump-pule pair arriving simultaneously, hence, with zero time-delay and opposing wave vectors $\vec{k}_1 = -\vec{k}_2$. The probe pulse corresponds to the third excitation pulse, causing the signal to be emitted into the same direction. Afterwards, the signal is resolved by spectral interferometry with the probe pulse itself as the local oscillator. Therefore, transient absorption and 2D spectroscopy are intrinsically connected. Reversing the point of view 2D spectroscopy can also be seen as a more advanced transient-absorption measurement with a spectrally-resolved pump-axis. Accordingly, experimental implementations are in use, where a near-monochromatic excitation pulse is scanned over many different frequencies and constructs a 2D spectrum step-by-step. However, there the time resolution is limited by the smaller excitation bandwidth [69, 94]. To the approach presented in this section is commonly referred to as Fourier transform 2D (FT-2D) and the maximal resolution, both in the time and frequency domain, is achieved.

3.3.4 Two-Dimensional Spectrometer for the Ultraviolet Regime

The 2D experiments in box geometry in Sec. 4.6 were performed with an all-reflective miniaturized setup optimized for ultraviolet applications developed by Selig and coworkers in this group [34,83,95]. While phase stability using pairwise beam manipulation is used, similar to another implementation present in the lab [83], the use of only conventional optics was not possible due to the need to generate four different beams in the ultraviolet.

The entire setup, depicted in Fig. 3.5, is surrounded by a protective housing and possesses a footprint of less than 0.1 m^2, which ensures minimal optical pathways of all beams and as little as possible introduced dispersion. The incoming laser light, consisting of a single beam, is focused onto a 2D-crossed grating (customized design, $g = 6.25$ μm, Carl Zeis MicroImaging), which generates multiple beams of differing orders. Choosing four of the same order via a mask in a squared arrangement, the three necessary excitation pulses and the local oscillator are generated. All four are nearly perfect copies of each other. Using two off-axis parabolic mirrors (OAP) with the same focal length $f = 15$ cm the beams are recollimated and focused onto the

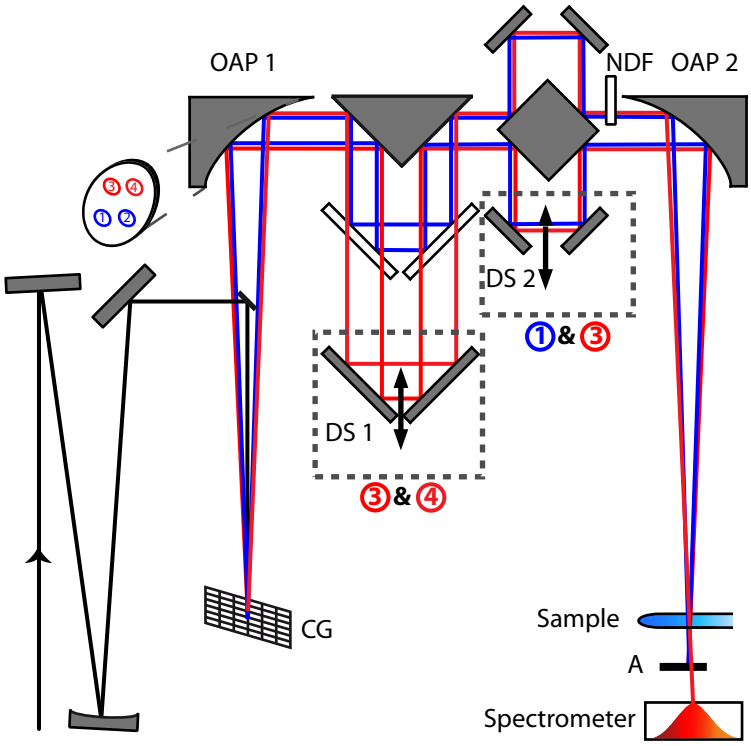

Figure 3.5: Schematics of the used 2D setup optimized for applications in the UV. After generation of four pulses by a crossed grating (CG), pair-wise beam manipulation is possible by two delay stages (DS1, DS2). Collimation and focusing is performed by off-axis parabolic mirrors (OAP1, OPA2). The beams travel in a perfect square (box geometry). All emitted signal contributions, which do not travel in direction $\vec{k}_{LO}$ are blocked and the signal response is measured in a heterodyned fashion. Adapted from Ref. [34].

sample plane after different pulse pairs travel over a pair of delay stages. Using a motorized delay stage (MFA-CC Newport) and a piezo actuator (PX 200 CAP, Piezosysteme Jena) beams three and four can be delayed in relation to one and two (DS 1). By usage of a second piezo actuator of the same type beams one and three can be delayed in relation to two and four (DS 2). This combination of three different delay adjustments enables a systematic scanning of T and τ as explained in detail in Ref. [96]. The local oscillator (pulse four) is additionally delayed by 2 ps using a neutral density filter wheel (the only dispersive element), which additionally enables adjustment of the signal strength. After the sample is excited, only the heterodyned signal is detected using the same type of spectrometer as in the transient-absorption setup described in Sec. 3.2.3. Pulses one, two, and three can be blocked by mechanical shutters, enabling measurements of the different scattering contributions as previously explained. However, as these shutters are not synchronized to the laser repetition rate no shot-to-shot measurements are possible. A more detailed summary of the setup is given in Ref. [92], detailing information about the construction, phase stability and obtained 2D spectra in the ultraviolet spectral range.

Chapter 4

Ultrafast Exciton Dynamics of a Bisporphyrin

4.1 Introduction

Porphyrins, a cyclic subclass of tetrapyrroles, constitute a class of molecules whose derivatives are of great importance for a wide facet of processes in nature. Tetrapyrroles and their congeners serve as cofactors in proteins where they fulfill a variety of functions: for example, chlorophyll a, a reduced porphyrin containing magnesium ions, plays a central role in photosynthetic electron and energy transfer, whereas heme, an iron porphyrin, participates in the transport and storage of diatomic gases. To understand the primary steps of the aforementioned processes, femtosecond investigations have emerged as an essential tool [97, 98]. The versatility of synthetic porphyrins is also widely exploited in many different emerging areas. In medicine, synthetic porphyrins are used for the treatment of neurodegenerative diseases [99] and cancer [100]. In physics and chemistry, applications comprise molecular electronics [101, 102], artificial light harvesting [103], ultrafast electron transfer in donor–acceptor complexes [104, 105], and efficiency control of organic solar cells [106]. Understanding the ultrafast processes involved in all of these applications is a necessity for a full physicochemical characterization of (artificial) porphyrins, as for example the light signal transmission in molecular photonic wires proceeds through excited-state energy transfer [107]. Actually, a multitude of time-resolved studies on various porphyrinoid systems, differing in their central metals and substitution patterns, some published recently, documents this trend [105, 108–113].

In this chapter the ultrafast dynamics of a directly β,β'-linked bisporphyrin, which contains a unique framework within the class of porphyrin dimers because of its intrinsic axial chirality, is explored in a racemic mixture and compared to the photophysics of its monomeric building block [114–117]. The results were obtained in a cooperation between three different research groups. Prof. Dr. G. Bringmann and coworkers were responsible for the synthesis (Dr. D. C. G. Götz) and the density functional theory (DFT) (Dr. T. Bruhn) (Institut für Organische Chemie, Universi-

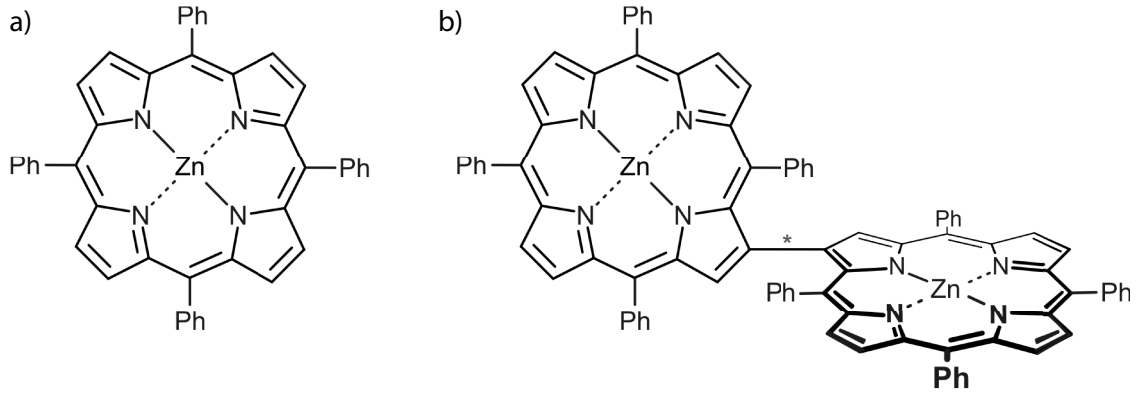

Figure 4.1: Molecular structures of: a) ZnTPP, a metalated monoporphyrin, and b) $(ZnTPP)_2$, which consists of two ZnTPP units connected via direct β,β'-linkage; only one of the two stable enantiomers (with P-configuration) of the racemic mixture is shown.

tät Würzburg), while Prof. Dr. D. Guldi and M. Sekita obtained the nanosecond data (Department Chemie und Pharmazie, Universität Erlangen-Nürnberg). Figure 4.1b) displays the structure of bis[tetraphenylporphyrinato-zinc(II)] [$(ZnTPP)_2$], which consists of two identical monoporphyrins, namely 5,10,15,20-tetraphenylporphyrins (ZnTPP) [Fig. 4.1a)], linked via a covalent bond between two β-positions. In contrast to directly linked bisporphyrins reported previously [118, 119], the axial chirality of the 'super-biaryl' $(ZnTPP)_2$ is independent of the substitution pattern of the two subunits, but solely arises from its intrinsically C_2-symmetric β,β'-coupling motif. The bulky phenyl substituents, introducing large steric hindrance in combination with the Zn-metalation, which rigidifies the molecular backbone, and the direct linkage without any spacers leads to a rigid bisporphyrin, effectively hindering aggregation and rotation of the monomeric subunits [115]. This results in two stable enantiomers in P- or M-configuration, contained in the racemic sample in which the experiments were performed. In contrast, directly *meso,meso'*-linked zinc bisporphyrins seem more flexible as far as temporal relaxation of photoexcited porphyrins is concerned, stressing the photophysical interest in β, β'-linked bisporphyrins [120].

In the following, the photodynamics of $(ZnTPP)_2$ are presented in a comprehensive way revealing the complex reaction scheme. Section 4.2 summarizes the state of literature for porphyrins and introduces the concept of molecular excitons. Transient-absorption measurements comparing the dimer (Sec. 4.5) to its building block ZnTPP (Sec. 4.4) together with excitation into the first and second electronically excited state show that excitonic effects strongly contribute to the photophysical behavior in the dimer. The influence of these excitonic contributions to the relaxation pathways is then directly visualized with the help of coherent electronic 2D spectroscopy in Sec. 4.6, additionally combined with degenerate transient-absorption and transient-grating measurements possessing ultrafast time resolution. These experiments reveal that in addition to ultrafast non-radiative relaxation, population transfer happens within the excited states of the dimer. All conclusions inferred from the different measurements are then summarized in Sec. 4.7.

Parts of this chapter were already published and are reproduced in part with permission from Ref. [116][1] (Sec. 4.4 and 4.5) and from Ref. [117][2] (Sec. 4.6).

4.2 Physicochemical Properties of Porphyrins

As a result of their diversity, porphyrins are the system of choice for many photochemical and photophysical experiments. Therefore, an overview of their molecular chemistry (Sec. 4.2.1) and the modeling of porphyrins (Sec. 4.2.2) is given, extended by the introduction of molecular excitons (Sec. 4.2.3).

4.2.1 Spectral Characterization of Porphyrins

Porphyrins, also called cyclic tetrapyrroles[3], are large planar molecular systems consisting of four pyrrole rings linked via methine groups, used as bridges, in a cyclic arrangement. As a result of this cyclic arrangement, a discoidal heterocyclic macrocycle with a common conjugated π-system is formed [121,122]. The basic porphyrin, with the Lewis structure shown in Fig. 4.2, is called "free base (porphin)" and possesses 18 π-electrons, thus, obeying Hückel's rule for aromaticity, which requires $(4n + 2)\,\pi$-electrons [123]. The free base is a tautomeric structure because the four inner nitrogen atoms are only bound to two hydrogen atoms in order to form an electronically saturated compound. Thus, two different stable configurations, each with the hydrogen atoms placed on the opposite site of each other are possible [124]. By changing the environment of this π-system, feasible by two different methods, the chemical properties of porphyrins are tailorable for a specific application [125].

First, the macrocycle possesses 20 different binding positions, separable into three categories. There are 8 α-positions where the carbon atom is next to a nitrogen atom, representing a functional unit, 8 β-positions, which are two carbon atoms apart from a nitrogen atom, and 4 *meso*-positions, which are located at a completely achiral environment. By adding substituents possessing positive or negative mesomeric and/or inductive effects the properties of the π-system are changed. Exemplary binding positions are shown in Fig. 4.2 by black arrows. In addition, the N-H-H-N axis is arbitrarily chosen as the x-direction (blue arrow) of all transition dipole moments while the N-N axis represents the y-direction (red arrow).

Second, via insertion of a metal into the center of the macrocycle the structure of the π-system also changes, resulting in three different kinds of metalloporphyrins. These are closed-shell metalloporphyrins with zinc or magnesium central atoms, which possess large spin-orbit couplings. These result in non-radiative transitions between singlet and triplet states, which are normally forbidden in a dipole-dipole approximation with neglected spin-orbit coupling. However, for these porphyrins the

[1] Copyright: PCCP Owner Societies [2013], DOI: 10.1039/C2CP23608G
[2] Copyright: Institute of Physics [2013], DOI: 10.1088/1367-2630/15/2/025006
[3] There exist also linear tetrapyrroles, which are not treated within this thesis.

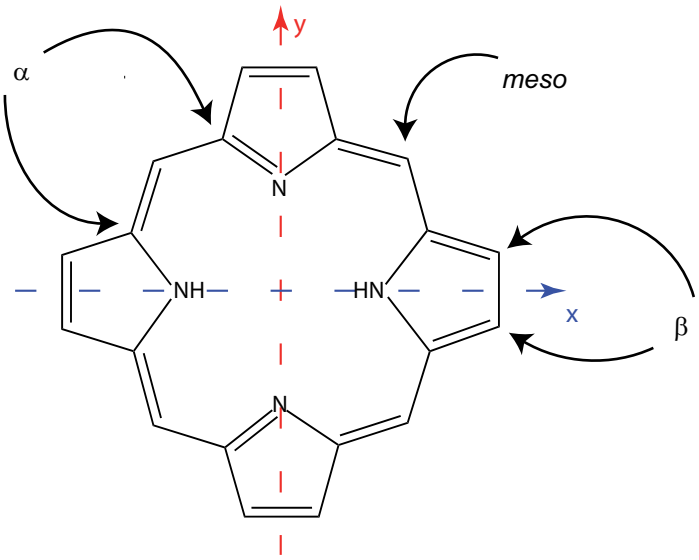

Figure 4.2: Chemical structure of the free base porphyrin. Exemplarily, binding positions are marked by black arrows and the direction of the two transition dipole moments through the N-N axis are marked by blue (x-direction) and red (y-direction) dotted arrows.

coupling contributions are so strong that they cause important reaction pathways. In open-shell, paramagnetic porphyrins with cobalt or copper atoms fluorescence is quenched while in open-shell diamagnetic porphyrins with nickel inside the emission properties are dominated by spin-orbit coupling due to low lying metal triplet states.

As a consequence of the aromaticity porphyrins possess multiple absorption bands reaching from the ultraviolet into the visible spectral range. These bands can be spectrally shifted and altered in their relative intensity by metalation and differing substitution patterns. Since basically the properties can be tailored to one's wishes, the physicochemical interest in these photosystems is explained. Porphyrins possess a broad but weak absorption in the visible spectral range, the so-called Q band, which represents the first electronically excited singlet state S_1. For the free base porphyrin four different absorptions are present resulting from the D_{2h}-symmetry, hence, possessing only 2 mirror planes and a twofold rotational axis, of the macrocycle, while after insertion of a metal only two bands remain. After metalation the tautomerism is no longer present and the transition dipole moments are now degenerate for x- and y-directions resulting in the new more symmetric point group D_{4h}, possessing a four-fold rotational axis. An additional consequence of this degeneracy is the E_u-symmetry of all transitions into the Q band, which are of the π-π^* kind [125].

A much stronger absorption (5 to 100 times more intense), the so-called Soret or B band, is located at around 400 nm and caused by transitions into the second excited singlet state S_2. For Zn-metalloporphyrins, which are used in this work, all emission and absorption properties are based on the properties of the π-electrons in the macrocycle and no additional absorption bands emerge resulting from metal-to-ring charge transfer [126].

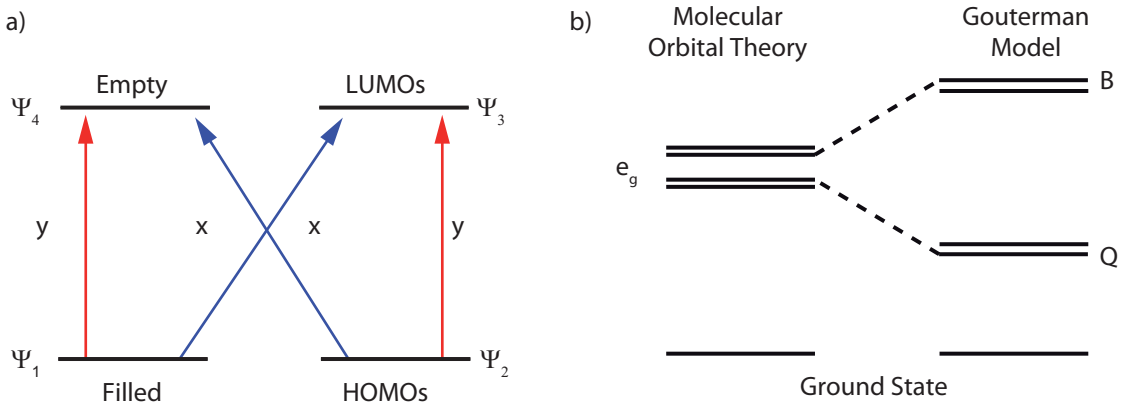

Figure 4.3: a) Gouterman's four orbital model for the free-base porphyrin. The directions of the transition dipole moments are marked in blue (x-direction) and red (y-direction) as defined via the two N-N axes. b) Resulting states after pure molecular orbital calculations (left) and after inclusion of a configuration interaction term (right).

4.2.2 The Gouterman Model

In porphyrins, two different electronically excited states, which strongly differ in their absorption strength, are present. Therefore, the classic molecular orbital theory consisting of one highest occupied molecular orbital (HOMO) and one lowest unoccupied molecular orbital (LUMO) cannot even sufficiently explain the linear photophysical characteristics. Martin Gouterman developed in the 1960's a model which explains all essential features of free-base and metalloporphyrins, which nowadays is still used for intuitive explanations of the observed photophysical effects [125,127]. His approach combines previously used molecular orbital calculations combined with configuration interaction theory [128].

In a first step the two highest occupied and the two lowest unoccupied molecular orbitals are calculated via Hückel theory. One HOMO and one LUMO are not sufficient because in porphyrins two HOMOs and LUMOs are always degenerate. Thus, they are not separable. Afterwards, configuration interaction theory, which generates new effective states by superimposing two molecular orbitals, is applied to both HOMOs and LUMOs. This is used to explain the large difference in the absorption coefficients of the first and second electronically excited singlet state. By considering configuration interaction electronic transition are no longer directly related to a single molecular orbital aggravating descriptive explanations. The relative contribution of each molecular orbital for a certain transition is strong if both states share the same symmetry and increases even further with shrinking energetic difference.

In Fig. 4.3a) the HOMOs and LUMOs for a non-metalated porphyrin are shown. All transitions are isoenergetic and the transitions $\Psi_1 \rightarrow \Psi_4$ ($\Psi_1 \rightarrow \Psi_3$) and $\Psi_2 \rightarrow \Psi_3$ ($\Psi_2 \rightarrow \Psi_4$) share the same symmetry, thus, interact strongly. The quantitative contribution of each transition dipole moment $\vec{\mu}_{j,g}^{MO}$ to the transition $\Psi_i \rightarrow \Psi_f$ (abbreviated $\Psi_i\Psi_f$) is the configuration-interaction coefficient $A_{j,g}^{i,f}$. $A_{j,g}^{i,f}$ denotes the relative contribution of the $\Psi_j \rightarrow \Psi_g$ transition to the effective transition from $\Psi_i\Psi_f$

with the transition dipole $\vec{\mu}_{i,f}^{CI}$, hence

$$\vec{\mu}_{i,f}^{CI} = \sum_{j,g} A_{j,g}^{i,f} \vec{\mu}_{j,g}^{MO}. \tag{4.1}$$

Since the energies of the two contribution states are degenerate the configuration-interaction coefficient $A_{j,g}^{i,f}$ for all contributions is $A_{j,g}^{i,f} = \pm 1/\sqrt{2}$. Accordingly, the first four singlet excited states resulting from all possible linear combinations are

$$Q_x = \frac{1}{\sqrt{2}} \left(\Psi_1 \Psi_3 + \Psi_2 \Psi_4 \right), \tag{4.2}$$

$$Q_y = \frac{1}{\sqrt{2}} \left(\Psi_1 \Psi_4 - \Psi_2 \Psi_3 \right), \tag{4.3}$$

$$B_x = \frac{1}{\sqrt{2}} \left(\Psi_1 \Psi_3 - \Psi_2 \Psi_4 \right), \tag{4.4}$$

$$B_y = \frac{1}{\sqrt{2}} \left(\Psi_1 \Psi_4 + \Psi_2 \Psi_3 \right), \tag{4.5}$$

with x and y as the direction of the resulting transition dipoles [125]. Two transitions belong to higher energetic states, thus, forming the Soret band (B_x, B_y). The remaining two transitions form the lower-energetic Q band (Q_x, Q_y) as visualized in Fig. 4.3b). The degeneracy of the HOMOs and LUMOs leads to an effective transition probability of 0 in both the Q_x and Q_y state. If the degeneracy is lifted but the states are still in close proximity upper tendencies (strong B-band/weak Q-band absorption) remain valid [127]. Moreover, the Q band is generally associated with the first electronically excited singlet state S_1 while the Soret band relates to the second electronically excited singlet state S_2.

Therefore, the Gouterman model provides a comprehensible picture for the description of photophysical processes in porphyrins. Furthermore, the necessity of separating the transition dipole moments into two effective ones, which possess orthogonal directions, is stressed. While they are degenerate in a monoporphyrin, this can lead to different states, possessing different energies in case of a dimer. This will become evident when excitons and/or more complex porphyrinoid systems are considered in the next sections.

4.2.3 Molecular Excitons

In solid state physics, especially to explain the absorption of a photon by an atomic lattice resulting in moving charge carriers, often the concept of excitons, introduced by Frenkel in 1931 [129] is used as an explanation for the observed characteristics. Over the course of time this concept was extended beyond the well-ordered lattice, via molecular crystals for polymers and finally for dimers in solution [130]. Three different definitions of an exciton, each stressing the importance of different properties, thus, explaining certain aspects better, are often used [131]. These definitions are:

- An exciton corresponds to an excitation of an assembly of atoms in concert in contrast to a localized excitation. This definition explains the properties of two-dimensional atomic lattices well.
- An exciton is a wave packet traveling through an assembly of atoms and arises from a superposition of states belonging to single atoms. Especially electronic energy transfer is explained well in this picture.
- An exciton is a moving, neutral excitation "particle", which consists of a negative charged electron combined with a positive charged hole and linked movements through the compound where it was generated. It is important to note that no actual ionization takes place but essentially the behavior in the valence and conduction band of semiconductors is explained within this definition.

These definitions and the deducted properties describe the spectroscopic characteristics and the flow of excitation energy within all kinds of media at different temperatures. The next section is based on the comprehensive study of excitons in [132] and is predominantly based on the second description.

Within this work only excitonic effects in dimers will be discussed for two reasons (a theoretical as well as an experimental treatment of excitonic effects in multichromophore systems can be found in Ref. [92]). On the one hand, the main focus of Chapter 4 is $(ZnTPP)_2$, a porphyrin dimer, and dimers are the simplest system where these excitonic effects occur. On the other hand, by treating all effects within the dimeric framework a solid theoretical background without many approximations can be used in contrast to very large systems, which require more assumptions, for example in regard to their number of allowed transition states. The following description is based on physical dimers, defined as two interacting molecules which do not need to be chemically-linked to each other [132]. Hence, a very generalized approach can be used and the results are applicable to a lot of different systems. In addition, strong coupling is assumed between the monomers and all wave functions are not properly antisymmetrized. This anti-symmetrization can be neglected as long as there is no exchange of electrons between the two subunits. All obtained results can be transferred to chemical dimers. The latter is defined by the existence of a real chemical bound between the building blocks, as it is the case for the covalently-linked $(ZnTPP)_2$.

The behavior of two identical monomeric units each with their own Hamiltonian $\hat{H}_n$ is determined by two independent Schroedinger equations

$$\hat{H}_n|\varphi_n^i\rangle = \varepsilon_n^i|\varphi_n^i\rangle. \tag{4.6}$$

The eigenenergies ε_n^i and their eigenstates $|\varphi_n^i\rangle$ are dependent on n which denotes the monomeric unit (using subscripts 1 and 2) and i referring to the ground or the first excited singlet state of each subunit (using superscripts 0 and 1). Accordingly, the Hamiltonian of the dimer $\hat{H}$ consists of the two monomeric terms ($\hat{H}_1$, $\hat{H}_2$) and an additional exchange potential ($\hat{V}$)

$$\hat{H} = \hat{H}_1 + \hat{H}_2 + \hat{V}, \tag{4.7}$$

where all three are described by point-dipole point-dipole terms obtainable via multipole expansion. By using only the quadratic term of this expansion the simplest possible approximation is used. While this is sufficient here, there are cases where higher order contributions need to be taking under consideration. In order to obtain the new dimeric eigenenergies and eigenstates, one has to solve the corresponding Schroedinger equation

$$\hat{H}|\Psi^f\rangle = E^f|\Psi^f\rangle. \tag{4.8}$$

The ground-state wave function $|\Psi^0\rangle$, where neither monomer is excited and the first excited-state wave function $|\Psi^f\rangle$, which is a linear combination of two terms, where one of the monomers is excited, are

$$|\Psi^0\rangle = |\varphi_1^0\varphi_2^0\rangle, \text{ and} \tag{4.9}$$

$$|\Psi^f\rangle = c_{f1}|\varphi_1^1\varphi_2^0\rangle + c_{f2}|\varphi_1^0\varphi_2^1\rangle. \tag{4.10}$$

Both are obtained via the valence bond or Heitler-London theory, i.e., the eigenfunctions of the perturbed system are equal to linear combinations of the product of molecular eigenfunctions. Therefore, only one ansatz is necessary to describe the electronic behavior in contrast to molecular orbital theory, which requires one ansatz for each electron [42]. The coefficients c_f represent the relative excitation of the two subunits. In a homodimer, this means for two identical monomers, the energies ε_n^i are the same, which simplifies the possible coefficients to $c_{11} = c_{12} = c_{21} = -c_{22} = \frac{1}{2}\sqrt{2}$ after performing the necessary normalization. Inserting these values in Equation 4.10 leads to two non-degenerate eigenstates belonging to the first electronically excited state

$$|\Psi^\pm\rangle = \frac{1}{\sqrt{2}}\left(|\varphi_1^1\varphi_2^0\rangle \pm |\varphi_1^0\varphi_2^1\rangle\right). \tag{4.11}$$

By solving the Schroedinger equation 4.8 with these wave functions in addition to an arbitrarily chosen ground-state energy of 0 the energy of the first electronically excited state of a dimer is

$$\begin{aligned}\mathcal{E}^\pm &= \langle\Psi^\pm|\hat{H}|\Psi^\pm\rangle \\ &= \frac{1}{2}(\varepsilon_1^1 + \varepsilon_2^1 + \underbrace{\langle\varphi_1^1\varphi_2^0|\hat{V}|\varphi_1^1\varphi_2^0\rangle}_{=:V_{11}} \pm \underbrace{\langle\varphi_1^1\varphi_2^0|\hat{V}|\varphi_1^0\varphi_2^1\rangle}_{=:V_{12}} \pm \underbrace{\langle\varphi_1^0\varphi_2^1|\hat{V}|\varphi_1^1\varphi_2^0\rangle}_{=:V_{21}} + \underbrace{\langle\varphi_1^0\varphi_2^1|\hat{V}|\varphi_1^0\varphi_2^1\rangle}_{=:V_{22}}).\end{aligned} \tag{4.12}$$

Again using the fact that for a homodimer the eigenenergies and corresponding wave functions are identical, i. e., $\varepsilon_1^1 = \varepsilon_2^1$ and $\varphi_1^n = \varphi_2^n$, resulting in $V_{11} = V_{22}$ and $V_{12} = V_{21}$, this term is simplified to

$$\mathcal{E}^\pm = \varepsilon^1 + V_{11} \pm V_{12}. \tag{4.13}$$

Equation 4.13 shows the energies of the two split excitonic states, which will be compared to the first electronically excited state in the corresponding monomers. The energies consist of three contributions. The main energy contribution in the dimer for both states is ε^1, which is also the excited-state energy of the monomeric

building block. In addition, both new states $\mathcal{E}^{\pm}$ are shifted by V_{11} towards lower energies in comparison to the monomer. This stabilization stems from increased van der Waals interaction in the dimer because the proximity of the two subunits is beneficial for the entire system from an energetic perspective. The third and most interesting term is the Davydov splitting $2 \cdot V_{12}$, because this term describes the energetic difference of the two non-degenerate states, which previously formed a single first excited state. This term basically is the main difference going from a monomer to a dimer and splits the energy level of the first excited state, resulting in a double peak structure. The Davydov splitting $2 \cdot V_{12} = 2 \cdot V_{\mathrm{D}}$ is mainly caused by dipole-dipole interaction and results from

$$\hat{V}_{\mathrm{D}} = \frac{\vec{\mu}_1 \cdot \vec{\mu}_2 - 3(\vec{\mu}_1 \cdot \hat{R})(\vec{\mu}_2 \cdot \hat{R})}{R^3}, \tag{4.14}$$

with the unit vector

$$\hat{R} = (\vec{r}_2 - \vec{r}_1)/|\vec{r}_2 - \vec{r}_1| \tag{4.15}$$

as the relative position vector of the two subunits positioned at $\vec{r}_1$ and $\vec{r}_2$ in relation to the origin, R as the spatial separation and $\vec{\mu}_n$ as the transition dipole moment of the first or second monomer.

Therefore, the absorption spectra of a dimer, which possesses two absorption bands in the vicinity of the monomeric transition from the ground state into the excited state, can be described by a shift and a subsequent splitting of the eigenenergies. The lower-energetic state is denoted as $\mathrm{S}_{1\alpha}$ while the higher-energetic state is denoted as $\mathrm{S}_{1\beta}$ from now on. The relative strength of the two absorption bands, which do not represent the excitation of a single monomer but are resulting from a superposition of excited monomeric states, can differ strongly. The absorption dipole strength for the two transitions is

$$D_{\pm} = \left| \frac{1}{\sqrt{2}}\vec{\mu}_1 \pm \frac{1}{\sqrt{2}}\vec{\mu}_2 \right|^2 = |\vec{\mu}|^2(1 \pm \cos\theta), \tag{4.16}$$

where θ represents the angle between the two transition dipole moments μ_n and $\pm$ denotes the energetically higher or lower state.

Two common configurations for dimers are the parallel arrangement of the building blocks, corresponding to head-to-tail configuration (J-dimer) or to the stacked sandwich-type arrangement (H-dimer) where one monomer is on top of the other. For both cases the angle $\theta = 0°$ is observed, thus, the absorption dipole strength has its maximum value for one transition while the other transition is completely forbidden. However, resulting from the in-line or parallel orientation of the transition dipole moments, the allowed or forbidden transition is exchanged for the two dimer configurations as visualized in 4.4. For a dimer with oblique transition dipole moments, which often corresponds to chemical dimers, both transitions are allowed albeit the effective transition for each transition is weaker. However, easy estimation whether the dimer is more of an J-type or more of an H-type system is possible because the main absorption is then either red- (J-type) or blue-shifted (H-type)

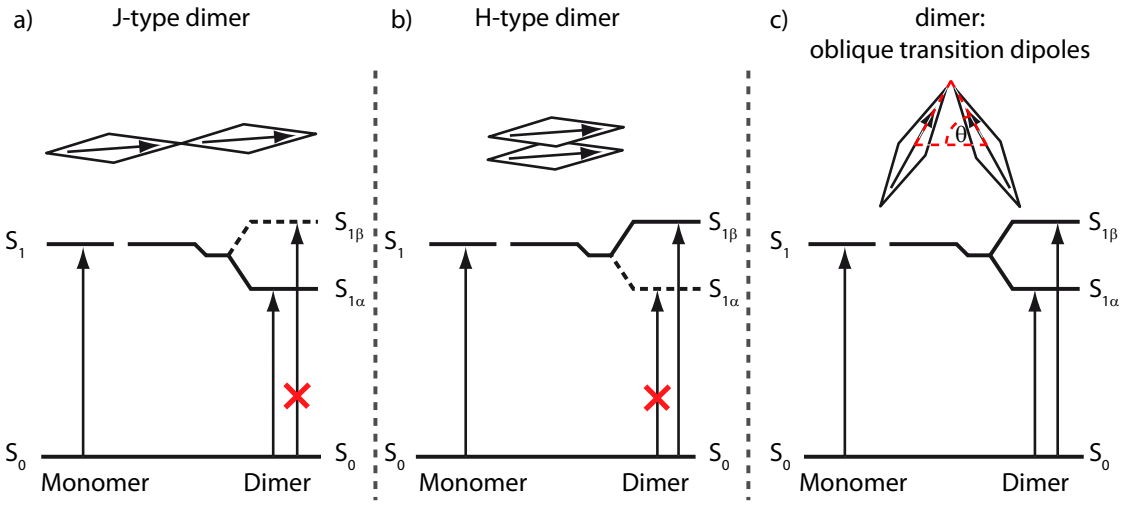

Figure 4.4: Transition dipole moment orientation and exciton energy level-diagrams for: a) a J-type dimer (transition dipole strength: 0 for $S_{1\beta}$); b) an H-type dimer (transition dipole strength: 0 for $S_{1\alpha}$); c) a dimer with oblique relative transition dipole moments: both transitions are allowed. Dotted horizontal lines represent states whereto no transfer occurs; solid lines represent the states which are populated after excitation. The dimer itself is represented by two rhomboid structures with inserted arrows indicating the direction of the main dipole moment above each diagram. Principle adapted from [130].

in regard to the monomer. This is only valid if the Davydov splitting is large in comparison to the increased stabilization caused by the additional van der Waals interaction ($|V_{11}| < |2 \cdot V_{\mathrm{D}}|$).

The previous paragraphs dealt with the splitting of the excited states in a dimer and considered the effects of a single light-matter interaction. However, time-resolved properties and multiple excitations were not considered. Taking these into account the energy level diagram has to be extended by an additional state, the so-called double-excited state at an energy level of $E = h\nu_{\mathrm{S}_{1\alpha}} + h\nu_{\mathrm{S}_{1\beta}}$. This state results from the fact that a system excited into either $S_{1\alpha}$ can absorb a second photon, before the first excitation has relaxed, and be excited into $S_{1\beta}$ and vice versa. In order to excite directly into this state a two-photon excitation is necessary as was theoretically and experimentally shown in Ref. [133]. This additional signal corresponds to an ESA signal in a pump–probe experiment and the first excitation to GSB, however, both the excitation into $S_{1\alpha}$ and $S_{1\beta}$ originates from the same ground-state belonging to the entire dimer [132]. The energy level diagram in Fig. 4.5a) corresponds to this scheme with violet arrows denoting transitions with the frequency of the $S_{1\beta}$-S_0 transition and blue with the $S_{1\alpha}$-S_0 transition. The black arrow symbolizes possible relaxation from $S_{1\beta}$ into the energetically more favorable $S_{1\alpha}$.

In the following paragraphs it is described how excitonic effects occur in a modeled pump–probe experiment. Fig. 4.5b),c) shows calculated difference spectra from a hypothetical transient-absorption experiment for a system with the energy level diagram in Fig. 4.5a). Arbitrarily Gaussian shaped pulses with a width of 7 nm centered at 427 nm ($S_{1\beta}$) and 443 nm ($S_{1\alpha}$) were chosen. All possible transitions

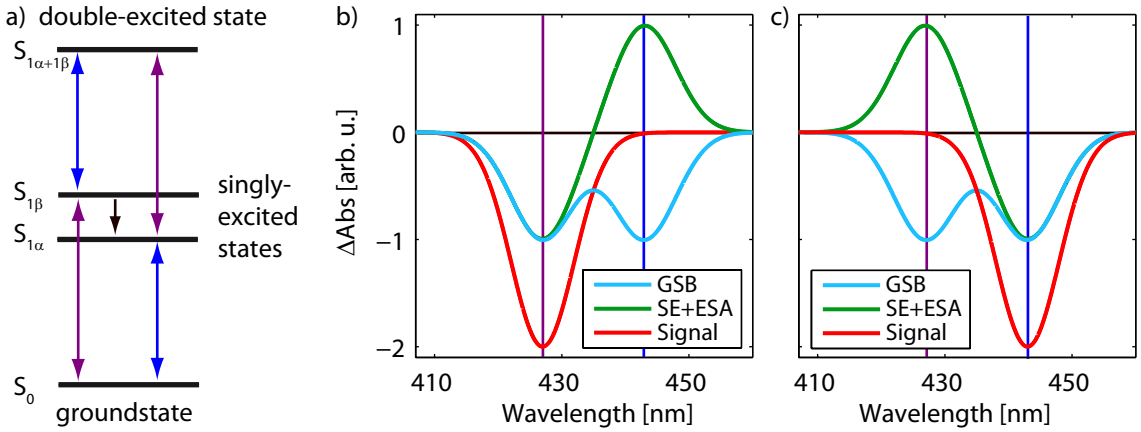

Figure 4.5: a) Energy level diagram of dimer consisting of S_0, $S_{1\alpha}$, $S_{1\beta}$, and the double-excited state. Transitions with the $S_{1\alpha}$-S_0 frequency are in blue, transitions with the $S_{1\beta}$-S_0 one are in violet. b) Difference spectra obtained by exciting directly into $S_{1\beta}$ consisting of GSB (blue) and a combined SE and ESA signal (green). c) Difference spectra after exciting directly into $S_{1\alpha}$ consisting of GSB (blue) and a combination of SE and ESA (green) signal.

(SE, GSB, and ESA) were assumed to be identical in their corresponding absorption strength. The red difference spectrum consisting of a large negative peak at 427 nm in Fig. 4.5b) corresponds to the signal received after excitation into $S_{1\beta}$. Accordingly, the common ground state is depopulated resulting in a bleach of both absorption bands (blue spectra). However, stimulated emission is only possible from $S_{1\beta}$ since the entire excited-state population is there, while a second photon can excite the dimer into the double-excited state resulting in a strong positive ESA. These two effects combined result in the green contribution. Hence, it seems that only the $S_{1\beta}$ transition is bleached while the entire excitable ground-state population is gone.

By contrast, Fig. 4.5c) corresponds to the difference spectra obtained after excitation solely in $S_{1\alpha}$ or after relaxation from $S_{1\beta}$ into $S_{1\alpha}$ has occurred. Here, seemingly only the weaker transition is bleached (red) while again the entire ground state is depopulated, as opposed to half of it, since half of the bleached signal has vanished (blue) but this time SE is possible from $S_{1\alpha}$, while the absorption of a photon with the energy of the $S_{1\beta}$ transition leads to the double-excited state. It is important to note that no relaxation effects are considered, the two spectra correspond to static configurations, where the entire population is either in $S_{1\alpha}$ or $S_{1\beta}$.

4.3 Experimental Conditions in the Transient-Absorption Experiments

ZnTPP and $(ZnTPP)_2$ were synthesized according to literature [114, 115] in the research group of Prof. Dr. G. Bringmann (Institut für Organische Chemie, Universität Würzburg), additionally purified by preparative gel permeation chromatography (GPC) and analyzed by NMR and UV/VIS spectroscopy before and after the optical

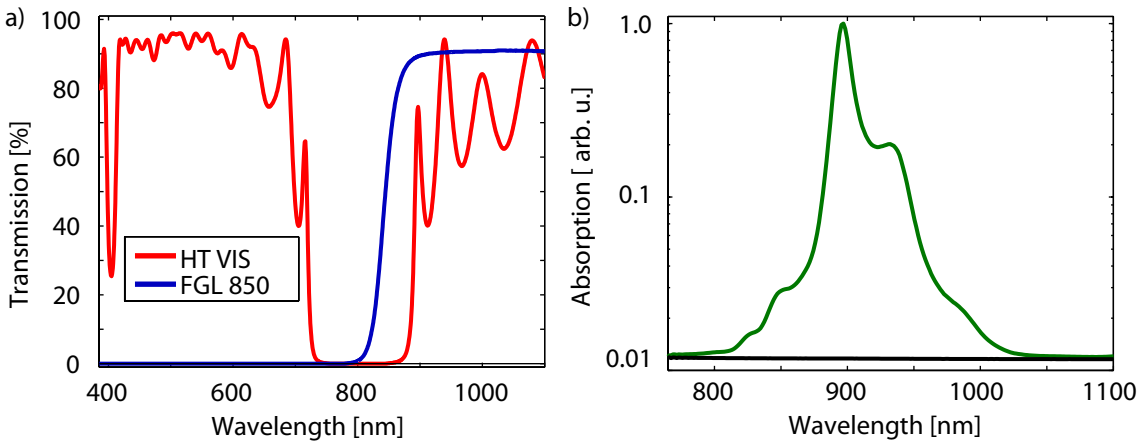

Figure 4.6: a) Optical transmission properties of two filters eliminating the seed in the probe beam. The HT VIS (red) possesses a rather flat high-transmission curve in the entire visible domain (the dip at 400 nm results from the dielectric coating, blocking the fundamental at 800 nm [26]). The FGL850 longpass filter (Thorlabs) transmits only above 850 nm (blue). b) Supercontinuum spectrum (green) obtained in the NIR after blocking of the fundamental and all visible contributions. Please note the logarithmic scale and the nonzero spectrometer noise level (black).

experiments to exclude photodegradation. The molecules were dissolved in ethanol with a concentration of 130 µM (ZnTPP) or 75 µM [$(ZnTPP)_2$], corresponding to a maximal optical density of 1 OD or 0.75 OD in the Soret band, respectively, directly prior to the femtosecond time-resolved measurements. This high absorption was chosen in order to measure the photodynamics of the first two excited singlet states, whose effective absorption strengths differ at least one order of magnitude, within a single measurement.

For the spectroscopic experiments, steady-state absorption spectrometers (Hitachi U-2000 or JASCO V 670) with a 200 µm flow cell and a fluorescence spectrometer (JASCO FP-6300) with a 1 mm flow cell were used. Both a femtosecond [20] and a nanosecond transient-absorption spectrometer setup were employed.

Details on the transient-absorption setup and the measurement procedures are given in Chapter 3.2. In this chapter both 400 nm excitation pulses, resulting in a time resolution of $\approx$ 100 fs, focused down to a diameter of $d = 200$ µm, as well as 560 nm pulses, resulting in a time resolution of $\approx$ 50 fs, focused down to 50 µm, were used. The continuum probe pulses had a width of $\approx$ 40 nm slightly depending on the respective probe wavelength. All measurements were performed in the magic angle configuration with an angle of 54.7° between pump and probe pulse polarization by changing the pump polarization direction with a half-wave plate in order to avoid anisotropic signal contributions [57].

In addition to common measurements with a probe continuum in the visible spectral range, also experiments with a probe in the NIR regime were performed [134]. One possibility to conduct these experiments would be the use of two (N)OPAs, e.g., used in Ref. [110] — one serving as the ultraviolet or visible pump pulse source and

the other one as the near-infrared probe pulse generator [135]. However, because of the small bandwidth of the probe pulse a combination of single measurements would be necessary in order to obtain pump–probe data, which is frequency-resolved along the probe axis. Using the fact that spectral broadening after focusing an intense beam into a nonlinear media is observed for both directions of the frequency axis (Fig. 2.2d), [136]) nearly the same experimental configuration as for transient-absorption measurements in the visible can be used for these kinds of experiments. For example, this was demonstrated for the laser dye IR140 by Xu and coworkers who identified and investigated a cis/trans photoisomerization in this dye [137–139].

The transient-absorption setup described in Sec. 3.2.3 is used for these experiments with the pump beam configuration unchanged. However, some modifications in the probe beam were necessary in order to access the spectral range above 800 nm. As explained there the fundamental is blocked after the probe continuum is generated, in order to avoid saturation of the detector because the intensity of the 800 nm exceeds the white-light intensity by multiple orders of magnitudes. Fig. 4.6a) shows the spectral transmission properties of the edge filter HT VIS (red) (custom designed by Laser Components) used in the standard setup, however, measured with unpolarized light in a steady-state spectrometer. Basically the entire visible spectral range and even parts of the near-infrared regime pass the filter with a transmission coefficient of more than 70%. The dip at 400 nm is a result of the dielectric coating of the mirror, which is designed to block 800 nm, which also impacts harmonics of this wavelength [26]. This edge filter cannot be used in the NIR because the employed monochromator (Acton SpectraPro 2500i) is based on a grating, thus, only one octave broad spectra are detectable at once in contrast to prism based detector systems. The reason for this is that the second order signal contributions of the 400 to 750 nm white-light contributions spectrally overlap with the near-infrared spectrum above 800 nm, thus, aggravating the signal identification and retrieval. This was avoided by the use of a commercial longpass filter (Thorlabs FGL850, 2 mm Schott Glass), which possesses very good transmission properties above 850 nm [blue curve, Fig. 4.6a)] instead of the standard HT VIS filter. In addition to the very flat transmission curve above 900 nm, the entire visible spectral range and the 800 nm fundamental is nearly completely blocked. In Fig. 4.6b) the measured supercontinuum (green) is shown in a semi-logarithmic plot. The black curve corresponds to the dark background of the CCD camera. The usable wavelength range is from 850 to 1000 nm, above which only very weak intensities were observed. In addition, the spectrometer can still be calibrated by common calibration lamps like Neon, Hg(Ar), and Krypton, which possess well documented line spectra up to 1000 nm. Calibration measurements on IR140 yielded similar results as obtained by Xu and coworkers [138, 139] confirming the usability of probe pulses in this spectral region.

The nanosecond transient-absorption measurements were also performed with a home-built setup albeit in the group of Prof. Dr. D. Guldi (Department Chemie und Pharmazie, Universität Erlangen-Nürnberg). The excitation was generated using the output of the second harmonic (532 nm) from a Nd:YAG laser (Quanta-Ray GCR-11, Spectra Physics). Pulse durations of less than 5 ns with energies of up to 7 mJ

were selected. The optical detection was based on a pulsed xenon lamp, a monochromator, a photomultiplier tube or a fast silicon photodiode with 1 GHz amplification and a 500 MHz digital oscilloscope. The laser power of every laser pulse was registered by detecting a picked off beam with a photodiode. Several time delays between 2.5 and 150 µs were measured at room temperature with a sample density of 0.1 OD at the excitation wavelength of 532 nm in argon-saturated ethanol.

Calculations were performed by Dr. T. Bruhn in the research group of Prof. Dr. G. Bringmann by using Gaussian09 [140] with the ωB97xD [141] functional for the optimizations and CAM-B3LYP [142] for the TD calculations both in combination with the 6-31G* basis set [143, 144] (6-311G* for Zn [145, 146]). For all calculations the conductor-like polarizable continuum model (abbreviated C-PCM in literature) was used to consider solvent effects [147]. Oscillator strength values were taken from the length formalism and overlaid with Lorentzian curves using SpecDis [148, 149] and a gamma value of 0.05 eV. The overall UV curve was redshifted as compared to the experiment and therefore a shift of 29 nm was applied to get a better fit of the computed curve with the experimental one.

4.4 ZnTPP — Introducing a Photophysical Model Compound

The motivation for a time-resolved study on ZnTPP despite the many known properties is twofold: first, the fairly well-understood ZnTPP serves as a reference compound for the study of $(ZnTPP)_2$ later on, which is the main topic of this chapter and represents a new class of porphyrinoid systems. Second, since multiple electronic states are participating in the photophysical relaxation, using excitation into S_1 and S_2 in combination with a global analysis scheme enables a more extensive analysis of the monomer than reported up to now. At first a summary about the basic properties of ZnTPP will be given (Sec. 4.4.1) and the non-time resolved properties analyzed (Sec. 4.4.2). Finally, the main part of this section, the pump–probe data, is presented (Sec. 4.4.3) and used to generate a comprehensive reaction scheme (Sec. 4.4.4). The results of the following section are published in Ref. [116].

4.4.1 Literature Overview

A serious discussion about and interpretation of the relaxation dynamics of $(ZnTPP)_2$ requires thorough understanding of its monomeric building block tetraphenylporphyrinato-zinc(II) [ZnTPP, Fig. 4.1a)] [150, 151]. ZnTPP consists of the free base framework (shown in Fig. 4.2) but with Zn metalation and four phenyl rings attached to *meso*-binding positions. In nature, porphyrins usually occur in the form of metal complexes. Zinc possesses a closed shell of valence electrons, a property greatly simplifying data interpretation because the absorption and emission properties are then to a large degree governed by π-electrons of the macrocycle [126].

Further reduction of complexity stems from the D_{4h}-symmetry of ZnTPP also used by Gouterman in his theoretical description of the electronic properties of porphyrins summarized in Sec. 4.2.2 [125]. Moreover, ZnTPP has reasonable fluorescence quantum yields from both the Q and the Soret band. Hence, exploration of the electronic structure with time-resolved optical measurements is feasible by detecting stimulated emission or fluorescence originating from there. In contrast to excited-state absorptions these two signals can intuitively be attributed to the responsible state by comparing the data to results obtained by linear techniques. In the following, an overview of results obtained with time-resolved methods in literature is given.

Group of	Solvent	τ_1/ fs	τ_2/ ps	τ_3/ ps	τ_4/ ns
R.P. Steer [152–154]	Ethanol	150	2.35	10–20	1.88
A. H. Zewail [150]	Benzene	200	1.5	12	1.7
R. M. Hochstrasser [108]	Chloroform	"inst"	1.2	18	2.2

Table 4.1: Exemplary time constants for ZnTPP where τ_1 corresponds to IVR in S_2, τ_2 is the lifetime of S_2, τ_3 corresponds to cooling dynamics in S_1, and τ_4 corresponds to the S_1 lifetime. The abbreviation "inst." stands for "instantaneous". In addition to the ultrafast time-scales given above, the T_1 lifetime was measured to be 23 ms in 2-methyltetrahydrofuran [155].

After excitation into S_1, ZnTPP undergoes intersystem crossing (ISC) into the lowest-lying triplet state T_1 with an efficiency of 97% in ethanol solution [152]. This effect dominates the S_1 lifetime of 1.88 ns. The T_1 lifetime was measured to be 23 ms in 2-methyltetrahydrofuran [155]. The remaining relaxation pathway constitutes S_1-S_0 fluorescence with a quantum yield of 3% [152]. From S_1, as well as from T_1, higher states are formed upon absorption of a further photon. The S_1-S_n transitions are of particular importance, since their extinction coefficients are as large as those of the Soret band, thus, large excited-state absorptions evolve in transient-absorption measurements [156]. In contrast to other photosystems one important relaxation pathway from these high-energy states S_n starts in S_2, namely fluorescence to the ground state exists. However, stronger fluorescence is observed from S_1 as expected from Kasha's rule. Furthermore, the photophysics of these higher-excited states can be controlled by multiphoton processes as theoretically shown in Ref. [157]. From S_1, several reaction pathways set in, like intersystem crossing and fluorescence. Excitation into S_2 also occurs upon direct absorption of a UV photon in addition to upper multi-step processes via S_1 [150]. Intramolecular vibrational relaxation (IVR) in S_2 marks the fastest hitherto resolved time-scale for ZnTPP. This time constant in ethanol has been determined to be 60-90 fs by Gustavsson and coworkers [158], using fluorescence up-conversion, and to be 150 fs by Fontaine-Aupart and coworkers [159] via transient-absorption spectroscopy. From the S_2 state, fluorescence is observed with a quantum yield of only 0.14% when excited at 400 nm [154]. Most molecules undergo internal conversion into S_1 with an S_2 lifetime of 2.35 ps in ethanol [153]. Finally, intermolecular vibrational-energy transfer proceeds on a 20 ps time-scale [108]. Table 4.1 summarizes time constants available from literature and visualizes the good agreement obtained by independent groups [116].

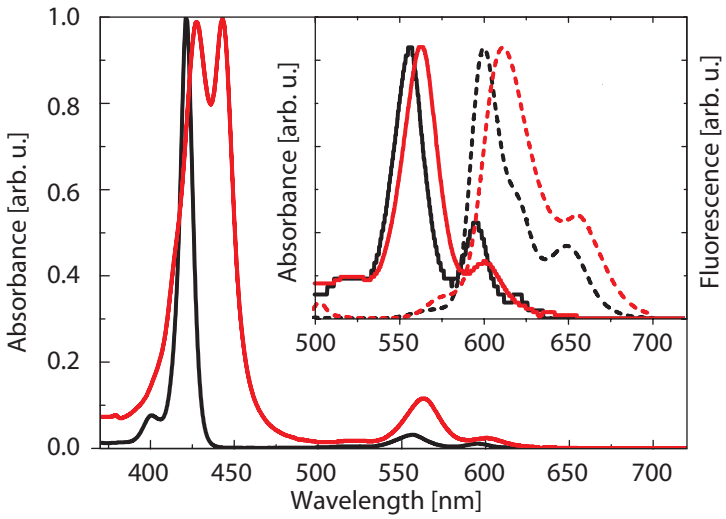

Figure 4.7: Steady-state absorption (solid lines) and fluorescence spectra (dashed lines) of ZnTPP (black) and $(ZnTPP)_2$ (red). Q-band absorption and emission (inset) is similar for ZnTPP and $(ZnTPP)_2$, consisting of two contributions each, the Soret band in $(ZnTPP)_2$, however, shows an additional Davydov splitting and no vibrational substructure [116]. The latter is clearly seen in the black spectrum of the monomer at ≈ 400 nm.

4.4.2 Steady-State Characterization

The steady-state absorption (black, solid) and fluorescence (black, dashed) spectra of ZnTPP dissolved in ethanol are displayed in Fig. 4.7. The absorption spectrum consists of four identifiable contributions. The Soret band S_2 itself peaks at 421 nm, while the weaker maximum at 400 nm is assigned to a convolution of transitions of vibrational states in accordance with literature [160]. The Gouterman four-orbital model [125] predicts two degenerate S_2 states, and a fit with multiple Gaussian-shaped functions in Ref. [161] provided the best results with three functions centered at 401.6, 420.9, and 421.6 nm indicating a slight splitting of 39 cm^{-1} between the nearly degenerate bands and the existence of at least three states in this spectral region, with the one at 401.6 nm identified as a vibrational substructure. The much weaker absorbing porphyrin Q bands are found at 556 nm [vibrational hot state Q(1,0)] and 594 nm [vibrational ground state Q(0,0)] and no loss of degeneracy is observable. The measured spectrum matches well known ones from literature [150, 151]. When compared to the free base which possesses four separate Q-band absorptions the influence of the metalation is visualized [110].

In the emission spectra (inset, dashed) clearly distinguishable fluorescence is observed at 600 nm [Q(0,0)] and 649 nm [Q(0,1)] originating from the excited-state population caused by the two Q-band absorptions. The emission spectrum measured is not corrected for possible re-absorption and both emission and absorption overlap around 600 nm. Thus, a quantitative signal analysis is not easily possible. However, the position of the bands and the twofold splitting agrees well with spectra published in literature [150, 151].

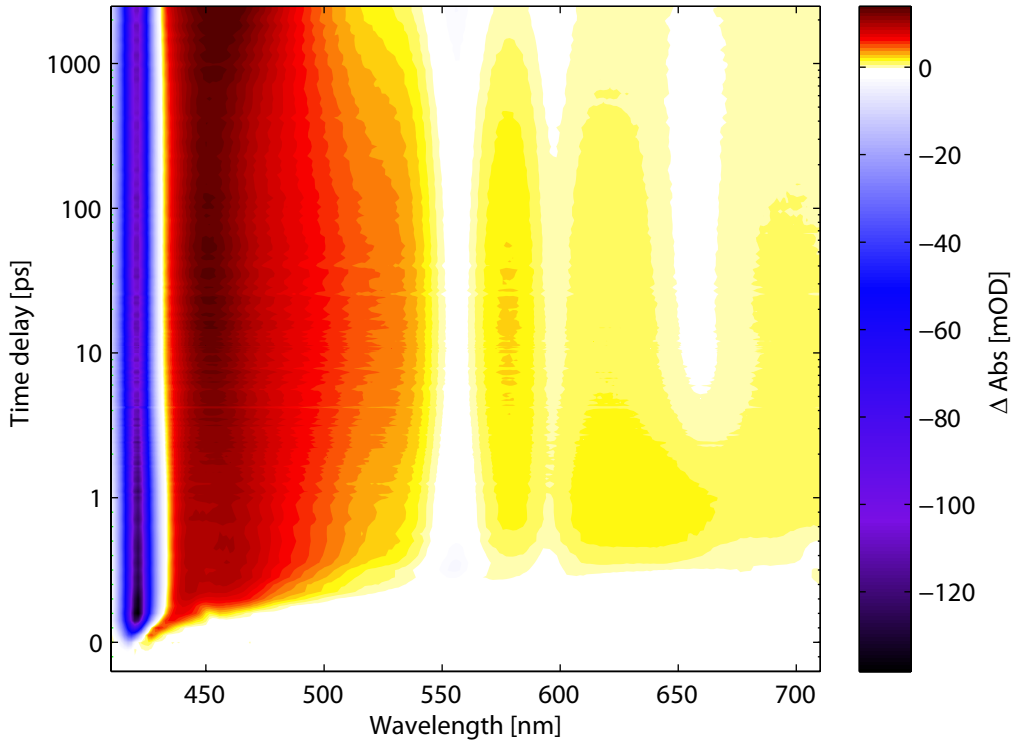

Figure 4.8: Transient-absorption data of ZnTPP after excitation with 400 nm pump pulses covering the visible spectral range. After a time delay of 1 ps the scale of the ordinate changes from linear to logarithmic spacing.

4.4.3 Transient-Absorption Measurements

Photodynamics after Soret-Band Excitation

Transient-absorption data after excitation into hot vibrational states of S_2 with 400 nm pump pulses are shown in a contour plot in Fig. 4.8. Up to 1 ps spacing of the data points is linear. Afterwards, logarithmic scaling is chosen in order to provide insight for long time delays of up to 3.5 ns in addition to resolving ultrafast contributions on the fs time-scale simultaneously. Bluish colors denote negative and reddish colors positive changes in absorbance. Soret-band absorption at 421 nm, Q-band absorptions (556 nm, 594 nm) and stimulated emission around 650 nm is clearly identified in addition to broad excited-state absorptions over the entire visible spectral range. The identified vibrational substructure could not be resolved with the continuum probe spectra.

For an intuitive understanding of the participating time-scales, transients representing the three most important absorption and emission bands, the Soret band (blue), the Q band (green) and the stimulated emission (red) in combination with corresponding fits (black) obtained via global fitting, whose background is explained in Sec. 3.2.2, are shown in the Fig. 4.9. The black curves visualize the excellent fit quality. Five time constants were needed to fit ZnTPP's dynamics after 400 nm

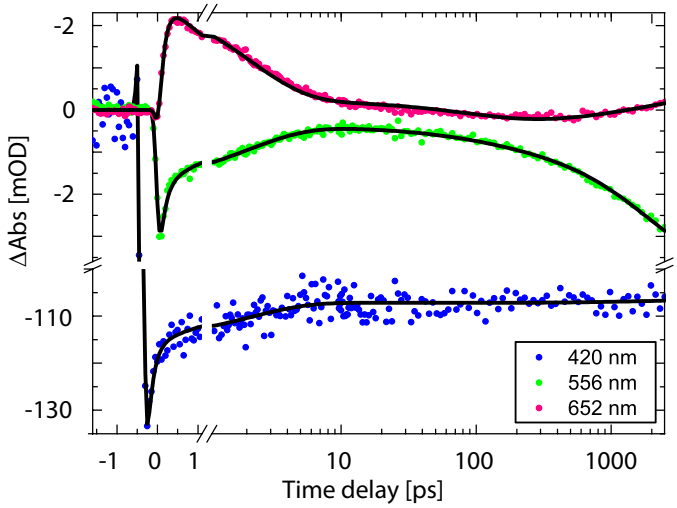

Figure 4.9: Transient behavior at selected wavelengths reflecting the dynamics of the Soret (blue) and Q band (green) and stimulated emission (red). Fit results from the global fitting routine are shown in black. Note the changing scale of the abscissa and the ordinate [116].

excitation and the spectrally resolved amplitudes are shown in Fig. 4.10 (EADS in top and DADS in bottom panel). The fifth time constant relates to a permanent offset in the measurements. It summarizes the relaxation processes, which occur on a time-scale beyond the first few nanoseconds and are therefore not resolved. For example, additional triplet pathways often occurring with µs time constants should be considered [116].

Some of the spectral features that are displayed in Fig. 4.10 are described in more details in this section. Because of the many overlapping contributions, whenever a dip is mentioned, it relates to a negative contribution often on top of another transient signal, such as an excited-state absorption (ESA). The discussion starts with explaining the EADS, which are very close to spectral cuts of the measured data, the difference spectra. First, the data in Fig. 4.10 exhibit a dominant negative signal right after the excitation (black), which is centered at 420 nm corresponding to the Soret band. This signal then loses 25% of its initial amplitude on a time-scale of 140 fs (red) and further decreases by 10% with 2.1 ps (blue). Beyond this point no significant evolution of this peak was noted (green and cyan).

Second, the black EADS clearly shows a dip at 447 nm, representing stimulated emission originating in S_2. It red-shifts to 452 nm and decreases in intensity on a time-scale of 140 fs. This signal completely vanishes on a time-scale of 2.1 ps.

Third, a positive signal, an ESA, is observed between 433 and 536 nm. Its strength increases with time until the blue EADS is reached. From there on, the ESA decreases slightly and its maximum red-shifts from 450 to 453 nm on a time-scale of 100 ps. The cyan EADS crosses the blue, green, and red EADS at approximately 489 nm. The evolution of the ESA for higher and lower energies connected at this isosbestic point reveals an increase and decrease, respectively, on a time-scale of 1.9 ns. Finally, the remaining signal is a rather sharp ESA centered at 460 nm.

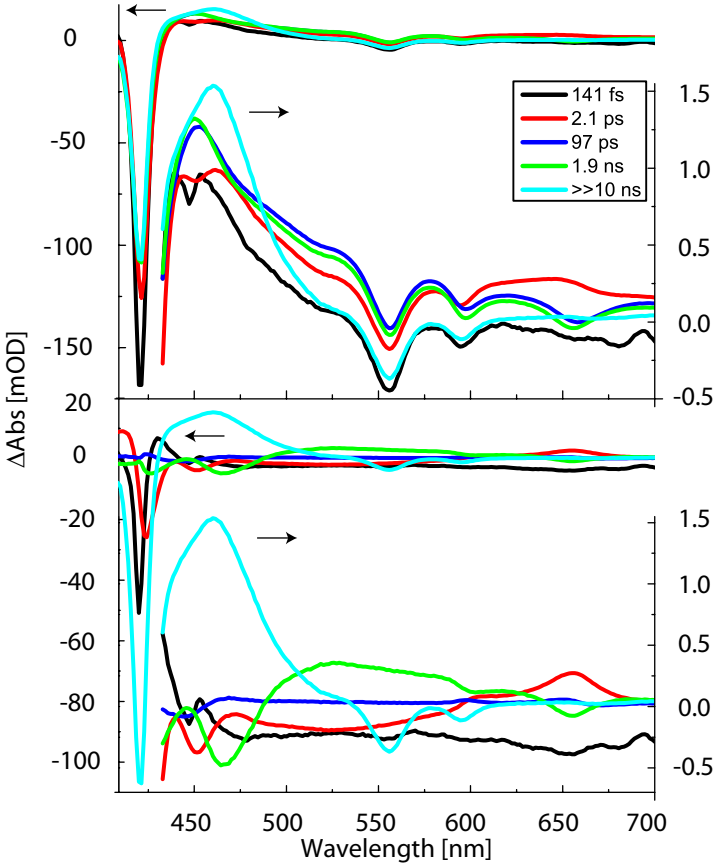

Figure 4.10: EADS (top) and DADS (bottom) of ZnTPP excited at 400 nm showing the temporal changes associated with five time constants: 141 fs (black), 2.1 ps (red), 97 ps (blue), 1.9 ns (green), and a constant offset (cyan). For better visualization, the data for wavelengths above 430 nm are additionally shown as a magnified graph (right-hand ordinate) and black arrows denote the corresponding ordinate [116].

Hence, the previous broadband ESA changed into a spectrally narrower more intense excited-state absorption, indicating a population transfer because of the large change.

Fourth, all EADS exhibit a dip centered at 556 nm [Q(1,0)]. Nearly the entire evolution at this probe wavelength is the same as that of the broad ESA, on top of which the dip is observed. However, a further dip at longer wavelengths, corresponding to Q(0,0), behaves differently. Its position is at 594 nm (red), then shifts to 597 nm (blue and green), before it blue-shifts back to 594 nm (cyan). The blue and the green EADS exhibit one further dip at 659 and 656 nm, respectively corresponding to the Q-band emission wavelengths observed in the fluorescence measurements. The other EADS are rather structureless in this wavelength region.

The connection between different relaxation processes is better seen in the DADS in the bottom panel of Fig. 4.10. Two of the most obvious findings are that the decay at 452 nm is directly connected to a rise at 656 nm with a time constant of 2.1 ps

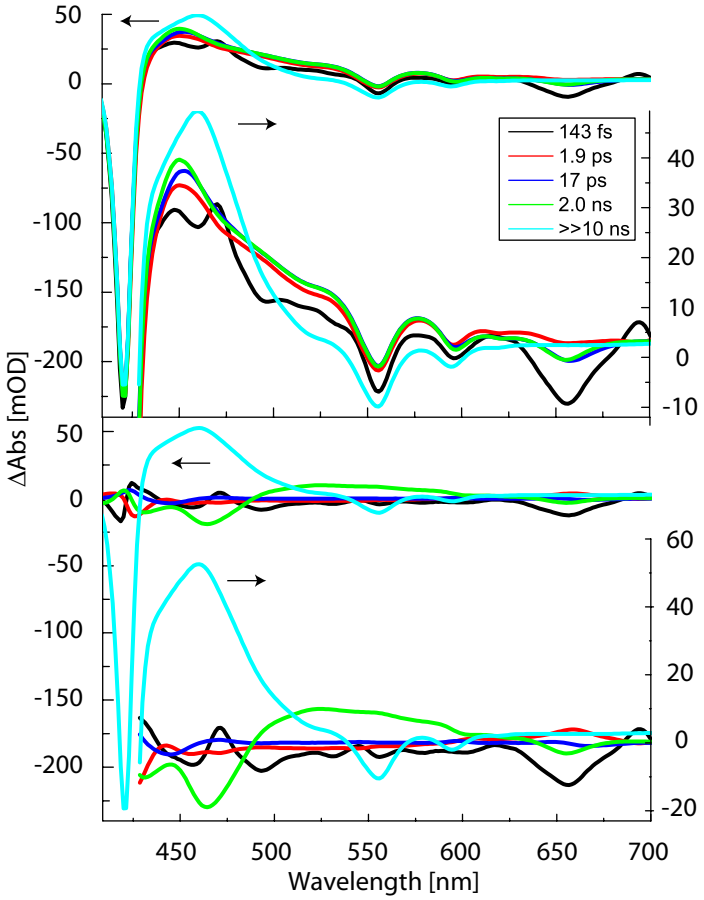

Figure 4.11: EADS (top) and DADS (bottom) of ZnTPP excited with 560 nm showing the temporal changes associated with five time constants: 143 fs (black), 1.9 ps (red), 17 ps (blue), 2.0 ns (green) and constant offset (cyan). For better visualization, the data for wavelengths above 430 nm are additionally shown as a magnified graph (right-hand ordinate) and black arrows denote the corresponding ordinate [116].

(red) and that the decays at 597 and 656 nm are both attributed to a time constant of 1.9 ns as evidenced by the two dips (green) and that they also correspond to the sharpening of the ESA at 460 nm.

Photodynamics after Q-Band Excitation

Figure 4.11 shows the corresponding EADS and DADS of ZnTPP when excited at 560 nm, thus predominantly the Q band is populated. They look very similar to those corresponding to the 400 nm excitation discussed previously, except that contributions from the fastest dynamics — occurring with 140 fs and 1.9 ps — are much smaller in amplitude. The description of the dynamics of ZnTPP upon S_1 excitation will be done by using DADS (Fig. 4.11, bottom) in the next paragraph.

The black DADS in Fig. 4.11 clearly shows the existence of SE at 652 nm right after excitation in contrast to Fig. 4.10 where the SE starts after 2.1 ps. In addition, a dip

at 418 nm and a positive peak at 424 nm, resulting in a slight red shift of the overall difference spectrum on the associated time-scale of 140 fs are identified. This effect is reversed on the 1.9 ps time-scale of the red DADS. One further significant contribution coming from the red DADS is a positive peak at 659 nm, which represents an increase in SE. The blue DADS has a positive peak at 423 nm and a negative dip at 445 nm indicative of the shift of the ESA maximum (as also observed in Fig. 4.10). Furthermore, the blue DADS shows a positive peak at 597 nm and a dip at 668 nm both of which are faint. The green DADS, associated with the 2.0 ns time constant, has negative dips at 430, 464, 655, and a faint one at about 604 nm. There is also a very broad positive signal with a maximum at 526 nm connected to the negative peak at lower wavelengths with an isosbestic point at 489 nm. The cyan DADS is identical to the cyan EADS and can be regarded as the offset for the measured evolution. There is also no noticeable difference between the four cyan curves in Fig. 4.10 and Fig. 4.11 as expected. Since they relate to a permanent offset, they should be identical for both parallel and sequential models. Table 4.2 compiles the time constants obtained by globally fitting the ZnTPP transient-absorption data. They are in very good agreement with the results in literature (see Table 4.1).

λ_P / nm	τ_1/ fs	τ_2/ ps	τ_3/ ps	τ_4/ ns
400	140 ± 30	2.1 ± 0.1	97 ± 2	1.9 ± 0.1
560	140 ± 30	1.9 ± 0.1	17 ± 1	2.0 ± 0.1

Table 4.2: Time constants obtained by global fitting routines for the relaxation dynamics of ZnTPP after excitation into S_1 (560 nm) and S_2 (400 nm).

4.4.4 Development of a Temporal Relaxation Scheme

The steady-state absorption spectrum shown in Fig. 4.7 (black) provides the basis for interpretation of the transient data. It directly reveals that the negative signals at 421, 556, and 594 nm are (at least partly) attributable to ground-state bleach. Negative contributions arising from stimulated emission from the Q band are discernible at 600 and 649 nm in accordance with the fluorescence measurement. The positive contribution followed by a negative dip at the latter wavelength relates to the occupation and depopulation of S_1, since it is solely due to SE from S_1. This SE and, in turn, the S_1 occupation increases on the time-scale of 2.0 ps (Fig. 4.10). Thus, this time constant is attributed to $S_2 \rightarrow S_1$ internal conversion. The same signal also enables the estimation of the lifetime of the S_1 state to 2 ns since the SE signal vanishes on this time-scale via intersystem crossing into T_1. While intersystem crossing often is a weak pathway this can be the dominating contribution in Zn metalloporphyrins as explained in Sec. 4.2.1. This also explains the signal changes between 433 and 536 nm, i.e., sharpening of the ESA at 460 nm and the decaying broadband absorption. The ESA to the blue of the isosbestic point at about 489 nm is a transition from T_1, while the ESA to the red is a transition from S_1. The former is growing at the expense of the latter with time [116].

The assignment of the two remaining time constants is more challenging. The 10-100 ps cannot be unambiguously identified. On the one hand, the spectral blue shift of the ESA at 451 nm indicates vibrational-energy transfer or excess energy transfer to the solvent since higher photon energies are required to induce a resonant transition into higher energy states after relaxation. On the other hand, the blue-shift of the peak at 649 nm is in contradiction to this interpretation, since SE generally red-shifts with increasing relaxation. A remaining explanation for the blue-shift of the SE band is a thermal equilibration between the two (nearly) degenerate states predicted by Gouterman's model after predominant population of the lower-lying S_1 state by $S_2 \rightarrow S_1$ IC. Both processes may happen on roughly the same time-scale, which hampers resolving their individual contributions. This would also explain the observed relatively large uncertainty, ranging from 20 to 100 ps, in the estimated value of the underlying time constant.

Figure 4.10 shows that the 140 fs component is large in the Soret band. The assignment is based on the following considerations: First, the amplitude decreases drastically upon 560 nm rather than 400 nm excitation. In other words, the corresponding transition has to involve the S_2 state directly. Second, the red EADS in Fig. 4.10 shows no SE at 649 nm, which rules out a transition into S_1. Third, a transition from S_2 directly to the ground state is observable via SE at 447 nm in Fig. 4.10 but no GSB recovery is seen in the Q band. The latter would be detectable if a direct ground-state transfer is a significant relaxation channel, so that this pathway is only very minor. Taken the aforementioned together, the 140 fs component must be attributed to a process involving the population of the vibrational ground state of S_2 — for example vibrational relaxation or IC from higher states into S_2.

However, the second state involved in the transition remains unknown. Since the black DADS in Fig. 4.10 does not show a transition into S_0 (no GSB recovery at 560 and 600 nm), its decay is not the GSB-related recovery of S_0. The two remaining options are an increasing ESA or a decreasing SE. The latter option appears reasonable because the system was excited into S_2 and SE may well arise from these initially excited states at wavelengths close to the Soret absorption band. As such, the negative peak of the red DADS at 424 nm must also relate to SE. The wavenumber difference to the peak at 420 nm in the black DADS is 240 cm^{-1}. Hence, from Fig. 4.10, it is possible to retrieve that SE is disappearing at 420 nm on a time-scale of 140 fs, reappearing red-shifted on the same time-scale, where the SE vanishes again with 2.1 ps. The latter time constant relates to the population of the Q band, therefore, the vanishing of SE from S_2 corresponds well to this population transfer. Identical statements are valid for the dips at 447 nm (black DADS) and 452 nm (red DADS), which are reasonable wavelengths for fluorescence and SE from S_2 [150]. Here the shift corresponds to 250 cm^{-1} but a clear estimation is hindered by the large ESA on top of the contribution.

In the following three processes are considered to explain the observed red-shift of stimulated emission around 450 nm. First, vibrational modes of tetrapyrroles are known to lie as close as 23 cm^{-1} above the vibrational ground state, so that the observed shift could be IVR [160, 162]. However, vibrational modes so close to the

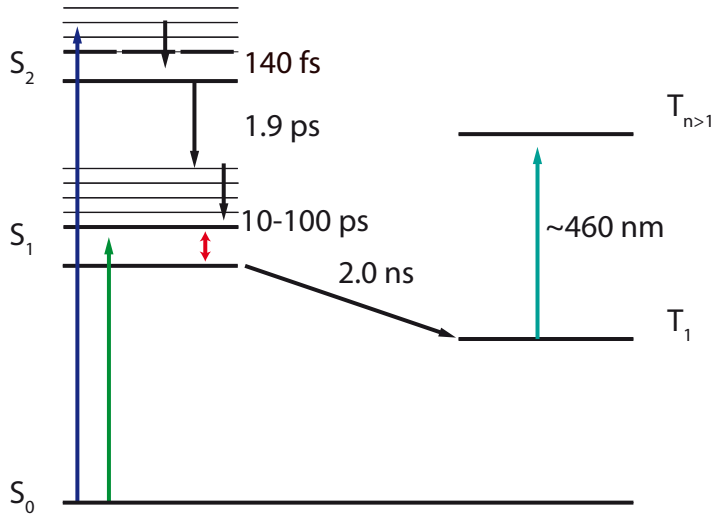

Figure 4.12: Reaction scheme for ZnTPP showing the relaxation pathways after excitation with 400 nm (blue) and 560 nm (green). Excited molecules relax with 140 fs within S_2, from there IC into S_1 with 2 ps sets in. After relaxation processes within S_1 on a ps time-scale most molecules proceed into T_1 via ISC within 2 ns [116].

vibrational ground state are very sparse. The median vibrational wavenumber is more in the realm of 1300 cm^{-1}, i.e., around 400 nm where the vibrational side band can be observed in the steady-state spectrum [162, 163]. Therefore, it seems rather unlikely that these few vibrational modes carry such extraordinary emission strength.

Second, the shift in SE could arise from a transition between the two (nearly) degenerate B states predicted by Gouterman's four-orbital model [125]. The energy spacing of 39 cm^{-1} estimated by fitting Gaussian functions to the steady-state spectrum shows the possibility of an SE shift in the data when the excited-state population relaxes from the higher-energetic into the lower-energetic state of the two, only nearly, degenerate states. Such an estimation of the energy splitting by fitting Gaussian functions– indicative of electronic states — is at best a very rough approximation, since it neglects vibrational fine structure. However, a lifting of degeneracy was already observed in the condensed phase [164] substantiating this possibility, whereas no splitting was observed in ZnTPP when seeded in pulsed supersonic expansions [160]. It is not possible in the experiment to detect the absorption belonging to each of the two states separately because of the small energetic difference, which is much smaller than the observed broadening caused by solvation, thus only one broad feature, shifting with time, is observed. Since both states share the same symmetry they should also carry comparable absorption and emission strengths. However, the excitation wavelength for the data represented in Fig. 4.10 was 400 nm, i.e., the molecules initially have excess vibrational energy, and vibrational relaxation has to take place. Excitation at 560 nm yields somewhat smaller but still observable contributions from S_2, for example SE around 450 nm, which can only be explained by two-photon absorption. Since the decay of SE yields the same time constant of

140 fs as after 400 nm excitation, relaxation from S_n, with $n > 2$, states excited by two-photon absorption with 560 nm (corresponding to an effective excitation at 280 nm) shows that the redistribution of the initial excess energy indeed happens on a time-scale much faster than 140 fs.

Lastly, the solvent might respond to the new distribution of electronic density in the S_2 state, which differs from the one in the ground state, by rearranging itself. This would lead to an effective energetic downshift of the S_2 potential energy surface and, hence, to a red-shift of emission as observed (Stokes shift). ZnTPP exhibits a very small S_2 Stokes shift of 115 cm^{-1} in ethanol [165], so that this option seems viable. However, while examples of rearrangements on sub-picosecond time-scales exist, it is known to usually take place on a fast picosecond time-scale [166] and is therefore relatively unlikely to occur within the observed time constant of 140 fs. Moreover, this option does not take into account that the main Soret-band absorption arises from more than one final state. In light of the aforementioned, none of these three processes should be excluded based on the data acquired over the course of this work, but a vibrational Stokes shift seems to be the most viable solution. In related studies on ZnTPPs relaxation dynamics, the preferred assignment is IVR, however, further possibilities were not discussed [158].

The determined time constants are consistent with those from literature, thus, demonstrating the analysis scheme's usefulness and reliability in relaxation process description and model establishment for ZnTPP. Additionally, a framework for the description of the relaxation processes of $(ZnTPP)_2$ is generated. Literature assignment of the 140 fs and the 10-100 ps components to vibrational relaxation are purely based on the order of magnitude arguments [108, 158, 159]. To the best of my knowledge, assignments based on spectral properties are not reported for these two components and it is therefore not surprising that the results presented here indicate that the addition of different processes to vibrational relaxation provide alternative explanations. All the discussed results are gathered in the energy scheme in Fig. 4.12, which corresponds well to the one obtained in Ref. [151].

4.5 $(ZnTPP)_2$ — How Dynamics Change upon Going from Monomer to Dimer

In the previous Section ZnTPP was thoroughly analyzed. The knowledge gained there is used in the following to assess the properties of $(ZnTPP)_2$, a directly β,β'-linked bisporphyrin. Attention is especially drawn to the excitonic behavior, expected in a dimeric system, and how this influence changes the temporal properties in the Soret band as well in the Q band. In principle the same technique, pump–probe spectroscopy, as before will be used, but in a wider variety of experiments. The results of the following section are published in Ref. [116] and it is organized as follows.

At first, a summary of porphyrin dimers in literature is given (Sec. 4.5.1), directly followed by a steady-state sample characterization of $(ZnTPP)_2$ (Sec. 4.5.2). After-

wards, a wide array of transient-absorption experiments is performed, with multiple excitation and detection spectral ranges, even time delays up to microseconds are analyzed in order to get as much information as possible (Sec. 4.5.3). Lastly, all the experimental information is analyzed and discussed within two different possible reaction schemes, especially differing in how the behavior in the Soret band is explained, and compared to the monomeric scheme.

4.5.1 Literature Overview

A multitude of time-resolved studies concerning covalently-linked porphyrins have been conducted since an efficient route for their synthesis has been developed independently by Therien and coworkers [167] and Osuka and coworkers [168]. Leading examples are dimers and polymers [56, 108, 120], linear arrays of various lengths [109, 169], thin films [170], rings [118], and boxes [171, 172]. In early work, Hochstrasser and coworkers, investigated an ethyne-bridged *meso,meso'*-linked and a β,β'-linked dimer [108]. The latter dimer differs from the dimer that is reported on here by the presence of an ethyne bridge rather than a direct linkage. This is important, since rotational movements of the different porphyrin monomers in non-directly linked systems are in most cases possible without restrictions. In ethyne-bridged dimers with large substituents, rotation is already exacerbated by an energetic barrier for β,β'-linkage [108]. Beyond that it is strongly hindered for the direct linkage, even resulting in two stereochemically stable enantiomers [114]. However, this hindrance does not exclude possible 'wobbling' of the dihedral angle. To explain the observed relaxation dynamics, Hochstrasser and coworkers developed a model, necessitating two conformers, differing in and distinguished by the dihedral angle between the subunits in *meso,meso'*-configuration, which both participate in the relaxation. In contrast, this assumption is discarded for the description of an ethyne-bridged β,β'-linked ZnTPP dimer, whose relaxation mechanisms are still not fully understood and could not be resolved because of their ultrafast occurrence [108, 116].

Kim and coworkers, who investigated a large variety of *meso,meso'*-linked oligomers, subsequently picked up and refined the two-conformers idea. The conformer that is predominantly present in the ground state is assumed to exhibit a dihedral angle of 90°, whereas it is believed that $0 \ll \Theta_D < 90°$ holds for the other, smaller fraction of molecules. The ratio of excited conformers is influenced by the excitation wavelength. The first relaxation step after S_2 excitation occurring on the 300 fs time-scale in the case of the *meso,meso'*-linked dimer in toluene solution happens solely in S_2 [120]. This step is followed by a temporally unresolved $\tau < 100$ fs internal conversion from S_2 to S_1. In S_1, the molecule can undergo isomerization between the $\Theta_D = 90°$ conformer and the $0 \ll \Theta_D < 90°$ conformer on a time-scale of 8 ps, while the S_1 lifetime was measured to be 1.93 ns [120].

Additionally, Kim and coworkers incorporated an excitonic model considering the electronic porphyrin structure [109, 120]. Dimers are the simplest model system for excitonic exchange in which degeneracy from two nearly identical electronic states is found as shown in chapter 4.2.3 for a model system with large Davydov splitting

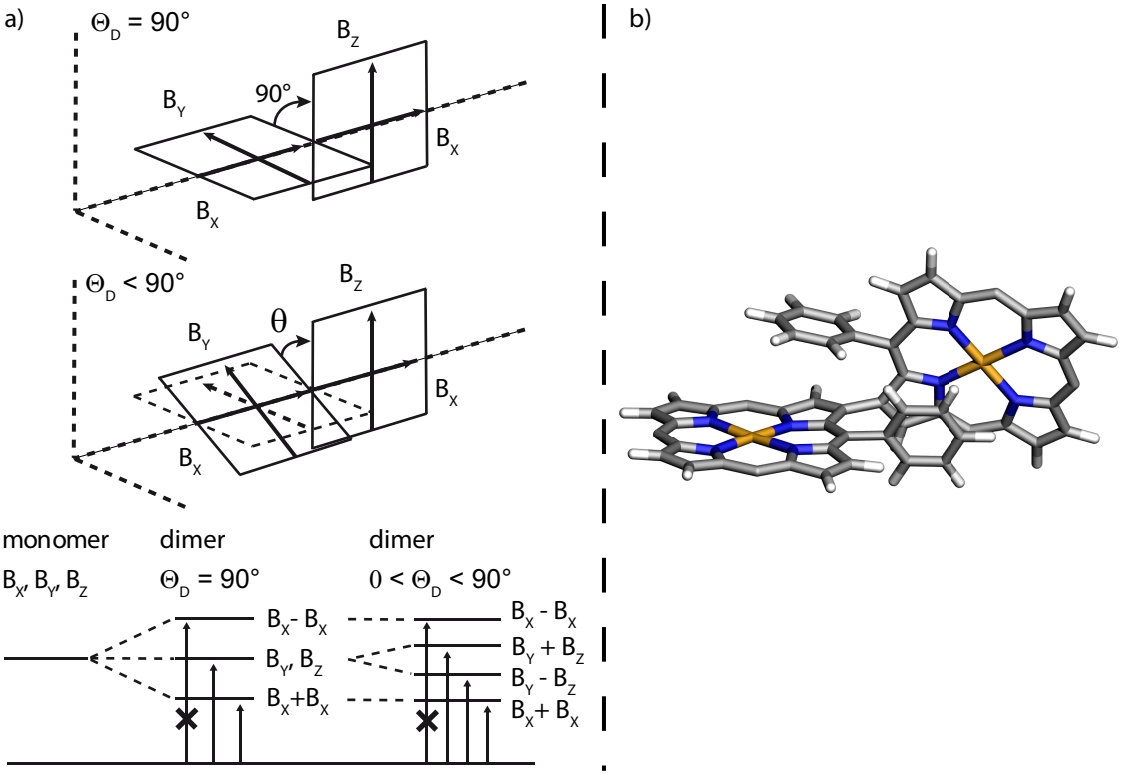

Figure 4.13: a) Directions of the transition dipole moments of the monomer (B_X, B_Y, B_Z) for dihedral angles $\Theta_D = 90°$ (top) and $\Theta_D < 90°$ (center), and the linear combination into the excitonic states of the *meso,meso'*-linked dimer (bottom) (illustration adapted from Ref. [109]). For $\Theta_D \neq 90°$, the degeneracy of the dimeric states is lifted. b) Calculated structure of $(ZnTPP)_2$ indicating similarities to the $\Theta_D < 90°$ *meso,meso'*-linked dimer. For clarity, only two phenyl substituents in meso-position are drawn [116].

in the first excited state. In contrast, porphyrins have a large splitting in the Soret band. Figure 4.13a) depicts how the electronic states of the monomer change due to excitonic interactions between two porphyrin moieties for a *meso,meso'*-linked dimer in the Soret band for two different dihedral angles. Both moieties have a transition dipole moment B_X aligned parallelly with respect to each other. The associated electronic states couple, thus, forming two excitonic states. On the one hand, the energetically higher-lying state is dipole-forbidden and, on the other hand, the lower-lying state is fully allowed [bottom panel of Fig. 4.13a)]. In addition to these excitonic states, two degenerate states resulting from the B_Z and the B_Y transition are noticed in-between the excitonic states. Owing to the perpendicular orientation of these two transitions, they do not couple. As a consequence, the associated states only exhibit a weak excitonic character and largely maintain their monomeric, i.e., localized character. For dihedral angles different from 90°, the degeneracy between the now coupled B_Z and B_Y states is canceled and the distinction between monomeric and excitonic states fades away, but remains valid in principle [109]. The 300 fs process mentioned above for relaxation in S_2 is explained by a transition between the two lowest-lying states. In the Q bands, similar excitonic splittings are not observed

due to the much smaller transition dipole moments [108, 120]. This observation indicates that the lowest-lying singlet electronically excited states are weakly coupled, localized states, which preserve the z-y degeneracy associated with the S_1 state of the monomers. The dimeric state associated with the Q band is simply denoted as S_1 without further differentiation in the following. A compilation of measured time constants for dimers similar to the one studied here is given in Table 4.3. Again there is a good agreement between different studies but the properties of different bisporphyrins vary in important details like the lifetime of the Soret band.

linkage	solvent	τ_1/ fs	τ_2/ ps	τ_3/ ps	τ_4/ ns
meso,meso' [120]	toluene	300	8	–	1.93
ethyne β,β' [108]	chloroform	150	18	–	1.6
meso, β [173]	acetonitrile	–	4.1	59	1.76
β,β'	acetonitrile	–	8.5	–	1.79

Table 4.3: Measured time constants for bisporphyrins with different linkage.

In this work, the excitonic model of Kim and coworkers will be transferred to dimers with β,β'-linkage. The presented approach is based on the common molecular building block ZnTPP for the *meso,meso'*- and β,β'-linked dimers and on the fact that the monomeric transition dipole moments are aligned in a similar way [Fig. 4.13b)]. Only a twofold splitting was observed with steady-state absorption measurements in the UV and VIS spectral range, indicating nearly degenerate states in the original publication where $(ZnTPP)_2$ was first introduced [115]. Therefore, it is aimed to understand the influence of excitonic interactions by comparing $(ZnTPP)_2$ to ZnTPP, and to investigate how appropriate the model developed for *meso,meso'*-linked porphyrin dimers is for $(ZnTPP)_2$.

4.5.2 Steady-State Characterization

Figure 4.7 shows the steady-state absorption spectrum (red, solid) of $(ZnTPP)_2$ dissolved in ethanol. The dimer exhibits two strong absorption bands in the Soret region as a result of excitonic Davydov splitting. The higher-energy absorption features a maximum at 428 nm and appears to be broader than the lower-energy Soret absorption with a maximum at 443 nm. The former one is red-shifted by ≈ 400 cm^{-1} with respect to the main Soret absorption of ZnTPP at 421 nm. An additional difference to ZnTPP is that no vibronic substructure is evident compared to the peak in the monomer centered at 400 nm. Nevertheless, small contributions from minor transitions might be hidden under the broader absorption features of the bisporphyrin, for example at 414 nm a shoulder is visible.

In addition, the dimer exhibits two Q-band absorptions at 563 and 601 nm (red, solid). The former maximum is red-shifted by ≈ 20 cm^{-1} with respect to the main Q-band absorption of ZnTPP at 556 nm but very similar in shape. Two fluorescence bands (red, dashed) are observed red-shifted compared to the Q-band absorptions,

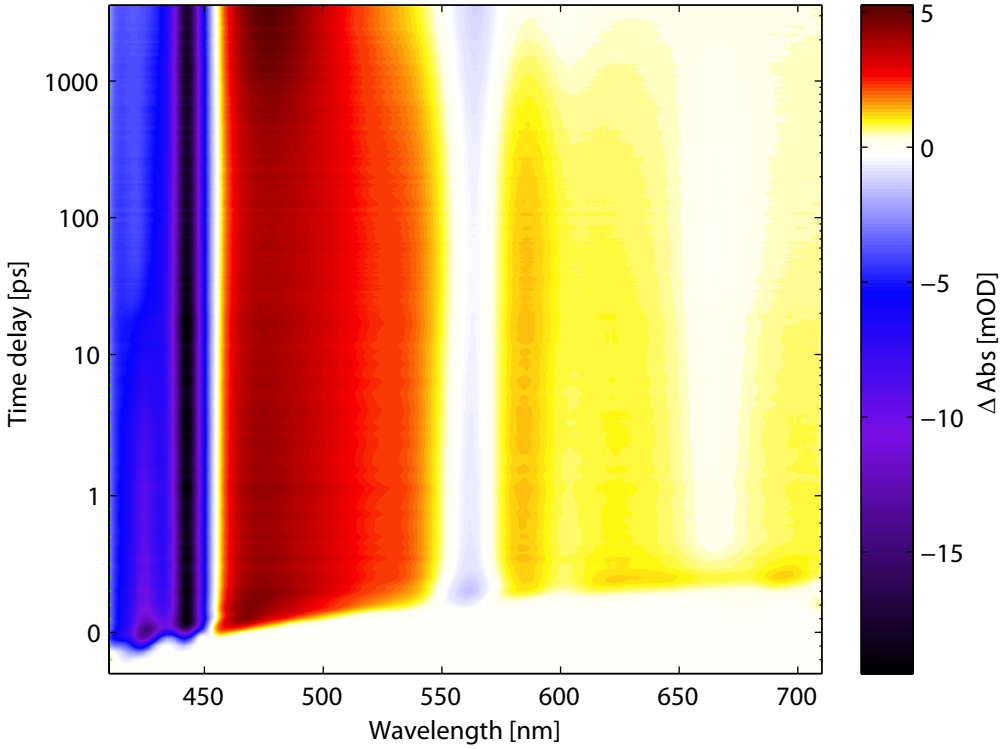

Figure 4.14: Transient-absorption data of $(ZnTPP)_2$ after excitation with 400 nm covering the visible spectral range. After a time delay of 1 ps the scale of the ordinate changes from linear to logarithmic spacing.

i.e., a stronger signal at 611 nm and a weaker fluorescence at 655 nm. The former is red-shifted by 300 cm^{-1} with respect to the strong S_1 fluorescence of ZnTPP at 600 nm, but again showing a similar shape.

4.5.3 Transient-Absorption Measurements

Photodynamics after Soret-Band Excitation

The transient-absorption data of $(ZnTPP)_2$ excited at 400 nm are shown in Fig. 4.14 with the same color coding and semi-logarithmic spacing as for the ZnTPP map (Fig. 4.8). Most noteworthy, the two negative signals in the Soret region behave vastly different when compared to the temporal relaxation in the monomer. In contrast, the behavior in the visible spectral range, which consists of a broad ESA overlapped with Q-band absorption and SE looks similar at first glance. The dynamics are better displayed in Fig. 4.15a), which shows transients for the Q band. The vibrational excited state at 563 nm is marked in green and the vibrational ground state at 611 nm in orange. The stimulated emission signal (red) corresponds well to the fluorescence at 658 nm. In addition, Fig. 4.14b) shows transients in the split Soret band (426 nm, violet and 443 nm, blue). For all transients the corresponding global fit is shown in black. Again five time constants were needed to model the

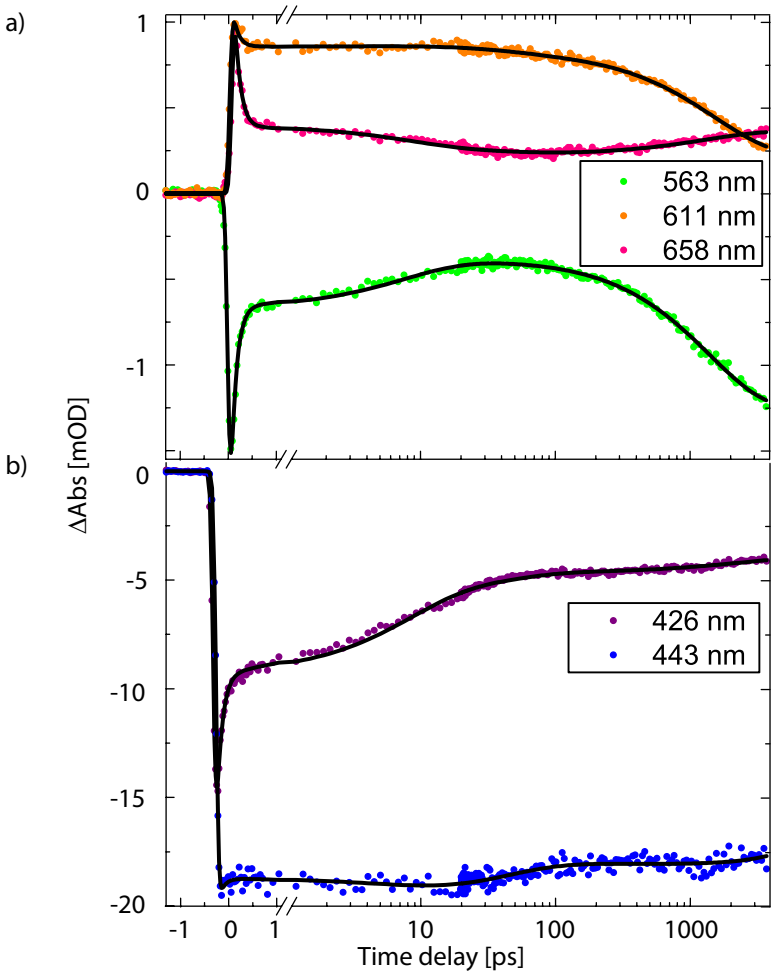

Figure 4.15: a) Transients reflecting the dynamics of the Q band (green, 563 nm, orange, 611 nm) and the stimulated emission signal (red, 658 nm). b) Transients reflecting the Soret band at 426 nm (violet) and 443 nm (blue). Fit results from the global fitting routine are shown in black. Note the changing scale of the abscissa after 1 ps [116].

data. The obtained EADS (top) and DADS (bottom) are displayed in Fig. 4.16 and the most important aspects will be discussed in the following paragraphs [116].

First, the black EADS — corresponding to the 113 fs component — induces large changes throughout the entire spectral range. The largest impact is seen on the high-energy Soret peak at 426 nm in form of a large negative contribution. The amplitude decreases strongly and the center slightly blue-shifts to 424 nm throughout the decay of the fastest component. In contrast to the monomer, a rise, as evident by the positive peak in the corresponding DADS (bottom panel, black curve), develops at 662 nm. The amplitude in the left Soret peak decreases even further in the red EADS associated with a time constant of 7.8 ps. With a time constant of 40 ps, the signal amplitude at 424 nm still decreases for the blue EADS and a dip at 415 nm becomes clearly visible for later times as indicated by the green EADS. This dip corresponds well with the unassigned shoulder observed in the steady-state spectrum. From there

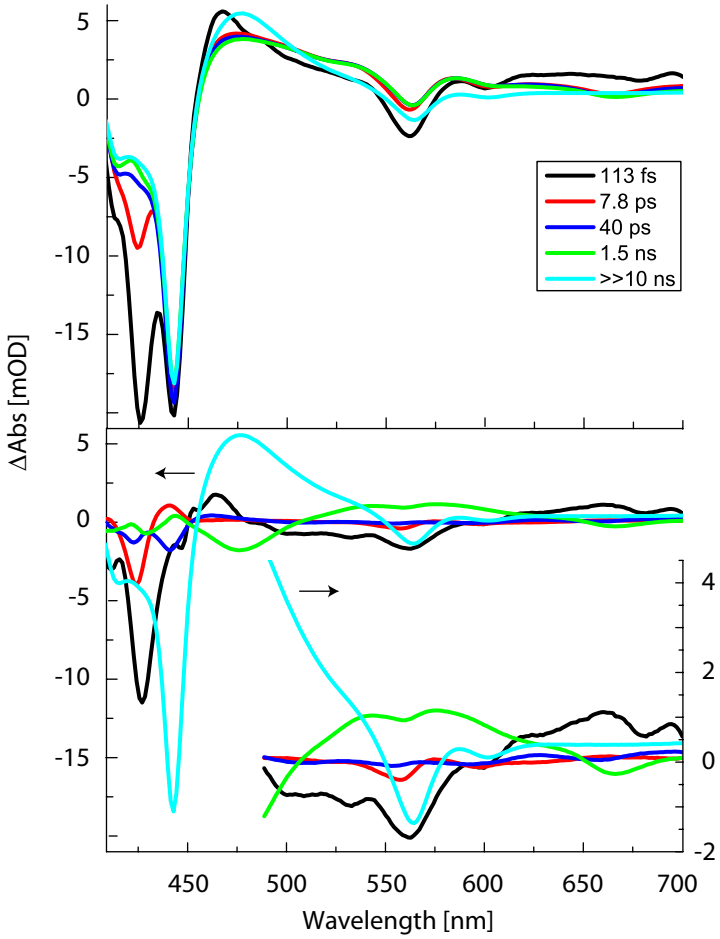

Figure 4.16: EADS (top) and DADS (bottom) of $(ZnTPP)_2$ excited with 400 nm showing the temporal changes induced by five time constants: 113 fs (black), 7.8 ps (red), 40 ps (blue), 1.5 ns (green) and constant offset (cyan). The inset (bottom, lower right panel) magnifies the signal to the red of the isosbestic point at 489 nm with black arrows indicating the corresponding ordinate [116].

on, the amplitude of this additional signal reduces slightly, but hardly any further changes occur at wavelengths shorter than 437 nm. The lower-energy Soret peak at 443 nm changes to a much smaller degree. Its amplitude only slightly varies with time but the position of the dip does not change at all.

Second, there is no stimulated emission (SE) from S_2 detectable as evident in the monomer via a dip around 450 nm. SE would be identified via a dip in the black EADS, which possesses no such feature.

Third, the large positive signal between Soret and Q band, attributable to ESA, is evident as in the monomer. But the black EADS has a positive contribution at 467 nm, which vanishes with 113 fs and builds up between 490 and 540 nm. This phenomenon does not occur in ZnTPP. The remaining positive signal decreases from the red to the blue and the green EADS. No peaklike structure reappears until the

1.5 ns component becomes important, resulting in a maximum at 477 nm. The latter component induces a decrease on the low-energy side of the isosbestic point at 504 nm. These contributions are shifted by ≈ 600 cm^{-1} towards lower energies in comparison to the monomer but behave in a very similar way.

Fourth, a dip is seen that is initially centered at 562 nm and that as such corresponds to the Q band in the absorption spectrum in Fig. 4.7. The amplitude of the dip decreases strongly and the contribution plateaus with 113 fs and subsequently with 7.8 ps, thus, most possible representing a combined GSB and SE signal. Furthermore, the dip red-shifts to 564 nm with the same time constant of about 8 ps. No significant changes are observed on a time-scale of 40 ps. Finally, the dip red-shifts slightly with a structure that remains nearly unaltered on a time-scale of 1.5 ns. A further dip is observed that initially absorbs at about 600 nm (black EADS). This dip flattens significantly for its low energetic contributions while the minimum position red-shifts to 606 nm as time progresses (red, blue EADS). On the nanosecond time-scale a clear minimum emerges at 601 nm, which corresponds well to the predominant fluorescence wavelength. The last observable feature is again a dip, centered at 665 nm in the red EADS, also due to stimulated emission or fluorescence in the steady-state experiments. The signal at this wavelength decreases with 7.8 and 40 ps and red-shifts to 666 nm on the latter time-scale.

Features that are better observed in the DADS will be pointed out in the following. Interestingly, the 660 nm band seems to build up much faster when compared to the 2 ps dynamics in ZnTPP — please compare the black DADS in Fig. 4.16 and the red DADS in Fig. 4.10. Additionally, the red DADS in Fig. 4.16 only contributes significantly in two regions, between 411 and 452 nm, and as well between 533 and 598 nm. At first glance the two contributions look very similar in these two regions — exhibiting a dip to the higher-energy side and a positive peak to the lower-energy side of the respective region. The blue DADS gives rise to a negative double-peak shape in the Soret region and apparent dips in the Q band. The green DADS exhibits a dip at 559 nm overlapped by a broad positive signal combined with a strong decrease in SE at 665 nm.

Photodynamics after Q-Band Excitation

The EADS resulting from global fits of the $(ZnTPP)_2$ transient-absorption data excited at 560 nm are shown in Fig. 4.17. Five time constants were again needed to fit the dynamics. The change in excitation wavelength has its largest impact on the black EADS. Here, the time constant of 260 fs is twice as large as in the case of 400 nm excitation. The Soret peak at 426 nm in the black EADS has a much smaller amplitude than its neighboring Soret peak at 442 nm in the same EADS. This is in sharp contrast to the black EADS in Fig. 4.16 with similar amplitudes for both peaks. Both black EADS furthermore have a positive peak-like contribution at about 468 nm independent of the excitation wavelength. However, no positive contribution stems from the very fast time component in the 560 nm excitation between 488 to 540 nm. Another noticeable difference evolves at 659 nm in the black EADS of

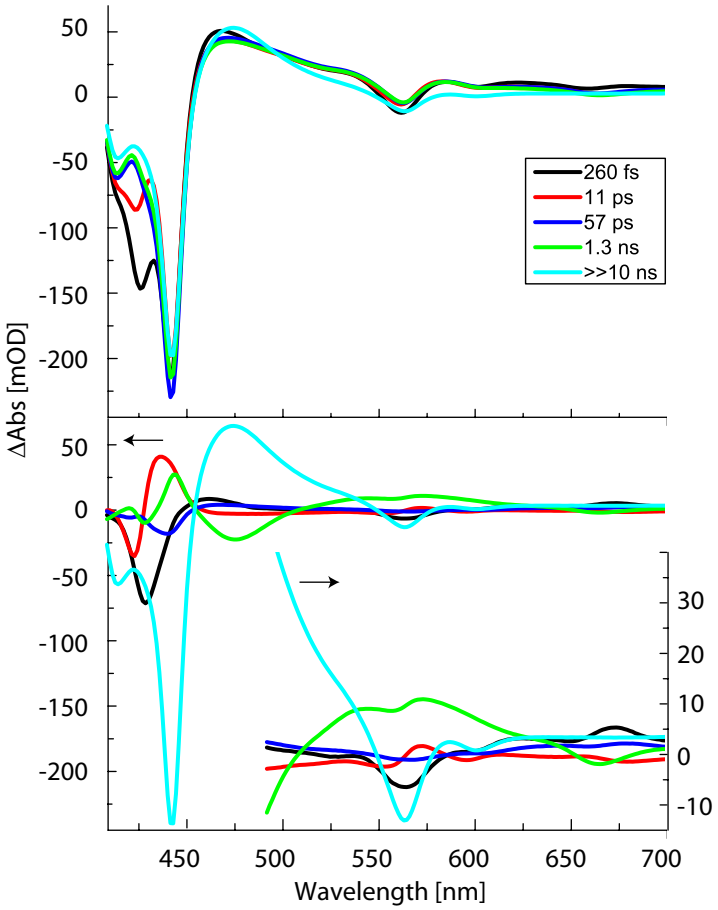

Figure 4.17: EADS (top) and DADS (bottom) of $(ZnTPP)_2$ excited with 560 nm showing the similar temporal changes induced by five time constants: 260 fs (black), 11 ps (red), 57 ps (blue), 1.3 ns (green) and constant offset (cyan). The inset (bottom, lower right panel) magnifies the signal to the red of the isosbestic point at 489 nm with arrows denoting the corresponding ordinate [116].

Fig. 4.17. In particular a dip is evident right from the start in addition to a positive signal build-up (as evidenced in the DADS), whereas the black DADS in Fig. 4.16 only shows positive build-up of this signal without a preceding stimulated emission signal.

It can be seen in the EADS in Fig. 4.16 and Fig. 4.17 that the difference spectra belonging to delay times larger than one picosecond exhibit only small differences for S_1 and S_2 excitation. The shape of all spectra except for the black one is generally unaltered. The cyan EADS shows the remaining signal at the maximum time delay of 3.7 ns, which is remarkably similar for both excitation wavelengths and even compared to ZnTPP. Table 4.4 compiles the time constants obtained by globally fitting the $(ZnTPP)_2$ transient-absorption data. The values are in agreement with Table 4.3, where different bisporphyrins are analyzed.

λ_P / nm	τ_1/ fs	τ_2/ ps	τ_3/ ps	τ_4/ ns
400	113 ± 25	8 ± 1	40 ± 7	1.5 ± 0.1
560	260 ± 30	1 ± 1	57 ± 3	1.3 ± 0.1

Table 4.4: Time constants obtained by global fitting routines for the relaxation dynamics of $(ZnTPP)_2$ after excitation into S_1 and S_2. In addition, a lifetime of 58 µs was measured for the triplet state.

Photoinduced Properties on the µs Time-Scale

In order to determine the lifetime of the triplet state of $(ZnTPP)_2$, whose lifetime exceeds the time-scale of the femtosecond experiments, transient-absorption measurements upon excitation at 532 nm with nanosecond pulses were performed in the absence of oxygen for lifetimes up to 200 µs. The results are shown in Fig. 4.18. The difference spectra in Fig. 4.10a) reveal large excited-state absorptions at 480 and 840 nm relating to the triplet states of the bisporphyrin. In addition, positive signals are evident between 400 and 1000 nm. The dominating ground-state bleach at 440 nm is still observable and seemingly the small Q-band bleach at 560 nm. At the end of the measurement nearly the entire excited population has returned to the ground state and no other photoproduct is formed. A kinetic analysis of the triplet excited-state absorption at 840 nm (blue) reveals a monoexponential decay with a lifetime of 58 µs [Fig. 4.10b)]. In comparison with the lifetime of $(ZnTPP)_2$ in toluene (52 µs), the more polar solvent ethanol seems to stabilize the triplet state.

Ultrafast Photodynamics in the Near-Infrared Regime

Fig. 4.19 shows transient-absorption data of $(ZnTPP)_2$ after excitation with 400 nm into the Soret band and a NIR continuum probe ranging from 800 to 1000 nm as a contour plot, again with logarithmic scaling after a time delay of 1 ps. The advantage of this spectral domain is that the first optically allowed electronic transition from the $(ZnTPP)_2$ singlet ground state corresponds to the Q-band absorption between 500 and 600 nm. Stimulated emission and fluorescence is also constrained to wavelengths shorter than 700 nm as shown in the fluorescence spectrum in Fig. 4.7 and the transient-absorption map in Fig. 4.14. Thus, only excited state or photo product absorptions are possible in this spectral range. However, excitation from S_1 into S_2 requires an excitation wavelength between 1500 and 2000 nm, calculated using the energetic spacing between Q and Soret band. Hence, this signal can be excluded and only higher states are accessible.

Examining the data, the existence of a strong coherent artifact caused by strongly overlapping and interaction pump and probe pulses in the solvent or the flow cell, is clearly seen around time zero by both negative and positive contributions with a short lifetime. In addition, a small signal for negative waiting times T is evident around 900 nm, the very symmetric shape resembles the so-called perturbed free induction decay [174]. This signal is common in the infrared, because it depends

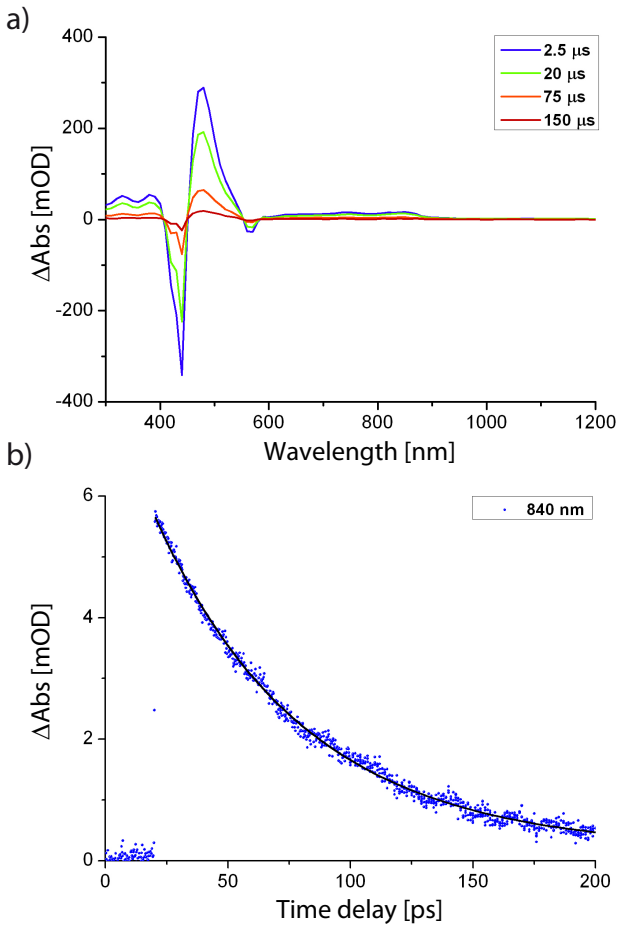

Figure 4.18: a) Broadband differential absorption spectra obtained upon nanosecond flash photolysis (532 nm) of $(ZnTPP)_2$ for time delays between 2.5 and 150 µs at room temperature, indicating the triplet state of $(ZnTPP)_2$ at 480 and 840 nm. b) Time-absorption profiles of $(ZnTPP)_2$ at 840 nm, monitoring the decay of the triplet state [116].

indirectly on the bandwidth of a transition, which is much smaller for pure vibrations. However, it has also been observed for electronic transitions in a porphyrin system [175]. It can only occur at a wavelength resonant with ground-state transitions, because, as a result of the negative time delays, it depends on the probe pulse interacting with the sample before arrival of the pump. No excited states are participating. $(ZnTPP)_2$ has no absorption band in this spectral range, seemingly excluding this explanation for the signal observed. However, the triplet state absorbs there as is evident in the difference spectra in Fig. 4.18a). Therefore, a possible explanation is that the pump does not exchange the entire sample between two laser shots, and the free induction decay is induced by population in T_1. While this free induction decay is used as a spectroscopic signal [176], here it is an unwanted artifact.

Both, the coherent artifact and this signal for $T < 0$, are decayed after 200 fs at most, and are not further considered in the data analysis. Afterwards, the measured absorption change is positive, indicated by reddish colors, over the entire measured

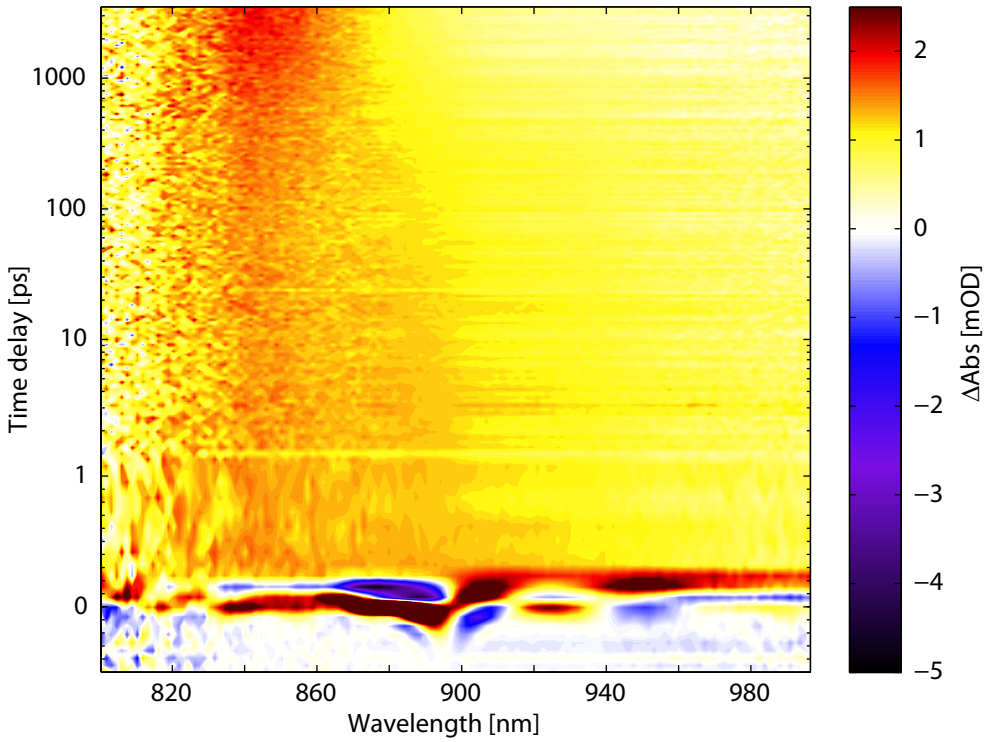

Figure 4.19: Transient-absorption data of $(ZnTPP)_2$ after excitation with 400 nm and a NIR probe. While the entire signal is positive (reddish colors), corresponding to increased absorption, the signal rises at ≈ 845 nm while it decays at ≈ 900 nm.

spectral range and shows nearly no change with time up to hundreds of picoseconds. Finally, with a nanosecond dynamic one peak around 845 nm increases and sharpens with time while around 900 nm a decay is evident.

For a more in-depth analysis a global fit, similar to the previous experiments, was performed but this time only two time constants were necessary and again an instrument response of ≈100 fs was obtained. There is no change with a fs or fast ps time constant, thus, the Soret band, which is excited by the used 400 nm pulses is not responsible for the behavior observed. The obtained time constants resulted in dynamics between 0.9 and 1.2 ns, depending on the measurement, and an additional global offset. While the difference for the time constants within two measurements is quite large, the spectral signature was exactly the same for both. Hence, this difference is attributed to the measured time delay of only 3 ns, which corresponds to only three times of the observed lifetime. In Fig. 4.20 three transients (dotted) and their corresponding fits (lines) in the same color are shown exemplifying the fit quality. The shown transients indicate the rise of a band with 0.9 ns at 845 nm (green), the existence of an isosbestic point at 872 nm (red) and a decay of an excited state at 926 nm (blue).

The spectral signature of the global scheme is displayed in Fig. 4.21 (EADS in top and DADS in bottom panel). The EADS has at first a very broad ESA covering the

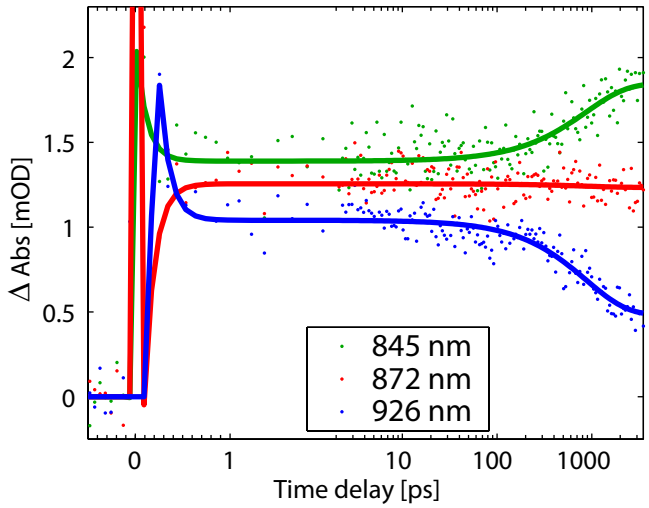

Figure 4.20: Transient behavior of $(ZnTPP)_2$ obtained with a NIR probe. A product absorption (green dots), an isosbestic point (red dots), and a decreasing ESA (blue dots) together with a global fitting routine (lines) are shown. The decaying signal around time zero corresponds to the coherent artifact.

entire spectral region (black), which changes with roughly 900 ps. This resembles the broad ESAs observed over the entire visible spectral range in the previous measurements (compare Fig. 4.16 and 4.17). The red EADS corresponds to the signal for very long times and a clear peak centered at 845 nm is present while for longer wavelength nearly no signal contributions remain. This peak corresponds well to the peak observed at 840 nm in the µs experiments (Fig. 4.18), which is associated there with the decay of a triplet state of $(ZnTPP)_2$. In addition the isosbestic point where all processes cancel each other is clearly identified at 872 nm. This entire behavior for the first 3 ns resembles the development of the sharp ESA centered at 477 nm found after probing in the visible.

The DADS in the bottom panel of Fig. 4.21 contain the same information but the influence of the 900 ps component is more clearly resolved (black). For higher wavelengths, relative to the isosbestic point, the absorption decays with time. In contrast, for lower wavelengths a rise is present, because the negative signal vanishes. Therefore, the positive absorption for the longest possible time delay remains (red).

4.5.4 Creation of Possible Temporal Relaxation Schemes

In the dimer, new electronic states are formed due to excitonic coupling, whose impact on the molecule's relaxation dynamics, as evident in the experimental data in Sec. 4.5.3, will be discussed here [116]. The changes in comparison to the monomer will be explained with the help of two models and a calculation of the transition dipole moments leading to the Soret-band absorption. The first model is based on the model of Kim and coworkers and particularly adheres to their distinction

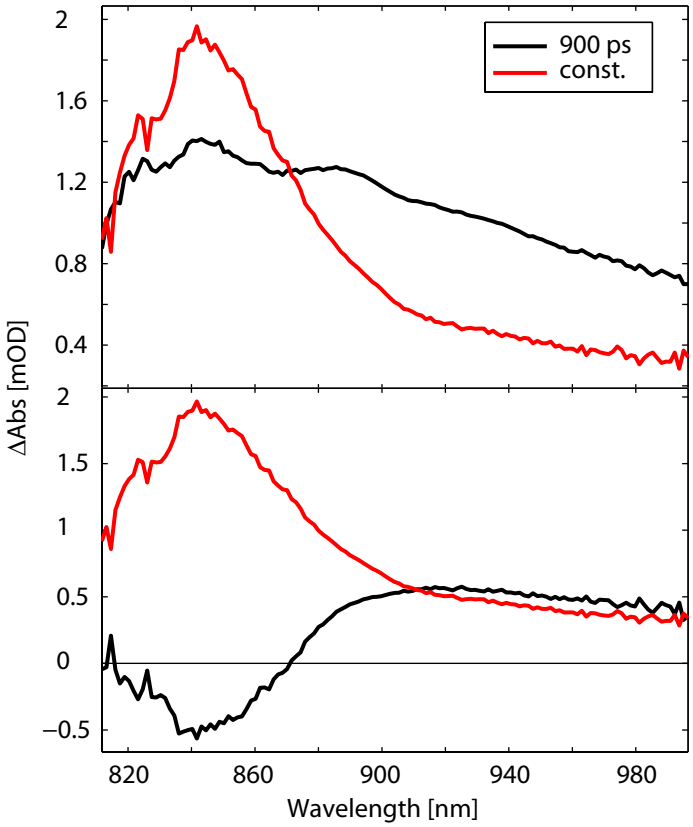

Figure 4.21: EADS (top) and DADS (bottom) of $(ZnTPP)_2$ probed with a NIR continuum showing the temporal changes with a 900 ps time constant (black) and the offset (red).

between monomeric and excitonic states [109, 120]. The second model is simpler but describes the measured spectra equally well while showing good agreement with the results from the TD-DFT calculations below. It is basically a transfer of the concepts presented for excitonic splitting in S_1 (visualized in Fig. 4.5) into the S_2 state.

To allow a more in-depth investigation of the excited states of $(ZnTPP)_2$ the molecular structure was optimized using DFT methods and the corresponding absorption spectrum was calculated (the following calculations were performed in the group of Prof. Bringmann). Earlier studies had shown that simple DFT methods (with either pure or hybrid functionals) cannot fully reproduce the conformational features of these compounds [115]. Thus, the long-range- and dispersion-corrected functional ωB97xD was used in combination with the 6-31G* basis set (and 6-311G* for Zn). Only this functional yielded a conformation of the molecule that closely resembles the one found in the X-ray structure of the free-base analogue of $(ZnTPP)_2$ corresponding to an angle of 57° between the porphyrin subunits. The calculated structure had a dihedral angle of 68°, which is rather close to 57°, especially, when considering the insertion of a Zn atom and the non-crystalline environment in the case of $(ZnTPP)_2$ in solution. Without dispersion corrections the calculations give a structure with a 90° angle and with pure or hybrid functionals in combination with Grimme's dispersion correction a conformation is found with a quite small angle of 34° between

these moieties (both conformations are nearly C_2-symmetric, corresponding to a single rotation axis). However, the angle between the monomers has a very strong impact on the excited states, and, accordingly, also on the absorption spectrum of the molecule. The ωB97xD-optimized structure is fully unsymmetrical with an angle of 68° between the porphyrin monomers and is shown in blue in Fig. 4.13b). As a consequence, the (B_X-B_X) excitation should no longer be dipole-forbidden, as the B_X transition dipole moments of the monomers are not in-line anymore, in contrast to the *meso,meso'*-linked porphyrins with nearly orthogonal building blocks [see Fig. 4.13a)]. To calculate the excited states of $(ZnTPP)_2$ the long-range-corrected hybrid functional CAM-B3LYP was used, because previous studies had shown that this functional reproduces the absorption spectra of porphyrins more reliably than standard functionals like e.g. B3LYP [177, 178]. Most importantly the functional introduces nearly no charge-transfer contributions in the Soret- and Q-band regions of porphyrins and chlorophylls, which is in agreement with high-level calculations such as SAC-CI, DFT/MRCI, or CASPT2.

For a better comparison, the optimized structures of three bisporphyrins with different angles between the porphyrin units and their corresponding absorption spectra were calculated and are shown in Fig. 4.22. The TD CAM-B3LYP calculations of the ωB97xD-optimized structure reproduce the experimental UV spectrum of $(ZnTPP)_2$ (blue) very well. As expected from the energy level diagram for *meso,meso'*-bisporphyrins in Fig. 4.13, the Soret region contains four different states, all of them without any significant charge-transfer character. Hence, the assignment of the states can be transferred directly to $(ZnTPP)_2$. The higher-energetic peak at 427 nm, called $S_{2\beta}$, consists of two quite close excitations with a distance of 2.9 nm, which comprise transition dipole moments belonging to the B_Y and B_Z coupling of the monomeric moments. The small energetic distance between the two states again validates the transfer because lifted degeneracy is expected for non-orthogonal dihedral angles. The shoulder at 415 nm, also found in the experiment as a dip for long waiting times, e.g., in the EADS in Fig. 4.16, is the no longer dipole-forbidden (B_X-B_X) transition. The state associated with the lower-energetic Soret peak is denoted as $S_{2\alpha}$ and originates from the (B_X+B_X) transition. This state is expected to be the most stable S_2 configuration because it possesses the lowest energy. In addition, there are four nearly degenerate states forming the Q band around 600 nm, to which will be referred as S_1 since no separation is possible. In principle they should possess the same lifted degeneracy as seen in the Soret band and calculated for a model dimer in Sec. 4.2.3. The Q-band absorption at 563 nm is known to belong to higher vibrational states of S_1 in porphyrins [150]. This is confirmed by the calculations, which are not able to predict vibrational states and accordingly fail to identify the experimentally found hot Q band. Hence, there is zero signal strength at this wavelength, even after broadening the observed transitions as a necessary extension of the calculations because the experiments are all performed in the condensed phase.

If the two monoporphyrins are fixed at an near orthogonal orientation the red spectrum (top) with the corresponding structure (bottom) is observed in Fig. 4.22 using D-PCM, a polarization model, to account for the used solvent ethanol. In order to

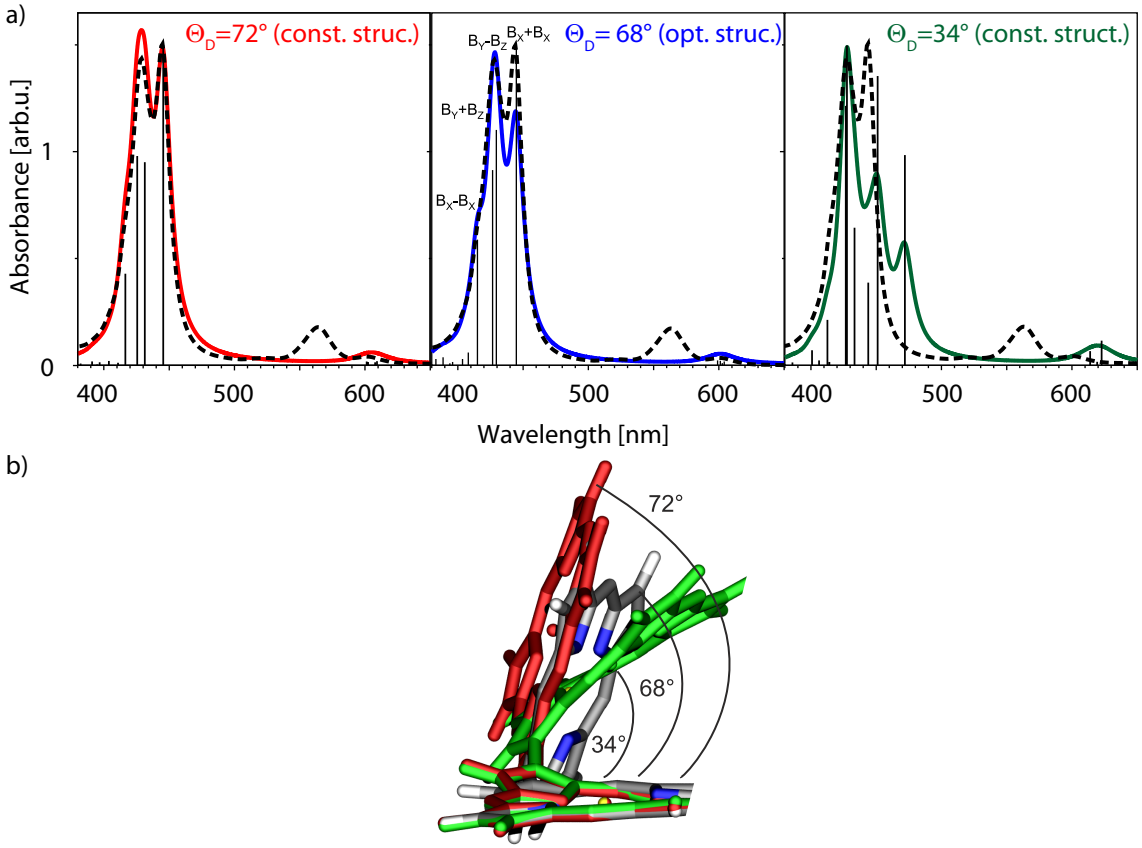

Figure 4.22: a) Calculated (solid) and experimental (black, dashed) absorption spectra of $(ZnTPP)_2$ for different dihedral angles. Transitions without spectral broadening are shown as bars at the corresponding wavelength. In addition, the couplings of the monomeric transition dipole moments of the prominent states are shown. b) Corresponding structures of the constrained (const., 72°(red), 34° (green)) and optimized (opt.) spectra [68°(blue)].

reach the energetic minimum of this structure the two linked porphyrin macrocycles bend towards each other so that an effective dihedral angle of only $\Theta_D = 72°$ is formed. This already demonstrates that a β,β'-linked bisporphyrin like $(ZnTPP)_2$ is most stable in a non orthogonal conformation. The UV spectrum obtained for $\Theta_D = 72°$ is quite similar to the one for the minimum configuration. This is not surprising due to the small effective change of the dihedral angle between the two structures. However, two differences are evident. First, the spectral difference between the $(B_Y{+}B_Z)$ and $(B_Y{-}B_Z)$ states is with 5.8 nm twice as large as before. Yet, even such a large broadening is not resolved in the experiments. Second, the oscillator strength belonging to the transition into $(B_X{-}B_X)$ is smaller so that the shoulder in the UV curve nearly vanishes. This lower value is in line with the larger dihedral angle because the transition dipoles B_X of each monomer possess higher effective overlap.

If a very small dihedral angle of $\Theta_D = 34°$ is chosen in order to achieve a more planar configuration the resulting absorption spectrum (green) does not match the experimental one at all. A much larger Davydov splitting can be found and addi-

tional excited states in the Soret band occur, which do not possess experimental counterparts. All these additional states show charge-transfer character in contrast to the ones observed for the more orthogonal configurations, thus, showing that they belong to artifacts caused by choosing wrong theoretical parameters. Furthermore, the Q-band excitations are shifted to lower energies as compared to the experiment, hinting at a slightly stronger conjugation between the monomeric halves in this configuration. Interestingly, the S_0–$S_2(B_X+B_X)$ transition has a much lower intensity than in the minimum configuration showing the higher symmetry of this geometry by which this transition is again dipole forbidden. Thus, the near orthogonal and parallel configurations computed for the conformers found show only poor matching compared to the minimum structure with a dihedral angle of 68°.

The key to understanding both the steady-state and the dynamical properties of $(ZnTPP)_2$ is the temporal evolution of the higher-energy Soret peak since multiple transitions are present in the calculated absorption spectra. The $S_{2\beta}$ peak decreases strongly and independently from the excitation wavelength on a femtosecond timescale. If this decay was attributable to SE between $S_{2\beta}$ and S_0, the initially observable GSB would be restored after the depopulation of the Soret states, which is expected to occur within a few picoseconds or faster. However, as is apparent from Fig. 4.16, the EADS do not support the observation that the ground state is repopulated since the GSB does not vanish completely. This leaves partial GSB recovery as the only viable explanation. GSB recovery implies that the ground state of a molecule is repopulated, though, a process that can be excluded in the present case since a population transfer into T_1 seems to occur and the $S_{2\alpha}$ peak does behave vastly different from the $S_{2\beta}$ peak. That means if GSB recovery takes place the relaxed S_0 would be subject to re-excitation into $S_{2\alpha}$. Accordingly this peak should decrease with exactly the same time constant as $S_{2\beta}$, which is, anyhow, not the case.

Intersystem crossing is evident when considering the behavior at 504 nm next to the isosbestic point, increasing signal for higher frequencies and decreasing signal for lower frequencies, and that SE from S_1 around 665 nm disappears with 1.5 ns without replenishing the ground state at Q(1,0) and Q(0,0). This dynamic is very similar to that of ZnTPP but somewhat faster — 1.5 ns versus 2 ns — and, thus, assigned to intersystem crossing originating in S_1. Moreover, the green and cyan EADS/DADS in Fig. 4.16 resemble the green and cyan EADS/DADS of the monomer ZnTPP shown in Fig. 4.10 and Fig. 4.11. The agreement in terms of spectral appearance and associated time constants implies the same origin for the respective time constant. In order to resolve the intersystem crossing directly, transient-absorption with a NIR probe was performed (see Fig 4.19). With a lifetime of one nanosecond a clear sharp peak emerges, centered at 845 nm, while a broadband ESA vanishes, which can be attributed to originate from the Q band because of the similar lifetime as observed for the decay in the VIS measurement. This is visualized in the transients in Fig. 4.20, which clearly show the population of an excited state (green) and the connected decay of the originating state (blue), in addition to the isosbestic point in between (red). The final evidence for the participation of triplet states is gained by the nanosecond transient-absorption measurements, revealing a lifetime of the

excited states of $(ZnTPP)_2$ centered at 480 nm and 840 nm of 58 µs (Fig. 4.18). This long lifetime is only attributable to a triplet state.

By combining all three measurements the photodynamic pathway is unveiled. The population transfer proceeds from S_1 to T_1 and finally back to S_0. The nanosecond measurements clearly link the absorption at 845 nm to the final triplet state. Thus, this state that is populated with one nanosecond and decreases latter on with 58 µs; therefore, no other transfer proceeds during this time. Hence, the participating triplet state T_n is identified as T_1.

After having explained the final reaction steps on a nanosecond scale, the discussion of the behavior in S_2 is continued. The apparent contradiction of the Soret-band behavior can be solved by employing D. Kim and coworkers' model that has already been described in section 4.5.1 [120]. The glaringly different dynamics of the two Soret peaks can be explained by their distinct localization character. According to this model, the $S_{2\beta}$ state is strongly localized at one of the two porphyrins, thus, is very similar to a Soret-band absorption in a monomer. By contrast, the $S_{2\alpha}$ state is completely delocalized over the dimer and has no monomeric equivalent. However, both states are excitonic states with a certain amount of delocalization, only the relative amount varies. The excitonic character of both states is also indicated by the observable splitting of the S_2 band in the absorption spectrum shown in Fig. 4.7 (red curve). This statement is strongly supported by Bringmann *et al.*, who showed that the doublet of the Soret absorption band originates from excitonic splitting by comparing UV absorption and CD spectra of atropo-enantiomers in directly β,β'-linked bisporphyrins such as $(ZnTPP)_2$ [115]. If a physical process like, for instance, coupling of these excitonic states to the (torsional) vibrational modes [179] of the dimer or structural imperfections [180] exists, it would force the excitation to become fully localized at one of its monomeric subunits. Such localization dynamics are indeed observable in various molecular systems [132,181]. For porphyrin dimers, it has been shown by transient conductivity techniques that the degree of delocalization varies for different electronic states, namely singlet versus triplet excited states [182, 183]. Decoherence of excitons disallows excitations into the initial, delocalized states, since the electron distribution and, in turn, the transition dipole moment of an excited molecule usually differs from that of the ground state. However, the confinement of the excitation to one of the monomeric halves leaves the other monomer moiety virtually unexcited. In other words, decoherence of the excitonic states essentially creates excited as well as unexcited monomeric halves. Thus, the unexcited moieties created can be excited by absorption of a photon giving rise to ESA that essentially resembles the ground-state absorption spectrum of ZnTPP. The model of Kim and coworkers predicts that these monomeric absorptions show up at exactly the wavelengths where the weakly excitonic states absorb. As a consequence, the states with a strong excitonic character remain bleached in the difference spectrum, while the states with a weak excitonic character seemingly recover to the ground state. However, the GSB of the latter band is only hidden by an ESA, which resembles the monomer absorption. This scenario agrees well with the observations during the first picosecond in the Soret-band region.

In addition, the evolution of the 562 nm dip underscores this interpretation. On time-scales of the excitonic decoherence, the dip decreases in amplitude — a trend similar to that discussed in the context of the Soret-band dynamics. The Q band arises from four electronic transitions — in full analogy to Fig. 4.13a) and the Soret band — two degenerate states for each monomer. However, no splitting into separate bands is observed for these states as discussed in Sec. 4.5.3. ESA from the monomeric ground state should decrease the observable GSB of the whole Q band. This again matches the observations presented in Sec. 4.5.3.

In line with the fluorescence spectra, SE from S_1 should emerge around 655 nm. This is, however, not seen in the black EADS of Fig. 4.16, but in the red EADS of the same Figure. Moreover, SE is already present in the black EADS when the samples are excited at 560 nm (Fig. 4.17). Here, the dip in the black spectrum serves as evidence for its presence. As a matter of fact, the fs time constant must also be assigned to internal conversion from $S_{2\beta}$ or $S_{2\alpha}$ into S_1 in addition to the localization process. Unfortunately, it cannot be concluded from the measurements when exactly the internal conversion into S_1 starts. However, Kim and coworkers [120, 184] observed that the IC rate k_{IC} into S_1 for different porphyrin oligomers obeys the energy gap law. The latter is given by

$$k_{IC} \propto 10^{13} s^{-1} e^{(-\kappa \Delta E)}, \tag{4.17}$$

with the proportionality constant κ and the energy difference ΔE between $S_{2\beta}$ and $S_{2\alpha}$ [184]. Using $\Delta E = E(S_{2\beta}) - E(_{2\alpha}) \approx 813\,\mathrm{cm}^{-1}$ and $\kappa \approx 2 * 10^4\,\mathrm{cm}^{-1}$ - as determined in Ref. [120] by a fit of the energy gap law to data obtained by excitation into the Soret band — k_{IC} is approximately $(120\ \mathrm{fs})^{-1}$. This value is in intriguing agreement with the time constant of (114 ± 25) fs measured in the present work. Therefore, it can be concluded that the $S_{2\beta} \rightarrow S_{2\alpha}$ transition is the rate-limiting step for the internal conversion into S_1. This agreement moreover provides evidence for the comparability of the oligomers in *meso,meso'* configuration investigated there and the dimer studied here. Compared to ZnTPP's internal conversion with 2 ps, $(ZnTPP)_2$ relaxes about one order of magnitude faster, which is in good agreement with the work by Hochstrasser and coworkers who reported a similar ratio for a monomeric and a dimeric structure (compare Tables 4.1 and 4.3) [108].

The ESA feature seen in the black EADS of Fig. 4.16 and Fig. 4.17 at about 467 nm is observable upon 400 and 560 nm excitation, but not detectable in the black EADS of ZnTPP (Figs. 4.10, 4.11). The occurrence of this feature only in the dimer implicates that an exciton-related state is populated by this ESA. Following this, the decrease of the amplitude of the ESA with both ps time-scales ($\approx$ 10 ps, $\approx$ 50 ps) resembles that of the S_2 peak. This again indicates the importance of excitonic coupling for the $(ZnTPP)_2$ dimer.

The red DADS in Fig. 4.16 associated with a time-scale of roughly 9 ps has only significant contributions in the wavelength range of ground-state absorption. In both, the Soret and Q band, the red DADS shape consists of a dip at shorter wavelengths and a positive peak at longer wavelengths. The positive peak of this component contradicts a GSB recovery. Owing to the fact that the Soret-band population decays

on the fs time-scale, this rules out that the red DADS, which has quite a large amplitude in the Soret-band region, originates from SE. The observable features therefore again arise from ESA. The following considerations explain the decay and neighboring rise of this ESA: A system consisting of two excitonic states yields upon back-to-back excitation a two-exciton state [132]. As a matter of fact, a molecule in the excited $S_{1\beta}$ is still excitable into $S_{1\alpha}$ and vice versa. Hence, a transition from $S_{1\beta}$ into $S_{1\alpha}$ would lead to an increase of absorption of photons with $E(S_{1\beta})$ and a reduction of absorption of photons with $E(S_{1\alpha})$. On the basis of $E(S_{1\beta}) > E(S_{1\alpha})$ (see Fig. 4.13 and Fig. 4.7) the red DADS in the Q-band region are well in line with the expectation. In the context of higher-energy excitonic states, a molecule in the excited $S_{1\beta}$ state can still be excited into $S_{2\alpha}$, but not into $S_{2\beta}$, whereas a molecule in the excited $S_{1\alpha}$ state can still be excited into $S_{2\beta}$, but not into $S_{2\alpha}$. Again, a good agreement between experiment and prediction is reached for the DADS in the Soret-band region. Further support for this notion is shown in Fig. 4.23, which shows the existence of two different kinds of states belonging to the B_X transition dipole moments on the one hand and to the B_Y and B_Z moments on the other hand. Additionally, the ps time-scale reveals a transition between states of comparable energetic spacing, namely IVR, for which $(0.1\text{-}10\ \text{ps})^{-1}$ rates are typical. This rationale necessitates that not only monomeric, but also excitonic states are populated and consequently probed in the molecular ensemble. While the origin of the fs time component is the relaxation from the excitonic into the monomeric state, the ps time constant relates to relaxation both in the excitonic and monomeric states in the Q band. Hence, the loss of excitonic coherence may result in an excitation that is localized in one of the two moieties. This redistribution of the excitation between both subunits of the dimer may give rise to incoherent excitonic excitations [132].

In *meso,meso'*-linked porphyrin dimers, either ethyne-bridged or directly-linked, the dynamics on a fast-picosecond time-scale are assigned to a change of the dihedral angle between the two porphyrin moieties [108, 120]. This rotation is assumed to happen within S_1 after photoexcitation into S_2. In contrast, this explanation was discarded for the 18 ps component observed in ethyne-bridged β,β'-linked bisporphyrin on the basis of strong steric hindrance [108]. Importantly, a high rotational barrier was also experimentally and theoretically determined by Bringmann and coworkers for $(ZnTPP)_2$ [115].

Based on the spectral shape of the blue DADS in Fig. 4.16, the $\approx$ 40 ps time constant in the Soret region is due to the reformation of the ground state, i.e., a typical GSB recovery for a small percentage of the molecules takes place. The time-scale for this process implies that the energy is transferred to the solvent. The dip in the green DADS of Fig. 4.16 at 560 nm (strongest Q-band absorption) relates to the $S_1 \rightarrow S_0$ relaxation that is dominated by the $S_1 \rightarrow T_1$ intersystem crossing. SE from the S_1 states is observed for 660 nm showing the existence and the temporal behavior of a $S_1 \rightarrow S_0$ transition. However, the fluorescence quantum yield Φ_F of $(ZnTPP)_2$ is between 2% and 3% in toluene, tetrahydrofuran, and benzonitrile [185]. Such values for the dimer are comparable to that of the monomer, where such a dip is unobservable, suggesting the existence of an additional contribution of unknown

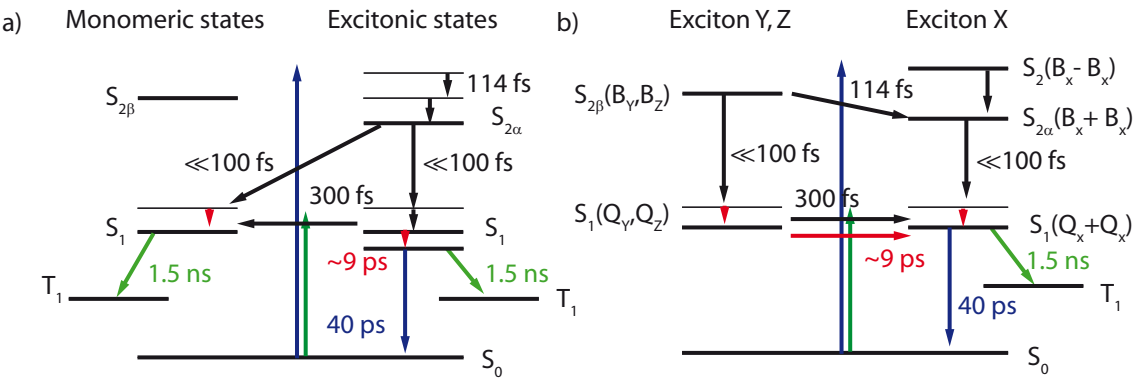

Figure 4.23: Two possible reaction schemes for $(ZnTPP)_2$ a) a mixed monomeric/excitonic approach with distinct monomeric behavior; b) a complete excitonic scheme based on superposition of monomeric states forming new ones. The red downward arrows are assigned to relaxation dynamics in S_1. Thinner lines represent vibrational states. The blue and the green lines in both schemes denote the actual excitation wavelengths [116].

origin. The inferences drawn so far in this section are combined in the model shown in Fig. 4.23a). While this model is able to account sufficiently for all measured time constants, discrimination between monomer-like and pure excitonic states is complicated and somewhat nontransparent.

The second, alternative model to rationalize the dynamics of the dimer is an alteration of the first model. It disregards the distinction between monomeric and excitonic states as it is explained for a physical dimer in the first excited state in Sec. 4.2.3. In fact, it extends the exciton concept and the idea of back-to-back excitation, resulting in a double-excited molecule, to the fastest component in the very same way it was applied in the assignment of the 9 ps component. The principle is also identical to the calculations for a dimer, which absorbs at the two wavelengths of the Soret band in Fig. 4.5. The aforementioned discussions concerning the spectral-temporal evolution of the difference spectra of the dimer on time-scales other than the fs time-scale are fully applicable to the latter model in Fig. 4.23b), only the first ultrafast component is described differently.

In addition, the model assumes redistribution of the excitation between the two moieties, leading to the formation of incoherent excitonic excitations on a femtosecond time-scale. It does, however, not emphasize the localization character. Instead, it explains the observations within a comparably simple excitonic framework. The fs time constant remains assigned to the excitonic loss of coherence and the $S_2 \rightarrow S_1$ IC, but is assumed to predominantly populate $S_{1\alpha}$, which enables the excitation of $S_{2\beta}$ (B_Y, B_Z) and $S_{1\beta}$ (Q_Y, Q_Z). By contrast, the (re-)excitation of $S_{2\alpha}(B_X{+}B_X)$ and $S_{1\alpha}(Q_X{+}Q_X)$ remain disallowed. In consequence, ESAs occur that result in a decrease of the higher-energy Soret peak and the Q-band absorptions; this consequence agrees well with the observations outlined above.

This model is strengthened by a closer inspection of the cyan DADS of $(ZnTPP)_2$ in Fig. 4.17. It shows one remarkable feature, namely a dip with a minimum at about

414 nm. A corresponding feature can also be identified at the same wavelength in the steady-state spectrum of the dimer as a shoulder peak, which is according to the TD-DFT calculations a higher-energy excitonic Soret state — denoted by $S_2(B_X\text{-}B_X)$ — that is dipole-forbidden in the stringent 90° alignment. Since the calculations reveal a non-orthogonal conformation, the transition into $S_2(B_X\text{-}B_X)$ is allowed unlike in the case of the *meso,meso'*-linked porphyrin dimers (Fig. 4.13). This gives rise to the additional transition centered around 415 nm. The oscillator strength is somewhat weaker but comparable to the other Soret transitions and the transition seems more stable when compared to the short-lived states with participation of B_Y and B_Z. The conclusive assignment of this transition substantiates a purely excitonic explanation without the need to consider both monomeric and excitonic states.

4.6 $(ZnTPP)_2$ — Accessing Population and Energy Transfer in Excited States

Two dimensional electronic spectroscopy is a powerful technique to detect couplings between different states [15]. One challenge with porphyrins is the spectral range of the Soret band, centered around 430 nm, which lies in-between the ultraviolet and the visible spectral range. Thus, nearly no multidimensional spectra are available in literature. Recently, a weakly-linked magnesium bisporphyrin was measured in a fluorescence based approach, which yielded information about the dihedral angle and suggested excitonic interaction [111,112]. With the same technique folding dynamics of a Zn bisporphyrin with a long spacer inside a liposome membrane were studied, however, the excited-state relaxation was deemed a future goal [186].

In the previous section two different models were introduced in order to explain the temporal behavior of $(ZnTPP)_2$ after photoexcitation. The pure excitonic approach necessitates direct coupling between $S_{2\beta}$ and $S_{2\alpha}$ resulting in population transfer. Via 2D spectroscopy in box geometry with degenerate pump and probe pulses this only indirectly inferred population transfer will be directly observed in the following chapters validating the latter model visualized in Fig. 4.23b). At first, the experimental conditions and necessary adaptations, when working with degenerate pump and probe pulses around 430 nm, will be explained (Sec. 4.6.1). Afterwards, transient-absorption spectroscopy with degenerate pump and probe pulses directly exciting $S_{2\alpha}$ and $S_{2\beta}$ in the Soret band without much vibrational excess energy is performed with high time resolution (Sec. 4.6.2). The obtained results are compared to the 400 nm excitation case (compare Sec. 4.4.3) in order to confirm the observed features. Subsequently, independent transient-grating measurements in box geometry using low excitation densities verify the observations from the transient absorption experiments (Sec. 4.6.3). At last, coherent electronic 2D spectroscopy is used to directly observe population transfer in the Soret band (Sec. 4.6.4). These findings are discussed and the energy transfer confirmed by calculating the corresponding 2D spectra of a simplified excitonic four-level model (Sec. 4.6.5). The results of the following section are published in Ref. [117].

4.6.1 Experimental Conditions

The synthesis and linear characterization of $(ZnTPP)_2$ is identical to the one described in Section 4.3 albeit the concentration was reduced corresponding to an optical density of 0.3 at 443 nm in a 200 µm flow cell. This reduction is possible because the Q-band behavior will not be investigated here, therefore, the reduced signal strength there can be neglected. The flow cell (Starna, Type 48/UTWA/Q) possesses silica windows of only 200 µm thickness in order to decrease material dispersion.

For all experiments in the following chapter a different but similar fs laser system, as described in Sec. 3.1, was used. In brief consisting of: A diode-pumped MaiTai Oscillator, a Spitfire regenerative amplifier, and an Empower pump laser (all Spectra Physics) resulting in laser pulses with 100 fs duration, 4 W output power, and 1 kHz repetition rate. The degenerate pump and probe pulses were obtained after frequency doubling 870 nm pulses, generated from a commercial NOPA (TOPAS White, Light Conversion), in a 65 µm thick β-barium borate crystal. This results in pulses centered at 435 nm with 12 nm FWHM and a minimal pulse duration of 23 fs in case of a bandwidth-limited pulse.

The 2D setup itself, described in section 3.3.4, was designed for applications between 250 and 375 nm. Hence, the necessary wavelengths for experiments in the Soret band of $(ZnTPP)_2$ (400 to 450 nm) are not contained in the original specifications [85]: Accordingly, slight modifications were necessary. Every optical element in use is reflective, hence, only little dispersion is introduced, and is coated with aluminum in order to enable an effective reflection of UV light. When comparing the overall reflection for 450 nm and for the UV spectral range, it decreases roughly by 5% per optical element in the VIS because the reflection changes from ≈90% (UV) to ≈85% (VIS). With 10 optical elements placed after the crossed grating the effective transmission decreases by more than 50%. However, a 750 µW seed beam results in up to 4 nJ of energy in each single one of the four pulses. This pulse energy corresponds well to the required energies in the low nJ domain used in Ref. [85] for 2D experiments. In addition to the higher losses on the Al coatings, the beams are separated further apart at the crossed grating because of diffraction. In Fig. 4.24a) the diffraction pattern for a broadband pulse ranging from 250 (violet) to 375 nm (red) is shown, defining the minimal size of all optical elements, which was used to minimize the entire setup as much as possible. However, while the setup was designed using (1,1)-type reflections (green) of the grating, it was modified to use the (1,0)-type beams (white) later on, which possess a higher signal strength as shown in Fig. 4.24b) just by turning the grating by 45°. Hence, the beams move closer together by a factor of $\frac{1}{\sqrt{2}}$. Accordingly, the maximal possible wavelength is extended to 530 nm when considering the limitations caused by the size of the used optical elements. Finally, the mask, blocking all unused grating reflections, and the shutters, which allow the usage of different beam combinations, were changed to models which fit to this wavelength change.

Transient-grating measurements of pure ethanol at the sample position showed a coherent artifact [60,61] combined with inseparable solvent dynamics. Their combined

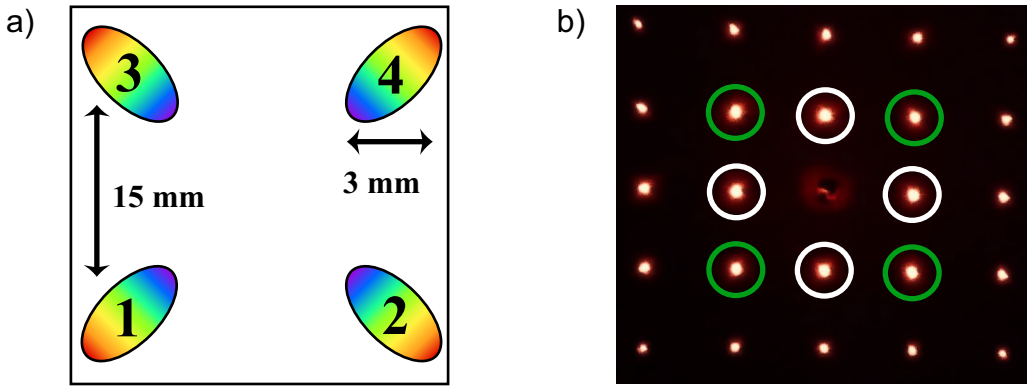

Figure 4.24: a) Spatial beam profile for a beam with a width from 250 to 375 nm (violet to red) if (1,1)-type beams are used, determining the size of the optical elements [95]. b) Reflections of the crossed grating after 633 nm illumination. Green circles correspond to (1,1)-type reflections while white circles correspond to (1,0)-type beams, which possess a higher reflection coefficient but move $\frac{1}{\sqrt{2}}$ times closer [34].

lifetime was approximately 50 fs, thus, determining the minimal time resolution in all experiments in box geometry with 435 nm excitation. For the 2D experiments the coherence time τ was scanned from -125 to 125 fs in steps of 1.4 fs. The absolute phase, necessary for data evaluation [75, 88] as described in Sec. 3.3.2, was adjusted to the measurement of the longest population time T of each scan over multiple times T before averaging over several different scans performed from short to long population times and vice versa. The longest measured population time $T = 500$ fs was chosen to avoid signals resulting from solvent contributions or phase twists [187], which aggravate the phasing procedure.

Transient-absorption data, necessary for the determination of the absolute phase in 2D measurements, were obtained in a setup similar to the one presented in Sec. 3.2. Though, in place of a continuum probe the 435 nm pulses were used as degenerate pump and probe pulses. In addition, dispersive elements were avoided, with the single exception being a 2 mm thin beam splitter, in order to achieve a good comparability with the all-reflective 2D setup. The spectrometer, the linear stages, and the acquisition and analysis software are of the exact same type as for the continuum mode transient-absorption setup (Sec. 3.2.3) [34, 188].

4.6.2 Transient Absorption with Ultrafast Time Resolution

Transient-absorption data after direct excitation into and probing of the Soret band are shown in a contour plot in Fig. 4.25 together with the pump and probe spectra (red) and the molecular absorption of $(ZnTPP)_2$ on top. The spacing on the time axis is linear since the absorption change was only measured up to a time delay of ≈750 fs. It is evident that the excitation spectrum covers both absorption peaks $S_{2\alpha}$ and $S_{2\beta}$ only partially. However, transient-absorption experiments only

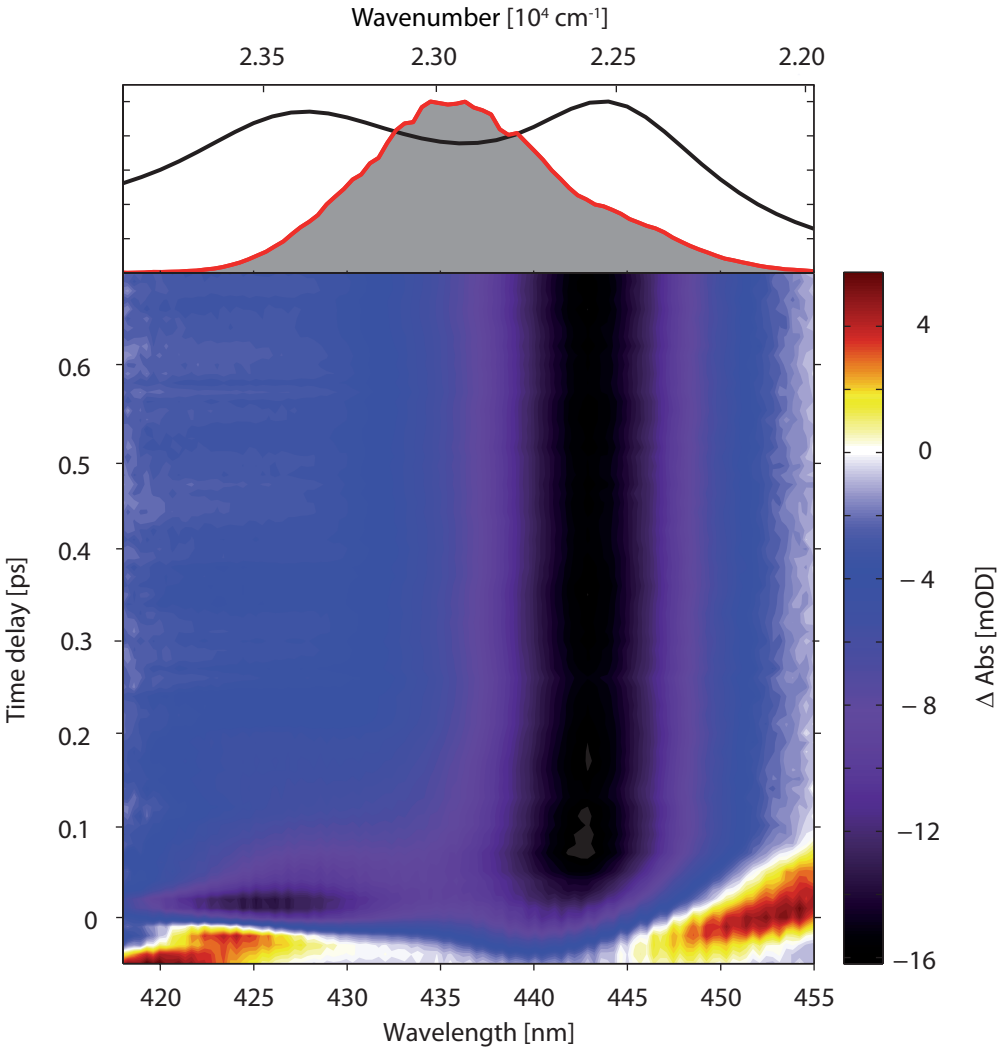

Figure 4.25: Transient-absorption data of $(ZnTPP)_2$ covering the Soret band showing only bleaching and emission signals, obtained with degenerate pump and probe pulses. Pump pulse (red) and molecular absorption (black) spectra are shown on top [117].

depend on the relative changes in the probe spectrum, thus, experimental results, which directly reflect the physicochemistry of $(ZnTPP)_2$, are obtained over the entire spectral bandwidth — only the noise increases toward the edges as a result of the low signal strength. After the decay of the coherent artifact, the entire remaining signal in the transient-absorption map is negative (bluish colors), thus, consisting of combined GSB and SE. The lower energetic peak $S_{2\alpha}$ shows only a small spectral downshift towards lower wavelengths within 200 fs but nearly no decay with time within ≈750 fs. By contrast, the higher energetic peak $S_{2\beta}$ decreases fast and no spectral shift is visible. After ≈750 fs a small negative offset remains [117].

For a better comparison two exemplary transients centered at the positions of the absorption peaks in the Soret band (compare Fig. 4.7 and the top of Fig. 4.25) are shown in Fig. 4.25a) together with results of a global fitting routine (black). Only

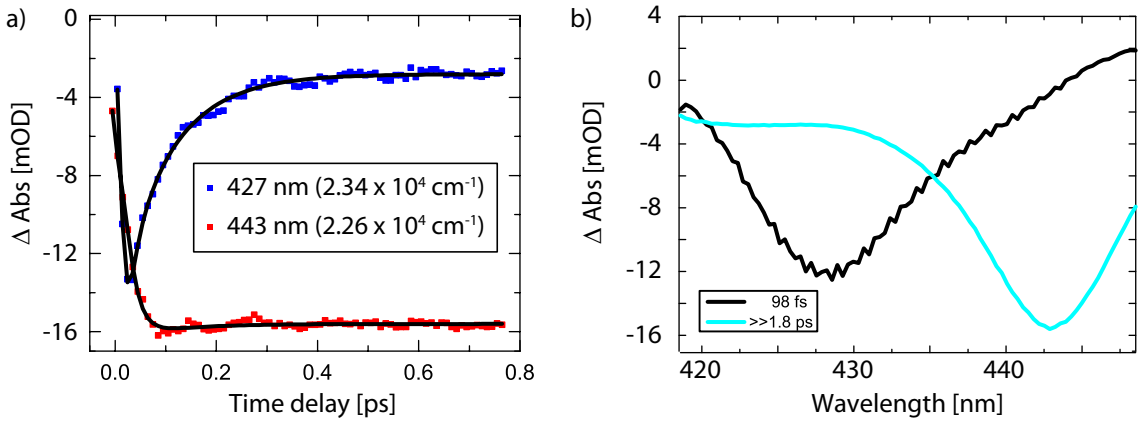

Figure 4.26: a) Transients reflecting the $S_{2\beta}$ (blue) and $S_{2\alpha}$ (red) states of $(ZnTPP)_2$ after 435 nm excitation together with corresponding fits from global analysis schemes (black). b) DADS corresponding to a time constant of 98 fs (black) and a constant offset (cyan) [117].

one time constant, resulting in a decay of 98 fs, and a constant offset were needed for a global fit with satisfying quality as a result of the short measured time delay. Hence, longer living processes like intersystem crossing into the first triplet state, are not resolved. Looking at the data, the transient at 427 nm (blue, $S_{2\beta}$) decreases with the fitted time constant of $\approx$ 98 fs while the transient at 443 nm (red, $S_{2\alpha}$) shows almost no decay with time. The data shown here after excitation with 435 nm pulses are in good agreement with the 400 nm excitation case used in the previous chapter 4.5.3, thus, the same conclusions about the excitonic coupling between the two states can be drawn.

In addition, vibrational relaxation seems to be an unimportant or unresolvable reaction pathway for molecules in $S_{2\beta}$ because the results for two different excitation energies are comparable and no Stokes shift is observable. This is confirmed by the shape of the DADS in Fig. 4.25b). While the black DADS ($\tau \approx 100$ fs) decays around 427 nm and is positive for wavelengths $>$ 443 nm, the offset mainly corresponds to the absorption shape of $S_{2\alpha}$ but with negative sign. This behavior is very similar to the DADS shown in Fig. 4.16. Unfortunately, it is not possible to determine more information about the depopulation of $S_{2\beta}$ than already known because all these experimental features were already discussed in Sec. 4.5.4. However, the better time resolution of this experiment resolves a previously unknown fast Stokes shift for $S_{2\alpha}$ shifting from 441 to 443 nm.

4.6.3 Transient-Grating Measurements — Transfer into the Box Geometry

In Fig. 4.27 transient-grating data of pure ethanol [a)] and of $(ZnTPP)_2$ [b)] are shown as a contour plot for a probe axis ranging from 420 to 450 nm. In transient-grating experiments in box geometry the measured signal is shown dependent on $S^{(3)}$, thus, the sign convention is inverted when compared to pump–probe techni-

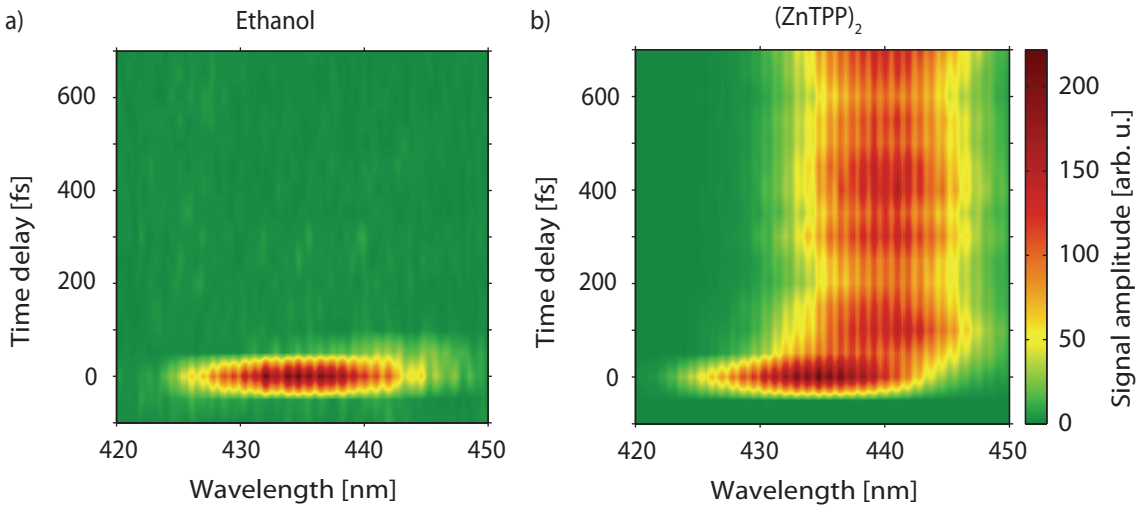

Figure 4.27: a) Transient-grating data of pure ethanol showing the coherent artifact determining the time resolution b) Transient-grating data of $(ZnTPP)_2$ covering the Soret band. One large decaying contribution, covering both absorption peaks, is evident.

ques. The color code is similar to the one used for the previous experiments with red denoting high signal intensities but for zero signal strength green was chosen in order to enhance the contrast. Both measured molecular responses possess oscillating contributions along the wavelength axis. These result from the fact that the transient grating signal, in contrast to the optical density change measured in transient-absorption measurements, corresponds to the molecular response multiplied by the shape of the spectrum of the local oscillator. It contains these oscillations, which are only detected when using a grating with many lines, for example 600 lines per mm in this case, which is necessary for the heterodyned detection scheme. They originate from a small post pulse coming out of the TOPAS resulting in fast oscillations when measuring spectral interferometry. They are normally not detected when a grating with less lines or spectrometer with lower resolution are used. The influence of this additional pulse on the observed signal in the experiment can be neglected because of the weak intensity ($< 1\%$), the strong shape change only results from the necessary multiplication with the spectrum. The used heterodyne detection in transient-grating measurements is a big advantage compared to transient absorption because very low pump intensities can be used. Thus, if the same conclusions can be drawn in both measurement techniques artifacts and multiphoton contributions can be excluded in the interpretation of the data. The former can be excluded because two different transient-absorption setups and additionally the four-wave mixing setup were used, resulting in three independent data sets. The latter can be excluded because the excitation density in the transient-grating measurements is much lower than in the transient absorption measurements in Sec. 4.5 and multiphoton processes should depend strongly on the pump power.

Fig. 4.27a) shows a transient-grating measurement of pure ethanol consisting only of a short-living coherent artifact (reddish colors) covering nearly the full bandwidth of

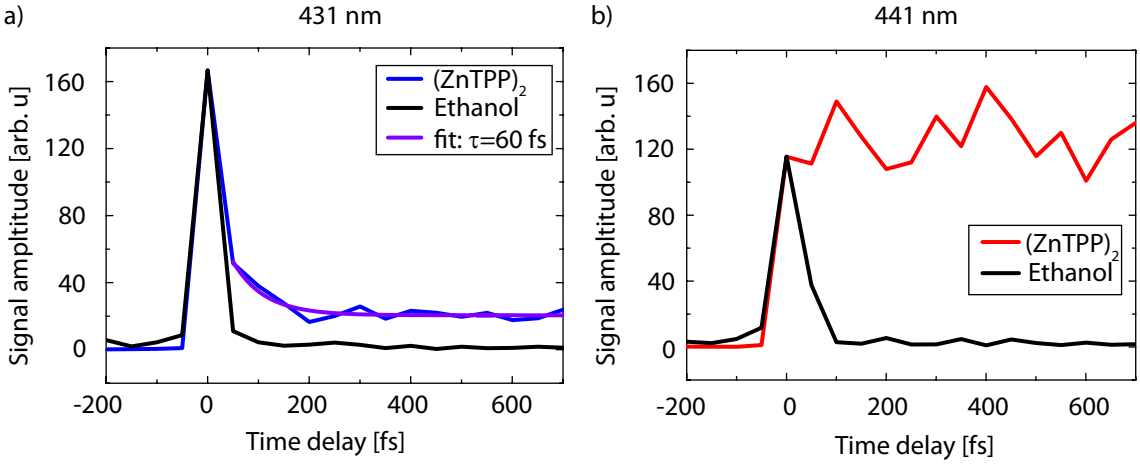

Figure 4.28: a) Transient-grating data for $S_{2\beta}$ (blue, 431 nm) showing ultrafast relaxation with $\tau \approx 60$ fs (violet) b) Transient-grating data for $S_{2\alpha}$ (red, 441 nm) showing almost no change with time. For both transients black denotes the corresponding solvent dynamics scaled to the absorption maximum at time zero.

the laser pulse. From this measurement the time resolution (≈ 50 fs) can be obtained and any long-living contributions are excluded. Figure 4.27b) shows a transient-grating measurement of $(ZnTPP)_2$ dissolved in ethanol. Only one very broad signal is detected, which is strongly wavelength-dependent. It shifts within 200 fs from 430 nm to higher wavelengths but remains unchanged for time delays > 200 fs.

To allow a better analysis, Fig. 4.28 shows single transients. Figure 4.28a) denotes the transient (blue) belonging to $S_{2\beta}$, but at 431 nm as a result of the small probe pulse spectrum. After a strong coherent artifact and solvent contribution at $T = 0$ (black) the signal decays rapidly. The corresponding exponential fit leads to a lifetime of (60 ± 10) fs in addition to a small positive offset. In contrast the transient belonging to $S_{2\alpha}$ (red) in Fig. 4.28b) remains unchanged over the first 600 fs corresponding to a permanent bleach without any stimulated emission. Both transients are in accordance with the transients in pump–probe geometry shown in Fig. 4.26.

4.6.4 Coherent Electronic 2D Spectroscopy

The results from coherent electronic 2D spectroscopy performed on $(ZnTPP)_2$ with 435 nm excitation pulses are shown in Fig. 4.29 for several population times T ranging from 0 to 250 fs in steps of 50 fs. Additionally, spectra for 500 fs are presented in order to observe long-living contributions in the Soret band. For each population time absolute (Abs), absorptive real (Re), and refractive imaginary (Im) parts (from left to right) of the 2D spectrum are pictured containing the complete information contained in the third-order response. Again the sign convention is inverted in regard to pump–probe techniques with black/violet denoting negative contributions like ESA and couplings while reddish colors visualize GSB and SE. Contour lines from 5 % to 95 % of the maximum signal amplitude of the $T = 0$ fs data are drawn in steps

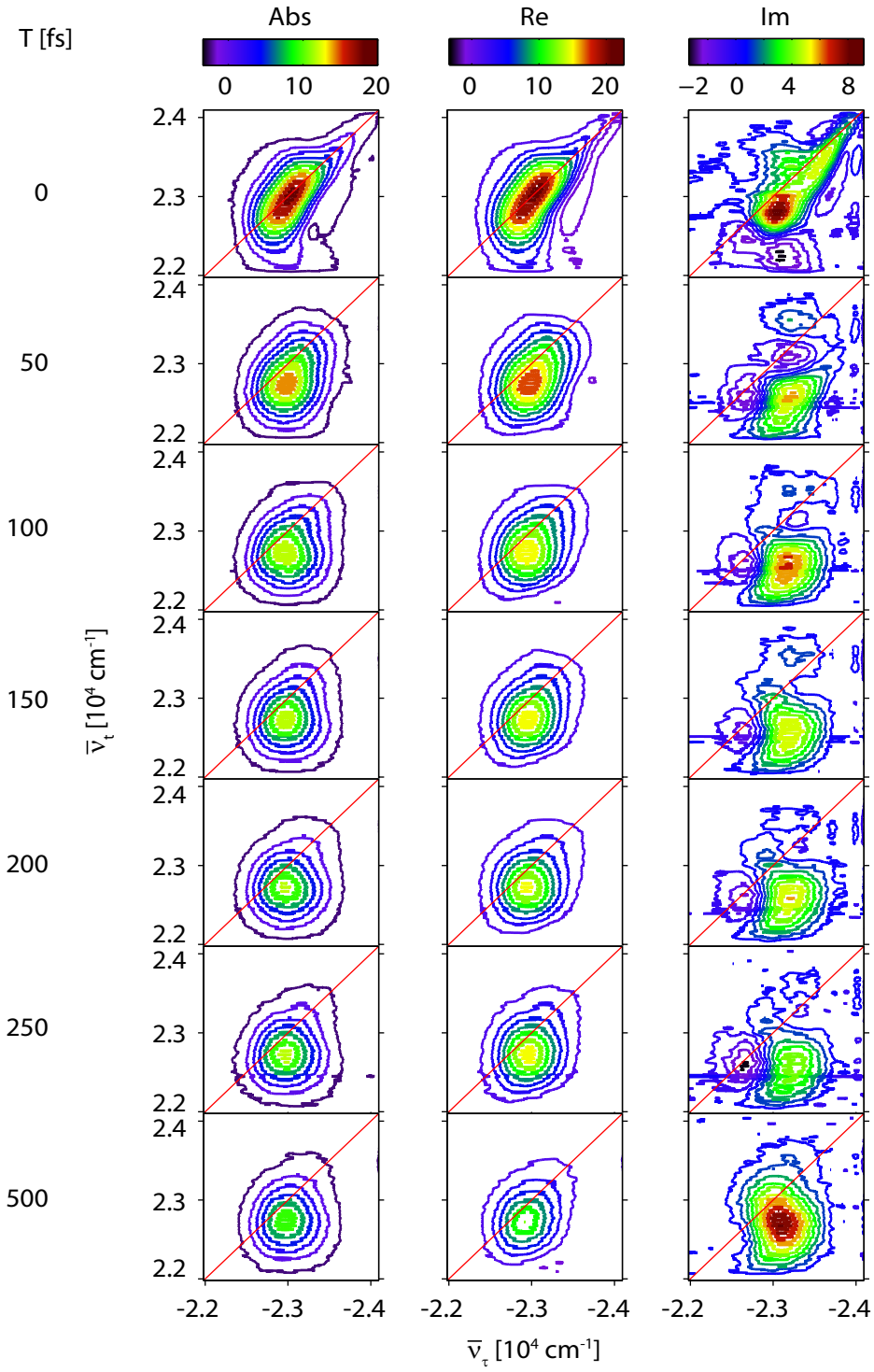

Figure 4.29: 2D data of $(ZnTPP)_2$ after 435 nm excitation consisting of absolute (Abs), real valued (Re) and imaginary (Im) spectra for population times T in 50 fs steps and additionally for $T = 500$ fs. Contour lines from 5 % to 95 % of the maximum signal amplitude of the $T = 0$ fs data are drawn in steps of 10 %. The color code is chosen to cover intensive positive (red) to negative (black) signal amplitudes [117].

of 10 %. Excitation corresponds to the horizontal $\bar{\nu}_\tau$ wavenumbers, and detection to the vertical $\bar{\nu}_t$ axis ranging from $2.2 \cdot 10^4$ cm^{-1} (455 nm) to $2.4 \cdot 10^4$ cm^{-1} (417 nm). The red line marks the diagonal, which corresponds to unshifted absorption and emission. As a consequence of the limited spectral width of the employed laser pulses, only partially covering the molecular absorption, the dynamics of the two excitonic Soret states are visible as 2D line-shape modifications rather than clearly separated peaks. In addition, it is necessary for the population time $T = 0$ fs to take signal contributions of the solvent into account. These signal contributions can be neglected for higher population times, as verified by transient grating in Sec. 4.6.3 and 2D measurements of the pure solvent ethanol. Furthermore, "phase twist" contributions originating from the temporal overlap of the third pulse with the two first ones may occur at $T = 0$ fs [187].

Considering the absolute and real parts, the latter corresponding to the absorption change also measured in a pump–probe experiment, a similar signal evolution is observed over time. At the beginning ($T = 0$ fs) the signal containing both excitonic states is elongated along the diagonal of the spectrum with a strong maximum at $|2.3 \cdot 10^4|$ cm^{-1} for both excitation and emission wavenumbers. This peak loses its diagonal shape within 100 fs becoming more circularly shaped combined with a shift towards $\bar{\nu}_t = 2.28 \cdot 10^4$ cm^{-1}, hence, $(ZnTPP)_2$ emission relaxes from higher to lower detection wavenumbers or eventually directly into S_1. In addition to this shift a large part of the higher energetic contributions vanish as seen for $\bar{\nu}_\tau = -2.32 \cdot 10^4$ cm^{-1}. The response decreases strongly (yellow to blue) and shifts from $\bar{\nu}_t = 2.32 \cdot 10^4$ cm^{-1} to $2.28 \cdot 10^4$ cm^{-1} resulting in a peak broadening and a strong pronunciation of the off-diagonal contributions for higher excitation and lower emission wavenumbers. After 150 fs the shape of the Abs and Re 2D spectra remain nearly unchanged but show an overall relaxation, which is especially seen when comparing the spectra for $T = 200$ fs and 500 fs. In both spectra only a weak, circularly shaped, slightly off-diagonal peak centered at ($\bar{\nu}_\tau = -2.3 \cdot 10^4$ cm^{-1}/$\bar{\nu}_t = 2.28 \cdot 10^4$ cm^{-1}) remains, which is very similar in shape albeit the signal is weaker for $T = 500$ fs. Summarizing, $S_{2\beta}$ seems to relax combined with a shift towards lower wavenumbers while $S_{2\alpha}$ shifts slightly and decays only weakly.

The imaginary parts of the 2D spectra exhibit a change in sign. The connecting nodal plane changes from a diagonal to a vertical alignment with increasing T. Again, the strongest changes happens when going from $T = 0$ to 50 fs and in the last spectrum for $T = 500$ fs. While the imaginary-valued spectra are necessary in order to present the complete data set, an interpretation similar to the absorption change, attributed to population and energy transfer in the excited molecule relaxing with time, is not intuitively possible and not required for a sufficient understanding of the excitonic coupling dynamics in $(ZnTPP)_2$, thus, on this data will not be commented further [117]. An in-depth study and interpretation allow the retrieval of previously unknown information, for example about vibrational wave packets, but only with strong theoretical support, as shown in back-to-back publications by Kauffmann, Manĉal, and coworkers [189, 190].

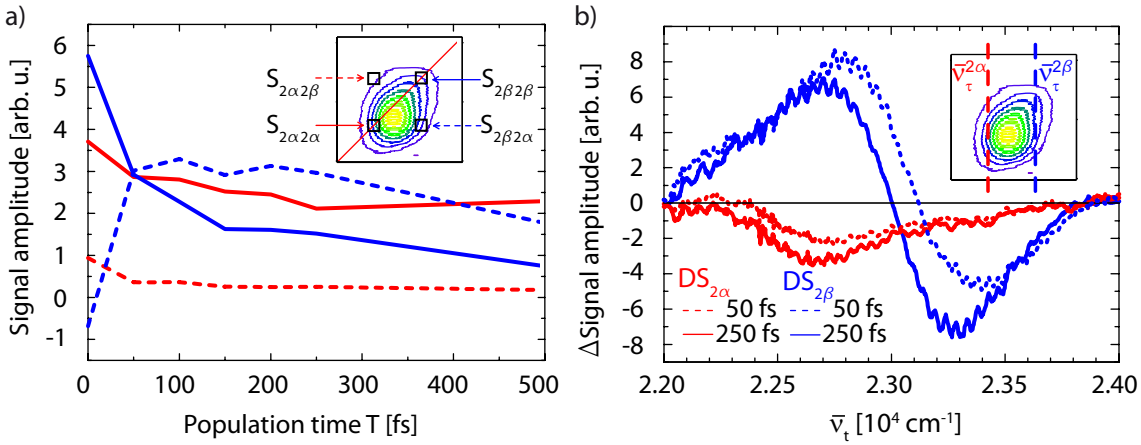

Figure 4.30: (a) Development of diagonal and off-diagonal signal amplitudes for four regions of interest marked in the inset. (b) Difference spectra with respect to $T = 0$ fs at $\bar{\nu}_\tau^{2\alpha} = -2.26 \cot 10^4$ cm^{-1} (red) and $\bar{\nu}_\tau^{2\beta} = -2.34 \cdot 10^4$ cm^{-1} (blue) for $T = 50$ fs (dashed) and $T = 250$ fs (solid) as marked in the inset [117].

Similar to transient-grating and transient-absorption experiments a discussion of the transient behavior of a specific emission frequency is beneficial for a better understanding of the photosystem. In 2D measurements this is, in addition, combined with information about a specific excitation frequency. Thus, to get a better impression of the different signal amplitude progressions in the 2D spectra, four square regions of interest (ROI) with side lengths of 188 cm^{-1} (corresponding to ≈ 3.5 nm) around the diagonal and off-diagonal wavenumbers corresponding to the linear absorption maximum [$\bar{\nu}_\tau^{2\alpha} = -\bar{\nu}_{2\alpha} = -2.26 \cdot 10^4$ cm^{-1} ($S_{2\alpha}$) and $\bar{\nu}_\tau^{2\beta} = -\bar{\nu}_{2\beta} = -2.34 \cdot 10^4$ cm^{-1} ($S_{2\beta}$)] are chosen instead of a simple cut as done in the other techniques. The signal evolution of these ROIs is shown in Fig. 4.30a) as a function of population time T for two diagonal contributions at $S_{2\alpha2\alpha} = (-\bar{\nu}_{2\alpha}, \bar{\nu}_{2\alpha})$ (red, solid), $S_{2\beta2\beta} = (-\bar{\nu}_{2\beta}, \bar{\nu}_{2\beta})$ (blue, solid) and two off-diagonal signals at $S_{2\alpha2\beta} = (-\bar{\nu}_{2\alpha}, \bar{\nu}_{2\beta})$ (red, dashed) and $S_{2\beta2\alpha} = (-\bar{\nu}_{2\beta}, \bar{\nu}_{2\alpha})$ (blue, dashed).

Starting at $T = 0$ fs, only the diagonal signals $S_{2\alpha2\alpha}$, $S_{2\beta2\beta}$ (solid) show a significant positive amplitude corresponding to a combined bleach and stimulated emission signal. With increasing population time T both diagonal contributions decrease, reducing the amount of SE, though the signal amplitude of $S_{2\beta2\beta}$ decreases faster and stronger than $S_{2\alpha2\alpha}$. In addition, $S_{2\alpha2\alpha}$ remains nearly constant after 200 fs while $S_{2\beta2\beta}$ decreases over the entire population time, seemingly approaching zero signal strength. Considering the off-diagonal evolution (dashed), $S_{2\alpha2\beta}$ is positive at first, proceeds with a slight decay during the first femtoseconds and then remains close to zero but still positive at the end. On the other hand, $S_{2\beta2\alpha}$, corresponding to molecules excited into $S_{2\beta}$ and absorbing at $S_{2\alpha}$, is nearly zero at $T = 0$ fs, which is in good accordance to the diagonal elongated peak behavior in the Abs and Re 2D spectra. For time zero each signal should emit at the same frequency where it was excited [75]. But afterwards, the signal increases rapidly during the first 100 fs, indicative of increased absorption like population transfer or excited-state

absorption. For even larger times T the signal strength subsequently decreases, but the remaining positive offset is nearly as large as the $S_{2\alpha 2\alpha}$ signal at $T = 500$ fs.

For further insight into the dynamics, especially about the relaxation pathways of each single excited state in the Soret band, Fig. 4.30b) visualizes transient difference spectra for two different pump-pulse frequencies corresponding to the two excitonic absorption maxima, labeled 2α and 2β. A transient difference spectrum along a specific pump frequency images where molecules excited into the corresponding state absorb for a specific waiting time. Decreasing signals correspond to population decay while increasing signals indicate rising populations.

The difference spectrum (DS_i), with $i = 2\alpha, 2\beta$ of the real valued 2D spectra with respect to the population time $T = 0$ fs, i.e., $DS_i = I(T, \bar{\nu}_\tau^i, \bar{\nu}_t) - I(T = 0, \bar{\nu}_\tau^i, \bar{\nu}_t)$ are evaluated and cuts along $\bar{\nu}_t$ for those $\bar{\nu}_\tau^i$ values corresponding to the linear absorption peaks $\bar{\nu}_\tau^{2\alpha} = -\bar{\nu}_{2\alpha}$ (red) and $\bar{\nu}_\tau^{2\beta} = -\bar{\nu}_{2\alpha}$ (blue) are displayed for population times of 50 fs (dotted) and 250 fs (solid) in Fig. 4.30b). The combined GSB and SE signal of $DS_{2\alpha}$ decreases over time indicative of a depopulation of this state. This is at least partially attributed to a ground-state recovery because the signal decreases, albeit weakly, also for $\bar{\nu}_t^{2\beta}$. Therefore, re-excitation of the entire molecule is possible. In addition to the strong decay for $\bar{\nu}_t^{2\alpha}$ the signal also shifts progressively towards lower wavenumbers with time similar to the shift seen in the degenerate transient-absorption data for $S_{2\alpha}$ in Fig. 4.25.

For $DS_{2\beta}$ (blue) the GSB and SE contributions at $\bar{\nu}_t^{2\beta}$ also decay with increasing population time T, but three times stronger as compared to $\bar{\nu}_t^{2\alpha}$ in $DS_{2\alpha}$ and the difference spectrum again shifts towards lower wavenumbers. But the behavior at $\bar{\nu}_t^{2\alpha}$ is decisively different. A strong positive signal, indicative of increased absorption, emerges after $T = 50$ fs. While it relaxes analogously to the other observed contributions it remains positive for $T = 250$ fs but somewhat shifted towards lower frequencies. Regarding the shifts in $DS_{2\beta}$ it is important to keep in mind the spectral width of the Soret band states which overlap. As a result if $S_{2\beta}$ is depopulated the signal strength around $\bar{\nu}_t = -2.3 \cdot 10^4$ cm^{-1} becomes stronger negative and the positive signal belonging to $S_{2\alpha}$ seemingly shifts. This also explains the different frequencies where zero signal strength is crossed.

4.6.5 Validation of the Purely Excitonic Reaction Scheme

In the previous experiments the dynamics of excitonic states in the Soret band of $(ZnTPP)_2$ were probed after direct excitation, in order to resolve possible linkage between $S_{2\beta}$ and $S_{2\alpha}$ as it was proposed in the reaction scheme in Fig. 4.12b). The degenerate pump and probe pulses used here result in a slightly better time resolution, thus, the dynamics within the first few femtoseconds are better resolved.

Analyzing the transient-grating data in Sec. 4.6.3, only one broad positive signal contribution is identified, albeit the two absorbing states are both covered by the pump pulse. Both, transient absorption and transient-grating measurements are used to measure population dynamics within excited states (Sec. 3.3.3). Thus, all infor-

mation contained in the transient-absorption map in Fig. 4.25 should be evident in the transient-grating map (Fig. 4.27). While the decay of the high energetic part at 431 nm with 60 fs is a little bit faster than the estimated 100 fs for both transient-absorption measurements (400 nm and 435 nm excitation) the behavior is in principle very similar. In addition, the lower energetic part at 441 nm remains nearly constant as also previously evidenced. Hence, the reaction pathways for the Soret band discussed in Sec. 4.5.4 are also found here. Therefore, this independent technique confirms the previous measurements and allows the transfer into the box geometry, because no unexpected artifacts or photodestruction were observed. In this geometry the more elaborate 2D measurements can be performed.

Looking at the transient-absorption data in Fig. 4.25, a slight shift in the lower-energetic band can be seen since the main absorption wavelength shifts from 441 nm ($2.268 \cdot 10^4$ cm$^{-1} > \bar{\nu}_{2\alpha}$) to 443 nm ($2.257 \cdot 10^4$ cm$^{-1} \approx \bar{\nu}_{2\alpha}$) within 250 fs. This time also corresponds well to the lifetime of the Soret band in porphyrins as previously shown by Hochstrasser and coworkers [108] and confirmed for $(ZnTPP)_2$ in Sec. 4.5. This shift is evident considering the behavior on both sides of the absorption band and how the spectral position changes with time. The observed shift corresponds to a wavenumber difference of roughly 100 cm^{-1} and can be, most probably, assigned to a Stokes shift or vibrational relaxation. By contrast, no such feature can be found for the higher-energetic Soret band corresponding to $\bar{\nu}_{2\beta}$.

Now looking at the 2D spectra in Fig. 4.29, this relaxation has to be considered in the interpretation of the data. As discussed all spectra shift towards lower wavenumbers with time. However, IVR is presumably not the main reason for the change of signal amplitude shown in the ROIs corresponding to the absorption at $\bar{\nu}_{2\beta}$ [$S_{2\beta 2\beta}$, $S_{2\beta 2\alpha}$, Fig. 4.30b)] since the lowest wavenumber contained in the ROIs for $\bar{\nu}_{2\beta}$ is more than 300 cm^{-1} above the observed maximal wavenumber ($2.3 \cdot 10^4$ cm^{-1}) of the observed Stokes shift; therefore, the changes at $\bar{\nu}_{2\beta}$ indicate the participation of other processes.

For a more in-depth analysis, calculations, which simulate absorptive 2D spectra, were performed based on solving the Bloch equations as proposed in [191] for a two-level system [117]. The reaction scheme of $(ZnTPP)_2$ is simplified to a four-level model shown in Fig. 4.31a) consisting of the ground state g, the exciton states $S_{2\alpha}$ and $S_{2\beta}$ corresponding to the splitting in the Soret band and the two-exciton state f, which implies that $S_{2\alpha}$ and $S_{2\beta}$ are both excited [132]. The depicted transition wavenumbers $\bar{\nu}_{g2\alpha} = \bar{\nu}_{2\alpha f} = 2.26 \cdot 10^4$ cm^{-1} and $\bar{\nu}_{g2\beta} = \bar{\nu}_{2\beta f} = 2.34 \cdot 10^4$ cm^{-1} correspond to the energy difference between the ground state g and $S_{2\alpha}$ or $S_{2\beta}$, corresponding to the twofold splitting measured in the steady-state absorption spectrum. The same level scheme was used for the calculated transient absorption in Fig. 4.5 and for the description of molecular excitons in Sec. 4.2.3. This simplification is possible, because only the behavior of the Soret band is of interest here and all other transitions are only observed indirectly for two reasons. On the one hand, the spectral bandwidth of the laser spectrum covers only the Soret band and, on the other hand, only population times T up to 500 fs were measured. Hence, no relaxation into S_1 states (Q band) or triplet states, as it will occur in porphyrins in the visible spectral range

and on at least a picosecond time-scale, are included. For example a decay from the excited state $S_{2\alpha}$ into the ground state g results in the calculated 2D spectra in a loss of SE and GSB, thus, a positive signal decays over time. For the bisporphyrin itself this process proceeds, as verified by the transient-absorption measurements, via a long living triplet state. Accordingly, only the loss of SE and no GSB recovery can be detected, which also results in the loss of a positive signal over time. As a result, this simple model should provide the right temporal and spectral behavior but with a much stronger amplitude. With this in mind, no quantitative information should be extracted from these calculations. More elaborate simulated 2D spectra are calculated for example in Refs. [192,193] by employing Redfield theory or by analytical calculation of the photon echo 2D signal. Both techniques exceed the capabilities of an experimental group and deliver, albeit more detailed, a very similar interpretation of the corresponding 2D spectra. This is even more evident in Ref. [194] where the 2D spectra of a porphyrin dimer, however, with *meso, meso'*-linkage and a spacer, are calculated, under full consideration of the degenerate nature of the Soret band and the discussion evolves around the four signals (two diagonal, two off-diagonal) also discussed here.

In the simulated data the corresponding excitonic states were fitted by Lorentzian functions (blue, solid) to the linear absorption spectrum (red, dashed) shown in Fig. 4.31b). For $S_{2\alpha}$, fitted curve and molecular absorption correspond very well. In contrast, the agreement for $S_{2\beta}$ is weaker. Unsurprisingly the fitted peak does not cover the high-energetic edge of the absorption band, because the third state centered at $2.4 \cdot 10^4$ cm^{-1} is not included in the calculation. In addition, the absorption band is much broader than the fit, resulting from the existence of two nearly degenerate states, as the corresponding Lorentzian function. However, the central frequency matches quite well. Summarizing, the two model states are adequately reproduced, especially when considering the simplified reaction scheme. The experimental excitation and detection pulses (black, dashed) were treated by Gaussian functions (green, solid) fitting quite well. Slight deviations on the edges are evident, which stem from the fact that the used NOPA pulses did not possess a perfect Gaussian-shaped spectrum. The resulting Re 2D spectra for 50 (upper row) and 250 fs (lower row) in addition to the corresponding experimental ones are shown in Fig. 4.31c). The calculations were performed with (middle column) and without (left column) inclusion of a coupling between the excitonic states to compare these with the experimental results (right column), while no additional environmental and inhomogeneous broadening effects were considered. The coupling was taken into account by an exponential population transfer from $S_{2\beta}$ to $S_{2\alpha}$ with a time constant of 114 fs as observed in Sec. 4.5.

Again looking at the experimental results for the degenerate pump and probe pulses, a look at the transient-absorption data in Fig. 4.25 reveals a signal decay in $S_{2\beta}$ on a time-scale of 100 fs, which corresponds to the 114 fs decay used for the simulated population transfer. The product state is not unambiguously identified but the ground state g can be excluded since then $S_{2\alpha}$ would need to show a similar signal decay: A populated ground state would enable re-excitation into both, $S_{2\alpha}$

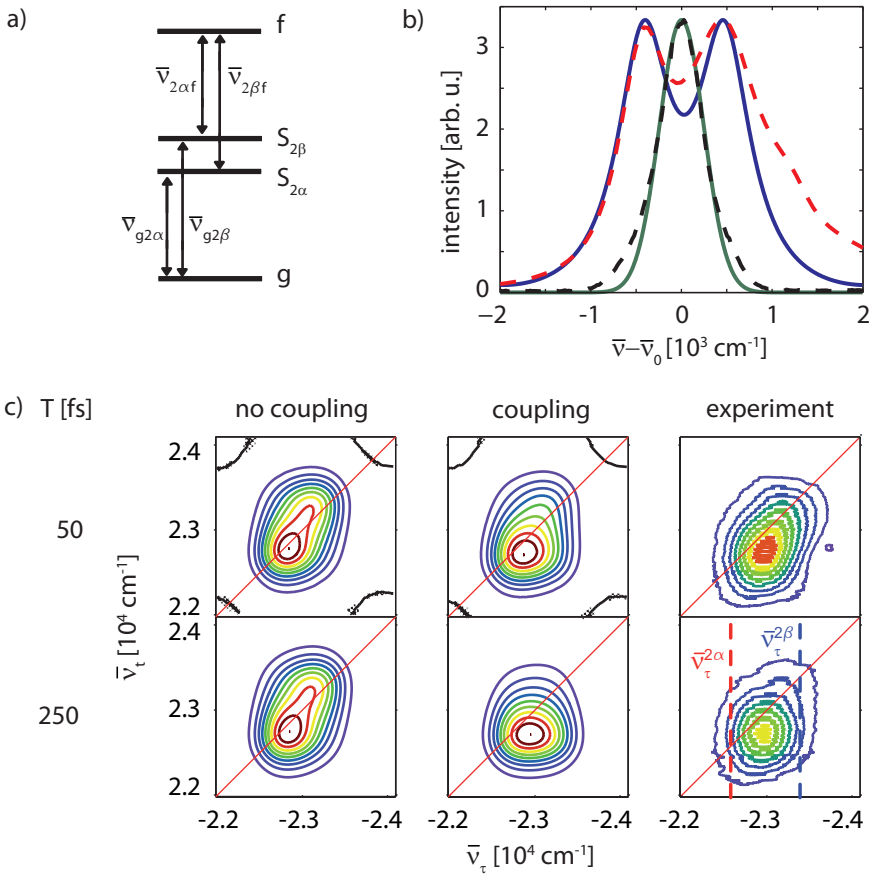

Figure 4.31: a) Four-level model consisting of ground state g, excitonic states $S_{2\alpha}$, $S_{2\beta}$ and biexcitonic state f, arrows are denoting possible transitions. b) Fit with two Lorentzians (blue) to the absorption spectrum (dashed red) and two Gaussian functions (green) to the used laser spectrum (dashed black). c) Calculated Re 2D spectra without coupling (left), with coupling (middle), and corresponding experimental data (right) for $T = 50$ fs (top) and $T = 250$ fs (bottom) [117].

and $S_{2\beta}$ as previously discussed in Sec. 4.5.4 and, in addition, deemed improbable by the transient-grating measurements. A reasonable assumption within the model is a population transfer from $S_{2\beta}$ to $S_{2\alpha}$, which would lead to an increased excited-state absorption into the two-exciton state f as calculated for this simple system in Fig. 4.5. Looking at the behavior in $S_{2\alpha}$, only a small Stokes shift and perhaps a vanishing SE signal on a femtosecond time-scale is directly observable but the amount of bleaching stays roughly the same over the entire time delay. This evidences that the ground state is not repopulated during the experiment.

Looking at the development of the signal amplitude and the simultaneous change of shape to lower energies in the real-valued 2D spectra in Fig. 4.29, all previously discussed relaxation processes within the Soret band are also evident because the information contained in transient-absorption experiments are part of the informational content in a 2D spectrum. The entire signal weakens with time, resulting

from overall relaxation, observable in all spectra, into the lower Q band (as also known for similar systems [108, 120]). Since the Q band absorbs in the visible this relaxation manifests itself only indirectly here since no SE from S_2 is possible any more. In addition, the signal amplitude for high excitation $\bar{\nu}_\tau$ and low detection $\bar{\nu}_t$ wavenumbers changes with time as discussed in the experimental section. This indicates a relaxation by solvent effects like a Stokes shift or by a population transfer from $S_{2\beta}$ to $S_{2\alpha}$ as the change mainly appears as an off-diagonal signal between the corresponding excitonic states.

The changes in the signal amplitude are more precisely seen in the difference spectra [compare Fig. 4.30(b)] relative to $T = 0$ fs. For $DS_{2\alpha}$ (red) a weaker decrease of signal amplitude compared to $DS_{2\beta}$ can be observed, which confirms the different dynamics already seen in transient absorption and the higher stability of $S_{2\alpha}$. Comparing the difference spectra for $T = 50$ fs and $T = 250$ fs, a progressive decrease to lower wavenumbers of the combined SE and GSB signal can be observed. At $T = 0$ the signal consists of GSB and SE contributions. After a given population time ($T = 50$ fs) the signal shifts to lower wavenumbers as the SE contribution is influenced by a Stokes shift. As the lifetime in the Soret band is ≈ 150 fs [108] the Stokes-shifted SE vanishes for $T \gg 150$ fs while the GSB still maintains, leading to the observed stronger signal decrease at lower wavenumbers. Crucial new information are gained when looking at $DS_{2\beta}$ (blue). Most importantly an increasing signal amplitude for $DS_{2\beta}$ at wavenumbers corresponding to the lower energetic state $S_{2\alpha}$ is evident. This is a direct consequence of a coupling between $S_{2\beta}$ and $S_{2\alpha}$ as proposed in Sec. 4.5.4. This signal is indicative of relaxation from $S_{2\beta}$ into $S_{2\alpha}$ since molecules excited into $S_{2\beta}$ now show absorption at frequencies corresponding to the state $S_{2\alpha}$, most probably belonging to increased SE, while at the same time the SE signal for $S_{2\beta}$ decreases. This signal was only deduced from the transient-absorption measurements because it is hidden within the strong ground-state bleach and stimulated emission signal, necessitating the additional 2D measurement.

This coupling between the two excitonic states and the corresponding relaxation dynamics are more intuitively visualized in the development of the signal amplitudes at the chosen ROIs in Fig. 4.30b), which are similar to a transient. The decreasing amplitudes $S_{2\alpha2\alpha}$ and $S_{2\beta2\beta}$, representing the diagonal contributions and monitoring the amount of molecules, which are excited, mirror the observation of the transient-absorption study. They show an overall decrease, again much faster for $S_{2\beta2\beta}$ than for $S_{2\alpha2\alpha}$. The nonzero signal after a population time of 500 fs necessitates the existence of a long living intermediate state, which was previously identified as T_1. The coupling in the excited state is visualized by the two off-diagonal contributions $S_{2\alpha2\beta}$ and $S_{2\beta2\alpha}$ corresponding to molecules excited into $S_{2\alpha}$ and still excitable into $S_{2\beta}$ and vice versa. After a given population time the dynamics are dominated by population relaxation processes from $S_{2\beta}$ to $S_{2\alpha}$. As this relaxation gives rise to contributions to the excited-state absorption for $S_{2\beta2\beta}$, stemming from twofold excitation, and to the SE for $S_{2\beta2\alpha}$, resulting from the increased population, it explains the time evolution of the related signal amplitudes. $S_{2\beta2\alpha}$ increases over the first 100 fs and accordingly $S_{2\beta2\beta}$ decreases as long as this transfer takes place.

This interpretation is also strengthened when considering the simulated spectra. Without two coupled excited states the signal starts in a diagonal orientation, quite similar to the experimental spectrum for short population times, but there are hardly any changes towards lower detection frequencies with evolving time. This is not surprising because only slow relaxation originating in $S_{2\beta}$ is included in the simulation, therefore, explaining the small differences between the spectra for $T = 50$ fs and 250 fs. The initially observable black contour lines around the edges are due to phase twist contributions because of effective pulse overlap between all used laser pulses, similar to a coherent artifact in transient absorption. This qualitative behavior does not match the experimental observations well. On the other hand, the calculation where the two excited states are coupled and have population transfer with a 100 fs dynamic shows a shift of intensity for high excitation wavenumbers going from higher to lower detection wavenumbers with time, i.e., a growth of contributions below the diagonal and a simultaneous decay of the signal for higher wavenumbers. In addition, the diagonal orientation for small T becomes horizontally symmetric with time similar to the experiment. Finally, the spectrum for $T = 50$ fs also matches the experimental one. Compared to the experiment the development of the spectral shape resembles the calculated coupled 2D spectrum qualitatively, especially the shift of center of gravity to regions below the diagonal is evident. Hence, regarding both the measurements and the simulated model spectra population transfer within the excited Soret band is considered to be a reasonable explanation for the observed effects. In Sec. 4.5.4 two different explanations for the excitonic relaxation behavior were introduced. One, shown Fig. 4.23a), required the definition of monomeric and excitonic states and the introduction of different states, sharing the same energy. The completely excitonic picture, however, is much simpler but a direct energy transfer between the two excitons was necessary, which could not be detected via pump–probe measurements. It was identified here in the 2D spectra, hence, the reaction scheme proposed for $(ZnTPP)_2$ in Fig. 4.23b) is validated.

4.7 Conclusion

The aim of this study was to develop an understanding of ZnTPP's relaxation dynamics, a porphyrin monomer, used as a precursor molecule for potential applications like molecular wires [102] and to gain insight into the relaxation dynamics of $(ZnTPP)_2$, a directly β,β'-linked bisporphyrin with hindered rotation around the biaryl axis [114,115]. Especially the behavior of the excited states and how they are connected was in the focus. By a combination of diverse techniques in addition to the use of three different excitation wavelengths a comprehensive understanding of the photo-induced dynamics of $(ZnTPP)_2$ was obtained. The corresponding reaction scheme is visualized in Fig. 4.32 with colored boxes denoting the primary technique responsible for a specific result. In summary, fs-resolved transient-absorption measurements supported by absorption and fluorescence spectra, a global analysis scheme (VIS: green, NIR: red), and TD-DFT calculations in addition to coherent electronic

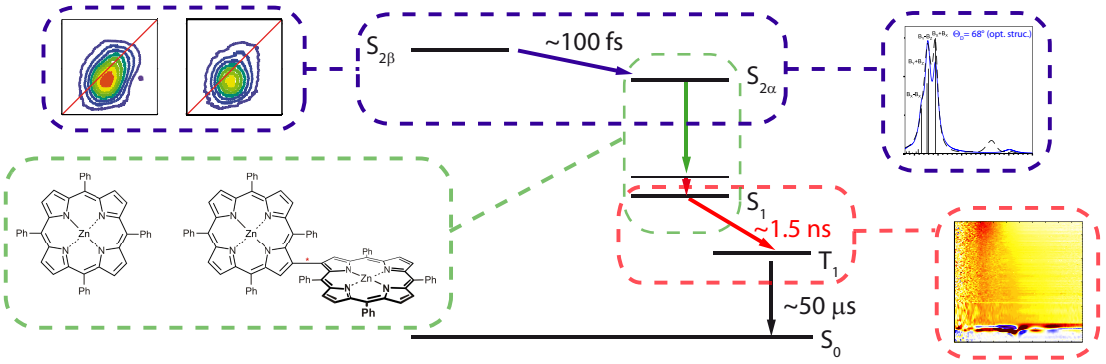

Figure 4.32: Simplified reaction scheme of $(ZnTPP)_2$ after photoexcitation into $S_{2\beta}$ with boxes denoting the primary technique which obtained the results. Coupling in the Soret within (violet) was predicted (right) with TD-DFT measurements and observed (left) with coherent 2D spectroscopy. Afterwards, relaxation into the Q band proceeds where cooling dynamics occur (green), as is evident by a transient-absorption study comparing $(ZnTPP)_2$ to ZnTPP. Lastly, intersystem crossing into T_1 is measured with transient absorption in the NIR (red).

2D experiments in box geometry combined with simulations were used to extract as much information as possible (violet).

While the results for the ZnTPP monomer are in good accordance with literature, the data for $(ZnTPP)_2$ differ from previous studies on similar dimers featuring *meso,meso'*-linkage (green dashed box). Thus, the models developed for those systems had to be extended, resulting in two alternative models taking into account the distinct features observed for the β,β'-linked dimer. Both models assign the largest of the determined time constants ($\approx$ 1.5 ns) to intersystem crossing into T_1 (red dashed box). A time constant of 40 ps is attributed to a small ground-state recovery most probably by fluorescence as radiant S_1-S_0 relaxation is observed. The dynamics taking place on the faster time-scales incorporate the excitonic nature of the electronic states. The interaction of the two monomeric units cancels the degeneracy and leads to Davydov splitting of the Soret band. Two time constants (i.e., 9 ps and 150 fs) are assigned to energetically favorable transitions into two groups of excitonic states. The smaller time constant is additionally combined with relaxation from the second into the first electronically excited state and possibly decoherence of the initially excited coherent excitons. The semi-monomeric, semi-excitonic model additionally assumes that a localization process happens on this ultrafast time-scale. The latter leaves one of the two moieties excitable from its monomeric ground state. By contrast the purely excitonic model based on superposition of former monomeric states forming non-trivial localized states does not rely on an actual localization step, which leaves only one subunit excited.

In order to obtain more detailed information about the excited-state behavior the ultrafast excitonic dynamics in the Soret band $(ZnTPP)_2$ was additionally analyzed by transient absorption and coherent two-dimensional spectroscopy with ultrashort

degenerate pump and probe pulses (violet dashed box). In the transient-absorption experiments the more stable $S_{2\alpha}$ state shows in addition to various relaxation dynamics a Stokes shift within 200 fs. However, only an indirect assignment of the participating states is possible. Whereas the energetically higher state relaxes with $\approx$ 100 fs into another state the energetically lower state relaxes on a much longer time-scale similar to the previous experiment. These relaxation dynamics are observed in more detail, allowing a direct assignment using coherent 2D spectroscopy. A simple model shows that these dynamics cannot result from a Stokes shift alone. Off-diagonal contributions in the experimental and qualitatively modeled 2D spectra provide an explanation: population transfer occurs between the corresponding excitonic states $S_{2\alpha}$ and $S_{2\beta}$ as a result of electronic coupling, confirming the validity of the second, purely excitonic model. Thus, this result contributes to a deeper understanding of the processes happening in the strongly absorbing yet very short-lived Soret bands of porphyrins.

Exploiting the information contained in the different measurements the results of the study corroborate a comprehensive reaction scheme based on one conformation of $(ZnTPP)_2$ and show that the dimer already possesses distinct excitonic characteristics. In addition, the importance to understand the photophysical behavior of higher excited states above the S_1 state is highlighted. These findings demonstrate that $(ZnTPP)_2$ is a versatile molecular model system for porphyrin science, even more when its chiroptical properties are considered. With its distinct excitonic character and pronounced axial chirality, the molecule may serve as a unique building block for larger porphyrin arrays with applications ranging from asymmetric catalysis over biomimicry of electron-transfer [115] to organic optical devices.

Chapter 5

6,8-Dinitro BIPS — Comprehensive Study of a Molecular Switch

5.1 Introduction

Photochromic compounds are promising molecular systems for organic electronic devices like ultrafast transistors because of their unique property to be switchable between two stable states with light [19], hence, serving as a possible molecular bit [195–197]. A multitude of different molecular systems exist in literature as, e.g., diarylethenes [198–200], fulgides [196, 201–204], and the spiropyran–merocyanine photosystem [205–210] all off them possessing strong photochromism [21]. Though the first articles about this topic were published more than a decade ago, still not all properties are known and well understood. Quite contrary, the results barely scratch the surface of their powerful potential and usability as indicated by recent studies for all these molecules: diarylethene-based switches were used for a non-destructive optical readout on a single-molecule scale [200]. Recent time-resolved studies on fulgide derivatives demonstrate how structural modifications tailor the optical properties [211] and prove that this system can perform all optical switching cycles repeatable with clock-rates of 250 GHz [196]. Finally, a spiropyran–merocyanine system showed the ability to be switchable between two states in addition to solubility in water [212]. Solubility under aqueous conditions allows for the integration of spiropyran into DNA strands, allowing optical triggering in biological applications.

All these publications have in common that they highlight the benefits of a logical bit, which performs switching on a fast time-scale, up to hundreds of GHz, and is ultimately restricted to dimensions of only a few nanometers. The first goal has been met for fulgides. However, three-dimensional optical data storage and readout on a molecular scale is limited by the diffraction limit of the used light source. Over the last years this challenge has been subject of numerous publications and now real working systems with a lateral resolution of less than 500 nm were realized [213–215].

After having elucidated the couplings and excited-state relaxations of a porphyrin dimer in the previous chapter, now the second focus of this thesis is discus-

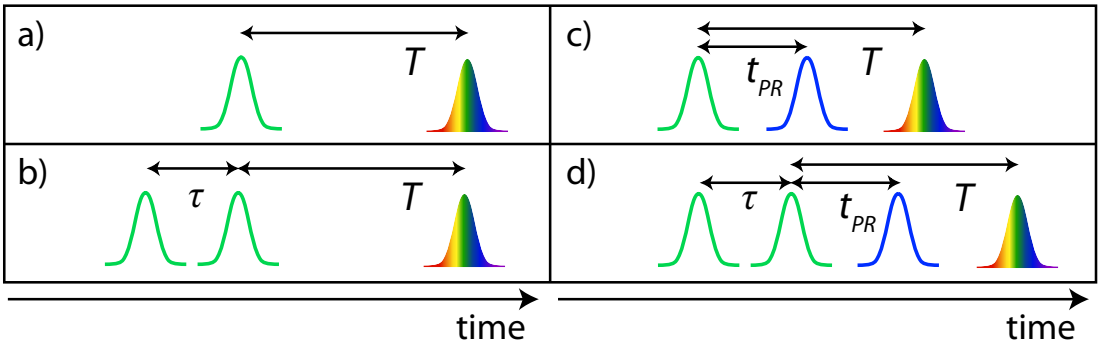

Figure 5.1: Ultrafast absorption-based time-resolved spectroscopic techniques. left: third-order excitation techniques: a) pump–probe/transient-absorption spectroscopy b) coherent 2D spectroscopy; right: two-color excitation: c) pump–repump/dump–probe spectroscopy d) triggered-exchange 2D spectroscopy [219].

sed. An indolino-benzopyran, more precisely 6,8-dinitro-1',3',3'-trimethylspiro[2H-1-benzopyran-2,2'-indoline] (6,8-dinitro BIPS) [216, 217], which is a spiropyran–merocyanine system based on a 6π-electrocyclic reaction is subjected to a series of photochemical experiments. Ring-closed spiropyran comprises two orthogonal chromophores (pyran and indole moiety), which do not absorb in the visible spectral range, whereas ring-open merocyanine consists of one large planar π-system strongly absorbing in the visible spectral range. The main goal is to determine the suitability of 6,8-dinitro BIPS as a molecular switch. For an effective conclusion the following open questions have to be addressed:

Is bidirectional switching between the open and closed form possible on an ultrafast time-scale? Are there disadvantageous reaction pathways which lower the quantum efficiency of a possible device and dilute the switching sample? This is important, because in an efficient switching device the existence of a third species, serving as the reactant in a competitive reaction path towards opening or closing (as observed in fulgides [218]), is disadvantageous. Does the photochemical behavior change after twofold excitation? This for example is important to determine the maximal speed of multiple read–write cycles.

In order to obtain all this information the comprehensive reaction scheme of 6,8-dinitro BIPS is unveiled in this chapter, showing a multitude of reaction pathways. All pathways are detected and accessed via different time-resolved spectroscopic methods including newly-implemented ones, like coherent electronic 2D spectroscopy with a supercontinuum probe [78, 220, 221], or newly-developed multicolor and multidimensional experiments, like electronic triggered exchange spectroscopy.

However, until now electronic 2D, and its possible extensions, have only been applied to photophysical processes like energy transport in photosynthetic compounds [15] or for the analysis of dimeric systems [117, 189, 222]. In the mid-infrared spectral range photochemical studies are far more common, especially for the study of non-equilibrium systems. In transient 2DIR spectroscopy, a preceding pump pulse triggers a chemical process, e.g., a switching process in peptides [87, 223], unfolding

dynamics in proteins [224], metal-to-ligand charge transfer [225], or bond cleavage in metal carbonyls [226]. In 2DIR triggered-exchange spectroscopy, this additional pump pulse starts the reaction after the IR excitation, linking vibrations in the reactant to those in the product [225, 226]. The molecules can also undergo a structural change between the excitation and detection steps without a further triggering pulse (2DIR exchange spectroscopy) [227–231]. In this chapter, these techniques are extended from vibrational to electronic transitions by using visible laser pulses.

The four different pulse sequences used in this photochemical study are highlighted in Fig. 5.1 with the ones known from the $(ZnTPP)_2$ experiments in Chapter 4 on the left and new techniques on the right side. Ordering of the experiments is as follows:

Section 5.2 summarizes requirements of molecular switches, describes the concept behind pericyclic reactions and introduces the state of literature for merocyanines, especially for the BIPS family. Transient-absorption spectroscopy [Fig. 5.1a)], with two different excitation wavelengths, allows for the discrimination of two merocyanine isomers in solution (Sec. 5.4). Subsequently, coherent electronic 2D spectroscopy [75] in pump–probe geometry [89, 94, 220] is implemented and used to assess the importance of isomerization (Sec. 5.5). Here, compared to transient absorption the pump pulse is split into a pump pulse pair [Fig. 5.1b)].

Spectrally-resolved pump–repump–probe measurements [Fig. 5.1c)] — pump–probe experiments with an additional repump pulse separated by the time τ_{PR} from the pump — are used to identify the product formed after S_1 excitation and for resonant excitation into higher-excited merocyanine S_n states (Sec. 5.6). By combining 2D and pump–repump–probe spectroscopy, electronic triggered-exchange 2D spectroscopy (TE2D) is implemented for the first time. Basically after performing a 2D experiment the repump interacts with the excited-state population connecting the spectral signatures before and after an additional light-matter interaction [Fig. 5.1d)] (Sec. 5.7). Lastly, a summary is given in Sec. 5.8 concluding this chapter and describing the photochemical reaction mechanisms of 6,8-dinitro BIPS.

Parts of this chapter were already published and are reproduced in part with permission from References [20, 27, 78][1] (Sec. 5.4, 5.6.2, and 5.5) and from Ref. [219][2] (Sec. 5.6 and 5.7).

5.2 Molecular Switches

The most common implementations for data processing and storage are nowadays based on semiconductors. A different approach is based on organic molecules which satisfy certain criteria, called molecular or optical switches. Their properties are summed up in the following sections. At first, their requirements are introduced in Sec. 5.2.1. Afterwards, pericyclic reactions are elucidated (Sec. 5.2.2), which are the

[1] Copyright: American Chemical Society [2013], DOI: 10.1021/ja2032037, DOI: 10.1021/jp108322u, DOI: 10.1021/ja1062746

[2] Copyright: American Physical Society [2013], DOI: 10.1103/PhysRevLett.110.148305

fundamental reaction mechanisms behind many optical switches. In Sec. 5.2.3 the spiropyran–merocyanine photosystem is introduced, which is a promising candidate for a molecular switch, based on its strong photochromism. 6,8-Dinitro BIPS, the molecular system whose reaction mechanisms will be unveiled in this chapter, is one of the representatives of this molecular class.

5.2.1 Properties of a Molecular Switch

The term molecular switch itself describes the photosystem, to which this tag is applied, intrinsically quite well. Basically an information storage device called a molecular switch has to be made of a molecule which is switchable between two distinguishable forms by light. Often photochromism is exploited to generate such a molecular bit, consisting of a "closed" state, representing zero, and an "open" state, representing one. Hence, the molecules act like a logical bit in a semiconductor device. In his seminal book Feringa presented a more detailed list of necessary properties that enable designation of the label molecular switch to a certain molecule [19] which is summarized below:

- A molecular or optical switch has to exist in (at least) two configurations, often different isomers. These two configurations have to differ in their optical properties, e.g., their respective absorption spectra are unambiguously attributable to each configuration. This is achieved by different extinction coefficients for at least one specific wavelength. Diarylethene derivatives, a well-studied class of molecular switches, including a cyclic unit, absorb in the ring-open form strongly in the UV at wavelengths < 400 nm. The ring-closed isomer, however, absorbs in the visible spectral range around 500 nm, allowing a clear distinction [198]. Different distinction possibilities are e.g. circular dichroism or the different response to magnetic fields after illumination [19].

- Both of these configurations have to be thermally stable. This means that both have to remain indefinitely in their ground state, if they are not illuminated. This is fulfilled by diarylethene derivatives and fulgide systems. Other possible candidates, like spiropyrans, remain in their switched configurations only for a certain amount of time, because of thermochromism [232].

- However, a light-induced conformation change causing the conversion of the "open" into the "closed" form and vice versa has to happen fast in regard to any thermal reactions and also very efficiently [201]. This represents the light-induced switching process, the centerpiece of a working molecular switch. "Open" and "closed" do not have to represent cyclic reaction schemes. However, cyclic reactions are often used.

- These light-induced conformation changes have to be repeatable many times for a single sample. This fatigue resistance is quasi observed in diarylethene derivatives, which can repeat a high number of photocycles ($n_{\text{cycles}} > 10^4$) while for furylfulgides the number of cycles is limited to $n_{\text{cycles}} \approx 100$ [19].

- Finally, a non-destructive readout has to be possible for determining the actual conformation state of the photosystem, without affecting it. This can, for example, be realized by infrared spectroscopy, which induces purely vibrational and no electronic changes, as shown for the time-resolved switching cycle of a fulgide or for spiropyrans [196, 233].

All these criteria should optimally be fulfilled by a certain molecular system in order to be called an optical switch. For achieving the goal of a data processing device on a molecular scale, different promising classes of molecules exist. Azobenzenes [234,235], spiropyrans [20, 205, 212], furylfulgides [211, 218, 236], indolylfulgides [202, 237, 238], and diarylethenes [198,239] are different molecular classes which satisfy at least some of the criteria, but each one has certain advantages and disadvantages. The quantum efficiencies for the photoreactions in both directions (opening reaction: Φ_{c-o}, closing reaction: Φ_{o-c}), in addition to the spectral range of the absorption maximum Abs_{c-o} and Abs_{o-c}, and the thermal stability after photoswitching are given in Tab. 5.1 for some selected compounds. As it is evident by recent publication dates (2009-2012), the properties of molecular switches undergo a continuous improvement and are part of current research projects.

mol. photoswitch	$\Phi_{c-o}[\%]$	$\Phi_{o-c}[\%]$	Abs_{c-o}	Abs_{o-c}	Stab.
diarylethene [19]	≈ 50	≈ 2	UV	VIS	Yes
furylfulgide [240]	≈ 50	< 30	UV	VIS	Yes
indolylfulgide [202]	< 50	< 17	UV	VIS	Yes
azobenzene [234]	25	50	UV	UV	No
mod. azobenzene [235]	> 90	> 90	UV	VIS	No
spiropyrans [212]	< 4	< 20	VIS	UV	No
6,8-dinitro BIPS [20, 27]	< 10	< 40	VIS	UV	No

Table 5.1: Quantum yields for opening (Φ_{c-o}) and closing switching-directions (Φ_{o-c}), together with the spectral region of the absorption maximum (Abs_{c-o} and Abs_{c-o}, respectively) for common molecular systems. Stab. denotes to the permanent thermal stability of both configurations. The mod. azobenzene is a unique bridged configuration, strongly altering the photochemical properties. The separated row relates to 6,8-dinitro BIPS, the molecule studied in this chapter. The values are partially obtained in later sections.

Basically two different types of chemical reaction can be used in a molecular switch. On the one hand, *cis/trans* isomerization is employed as the mechanism, as for example in azobenzenes. In these systems very high quantum efficiencies in both directions are possible. However, the absorption spectra are typically not completely separable – both azobenzene conformations absorb between 300 and 400 nm – aggravating photochemical access to only one species [234]. This problem was recently synthetically addressed and a modified azobenzene with additional bridges circumvents this problem by shifting one band into the visible regime [235]. As an additional benefit even higher reaction yields are determined in both directions. However, long-lasting thermal stability is not observed for these compounds.

On the other hand, the electrocyclic process of ring-closure and opening in diarylethenes, fulgides, and spiropyrans is a promising reaction type for a potential photo switch. Since 6,8-dinitro BIPS undergoes this reaction mechanism, it is explained in more detail in Sec 5.2.2. For this mechanism both molecular configurations have well separated spectral absorptions, one conformation absorbing in the UV and the other one in the visible spectral range. Diarylethenes were one of the first suggestions for a switching device, because of their strong fatigue resistance, however their quantum yield in closing direction is very low [19]. Fulgides have high quantum yields in both directions, good fatigue resistance and well separated absorption bands. Merging all these attributes the high promise of fulgides for developing molecular switches is explained. However the open form undergoes partial isomerization into a third configuration not capable of closing. Such an unwanted side product reduces the amount of photoswitchable molecules with each photocycle and leads to a nontrivial readout signal because more than two possibilities exist.

From this short review, discussing azobenzenes, diaryelethenes, and fulgides, it is evident that it is not easy to find a system which satisfies all necessary criteria: Most of the systems excel in some aspects, while not fulfilling one condition at all. However, the spiropyran–merocyanine photosystem, discussed in this thesis, satisfies all criteria to a certain extent, as elucidated in the following. Both bands are well separated, though, as a unique property the ring-open form absorbs in the visible and the closed in the UV contrary to the previous examples. No side products, beyond thermal isomerization for different merocyanine isomers [241], are known and the system performs reasonably well in both directions. Thermal stability is observed on a time-scale of minutes [71]. When taking all these properties into account the potential of 6,8-dinitro BIPS, the actual photosystem used, is evident. Therefore, additional research is necessary, which will be addressed in this chapter.

5.2.2 Pericyclic Reactions

Pericyclic reactions are an important reaction mechanism for the understanding of many molecular switches [123]. These reactions typically involve the π-electron system of a molecule. Therefore, over the course of the reaction, large changes in the electron density are induced. Hence, optical properties like absorption are strongly influenced. A pericyclic reaction is a so-called concerted reaction. This term denotes a direct reaction without a (meta-)stable intermediate state; instead, these reactions proceed via a short-lived transition state. After excitation into this highly unstable reaction intermediate, multiple chemical bonds are formed or broken in a single reaction step. While a lot of pericyclic reactions consist of two or more interacting π-systems, as, e.g., the famous Diels–Alder-reaction [242] – a cycloaddition and bimolecular reaction – the only case treated in this work is the interaction of different π-electrons within one molecule (unimolecular reaction).

The most common reaction scheme for molecular switches, as shown by the amount of examples in Sec. 5.2.1, is the electrocyclic reaction. This corresponds to a subclass of the pericyclic reaction principle. In this case a molecular π-bond (or double bond)

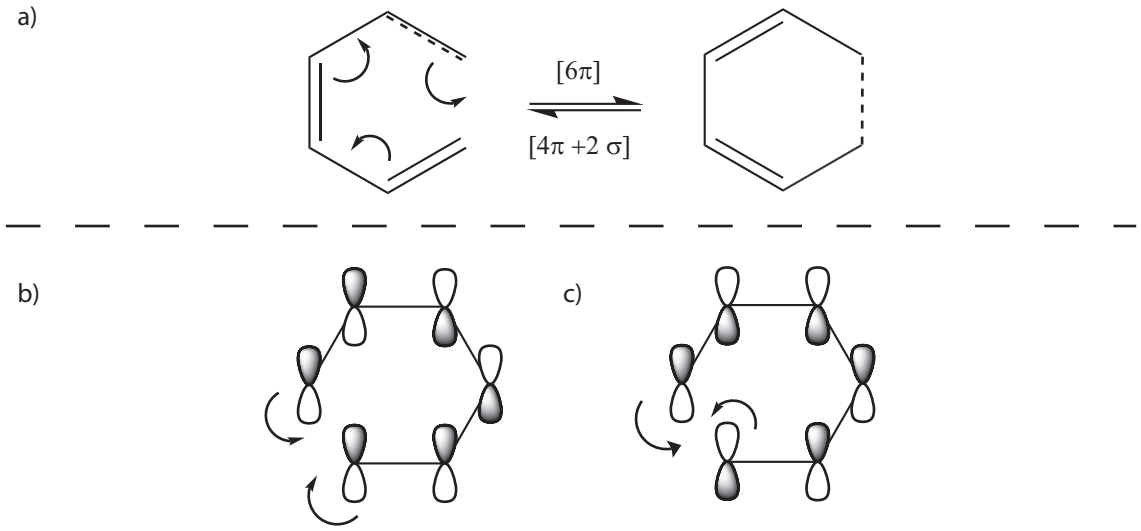

Figure 5.2: a) Visualization of the [6π]-electrocyclic ring closure/opening of 1,3,5-hexatriene/1,3-cyclohexadiene. For the closure direction every π-bond shifts one position and the last one (dashed) is cleaved and reformed into a σ-bond. This results in 1,3-cyclohexadiene which performs a [$4\pi + 2\sigma$] ring opening. b) HOMO of 1,3,5-hexatriene, capable of a disrotatoric ring-closure, c) and LUMO, showing conrotatoric behavior.

is broken and creates a single σ-bond. This results in a ring-closure reaction because an additional bond covalently links two previous unconnected atoms. Accordingly, the reversed reaction is called a ring-opening reaction and separates two previously directly-linked atoms via cleavage of a σ-bond. The exact reaction mechanism is defined by the number n of π-electrons and k of σ-electrons contained in the ring-system, resulting in an $[n\,\pi + k\,\sigma]$ ring-closure or ring-opening reaction.

Fig. 5.2a) visualizes the [6π]-ring closure of 1,3,5-hexatriene, which possesses 3π-bonds, leading to 1,3-cyclohexadiene. Each participating bond shifts by one position, until the ring closure is possible, resulting in a new photosystem. Here two electrons, which previously formed a π-bond (dashed), are used to link a new σ-bond. This reaction mechanism, which forms or breaks a π-bond in a ring-system, containing 6 carbon atoms, is one of the most fundamental electrocyclic reactions. The photochemical ring-opening reaction, starting with 1,3-cyclohexadiene, is both theoretically and experimentally well studied [243–246]. After vibrational relaxation of cyclohexadiene in the excited state 1B the excited molecule relaxes into the 2A state and from there proceeds into the vibrationally excited ground state of hexatriene via a conical intersection (CI). The entire reaction proceeds on an ultrafast time-scale. Within 100 fs the hot ground state is reached and afterwards a fast ps relaxation sets in until metastable, vibrationally completely relaxed, hexatriene is observed.

In order to assess the stability of an entire molecular system or a specific reaction pathway, molecular orbital theory has emerged as an important tool. If only the highest occupied (HOMO) and lowest unoccupied molecular orbitals (LUMO) are used, both types of orbitals are called frontier orbitals [247]. Figure 5.2 shows the

HOMO [Fig. 5.2b)] and LUMO [Fig. 5.2c)] of 1,3,5-hexatriene. Each π-electron is visualized as a dumbbell-shaped p-orbital, with black and white halves denoting opposite signs of the atomic wave functions. A superposition of the atomic orbitals, containing all atoms forming a molecule, results in the molecular orbitals. For molecular systems the energy is minimized if the system reaches its most stable configuration and stability is enhanced if the corresponding atomic wave function can overlap constructively. Thus, the interacting halves of two p-orbitals have to share the same sign. As a result, systems with even parity perform electrocyclic reactions via disrotatoric movements, meaning both p-orbitals have to turn in opposite directions (as shown for the HOMO of 1,3,5-hexatriene), while odd parity leads to conrotatoric behavior, meaning they turn both in the same direction [LUMO in Fig. 5.2c)]. Thermal reactions start from the HOMO, while photochemical reactions, because of the excitation, normally begin with the LUMO. Thus, normally one type of reaction (thermal or photochromic) is energetically preferred and the other forbidden, since these two orbitals possess different parity [248]. This is valid for the hexatriene-cyclohexadiene system, which only performs a light-induced, conrotatoric, ring-opening but no photochemical ring-closure reaction is observed [246, 249]. However, according to Woodward–Hoffman rules the thermal back-reaction is possible. Hence, by calculating the molecular orbitals an estimation about plausible photochemical and thermal reaction pathways is intuitively gained.

An efficient molecular switch utilizes the following behavior: Efficient photochemical reactions for both directions and nearly no thermal activity. Often the hexatriene-system is incorporated, however with additional substituents and chromophores to tailor the behavior to satisfy many of the required criteria summarized in Sec. 5.2.1.

5.2.3 Merocyanines and Spiropyrans

The spiropyran–merocyanine photosystem constitutes of a class of molecules which can perform a 6π-electrocyclic ring-closure or -opening reaction via the same mechanism as 1,3-cyclohexadiene, resulting in strongly differing photochemical properties as explained in the previous Section 5.2.2. Fischer and Hirshberg detected these dyes when their samples changed color after continuous illumination. They returned to their original coloration after a macroscopic waiting time and without further illumination, performing a photochemical and a thermal reaction [250].

The reason for the different color is the substantially different π-systems of both isomers. Spiropyrans (SP), from which the simplest possible configuration is shown in Fig. 5.3a), consist of at least a pyran unit (blue) fused to an orthogonally oriented indole moiety (black). Both units are connected at a single carbon atom C_{spiro}, the spiro-carbon, and possess only weak electronic interaction [207, 251]. Accordingly, this system is optically transparent in the visible spectral range and absorbs only in the UV, nearly identical to the behavior of each of the two chromophores, indole and pyran. After (resonant) illumination in the UV, the C-O bond in the pyran moiety is cleaved, and the new isomer forms a methine bridge, defined by the three dihedral

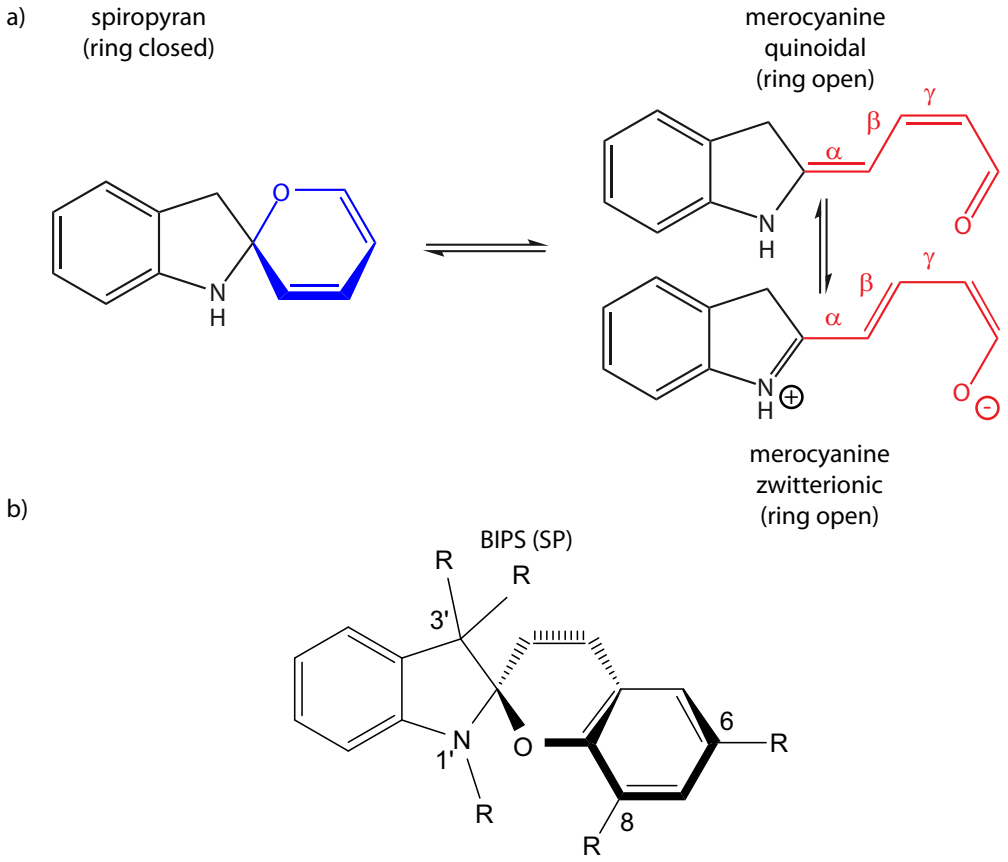

Figure 5.3: a) A photochromic spiropyran–merocyanine model system. Spiropyran (left) consists of an indole (black) and an orthogonal pyran (blue) moiety. Planar Merocyanine (right) still consists of the indole, while, via bond breaking, the pyran is changed into a methine bridge defined by three dihedral angles (red). With increasing solvent polarity the equilibrium shifts from a quinoidal (top) to a zwitterionic conformation (bottom). b) Completely unsubstituted BIPS (R = H) in spiropyran conformation. Common binding positions are marked by numbers and the not specified substitutes are marked as R.

angle configurations[3] $\theta_D = \alpha,\ \beta,\ \gamma$ (red). Additionally, the ring-open remains of the pyran rotate by about 90°, from an orthogonal orientation directly into the plane of the indole. Hence, a large planar system with only one shared, but enlarged π-electron system is formed. This results in a strong new absorption in the visible spectral range, responsible for the coloring, because the energy requirement to induce changes in the π-electron density are greatly reduced. This new ring-open form is called merocyanine (MC). Thermal relaxation or illumination with visible light leads back to the spiropyran, completing the electrocyclic reaction circle.

One very well studied class of spiropyrans is the so-called 1',3',3'-trimethylspiro[2H-1-benzopyran-2,2'-indoline] (BIPS) molecule and differently substituted derivatives.

[3]A dihedral angle is the angle between two planes and contains normally 4 atoms in a chemical compound and not three like a bond angle.

The basic structure of the molecule is shown in Fig. 5.3b) with an additional benzene ring attached to the pyran moiety, forming the so-called chromene or benzopyran, compared to the previous model system [206,232,233,252]. The most important binding positions are marked by numbers and for BIPS itself the possible substituents R are either methyl groups CH_3 (1',3',3') or simple R = hydrogen (H) for the 6,8 positions. Time-resolved photochemistry, from femtoseconds [233] up to μs [253], of BIPS derivatives with differing substitutions patterns focused mostly on the ring-opening mechanism out of two reasons. On the one hand, the ring-opening is photochemically allowed. Thus, it is accessible with high yield as shown for 1,3-cyclohexadiene. On the other hand, spiropyran is, at least at room temperature, the most stable configuration. Therefore, easy access without the need of additional light sources necessary for photoconversion [254], is provided. For BIPS itself, merocyanine is formed with a 28 ps time constant after excitation of spiropyran dissolved in tetrachloroethene with a quantum yield of $\Phi_{c-o} = 10\%$ [233], and within $\approx$ 1 ps in ethanol and n-pentane [206, 207]. While some ambiguities exist, like the existence of a short-living intermediate species, possibly in a cisoid conformation (resembling spiropyran, but with an already cleaved C-O bond) [233], the existence of an inefficient, but fast singlet reaction pathway is generally agreed upon.

After attaching a nitro group in position 6 on the pyran [compare Fig. 5.3b)], resulting in the so-called 6-nitro BIPS, the photochemical properties change drastically. The switching efficiency increases to a much higher yield. However the reaction mechanism now seems to involve strong triplet contributions [255]. While theoretical models for the BIPS family propose an ultrafast ring closure proceeding via a conical intersection seam, this reaction is not observed for 6-nitro BIPS. To follow the mechanisms competing with the ring-closure reaction, 6-nitro BIPS was continuously illuminated with UV light, followed by a pump–probe experiment with visible excitation and detection [254]. Several merocyanine isomers, at least two, possibly three, were observed after excitation of merocyanine in the ground state, but no reaction pathway to the spiropyran was detected. Despite this quite severe limitation in regard to a switching device, 6-nitro BIPS is probably the most studied molecule of the entire BIPS family, with the results covering all states of matter. In the gas phase, a four-step isomerization process, completed within 100 ps, was observed, leading from spiropyran over intermediates to merocyanine [256]. The behavior in phospholipid layers resembles, quite surprisingly, the behavior in the liquid phase, meaning a light-induced ring-opening reaction is detected [257]. An enhancement in the ring-opening yield was observed when using chirped pulses on 6-nitro BIPS enclosed in a solid state polymer [258–260] and substantiated by theoretical calculations [261]. Laser desorption-electron diffraction measurements were used to directly identify spiropyran, the lowest merocyanine triplet state, and merocyanine in its ground state contained in the used sample after UV excitation, which contained pure spiropyran before excitation [262].

This chapter focuses experimentally solely on 6,8-dinitro BIPS, having two nitro groups attached to the pyran, at position 6 and 8, while the indole unit remains unchanged [58, 216, 217, 263, 264]. As a result of this substitution pattern, thermal

stability is observed for merocyanine in contrast to most other BIPS derivatives where spiropyran is more stable [263]. Each nitro group induces an electron-withdrawing effect. Hence, one group is weakening the bond between the spiro carbon and the oxygen, while adding a second one cleaves the bond [212]. Minami and Taguchi also determined that the absorption maximum shifts to the blue with increasing solvent polarity, starting at 560 nm in chloroform and moving down to $\approx$ 520 nm in different alcohols [263]. This is due to the fact that merocyanine either exists as a zwitterionic (Fig. 5.3a) bottom), or a quinoidal structure (Fig. 5.3a) top), depending on the solvent. The zwitterionic structure is dominant in solvents with high polarity but generally an equilibrium of both is present. First time-resolved experiments with 25 ns-time resolution showed that 6,8-dinitro BIPS ground-state absorption occurs within the time resolution, and changes with $\tau = 200$ ns. Furthermore, they verified the existence of a new spiropyran absorption. Thus, the existence of a photochemical ring-closure pathway for a merocyanine is proven, albeit the exact mechanism proceeding via singlet, via triplet, or via a combination of both kind of states remains unknown [264]. Using pump–probe Brewster angle reflectometry the other direction, spiropyran to merocyanine was observed with 10 ns time resolution [265].

Hobley *et al.* highlight, using transient-absorption measurements, that after photoexcitation of 6,8-dinitro BIPS in acetonitrile with 400 nm pulses a permanent photo-induced bleach remains in the visible spectral range [217]. Additionally, a high percentage of the excited molecules were radiatively relaxing back to the ground state with time constants of either $\tau \approx 80$ ps or $\tau \approx 400$ ps. Hence, an electrocyclic ring-closure reaction is indicated on a fs-time-scale but the product was not directly identified. Moreover, the time-scale of the mechanism was inaccessible, because it was inseparable from the decay of stimulated emission. Furthermore, the 400 nm pulses provided significant excess energy, which could change the photochemical behavior; excitation into S_1 is beneficial, since the amount of participating states is restricted to S_1, possibly T_1, and the ground state. Using transient MIR measurements and visible excitation pulses, previous work by J. Buback and myself provided the missing evidence for ultrafast ring closure in 6,8-dinitro BIPS. Vibrational bands belonging to merocyanine and spiropyran, centered around 1350 cm^{-1}, and identified by Futami *et al.* using low-temperature measurements and DFT calculations [266], are detected. Merocyanine absorption vanished within the time resolution of < 100 fs and a new absorption band belonging to spiropyran emerged [20, 58, 71]. Further transient-absorption experiments with visible excitation pulses confirmed the previous observations (missing merocyanine and the existence of two time constants). In addition, the photochemical back reaction, an electrocyclic ring opening, was also observed using UV excitation with an efficiency of $\approx 10\%$ [20]. Hot merocyanine is formed on a picosecond time-scale and subsequently relaxes to its ground state with a decay time of ≈ 40 ps. Summing up, the ring-opening behavior of 6,8-dinitro BIPS resembles the one of BIPS. The reaction mechanism for the closing, though, resulting in spiropyran, is quite unique. Hence, 6,8-dinitro BIPS is one of the few examples of a spiropyran–merocyanine system able to perform as a photoswitch, providing the motivation for the studies explained in the following sections.

	τ_{c-o} [ps]	Φ_{c-o}[%]	τ_{o-c} [ps]	Φ_{o-c}[%]
BIPS (TCE) [233]	$\approx$ 30 (S)	< 10	–	–
6-nitro BIPS (TCE) [255]	(T)	≈ 60	–	–
Py-BIPS (water) [212]	≈ 2 (S)	< 4	≈ 25 (S)	< 20
6,8-dinitro BIPS ($CHCl_3$) [58]	< 6 (S)	≈ 10	≈ 30 (S)	40

Table 5.2: Summary of the photochemical properties for differently substituted BIPS. (S) or (T) denotes singlet or triplet pathways. TCE corresponds to tetrachloroethene and $CHCl_3$ to chloroform as the solvent. While BIPS and 6-nitro BIPS differ from 6,8-dinitro BIPS and perform no ring closure, the latter compares very well to Py-BIPS.

Table 5.2 provides an overview of the time-scales and efficiencies for different BIPS derivatives. While BIPS and 6-nitro BIPS differ quite drastically from 6,8-dinitro BIPS, the results of a recent study of a new kind of BIPS (Py-BIPS) correspond well to the results obtained for 6,8-dinitro BIPS. There, water-solubility was achieved by adding a large alkyl-chain to the nitrogen atom and by inclusion of a pyridinium (Py) structure altering the benzene unit. Thus, the common BIPS configuration was strongly altered [212]. Indeed, Py-BIPS in aqueous solution performs a ring-opening reaction within 1.6 ps and an efficiency of $\approx 3\%$ and a ring closure in less than 25 ps with $\approx 20\%$ quantum yield. Interestingly, the thermal equilibrium is, at least with a probability of more than 95%, on the spiropyran isomer. This strongly indicates that the ability to perform a complete photocycle does not depend on whether the merocyanine is more stable (6,8-dinitro BIPS) or the spiropyran (nearly all substitutions patterns), confirming the unique nature of 6,8-dinitro BIPS.

5.3 Sample Characteristics and Preparation

6,8-dinitro BIPS was synthesized via the Knoevenagel condensation reaction of commercially available 1,2,3,3-tetramethyl-3H-indolium and 3,5-dinitrosalicylaldehyde resulting in the merocyanine form of 6,8-dinitro BIPS in 79% yield according to literature [21] and characterized by HPLC and 400 MHz NMR spectroscopy. The synthesis, including NMR measurements, confirming the purity, was performed by R. Schmidt in the research group of Prof. Dr. F. Würthner (Institut für Organische Chemie, Universtät Würzburg) [20].

Steady-state absorption spectra in the visible spectral range were measured in a 2 mm suprasil cuvette with a Hitachi U-2000 spectrophotometer. Fluorescence spectra were recorded with a Jasco FP-6300 fluorescence spectrometer in a 1 cm flow cell (Hellma, Type 176-050-40). All spectra were recorded directly after solving the crystals in chloroform with spectroscopic grade purity [78].

For the transient-absorption (Sec. 5.4) and 2D measurements (Sec. 5.5) an absorbance of 0.3 OD around the absorption maximum was chosen, while the density was increased towards 0.5 OD for the multipulse experiments (Sec. 5.6 and 5.7). This was done in order to increase the signal strength subjected to the additional pump

pulse(s), thus, effectively increasing the retrieved signal. All measurements were performed in a 200 µm suprasil flow cell (Starna, Type 48/Q/0.2). Sufficient flow was ensured using a low pulsation Micro Annular Gear Pump (HNP Mikrosysteme, mrz-4605) and a sample reservoir of 25 ml in a brown, light-absorbing, storage glass. All used pulses were spatially overlapped within the flow cell by employing a number of small pinholes with variable diameter d (25 µm $< d <$ 200 µm), but sharing the macroscopic dimensions of the flow cell. Therefore, they can be inserted into the sample holder instead, allowing adjustments and fine tuning.

5.4 Following an Electrocyclic Ring-Opening Reaction

The transient-absorption study in the following section introduces the photochromic compound 6,8-dinitro BIPS, which is the focus of this entire chapter. The spectral signatures and lifetimes of two merocyanine isomers in solution are identified and their photochemical behavior after excitation is explained, demonstrating an electrocyclic ring-closure mechanism. The section is organized in the following way:

First, steady-state absorption and fluorescence measurements are used for a simple characterization of the compound, confirming the broad absorption in the visible spectral range for the merocyanine and the occurrence of UV absorption bands for the spiropyran form (Sec. 5.4.1). Second, pump–probe measurements with two different excitation wavelengths in the visible spectral range are presented and the origin of the observed spectral signatures is explained (Sec. 5.4.2). Finally, a photochemical reaction scheme based on two isomers is presented and the quantum yield for the closing reaction is estimated (Sec. 5.4.3).

5.4.1 Steady-State Characterization

The steady-state absorption spectrum of 6,8-dinitro BIPS, thermally stable in the merocyanine form [20, 27, 216], dissolved in chloroform is displayed in Fig. 5.4a) (green, solid) together with the corresponding structure shown as an inset on the right upper side. The absorption spectrum consists of a dominant absorption peak centered at 560 nm, covering wavelengths from 450 to 650 nm, most probably belonging to the S_1-S_0 transition of the merocyanine form [217]. It is evident that the low energetic side ($\lambda > 600$ nm) cannot be described by modeling the photochemical transition with a single Gaussian function centered at 560 nm. Accordingly, either a weaker feature is hidden under the strong main absorption, or the absorption band has a more complex origin. Centered at $\approx$ 370 nm, the S_2-S_0 transition of merocyanine is identified, more than two times weaker as the S_1-S_0 absorption in the visible. The feature at 370 nm is due to a small perturbation induced by the lamp change within the spectrometer. Going even further in the UV additional weak absorptions

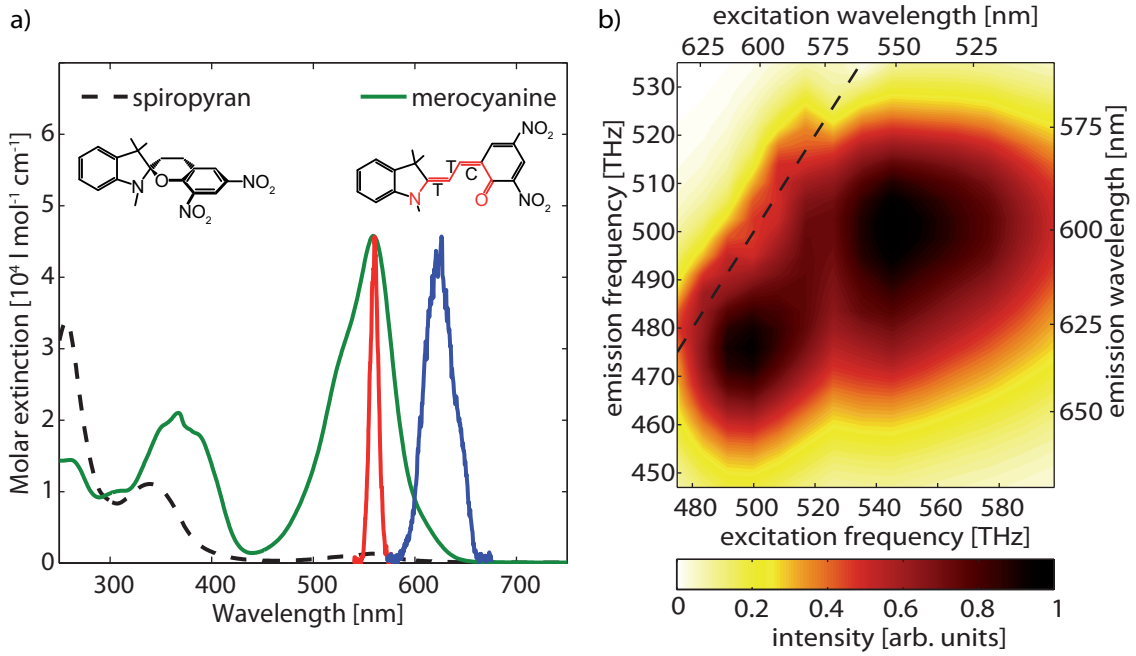

Figure 5.4: a) Steady-state absorption spectra of 6,8-dinitro BIPS dissolved in chloroform for both conformations. Spiropyran (black, dashed) absorbs solely in the UV, merocyanine (green, solid) possesses a strong absorption band in the visible. Corresponding structures are drawn below their legend entry. The spectra used for pump–probe experiments are shown in red (560 nm) and blue (620 nm) [20]. b) Emitted fluorescence of 6,8-dinitro BIPS with spectrally-resolved excitation and emission axis. Two separate peaks after excitation at 560 and 610 nm, leading to emission at 600 and 630 nm, are identified (dark signals). The black dashed line represents scatter along the diagonal and the excitation axis was generated by tuning of a monochromatic light source [78].

set in, belonging to even higher transitions into states S_n. Solvent contributions of chloroform can be neglected down to 250 nm.

Steady-state absorption properties (black, dashed) of the ring-closed spiropyran [left inset of Fig. 5.4a)], are obtained after illumination of the merocyanine sample with an array of green and orange LEDs resulting in a ring-closure reaction. The thermal stability was checked and the photoproduct is stable on a time-scale of minutes or longer, which is sufficient for any time-resolved measurement. The sample reservoir can be continuously illuminated, if spiropyran is needed, only the small amount within the transfer tube is not subjected to any photoconversion. The main absorption bands are now centered at ≈ 255 nm and ≈ 340 nm and the visible spectral range is, as expected from literature, completely transparent. Only weak absorption remains, which corresponds to a small remaining fraction of merocyanine. After illumination of 6,8-dinitro BIPS with a continuum extending into the UV obtained from a Xe-flash lamp a stable equilibrium consisting of a mixed solution of merocyanine and spiropyran is formed, which absorbs both in the UV and the visible spectral range (not shown). This mixture with strong concentrations of each form results from the effective absorption in the UV of both molecules. While merocyanine can

be accessed purely by excitation in the visible, a pure spiropyran excitation is not possible. However, by proper choice of the UV excitation-wavelength, a coefficient of about 3:1 is possible (at $\approx$ 267 nm, corresponding to the third harmonic of the laser fundamental). In addition, the depicted spiropyran spectrum shows that bleaching with a visible light source allows a nearly complete photoconversion from the merocyanine conformation to spiropyran.

The existence of two separate, partially overlapping, absorption bands for the merocyanine form of 6,8-dinitro BIPS, hidden below the S_1 absorption, is even stronger suggested in the fluorescence spectrum shown in Fig. 5.4b) with spectrally-resolved excitation and detection axis. The wavelength axes on the right and upper side are in nm while the left and lower frequency axes are scaled in THz to provide a better overview and a simple conversion tool. The frequency axes scale linearly, while the wavelength axes are spaced nonlinear. White and yellow denote weak emission signals and more reddish colors denote more intense fluorescence. After excitation around 560 nm strong emission at 600 nm is detected (signal 1: $\lambda_P = 560$ nm,$\lambda_{Pr} = 600$ nm). Excitation around 610 nm leads to emission at 630 nm (signal 1: $\lambda_P = 613$ nm,$\lambda_{Pr} = 630$ nm). Both features are clearly separated as is evident by the fluorescence minimum around 575 nm and are not parallelly oriented along the diagonal (black, dashed line). This line additionally corresponds to remaining scattered light originating from the flow cell or the solvent. However, the scatter is strongly reduced because the depicted spectrum consists of the fluorescence of merocyanine minus a pure solvent measurement. Identification of the scattered light is possible, because absorption and emission wavelengths are identical and pure chloroform possesses no visible fluorescence, but shows the same scattered light feature.

5.4.2 Transient-Absorption Measurements

Relaxation Dynamics after Excitation at 560 nm

Transient-absorption data of 6,8-dinitro BIPS after excitation with 560 nm pulses into S_1 are shown in a contour plot in Fig. 5.5 for pump–probe delays T up to 3.5 ns. The corresponding pump pulse in relation to the absorption spectrum is shown in Fig. 5.4a) in red. Bluish colors denote negative and reddish colors positive contributions. Clearly three separate contributions are identified, which all decay within the first 500 ps. They are attributed in the following way, by using information obtained from the linear measurements in Sec. 5.4.1: The observed ground-state bleach (GSB), with only a partial recovery, is centered at $\approx$ 559 nm and identified by a comparison to the main absorption band in the steady-state absorption spectrum with a peak at $\approx$ 560 nm resulting from the S_1-S_0-transition. A very broad stimulated emission (SE) signal is seen around 610 nm, ranging from $\approx$ 580 to 680 nm. This stimulated emission signal, which is directly related to fluorescence in the non-time resolved experiments, corresponds well to the measured fluorescence spectrum, possessing emission around 600 nm when excited at 560 nm. Finally, excited-state

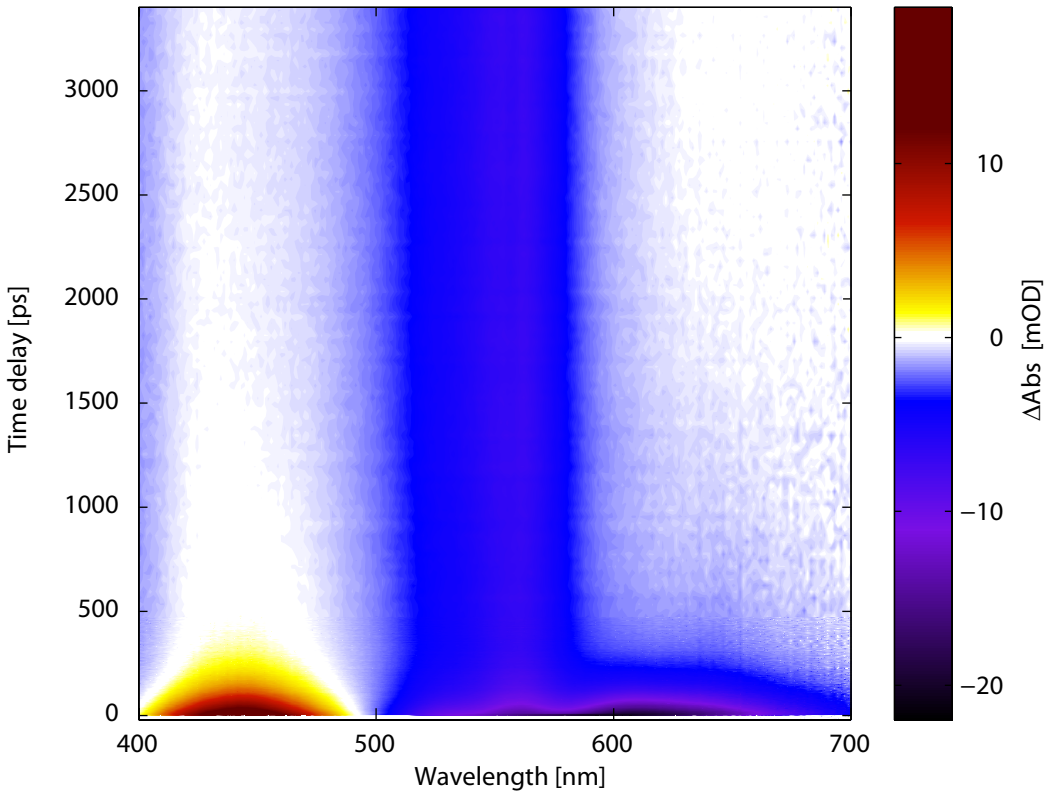

Figure 5.5: Transient-absorption data of 6,8-dinitro BIPS after excitation with 560 nm pump pulses. Strong, partially permanent, GSB (560 nm) combined with SE (610 nm) and ESA (445 nm) is clearly seen. Dominant temporal changes happen only for $T < 500$ ps.

absorption (ESA) centered at 445 nm is seen, which possesses no analogue in simple excitation or emission spectroscopy, since the entire signal relates to a photochemically induced transition happening between two excited states. After 500 ps nearly no further change is evident in the data, but a permanent bleach, ranging from 500 nm$< \lambda_P <$ 580 nm, is seen, which corresponds to a reduced concentration of the reactant, hence, photoconverted merocyanine.

The temporal behavior of these contributions is visualized by colored transient cuts in Fig. 5.6a), which are extracted from the contour map (Fig. 5.5), together with the results of a global fitting routine underlaid with black lines. All three transients, representing ESA (blue), GSB (green), and SE (red) seem to decay on the same time-scale, thus, are directly connected, most probably via photochemistry happening in the S_1 state. In addition, ESA and SE seem to possess a smaller, longer living decay on a fast nanosecond time-scale, while the GSB seems to remain unchanged, resulting in a strong negative constant offset after 500 ps.

Data were globally described with two exponential decays, numbered 1 and 2 in the following, and a remaining constant, accounting for permanent or long-living contributions, which exceeds the maximal waiting time of 3.5 ns, and the obtained results model the data convincingly. A purely parallel model was chosen, whose fun-

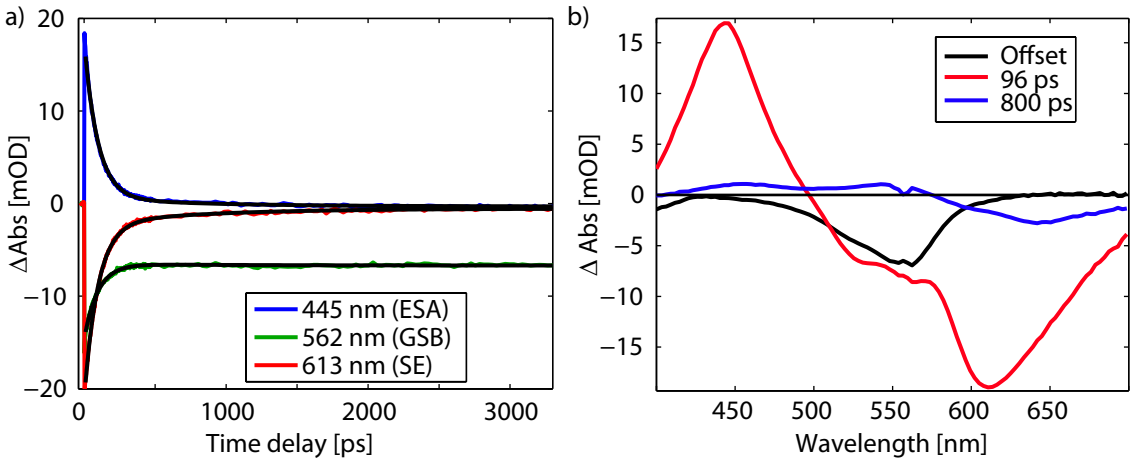

Figure 5.6: a) Transient behavior after 560 nm excitation at selected probe wavelengths reflecting ESA (blue), GSB (green), and SE (red) together with global fitting results (black). b) DADS corresponding to lifetimes of $\tau_1 = 96$ ps (red) and $\tau_2 = 800$ ps (blue) and a permanent offset (black).

damentals are explained in detail in Sec. 3.2.2. The first 10 ps were not included in the fitting routine, thus, neglecting fast-living vibrational contributions, which would hinder the choice of pure exponential fit functions [245]. The resulting decay-associated difference spectra (DADS) are shown in Fig. 5.6b) and their spectral properties will be discussed now in greater detail. In all difference spectra a distortion is seen at ≈ 560 nm belonging to pump-induced scatter, which should not aggravate the analysis any further. The red DADS, belonging to a time constant $\tau_1 = (96 \pm 1)$ ps, is the dominant spectral contribution with signal over the entire probe wavelengths, as already indicated by the transients. While both, a strong SE centered at 615 nm and an ESA at 445 nm with similar signal strength decay on this time-scale, the ground state centered at 559 nm is replenished only partially and shows a much lower absorption strength. The entire behavior of this DADS visualizes a radiative relaxation from S_1 back to S_0, without further steps in-between, because the decay of ESA and SE, which both monitor the S_1 population occurs simultaneously with repopulation of the ground state.

The second, blue, DADS, corresponding to a time constant of $\tau_2 = (800 \pm 20)$ ps, behaves much differently and is much weaker. A broad negative signal, ranging from 580 to 680 nm, is seen. One possibility would be SE centered at 640 nm, corresponding nearly to the second emission in the fluorescence spectrum combined with the strongly overlapping unknown GSB centered at ≈ 600 nm. This seams a reasonable explanation, because the overall curvature changes at 615 nm, an indication of a more complex shape caused by two different, but overlapping contributions. In combination with these two negative signals, two connected positive ESAs are also evident centered at 455 and 550 nm. Again, this behavior is indicative of a radiative relaxation into the ground state, however the observed wavelengths indicate other states as the origin of the signals.

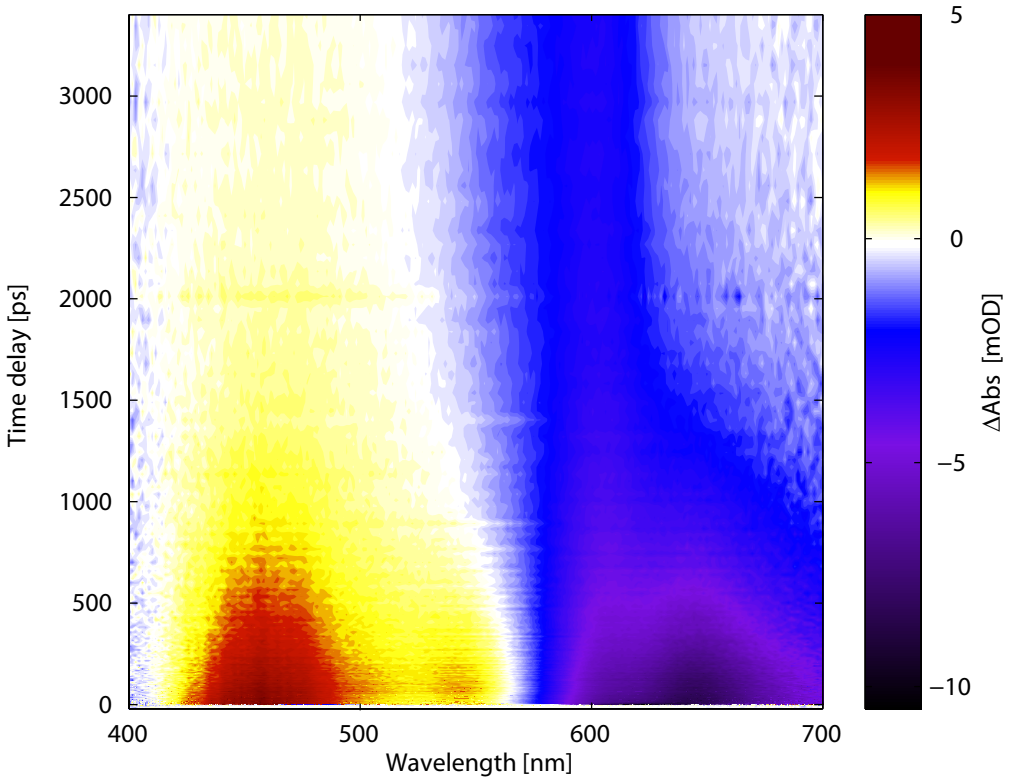

Figure 5.7: Transient-absorption data of 6,8-dinitro BIPS after excitation with 620 nm pump pulses. The long-living component is dominating compared to 560 nm excitation, resulting in two strong ESAs (460 nm, 552 nm), a GSB (600 nm), and SE (650 nm), which are all shifted towards longer wavelengths.

Last, the permanent offset, shown in black, possesses two negative contributions. One in the visible centered at 559 nm, which seems to mirror the S_1-S_0 steady-state absorption, and a second, weaker one below 400 nm. While the spectral signature is not completely resolved, the S_2-S_0 transition is beginning in this spectral region. Overall, a permanent reduction of merocyanine is a viable explanation, resulting in formation of ring-closed spiropyran, because a similar behavior is identified after continuous-wave irradiation.

Relaxation Dynamics after Excitation at 620 nm

Transient-absorption data of 6,8-dinitro BIPS after excitation with 620 nm pulses, into the low-energetic edge of the S_1 band, are shown in a contour plot in Fig. 5.7 for delay times up to 3.5 ns. The pump pulse, compared to the absorption spectrum, is shown in Fig. 5.4a) in blue. At first glance the data looks much different from the previous case with 560 nm excitation pulses (Fig. 5.5), possessing dominant long-living contributions on a nanosecond time-scale. There are four different contributions, which change over the course of the entire measurement. Positive ESA is seen at 460 and 550 nm and a strong SE signal is centered at 650 nm. The latter

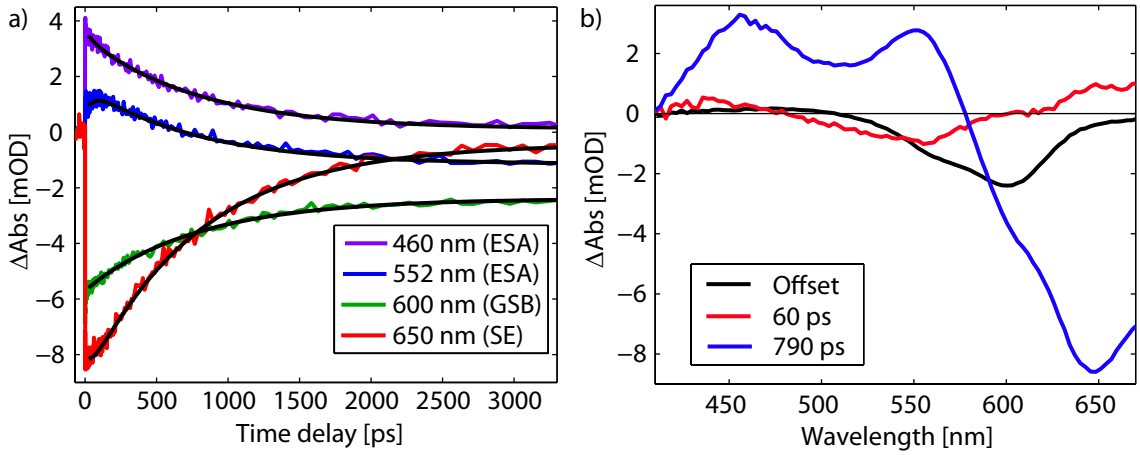

Figure 5.8: a) Transient behavior after 620 nm excitation at selected wavelengths reflecting ESA (violet, blue), GSB (green), and SE (red) together with global fitting results (black). b) DADS corresponding to lifetimes of $\tau_1 = 60$ ps (red) and $\tau_2 = 790$ ps (blue) and a permanent offset (black).

overlaps strongly with the long lasting GSB signal at 600 nm. This bleach, again indicating a reduced reactant concentration, is not located at 560 nm as expected but rather at the absorption wavelengths responsible for the second emission peak in the fluorescence measurement. In addition, the stronger overlap of SE and GSB relates well to the spectrally narrower emission peak centered at 630 nm in the fluorescence spectrum in Fig. 5.4b), also indicating a smaller Stokes shift.

The transient behavior of these four contributions is shown in Fig. 5.8a). The strongest signal, SE at 650 nm (red), decays nearly completely, approaching zero at long time delays. The corresponding bleach at 600 nm (green) decays on the same timescale, albeit, the initial signal is much weaker and the remaining offset is significant, indicating an efficient radiative relaxation pathway after excitation into the red edge of the absorption band. The ESA at 460 nm (violet) corresponds well to the other signals, analogously decaying and approaching zero at long delays. However, the second ESA at 552 nm (blue) has an initial rise, followed by a decay parallel to all other processes. The corresponding global fitting routine (black) models the data well, again consisting of a parallel fitting model with two exponential decays and a long-living offset. The fit results in the three DADS — shown in Fig. 5.8b) — which will be discussed in the next paragraph.

The first, weak DADS attributed to a time constant $\tau_1 = (60 \pm 5)$ ps (red), possesses a negative contribution around 560 nm, ranging from 500 to 600 nm. No peculiar shape is evident because the maximum signal strength is below 1 mOD, but the wavelength relates well to the GSB signal as expected when compared to both linear measurements in Fig. 5.4; the signal is slightly broadened most probably because of additional SE. In addition a small positive signal around 450 nm is indicated, corresponding to ESA. However, for this excitation wavelength the dominant spectral contribution occurs with $\tau_2 = (790 \pm 10)$ ps (blue DADS). The spectral distribution

is exactly as visually inferred from the contour map. There are two separated ESAs (460 nm, 550 nm), SE (650 nm), and GSB recovery (600 nm). All collectively decay over the entire measured time delay of 3.5 ns. The latter two signals strongly overlap, but are clearly separable because of the curvature of the DADS. Lastly, the black offset spectrum remains, characterized by a strong bleach at 600 nm and a weaker, but visible, shoulder at 560 nm.

Interestingly, when comparing the measurements at different excitation wavelengths ($\lambda_P \approx 560$ nm or $\lambda_P \approx 620$ nm), the respective shapes of the red DADS (attributed to $\tau_1 \approx 95$ ps, the smaller value for τ of the second measurement with $\lambda_P \approx 620$ nm is weighted less, because of the weak and noisy signal contribution) and the blue DADS ($\tau_2 = 800$ ps) are very similar but the relative strength has changed a lot. By contrast, the black spectrum, belonging to a permanent reactant loss, differs strongly: Upon 560 nm excitation, it is also centered at 560 nm, which corresponds to the main absorption band in the absorption spectrum. In addition, it corresponds well to the pump-wavelength causing the blue of the two fluorescence peaks. Upon 620 nm excitation the long lived bleach is centered at 600 nm, which is the pump-wavelength responsible for the second, red peak in the fluorescence measurement. This strongly indicates the existence of two different species, hidden in the one absorption peak, which can be excited separately. Each species decays with its own time constant of approximately $\tau_1 = 95$ ps or $\tau_2 = 800$ ps.

5.4.3 Simple Spiropyran–Merocyanine Reaction Scheme

The following section explains the photochemical behavior of 6,8-dinitro BIPS by combining the results obtained from the global fits, the steady-state measurements and information known from literature, forming together a cohesive picture. The differences caused by the two different pump wavelengths already showed that a simple photochemical scheme consisting of only one excited state and the ground state is not sufficient to explain the data. Thus, a more complex scheme is necessary.

The steady-state absorption spectrum in Fig. 5.4a) provides the basis for interpretation of the transient-absorption data. Figure 5.9a) shows a comparison between the offsets, corresponding to the signal after 3.5 ns, obtained in time-resolved measurements (red: $\lambda_P = 560$ nm, blue: $\lambda_P = 620$ nm), compared to the inverted steady-state spectrum (black). The signal strength is arbitrarily chosen in order to provide insight into the observed signals. The red spectrum corresponds very well to the absorption spectrum, only for $\lambda_{Pr} > 580$ nm a deviation is visible, hence, it can be attributed to missing merocyanine. The absorption spectrum (black) is broader than the observed bleached contribution, indicating that a second reactant is present. By contrast, the remaining offset obtained by using excitation pulses centered at 620 nm does not match at all the absorption spectrum at first glance. However, it fits adequately the red edge, supporting the existence of a second contribution.

A similar bleach was observed, recovering partially with two time constants in a time-resolved study of 6,8-dinitro BIPS in acetonitrile with 400 nm excitation [217].

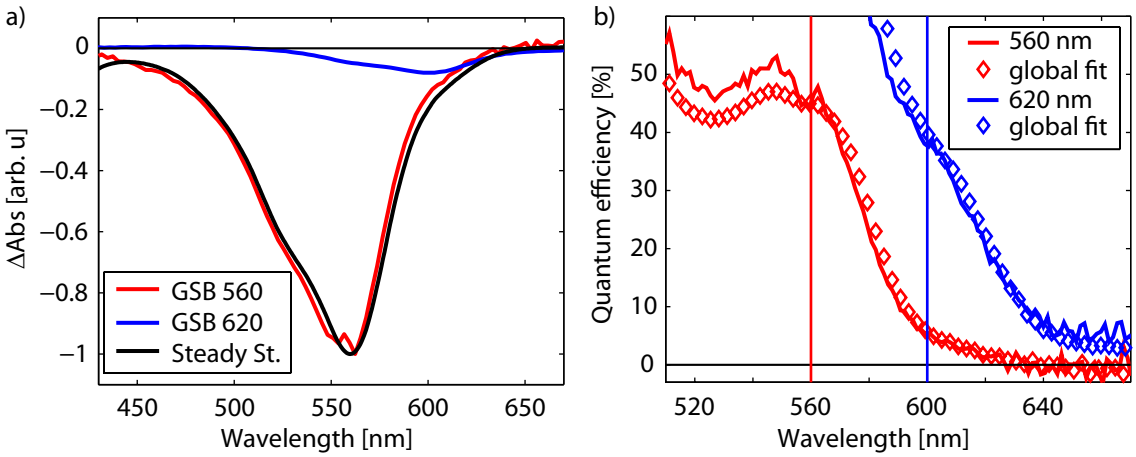

Figure 5.9: a) Comparison of the offsets after 560 nm (red) and 620 nm excitation (blue) with the inverted absorption spectrum (black). The red spectrum corresponds to the main absorption band, while the blue one overlaps with the low-energy shoulder at 600 nm. b) Spectrally-resolved quasi quantum efficiencies by using the data (solid) or the fitting results (diamonds). For 560 nm excitation $\approx (40-45)\%$ of the excited population vanishes at the GSB band (red). For 620 nm excitation the broad SE signal disturbs evaluation leading to $\approx (35-40)\%$ loss at 600 nm (blue).

There two possible explanations were proposed for this behavior. The first involves formation of a cisoid species relaxing in different excited states, while the other scheme necessitates the existence of two different isomers in merocyanine configuration, which are both present in solution. Both relax with their corresponding time constants and their spectral emission and absorption properties are shifted when compared to each other. However, Hobley *et al.* could not distinguish between these schemes and preferred the first one because the offset (showing a lower signal-to-noise ratio than the data shown here) obtained in their measurements was seemingly in agreement with the inverted steady-state spectrum [217]. The new measurements presented here, though, enable the confirmation of the isomerization theory.

The idea behind different merocyanine isomers in solution is based on the properties of the methine bridge, formed by the cleavage of the pyran unit. This bridge possesses, as explained in Sec. 5.2.3, the dihedral angles α, β, and γ. Each of them can either be in trans (180°, T) or in cis configuration (0°, C). Therefore, theoretically $2^3 = 8$ isomers are possible, all differing in their dihedral angle configuration. Figure 5.10a) visualizes their configurations using the concept of an isomeric cube. The three-dimensional coordinate system is formed by the dihedral angles in the methine bridge. Spiropyran itself resembles most closely $\alpha = 90°$, $\beta = 0°$, and $\gamma = 0°$, while all merocyanine isomers are placed on the outer edges. Only configurations with $\beta = 180°$= T are stable for the BIPS family [207]. NMR line-shape measurements clearly identified the TTC isomer of 6,8-dinitro BIPS [marked in red in Fig. 5.10c)] as the most stable one in chloroform and, accordingly, from now on every contribution corresponding to this isomer is marked in red. The second most stable one is the TTT isomer [marked in blue in Fig. 5.10c)], which is only found in a minor

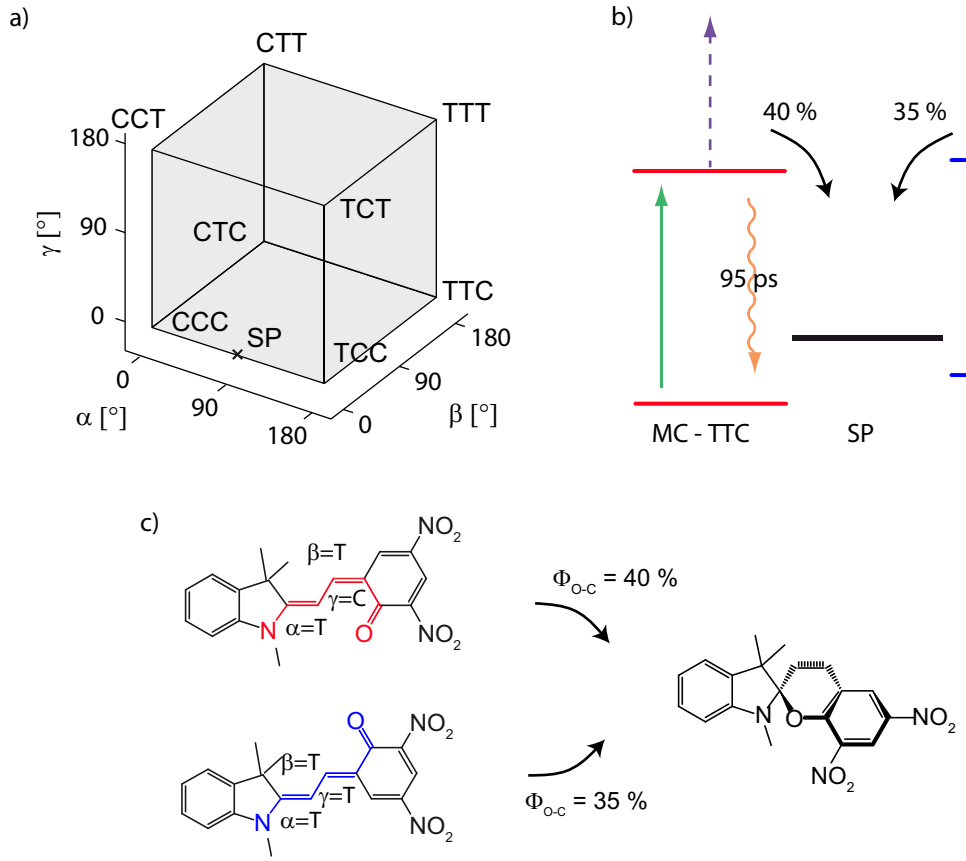

Figure 5.10: a) Possible isomers of 6,8-dinitro BIPS in an isomeric cube. Axis are the dihedral angles α, β, γ with 0° (cis) and 180° (trans). SP is approximately $\alpha = 90°$, $\beta = 0°$, and $\gamma = 0°$. Adapted from [54,207]. b) Energy level diagram, consisting of two MC isomers [TTC (red), TTT (blue)] and spiropyran (black). Arrow colors denote the wavelengths, with solid lines corresponding to GSB, dashed ones to ESA, and curled ones to SE. All TTT contributions are red-shifted relative to TTC, and TTC is the most stable form. Curved lines denote the non-radiative electrocyclic ring-closure mechanism. c) Molecular structure of all participating molecules, combined with the resolved direction of the mechanism.

concentration in solution when compared to TTC [216]. Subsequently, contributions arising from the TTT isomer will be marked in blue. Spiropyran possesses, at least for 6,8-dinitro BIPS, the highest ground-state energy of these three conformations. This behavior is sketched in the energy level diagram in Fig. 5.10b), containing the ground and, additionally, the first-excited state. By contrast, 6-nitro BIPS possesses the same energetic ordering of the possible merocyanine isomers, but spiropyran is the energetically preferred isomer of the complete photosystem [255].

The spectrally-resolved fluorescence measurement resolves two peaks ($\lambda_P = 560$ nm, $\lambda_{Pr} = 610$ nm; $\lambda_P = 600$ nm, $\lambda_{Pr} = 630$ nm). These two peaks directly correspond to the absorption and emission properties obtained in the pump–probe experiments and are assigned as follows. Excitation at 560 nm leads to bleach and emission of the first peak, hence, corresponds to the dominant TTC isomer. Excitation at 620 nm

leads to bleach and emission of the second peak, belonging to a small admixture of TTT in solution. The seemingly much stronger emission of the red-shifted component can be explained by the longer lifetime, which results in stronger fluorescence, as predicted by Einstein coefficients. Both isomers show a remaining bleach after their excited-state population has completely relaxed but no product formation is resolved in the visible. Hence, dominant isomerization can be excluded. Transient MIR measurements, previously performed by Buback in this group [58,266], showed that after merocyanine excitation vibrations belonging to spiropyran are resolved. Thus, the photoproduct is positively identified as the ring-closed spiropyran [266]. Figure 5.10c) visualizes all three molecular structures and how they are connected via photochemical ring-closure reactions. Spiropyran has the greatest similarity to a somewhat cisoid merocyanine structure, lying between the CCC and TCC isomer. Hence, the most stable TTC needs at least one isomerization step while TTT needs two to reach spiropyran. This theory of two merocyanine isomers in solution explains Fig. 5.9a) very well, because the sum of the blue and the red signal matches the steady-state spectrum. A more extensive study of 6,8-dinitro BIPS in chloroform, which combines the transient-absorption data obtained for multiple excitation wavelengths in a single global fit, determines a relative yield of $\frac{[TTC]}{[TTT]} = \frac{10}{1}$ [27]. Thus, the qualitative assumptions derived here, regarding the existence of two isomers, their lifetimes, and concentration percentage, are confirmed there.

λ_P [nm]	τ_1 [ps]	τ_2 [ps]	λ_{offset} [nm]	Φ_{o-c} [%]
560	96 ± 1	800 ± 20	559 (TTC)	40
620	60 ± 5	790 ± 10	600 (TTT)	35

Table 5.3: Time constants, center wavelength of the permanent bleach, and the quantum yield obtained from exciting 6,8-dinitro BIPS with light pulses centered at 560 nm (top) and 620 nm (bottom). The discrepancy for τ_1 is attributed to the weak signal for 620 nm excitation.

In order to estimate the effective quantum yield Φ_{o-c} the bleach after 3.5 ns, directly corresponding to the percentage of missing excited reactant molecules, has to be divided through the initial observable signal, which is directly proportional to all excited molecules. This is visualized for both isomers in Fig. 5.9b). Solid lines represent the values obtained using the measured data itself, thus, are not netted for contribution of the other isomer. By contrast, the diamonds are obtained using the offset and the corresponding decaying signal taken from results of the global fitting. Only small differences between the two methods are evident, clearly confirming that each wavelength excites one isomer predominately. In principle, Φ_{o-c} has to be wavelength independent over the entire bandwidth of the molecular ground-state absorption. Thus, it should appear as a constant contribution in Fig. 5.9b), as it is approximately the case for the TTC isomer (red). The ring-closure efficiency is $40\% < \Phi_{TTC} < 45\%$, using the results from the fitting routine. For further reference $\Phi_{TTC} \approx 40\%$ is used. For TTT no plateau is observed (blue), because SE ($\lambda_{Pr} > 600$ nm) and ESA ($\lambda_{Pr} < 580$ nm) overlay with the pure GSB signal, interfering with the calculation. Using the small remaining window $30\% < \Phi_{TTT} < 40\%$

is a valid estimation. Taking the value directly at 600 nm, corresponding to the maximum of the steady-state absorption, $\Phi_{TTT} \approx 35\%$ is obtained. The latter result is important, because it means 6,8-dinitro BIPS is capable of ring-closure for both isomers. Hence, there are no dead pathways as for example present in fulgide molecules. In addition, the obtained pathway is quite efficient when compared to the data shown in Tab. 5.1, again visualizing the promise of this system. All important properties are combined in Tab. 5.3, basically showing that excitation at 560 nm dominantly excites TTC merocyanine. Whereas, excitation at 620 nm is too far in the red to excite a significant amount of TTC. Therefore, the red-shifted, less stable, TTT isomer dominates the photochemical behavior.

Summing up, this pump–probe study gives a first overview of the molecular reaction scheme of 6,8-dinitro BIPS. However, neither the product is directly identified, nor the excited-state pathways accessed. Seemingly, this molecular mixture consists of two different merocyanine molecules, which do not interact after photoexcitation, but share a common product, spiropyran. This is visualized in Fig. 5.10b), with TTC on the left, SP in the middle, and TTT on the right side of an approximated energy level diagram. Additionally, all measured signals in the pump–probe study (arrows) are colored according to their central wavelength. Ground-state absorption is shown by solid arrows, stimulated emission by undulated ones (with the estimated lifetime of S_1 shown in ps), dashed ones represent excited-state absorption. Lastly, the ultrafast ring-closure, together with the corresponding quantum efficiency, is indicated by a curved black arrow. Despite the large amount of information already obtained for the photochemistry of 6,8-dinitro BIPS, further questions will be addressed in the following sections.

5.5 Assessing Possible Isomerization Dynamics in the Excited State

Using transient-absorption experiments with varying excitation wavelength the existence of two different isomers in solution, attributed to TTC and TTT configuration, and an efficient electrocyclic ring-closure reaction for 6,8-dinitro BIPS was directly observed in the previous section. However, no information about a possible interconversion between the two isomers was obtainable. Isomerization would result in a negative ground-state bleach for one isomer and a new positive photoproduct signal for the second one, mirroring the shape of the ground-state absorption. However, while in principle the spectral signatures of both isomers are known, this information was not separable from the data, because always both isomers were excited to a certain degree. Accordingly, bleaching is observed at 560 nm (GSA TTC) and 600 nm (GSA TTT), thus, hiding effectively an isomerization reaction pathway. By performing multiple pump–probe measurements and an incremental scan of the excitation wavelength from $\lambda_P \approx 520$ nm to $\lambda_P \approx 650$ nm, analyzing many overlapping signals, and finally applying various reaction models, Buback and coworkers estimated that the photoisomerization yield is below 2% [27, 58]. This result is only indirectly in-

ferred from the data, though, and not directly evident (as indicated by the quite complicated description), highlighting the necessity to perform extensive measurement routines and data analysis in a pure pump–probe study to access information regarding the pump wavelengths.

Direct visualization of an isomerization, within a single measurement and without extensive post-processing of the experimental data, is possible using coherent electronic 2D spectroscopy. There, the spectral response of a system is spread alongside every pump wavelength, as shown in the previous chapter for analysis of the excited-state behavior of $(ZnTPP)_2$ (Sec. 5.5). The following section is ordered as follows:

First, the implementation of a coherent electronic 2D spectroscopy setup in pump–probe geometry [187] with inherently phase-stable pump-pulse pairs, generated and delayed with a femtosecond pulse shaper [68,77,89,267,268], and a supercontinuum probe [220] is described (Sec. 5.5.1). This represents an alternative to the implementation in box geometry used for the experiments on the bisporphyrin. Subsequently, the experimental conditions for the isomerization study on 6,8-dinitro BIPS are presented (Sec. 5.5.2), followed by an introduction of three possible isomerization schemes (Sec. 5.5.3). Then, the experimental results are presented and discussed (Sec. 5.5.1). The section is concluded by the assessment that isomerization is negligible and how this affects the spiropyran–merocyanine photosystem (Sec. 5.5.5). This section has already been published in Ref. [78]

5.5.1 2D Setup with a Continuum Probe in Pump–Probe Geometry

For the 2D measurements a partially collinear, pulse-shaper-assisted approach in pump–probe geometry was implemented using the transient-absorption setup described in Sec. 3.2 as the experimental backbone. The modifications are applied in the same way as introduced in literature, similar to those for 2D IR [94,267,268], for 2D VIS [68, 89, 220] and for 2D UV experiments [84], showing the great flexibility of the 2D configuration in pump–probe geometry. The first pump pulse interacts with the sample in the electronic ground state, followed by a second collinear pump pulse, phase-stabilized relative to the first one, after the coherence time τ. After a waiting time T the probe pulse, in a non collinear beam arrangement, interacts with the sample. The emitted response is heterodyned by the probe itself, who acts as the local oscillator and measured in a spectrally-resolved manner. There is no need for an additional local oscillator pulse. Fourier transformation along τ yields the intrinsically phased electronic 2D spectrum. Hence, the continuum probe pulse remains unchanged, when compared to the previous transient-absorption experiments, as proposed by Tekavec and coworkers [220]. However, the pump pulse arrangement has to be adapted in the following way:

The visible pump pulses are generated with a NOPA, identical to the transient-absorption measurements. Afterwards, these pulses were compressed and split into phase-stable double pulses with an adjustable time delay τ by a LCD-based femto-

second pulse shaper and characterized via pulse-shaper-assisted collinear frequency-resolved optical gating (cFROG) [39,40] (compare Sec. 2.2.2). The pulse pairs where generated by the LCD, which is placed within the Fourier plane of a pulse shaper in 4f-design[4], by applying the phase mask $M(\omega)$,

$$M(\omega) = \frac{1}{2}[\exp(i[\omega - (1-\gamma)\omega_c]t)\exp(i\Phi_1) + \exp(i\Phi_2)], \tag{5.1}$$

resulting in a pulse centered at $\tau = 0$ with initial phase Φ_2 and a second pulse delayed by time t with initial phase Φ_1 and carrier frequency ω_c [94]. The adjustable factor γ represents the relative change compared to the carrier-envelope phase when the pulse is shifted. A mechanical delay stage combined with a retroreflector, like in a Fabry–Pérot interferometer, changes both the envelope and the carrier phase of a pulse pair when τ is scanned, thus, $\gamma = 1$. With a pulse shaper only the desired phase difference in the envelope can be adjusted ($\gamma = 0$), a so-called rotating frame measurement, or even an intermediate setting between these two cases ($0 < \gamma < 1$) is possible. The smaller the used γ-value is, the fewer data points are required to resolve the signal. This oscillates with the effective frequency $\omega_{\text{signal}} = (\omega - (1-\gamma)\omega_c)$, which contains the 2D signal, because the Nyquist limit is extended by using a (partially) rotating reference system. As an unwanted result of this undersampling, a Fourier transformation of the measured data set does not yield the correct frequency axis because the measured frequency is not ω itself. This can easily be corrected by shifting the frequency back to its original value after data evaluation is performed. This is possible because the value of γ, as well as the laser pulse frequencies, are known. However all measurements in this work were performed without (partially) rotating frame ($\gamma = 1$), thus, did not require any frequency shifting. A comparison of different data sets for different values of γ can for example be found in Ref. [94] and for the same setup and pulse shaper as employed here in Ref. [16].

As a result of the collinear pump pulse pair alignment, there are two inseparable phase matching directions in which the 2D signal is emitted. These are $\vec{k}_S = -\vec{k}_1 + \vec{k}_2 + \vec{k}_3$ and $\vec{k}_S = +\vec{k}_1 - \vec{k}_2 + \vec{k}_3$. Accordingly, the signal phase is obtained as:

$$\Phi_{\text{signal}} = \pm(\Phi_1 - \Phi_2) + \Phi_{\text{Pr}} - \Phi_{\text{Pr}} = \pm(\Phi_1 - \Phi_2). \tag{5.2}$$

Thus, the measured 2D signal depends directly on the phase difference between the two collinear pump pulses, which is directly adjustable by the pulse shaper using the mask in Equation 5.1. In addition to this phase-dependent signal, also a phase-insensitive transient-absorption signal generated by two interactions with either signal field 1 or 2 is contained in the detected signal field because it is emitted in the same direction. This interfering signal cannot be separated spatially since the wavevector $\vec{k}_S$ of the emitted response is oriented in the same direction. Hence, the necessary data for a 2D spectra has to be disentangled by using phase cycling, i.e. combining datasets for the same pulse pair delay τ but with different relative phases between pulse 1 and pulse 2. While many different schemes are proposed

[4]Details about the possibilities and limitations of this design can be found in Ref. [269] (construction) and Ref. [73] (polarization pulse shaping).

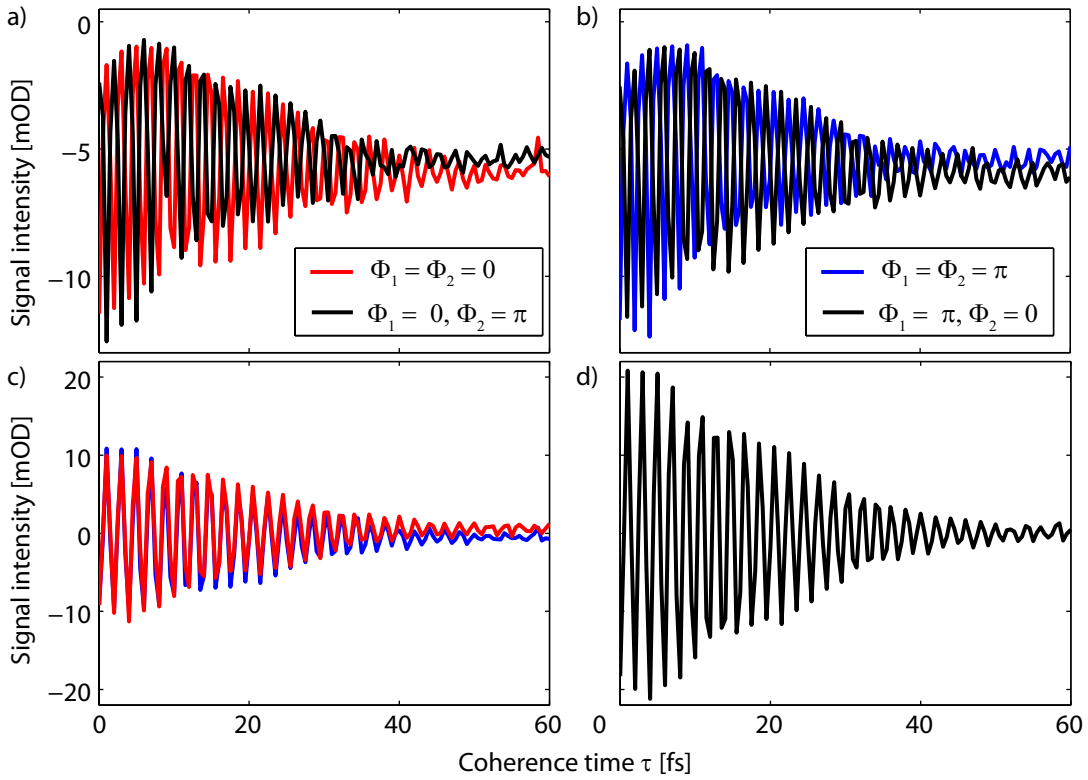

Figure 5.11: Transient cuts at 584 nm recorded for a pulse pair separated by τ for 6,8-dinitro BIPS at $T = 100$ ps. a) Measured data $S_{\Phi_1=\Phi_2=0}$ (red) and $S_{\Phi_1=0,\Phi_2=\pi}$ (black) possessing constant pump–probe and oscillating 2D contributions. b) Measured data $S_{\Phi_1=\Phi_2=\pi}$ (blue) and $S_{\Phi_1=\pi,\Phi_2=0}$ (black) similar to a). c) Two-step phase cycling schemes applied to the data in a) (red) and the data in b) (blue). d) Four-step phase cycling scheme using every dataset in a) and b).

in literature, in this work only the two simplest ones are used to extract all phase dependent contributions [90]. These are a two-times phase cycling scheme, combining just two datasets corresponding to the simplest possible one, and a four-times phase cycling scheme, delivering spectra with strongly reduced noise. Both are explained and visualized in the next paragraph.

Fig. 5.11 shows measured transient data for increasing coherence time τ, up to 60 fs at $\lambda_{\mathrm{Pr}} = 584$ nm and population or waiting time $T = 100$ ps for 6,8-dinitro BIPS in chloroform. The whole measured data set consists of an array with 256 different wavelengths. Figure 5.11a) shows the measured data without any corrections for two separate measurements, containing both the phase dependent (oscillating) and the phase-independent (constant) signal contributions: for $\Phi_1 = \Phi_2 = 0$ (red) and for $\Phi_1 = 0$, $\Phi_2 = \pi$ (black). Since the constant parts for long coherence times are identical within the precision of the experiment, they correspond to the pure transient-absorption contribution. By contrast, the oscillating terms are exactly out of phase. This was achieved by using an effective phase change $|\Delta\Phi| = |\Phi_{1,1} - \Phi_{1,2} + \Phi_{2,1} - \Phi_{2,2}| = \pi$ between the two pulse sequences. Hence,

one signal is a damped sine-shaped signal and the second one a cosine one. Figure 5.11b) shows the measured data for $\Phi_1 = \Phi_2 = \pi$ (black) and $\Phi_1 = \pi$, $\Phi_2 = 0$, again the effective total phase difference is $|\Delta\Phi| = \pi$, resulting in similar oscillating contributions, albeit, the applied offset phases are slightly different. Therefore, both measurements a) and b) possess an identical envelope function, which is confirmed by the experiment. However, it has been shown that large parts of scatter, induced by the first or second pulse interacting with the cuvette and/or the solvent two times, depends strongly on the initial phase, thus, explaining differences in the phase-sensitive signal [94]. Accordingly, the scattering contributions in measurements a) and b) are exactly out of phase. Figure 5.11c) depicts the most simple, two-step, phase-cycling scheme, which is not employed later-on in this work but serves as proof-of-principle that the newly implemented setup works. Here, the two individual measurements in Fig. 5.11a),b) are just subtracted resulting in the identical curves shown in red [a)] and blue [b)], oscillating around zero signal strength. The 2D signal is either

$$S_{\text{2D, two step}} = S_{\Phi_1=\Phi_2=0} - S_{\Phi_1=0,\Phi_2=\pi} \text{ (red), or} \tag{5.3}$$

$$S_{\text{2D, two step}} = S_{\Phi_1=\Phi_2=\pi} - S_{\Phi_1=\pi,\Phi_2=0} \text{ (blue).} \tag{5.4}$$

A much more efficient phase cycling scheme is the four-step scheme, taken from Ref. [84, 94] and used for the following measurements, with

$$S_{\text{2D, four step}} = S_{\Phi_1=\Phi_2=0} - S_{\Phi_1=0,\Phi_2=\pi} + S_{\Phi_1=\Phi_2=\pi} - S_{\Phi_1=\pi,\Phi_2=0}, \tag{5.5}$$

which is depicted in Fig.5.11d) (black). On the one hand, the effective oscillating signal is increased by four times, as compared to the oscillating term in a single measurement ($\pm$5 mOD compared to $\pm$20 mOD), because this four-times summation scheme extracts all measured 2D contributions in all four combined measurements. In addition, phase insensitive pump–probe signals are effectively eliminated, noticeable because the signal oscillates around zero signal strength. On the other hand, scatter is dramatically reduced without increasing the measurement time by an additional recording of correction terms. Hence, the four-step phase-cycling scheme is advantageous to the two-step scheme in the sense that it is comparable in measurement time to a simple averaging of two measurements with a two-step scheme. However, the obtained 2D spectra are additionally cleaned of pump-induced scatter [84, 89, 94, 268]. Compared to 2D measurements in box geometry no additional recording of scattering correction terms is necessary, every recorded spectrum is used for the evaluation.

Afterwards, automatically phased absorptive 2D spectra are generated by Fourier transformation along τ and taking only the real valued parts, resulting in a spectrally resolved pump axis. The probe axis is generated by measuring the spectrally dispersed absorption change induced in the probe, the necessary Fourier transformation is automatically performed by the spectrometer. There is no additional phasing procedure necessary as for example for 2D in the box geometry [13, 75] because of the employed collinear scheme of pulses 1 and 2.

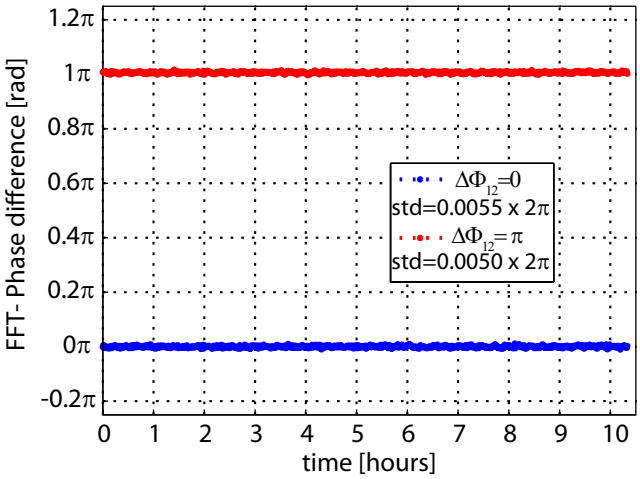

Figure 5.12: Phase-stability measurement over the course of 10 h, generated by alternating a relative phase difference of $\Delta\Phi_{1,2} = 0$ (blue) and $\Delta\Phi_{1,2} = \pi$ (red) between a pulse pair separated by coherence time $\tau = 100$ fs. No long-living drift is noticeable and the standard deviation is below $0.01 \cdot 2\pi$ for each single curve.

The two-layer, 640-pixel mask (SLM-640, CRI) of the broadband shaper allows for independent amplitude and phase shaping resulting in pulses with about 200 nJ of energy. The temporal shaping capability, i.e., the largest possible time delay a generated pulse shape can be shifted, is limited to a temporal window of ≈ 2.2 ps. Therefore, the necessary population time T between the second pulse and the third pulse, the white-light probe, has to be introduced by conventional means. Hence, the same mechanical stage as employed in the transient-absorption experiments is used to delay the two pump pulses, allowing population times of $T < 3.6$ ns. The supercontinuum probe pulses, fixed in time, ranged from 420 THz to 820 THz (corresponding to 390 nm to 720 nm). The pump and probe pulses had parallel polarization relative to each other and were spatially overlapped in a 200 µm flow cell. The measurement of changes in the optical density of the sample introduced by the pump pulses was carried out with 1 kHz acquisition rate by blocking every second pair of pulse-shaper generated double pulses. In this way all spectra are spectrally normalized to the white-light spectrum of the probe pulse as in conventional transient-absorption experiments.

Coherent 2D measurements are very sensitive to the relative phase difference between the first two pump pulses, thus, stringent requirements have to be fulfilled in regard to phase stability. Pulse shapers have emerged as a very precise tool for generating double pulses. Baumert and coworkers, for example, proved that a pulse-shaper generated pulse pair can be created with a known separation adjustable up to zeptoseconds or 10^{-21} s, which easily exceeds the necessary phase stability [270]. In order to assess the phase stability of the new 2D setup a double pulse sequence was generated repeatedly with a pulse separation of $\tau = 100$ fs, centered at 600 nm, and iterating effective phase differences of zero or π. Afterwards, the spectrum was measured and the phase difference determined via Fourier transformation. This mea-

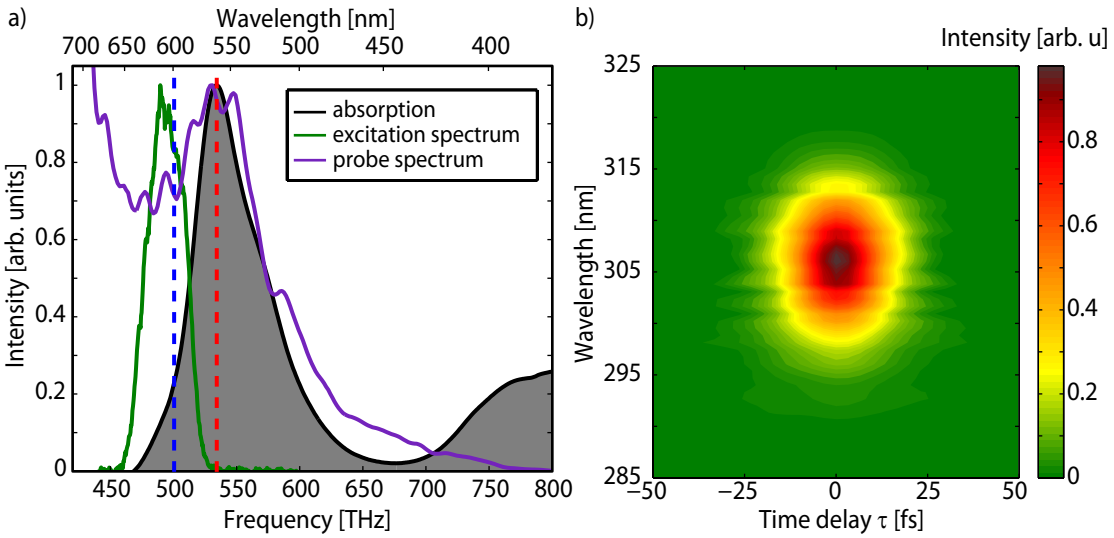

Figure 5.13: (a) Normalized absorption spectrum of 6,8-dinitro BIPS dissolved in chloroform (black/gray), together with experimental spectra of pump (green) and probe (purple) pulses. The absorption maximum of the two ring-open isomers TTC (red) and TTT (blue) are shown as dashed lines [78]. b) Measured SHG-cFROG trace of the pump pulse, after a compression routine. The FWHM is below 20 fs, and no subpulse structure is evident, both indicating a bandwidth-limited pulse.

surement was recorded over the course of 10 hours in order to determine short-term and long-term precision. The results are shown in Fig. 5.12. Both the zero phase difference (blue) and the relative difference of pi (red) between the two pulses correspond to straight lines parallel to the x-axis, thus, no long-term drift occurs. In addition the standard deviation of each measurement is below $2\pi/100$, which is comparable to recorded precisions for coherent 2D setups in box geometry [83, 85]. Moreover, the relative phase difference between zero and π represents the case where the highest changes in transmission (maximal to minimal) occur. Therefore, it serves as a test of the necessary waiting time between re-orienting the liquid crystals in the LCD and measuring the spectrum. A waiting time of 500 ms is sufficient for the applied sequences. Additionally, both pulses of the pulse pair have an unknown phase offset because the laser system is not carrier-envelope-phase stabilized. This additional offset is unimportant for the measurement procedure because it affects both pulses equally and is, thus, eliminated via the phase-cycling scheme. On the one hand, no phasing of the data is necessary when compared to the box geometry but, on the other hand, the imaginary part of the 2D spectrum is not obtainable without further approximations [89].

5.5.2 Experimental Parameters

Figure 5.13a) illustrates the absorption spectrum of the open form of 6,8-dinitro BIPS (black/gray), which comprises a broad absorption band in the visible spectral range ($\nu_{\max} = 540$ THz, $\lambda_{\max} = 560$ nm) resulting from a molecular

mixture as discussed in Sec. 5.4.3. Two isomers exist, predominantly in TTC configuration and (about one order of magnitude less) in TTT configuration, absorbing at 540 THz (560 nm, TTC, red dashed line) and 490 THz (600 nm, TTT, blue dashed line), respectively [20, 27]. The center wavelength of the laser was adjusted to 605 nm/500 THz, and the pulse compressed to a duration of 20 fs (green), representing an intermediate case of the previously used excitations at 560 nm and 620 nm. Therefore, roughly the same amount of both isomers and not only one dominantly is excited. The probe continuum (violet) covers the complete visible spectral range. As discussed, both isomers undergo a ring-closure reaction after excitation, with quantum efficiencies of 40% (TTC) and 35% (TTT) and the excitation-frequency-dependent fluorescence clearly shifts from around 475 THz to 500 THz with increasing excitation frequency, as shown in Fig. 5.4b) in the previous section. Thus, each isomer can e.g. be identified by the corresponding stimulated emission signal in the 2D spectra [78].

Figure 5.13b) visualizes the SHG-cFROG trace after compression of the pulse. The measured trace possesses nearly no asymmetries and is of oval shape, indicating the success of the compression [35], resulting in a near bandwidth limited pulse with a time-bandwidth product of 0.44 and a duration below 20 fs. The pulse shaper is first used to compress the pulse, the offset phase is permanently applied, and afterwards the pulse pair is generated and shifted using the phase mask in Equation 5.1, introduced in the previous section.

For all measurements the coherence time τ was scanned over 60 fs in steps of 0.5 fs. Since no oscillating contributions are resolved after 60 fs, as seen in Fig. 5.11d), this range is sufficient. In order to obtain a smoother 2D spectrum the time axis was additionally lengthened by zero padding. This means, the signal was assumed to be perfectly zero after 60 fs up to a coherence time of 300 fs. Thus, the frequency resolution $\Delta\omega$ was artificially enhanced by a factor of four by means of the applied Fourier transformation. The four-step phase cycling measurement was repeated three times resulting in a total measurement time of three hours per waiting time T, while each data point $\mathrm{S}(T, \tau)$ was averaged over 1000 ΔAbs single shot values. Hence, this three-fold averaging is reducing long-term and short-term-noise in addition to enabling a scattering correction.

5.5.3 Possible Isomerization Schemes of 6,8-dinitro BIPS

In this section the reaction pathways of different isomerization schemes are introduced and discussed. Furthermore, it is elucidated how a possible cis-trans isomerization in 6,8-dinitro BIPS can be tracked over time via a series of 2D spectra. Possible reaction schemes and corresponding schematic 2D spectra are depicted in Figure 5.14. Expected signals, all identified in the pump–probe experiments in Sec. 5.4, are numbered from 1 to 7 as indicated in the 2D spectrum in the upper left, going from the highest-energetic one (ESA TTC) down to the lowest-lying one (SE TTT). After excitation to the S_1 state, both isomers (TTC and TTT) undergo a partial ring-closure reaction to spiropyran. The diagonal signals are due to ground-state

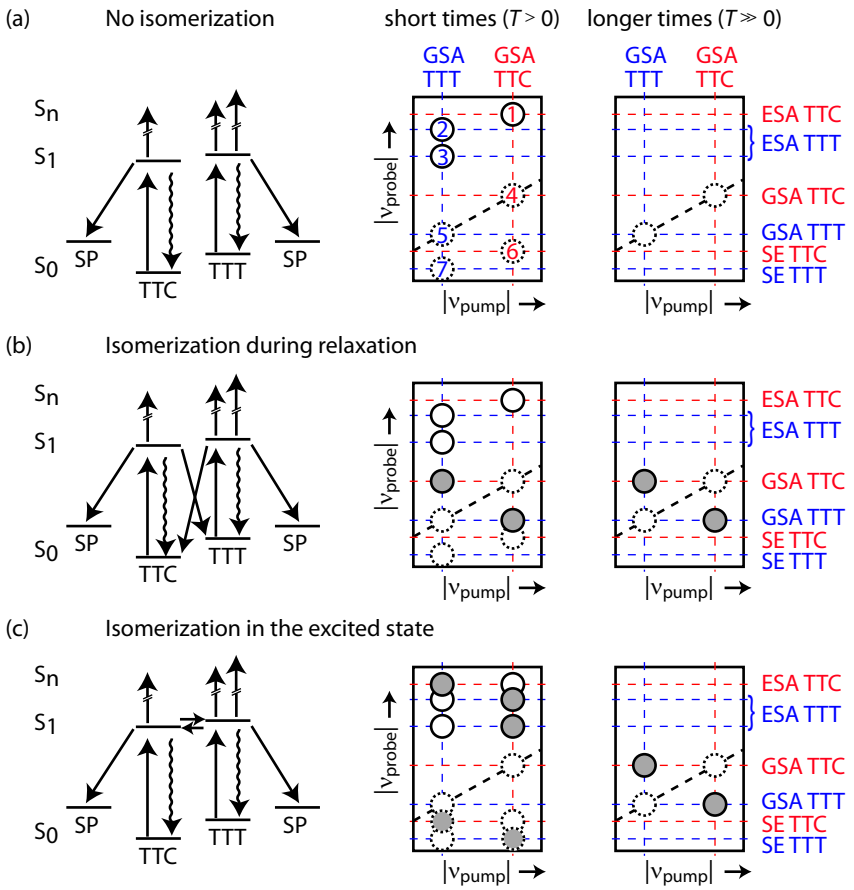

Figure 5.14: Possible isomerization schemes of 6,8-dinitro BIPS and schematic 2D spectra (TTC: red, dashed; TTT: blue, dashed). Solid circles illustrate positive, dashed negative signals. Isomerization peaks are filled in gray. a) No isomerization: No cross peaks emerge in the 2D spectrum neither at short (left) nor at long waiting times (right). b) Isomerization during relaxation: Peaks appear at the GSA for $T > 0$ and remain. c) Isomerization in the excited state: Peaks are at first in the region of ESA and SE for $T > 0$ (short-living) and will appear later on in the region of the GSA for $T \gg 0$ [78].

absorption (GSA). As discussed, the GSA of TTT (Signal 5) is slightly red-shifted compared to that of TTC (Signal 4), because TTC is more stable than TTT. The same red-shift is seen in the off-diagonal contributions arising from stimulated emission for each individual isomer (Signal 6 for TTC, 7 for TTT). Each SE signal has to appear vertically displaced from the respective GSA signal, identified in the steady-state absorption spectrum in Fig. 5.4a), while the SE frequency is identified in the fluorescence spectrum in Fig. 5.4b). Excited-state absorption appears for both isomers and has to be shifted vertically upwards with respect to GSA in the 2D spectra because the ESA is blue-shifted relative to the GSA. TTT exhibits two transitions instead of one for TTC to higher lying states and the TTT signals are again red-shifted with respect to TTC (Signal 1 for TTC, Signals 2 and 3 for TTT).

Now three scenarios of possible chemical reaction pathways, introduced in Ref. [27] and used there for the analysis of pump–probe data of 6,8-dinitro BIPS, are discussed:

- No isomerization between TTC and TTT [Fig 5.14a)],
- isomerization during relaxation to the ground state via a conical intersection connecting the S_1 and S_0 merocyanine potential energy surfaces [Fig 5.14b)],
- and isomerization in the excited state by crossing an isomerization barrier in S_1 connecting parts of the potential energy surfaces belonging to TTT and TTC [Fig 5.14c)].

Schematics of the absorptive 2D spectra are shown in the right column of Fig 5.14 for short ($T > 0$) and long waiting times, compared to the TTT lifetime $\tau_{\mathrm{TTT}} \approx 800$ ps ($T \gg 0$). If no isomerization occurs, the two chemical systems TTC and TTT are separated and, thus, any 2D peak can only arise at a crossing between lines of the same color in Fig 5.14 (either red/red or blue/blue). If, on the other hand, the two species interconvert, 2D peaks may also arise at red/blue crossings since they originate from one isomer and end up in the other one.

More specifically, if no isomerization occurs, only the cross peaks belonging to ESA and SE will emerge for each isomer, and for $T \gg 0$, only the photobleach, indicating permanently missing merocyanine and spiropyran product formation, at the GSA frequencies will remain [Fig 5.14a)]. If ultrafast isomerization takes place directly to the ground state, additional positive cross peaks (indicated by filled circles) will appear in the GSA region of both isomers shortly after excitation and will remain for $T \gg 0$ [Fig 5.14b)] because the amount of TTC and TTT after excitation of the other isomer would be higher, resulting in increased off-diagonal absorption. In the case of isomerization in the excited state, new cross peaks in the SE region (negative) and in the ESA region (positive) of the respective other isomer will emerge for $T > 0$ [Fig 5.14c)] because after the initial excitation of TTT (vertical blue line) the relaxation would happen alongside the photochemical channels of TTC (horizontal red lines) and vice versa. After relaxation, these give rise to positive cross peaks in the GSA region for $T \gg 0$. The idea is now to assess, which of the three scenarios is correct by comparing measured 2D spectra with the schematic illustrations in Fig 5.14. In this comparison, one has to keep in mind that experimental 2D spectra may exhibit broad and overlapping contributions complicating the identification of isomerization peaks. The measured 2D spectra also reflect the shape of the excitation laser spectra (Figure 5.14), which can lead to an apparent shift in peak positions as shown in Sec. 4.6, where the two separate absorption peaks of $(\mathrm{ZnTPP})_2$ seemingly merge, forming one broad absorption feature. However, the probe axis is not influenced. Thus, every contribution is located at the same frequency as in transient-absorption measurements [78].

5.5.4 2D Measurements Unveiling the Dynamics of Both Isomers

The real parts of the experimental electronic 2D spectra, called absorptive 2D spectra, of 6,8-dinitro BIPS dissolved in chloroform are shown in Fig. 5.15a)-f) for waiting times of $T = 3, 30, 100, 300, 1000$, and 3000 ps, respectively. The diagonal is indicated by the black dashed line. Contour lines are drawn in equally spaced intervals with 60 levels, where solid (dashed) lines indicate positive (negative) values. All spectra were normalized relative to the minimum of the 3 ps spectrum corresponding to an absorption change of -1. Positive values (reddish colors) describe increased absorption, negative values (bluish colors) correspond to a decreased absorption change of the probe pulse, analogous to transient absorption. Vertical grid lines indicate the maxima of the GSA spectra of TTC (red) and TTT (blue) additionally multiplied by the excitation spectrum. Horizontal grid lines correspond to unchanged frequencies of GSA, ESA, and SE of both isomers, as labeled. The frequencies have been assigned by global fitting routines of transient-absorption data obtained in Sec. 5.4. As can be seen in Fig 5.13 and the upper part of Fig 5.15a), the pump pulse spectrum only partly overlaps with the absorption spectrum. Note that this shift towards red frequencies was done in order to excite both isomers substantially despite their different concentrations in thermodynamic equilibrium, assessing the possible isomerization for both isomers in a single measurement. As a consequence, the major contributions of the TTC isomer are not observed at 540 THz, but at lower pump frequencies of about 515 THz, as marked by the vertical red line indicating the signal maximum of the GSA of TTC. Nevertheless, this contribution is clearly identified via the horizontal red line indicating TTC GSA at 540 THz [see position of Signal 4 in Fig 5.15f)]. This example visualizes the effect of the pump spectrum on the measured 2D spectra [78].

After 3 ps the 2D spectrum at lower probe frequencies is dominated by the SE of TTC (Signal 6). At higher probe frequencies, one observes ESA located at the frequency corresponding to TTC (Signal 1). ESA is also observed for probe frequencies down to about 525 THz, but only at low pump frequencies (near the GSA of TTT), as expected due to the existence of the two ESA signals of TTT (Signals 2 and 3). The low-energy ESA band (Signal 3) becomes particularly evident for $T = 30$ ps and 300 ps due to the curvature of the contour lines, indicating two different but overlapping bands and not a single broad contribution. In the 2D spectrum for $T = 3$ ps, oscillations along the probe axis are visible in the ESA (at lower pump frequencies) that are related to Raman-active modes of the solvent and the chirp of the continuum probe [26, 59, 271], since T slightly varies for different probe frequencies because of this chirp. However, signals due to Raman modes are not observed anymore after a few picoseconds, which is significantly shorter than the lifetimes of excited 6,8-dinitro BIPS. Second- and third-order dispersion of the probe continuum were determined as 300 fs^2 and 130 fs^3, respectively, and do not play a major role for long waiting times again due to the larger time constants of excited merocyanine [272]. In order to access very short population times in a 2D experiment with a

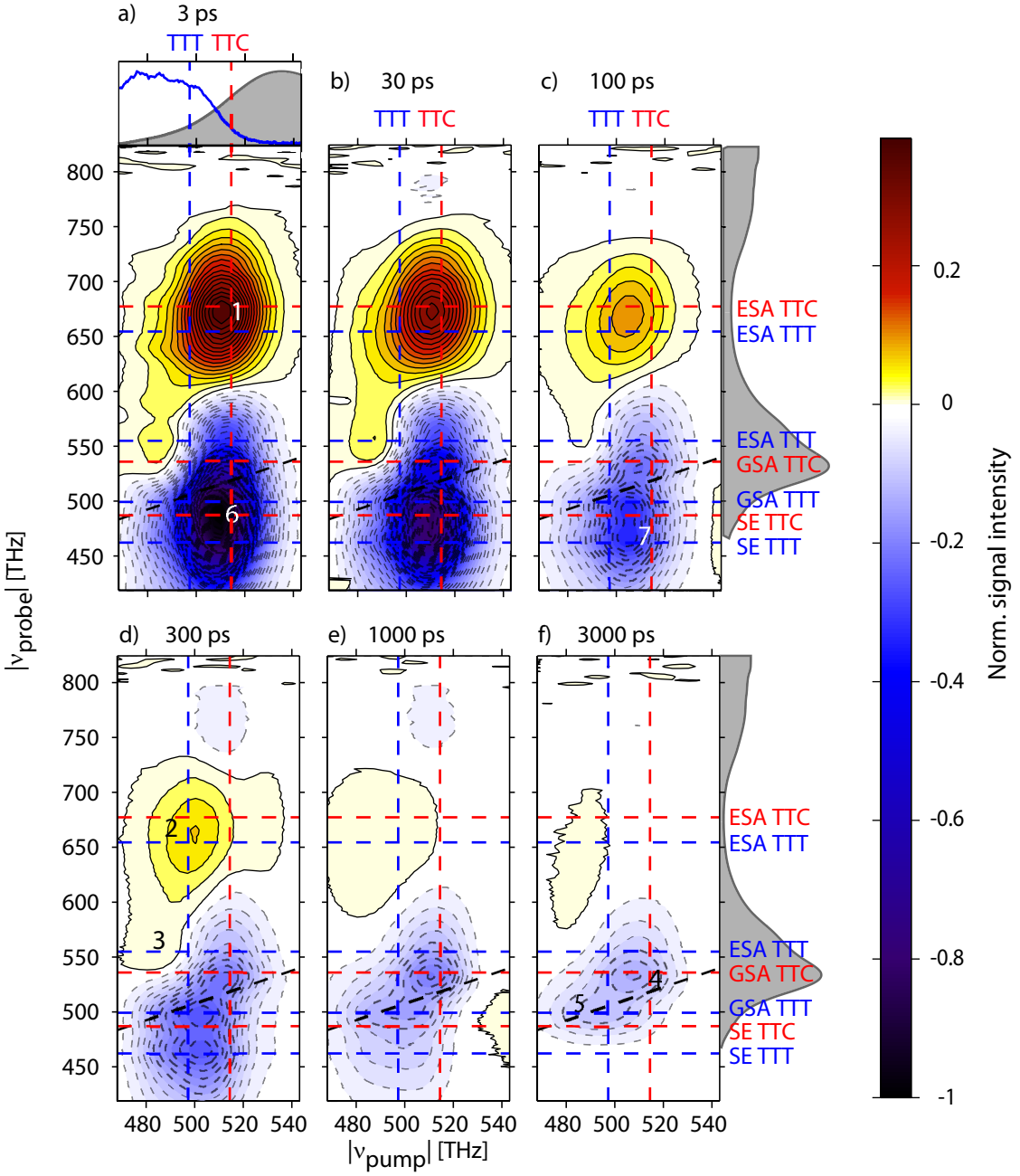

Figure 5.15: Absorptive 2D electronic spectra of 6,8-dinitro BIPS for waiting times of a) 3 ps, b) 30 ps, c) 100 ps, d) 300 ps, e) 1000 ps, and f) 3000 ps. The frequencies of GSA, SE, and ESA are indicated by red dashed lines for TTC and by blue dashed lines for TTT. All contributions are numbered where they are unambiguously identified. The pump pulse spectrum (blue) is shown on top of spectrum a) with the merocyanine absorption spectrum (black/gray), which is additionally shown on the right side of spectra c) and f) [78].

continuum probe, one has to record multiple 2D spectra around time zero and shift each frequency, similar to a chirp correction procedure often used in the analysis of pump–probe data, as shown by Ogilvie and coworkers [221]. Using 2D spectroscopy

in box geometry with degenerate pulses this challenge can also be circumvented, as shown in Sec. 4.6, revealing energy transfer within 100 fs in a porphyrin dimer.

One approach to investigate the role of the isomers and their photoinduced behavior with 2D spectroscopy could be to decompose the data into decay-associated 2D spectra [67–69]. This approach resembles the global fitting methods summarized for transient-absorption data in Sec. 3.2.2. However, here a series of 2D electronic spectra is combined with the information on the photodynamics obtained in transient-absorption studies in the previous section, where strongly differing excited-state lifetimes of 95 ps for TTC and 800 ps for TTT (Sec. 5.4.3) were determined. Hence, the ESA shifts to lower pump frequencies during the first 300 ps [Fig. 5.15a)-d)] and a weak ESA contribution of TTT is remaining after 3000 ps in Fig. 5.15f). For $T = 3000$ ps, the signals 4 and 5 originating from GSA of TTC and TTT, respectively, are observed. They persist permanently due to the absence of merocyanine and the formation of ring-closed spiropyran. SE of TTC (Signal 6) initially disappears, leading to the dominant contribution of TTT in the region of SE after 300 ps (Signal 7). A separation of TTT GSA (Signal 5) and TTC SE (Signal 6), both peaking around 500 THz (600 nm) (compare the linear absorption and fluorescence spectra in Figure 1), is possible when the temporal behavior is taken into account. Up to $T = 100$ ps, TTC behavior dominates, while TTT contributions remain nearly unchanged with a small decay of only 10%. This allows for the assignment of the intense negative features at 500 THz to S_1 emission of TTC in panels a)-b). For larger T the behavior of the TTT GSA is visible. This distinction is also possible considering the TTC ground-state bleach (Signal 4), which remains nearly unchanged in panels c)-f). Therefore, it is shown that photochemical reactions of TTC are over. Other evidence for the different dynamics of both isomers is the slight shift of the strong negative feature consisting of TTC SE, TTT GSA, and TTT SE: for small values of T, it is mainly due to TTC SE (Signal 6), whereas for large T, it is due to the bleach of TTT (Signal 5). This is directly evidenced by a shift of the center frequency along the pump axis from 515 THz to 500 THz, i.e. from the energetically higher TTC to the slightly lower-energetic TTT. In the 2D spectrum for $T = 300$ ps, one can even clearly separate the three negative, partially overlapping features 4, 5, and 7, which belong to the bleach of TTC and TTT, and the SE of TTT, respectively. A negative contribution for probe frequencies above 720 THz, best seen for $T = 300$ ps and 1000 ps, can be assigned to the bleach of the second merocyanine absorption band extending from 670 THZ (450 nm) into the UV [as also identified in the black DADS in Fig. 5.6 and seen on the right of Fig 5.15f)] [78].

5.5.5 Discussion of the Isomerization Schemes

After having discussed all features of the 2D spectra, the isomerization schemes in Fig 5.14 are taken into account for interpretation of the data. Basically, all schemes comprise a set of 7 peaks, corresponding to ESA, GSA and SE unique for each isomer and a set of off-diagonal peaks centered at crossings of TTC and TTT frequencies. The latter are defined by their occurrence at an intersection of a blue and a red line.

If the isomerization between both isomers happens in the excited state [Fig. 5.14c)] five additional isomerization peaks for $T \leq 100$ ps are expected in the corresponding 2D spectrum of Fig. 5.15. The negative contributions in the expected 2D spectra for $T = 3$ ps and 30 ps are dominated by the strong SE of TTC, but for $T = 100$ ps three contributions belonging to SE (Signal 7) and GSA (Signal 5) of TTT and GSA of TTC (Signal 4) are identified. These signals also dominate the $T = 300$ ps spectrum, no additional features emerge. Further information is provided by the positive ESA: the only detectable features are the expected frequency shift with increasing T (since TTC decays faster than TTT) and the overall decay due to relaxation to the ground state. The absence in the experimental spectra of clear isomerization peaks or strong changes in the curvature as marked in Fig. 5.14c) by the filled gray circles rules out a reaction pathway with high quantum yield between the isomers in the excited state.

The very small yield or the nonexistence of isomerization can be explained by the presence of a barrier between the minima of TTT and TTC excited-state potentials. Barriers in the excited state are well known for merocyanines as shown by theoretical calculations for merocyanines without ring-closure capability [273]. Additionally, a spiropyran–merocyanine model neglecting the indole and any substituents was used in order to explore the ring closure via conical intersections theoretically. Barriers, connecting different isomers, and a fast pathway to a ring-closed form were found [252]. The barrier heights were estimated to be around 0.5 eV. While this study assumed S_2 excitation, which would enable the passing of the barrier with the help of excess energy, direct excitation into S_1 basically reduces the available energy, possibly hindering isomerization. The effect of high-energy excitation will be addressed in Sec. 5.6. These theoretical findings can be transferred to the related but not identical 6,8-dinitro BIPS. They explain the negligible TTC/TTT isomerization in the excited state because the pump pulses, centered at 500 THz, possess only an energetic window of (2.05 ± 0.15) eV, which is not sufficient to make the crossing of such a high barrier probable.

Further insight into the absence of isomerization in this system is provided by a comparison of the relaxation in 6,8-dinitro BIPS with TA measurements on 6-nitro BIPS [254]. In the latter continuous UV illumination leads to the formation of 2 merocyanine isomers in solution, namely TTC and TTT absorbing in the visible spectral range. However, the photoinduced reactions are very different for these isomers. While photoexcitation of TTC is followed by changes in the first stereo configuration of the methine bridge from trans to cis, the TTT isomer is additionally capable of TTT-TTC isomerization, if enough excess energy is available, i.e., by exciting it on the blue edge of its absorption band. As a consequence different isomerization processes are observed as a function of the excitation wavelength. Yet, no ring closure is detectable for this system. In 6,8-dinitro BIPS the second nitro group affects the potential energy surfaces in such a way that the merocyanine isomers are thermally more stable than spiropyran and photochemical ring closure becomes accessible, which is very rare for merocyanines. Variation of the excitation wavelength only affects the relative amount of excited isomers, but no effect of the excess energy on the photoisomerization yield is visible (see also the shape of the DADS in Fig. 5.6

and Fig. 5.8 in Sec. 5.4), since the photochemistry can change quite radically due to the substituents. It is plausible to ascribe the negligible isomerization yield in the excited state to the existence of energetically preferred ring-closure pathways and to even higher barriers between the isomers.

Having excluded isomerization through the excited state, now isomerization during relaxation to the merocyanine ground state via conical intersections connecting TTC and TTT in S_1 and S_0 is considered [see Fig. 5.14b)]. This would result in positive contributions in off-diagonal areas of the 2D spectra where GSA lines of both isomers intersect. Straightforward insight is gained for the waiting time $T = 3000$ ps: no isomerization peaks [located at the gray filled circles in Fig. 5.14b)] or strong positive disturbances in the contour lines are visible in the vicinity of the experimental GSA of both molecules (Signals 4 and 5). Hence, isomerization between TTC and TTT during relaxation can also be ruled out as a relevant reaction pathway. This is again in accordance with Ref. [273], which compares the excited states of merocyanines, cyanines, and polyenes. While polyenes possess a biradicaloid structure, an even number of π-orbitals in the excited state, and conical intersections between S_1 and S_0, the excited states of cyanines have charge-transfer character and an odd number of π-orbitals. Merocyanine shares the latter properties and the calculations for the merocyanine structure in Ref. [273] show a very high barrier hindering photoisomerization via crossing of a conical intersection, if such a conical intersection exists at all. Thus, the minor contribution or non-existence of isomerization to the photoreaction pathways for 6,8-dinitro BIPS by passing a conical intersection in S_1 seems plausible [78].

Hence, the 2D spectroscopy data is in accordance with the simplest model [Fig. 5.14a)], which does not involve any photoisomerization between the two merocyanine isomers. For $T > 0$ three positive (Signals 1-3) and four negative peaks (Signals 4-7) are expected, which are all evident in our data as discussed above. For $T \gg 0$, when the ground-state relaxation is over, only the permanent bleach should remain in our data. Since this is the case (with some TTT still in the excited state in the $T = 3000$ ps spectrum), the reaction scheme in Fig. 5.14a) is the most probable one. No isomerization cross-peaks or even distinct deformations are observed, substantiating that indeed isomerization does not play a major role in the photochemistry of 6,8-dinitro BIPS. Isomerization with very low quantum yields (compare the upper boundary of 2% determined indirectly in Ref. [27]), however, would cause a very slight contour-line deformation, which cannot be ruled out with absolute certainty.

Summarizing the results of the presented 2D study, the reaction scheme of 6,8-dinitro BIPS in Fig. 5.16 is obtained. Besides confirming the scheme suggested by the transient-absorption results [Fig. 5.10c)] the excited-state behavior is also explained. After photoexcitation of both isomers into S_1, significant cis/trans isomerization is excluded between TTC and TTT excited states, as well as via a conical intersection (red-crossed black lines). As a result, only the shown reaction pathways take place. Both isomers partially undergo a ring closure to the identical spiropyran form with yields of 35% to 40%, possibly by passing of a conical intersection, while the

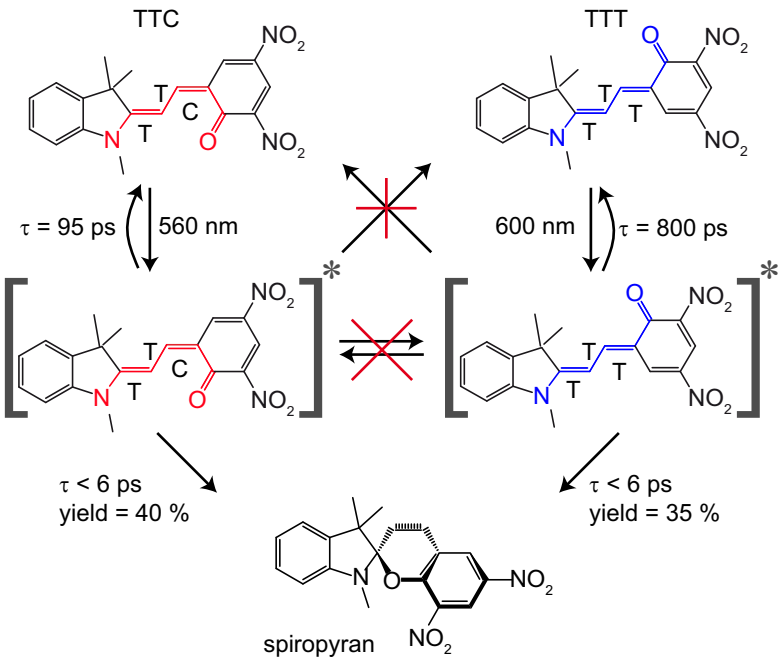

Figure 5.16: Photochemical reaction scheme of 6,8-dinitro BIPS consisting of two merocyanine isomers (TTC and TTT) in the ground state (top row), their excited states (middle row), and the spiropyran product (bottom). As evidenced by 2D measurements isomerization pathways can be excluded as major channels (red crosses). The remaining reactions (black arrows) are relaxations to the corresponding ground state via stimulated emission or fluorescence with 95 ps/800 ps (TTC/TTT) and ultrafast ring closure to spiropyran [78].

remaining part of the excited molecules return to their ground state by fluorescence. As a result, the photochemical fate of the excited merocyanine is determined in the first picoseconds, with the alternatives being either ring closure or fluorescence back to the corresponding ground state. In addition, the reaction schemes of TTC and TTT are not connected at an intermediate state but only possess the same product.

Thus, this experiment exemplifies that electronic 2D spectroscopy is able to assess the photochemistry within a molecular mixture and separate photochemical behavior of two molecular species in a single measurement.

5.6 Exploring Multi-Step Reaction Pathways

The previous two sections explained the photochemical behavior of 6,8-dinitro BIPS in solution after direct excitation into S_1. Both experiments, transient absorption and coherent electronic 2D spectroscopy, showed congruently that basically two dominant reaction pathways exist. However, these experiments could not completely elucidate the relaxation details and several questions remain open.

One reaction mechanism, affecting $\approx 1/3$ of the excited merocyanine molecules of both isomers, is an ultrafast electrocyclic ring closure resulting in spiropyran. How-

ever, it is not known if spiropyran is formed directly in the ground state, if it is vibrationally hot, or if triplet states are involved in the reaction. While these questions could be answered in principle by using a novel transient-absorption approach with a continuum probe in the UV [34], also envisioned for 2D measurements in the UV [274], a different solution is presented here.

The second reaction pathway, occurring for the remaining $\approx 2/3$ of the excited merocyanine molecules, is fluorescence from S_1 into S_0 on a slow picosecond time-scale (TTC: 95 ps, TTT: 800 ps). Even though the 2D experiments have directly unveiled that isomerization does not occur between the two present merocyanine isomers, unanswered questions remain: Why does no isomerization takes place? Could additional excitation energy change the photochemical behavior? Is isomerization in principle prohibited, e.g., because of steric hindrance? Or is the energetic barrier in the excited state, either separating TTT/TTC potential energy surfaces or a conical intersection from the S_1 potential well, just too high?

All these remaining questions for both reaction pathways cannot be answered by using the previous methods, because an additional light-matter interaction is necessary. In the following pump–repump–probe experiments are introduced. These are basically an extension of pump–probe spectroscopy (Sec. 3.2). However, a second pulse, in the temporal ordering between pump and probe, initiates additional photoreactions. This is explained in more detail in Sec. 5.6.1. The first set of questions is addressed by immediate re-excitation of photochemically generated spiropyran by a UV pulse on a picosecond time-scale. This experiment visualizes that the electrocyclic mechanism is really a concerted reaction in the direction MC-SP-MC. By contrast, the direction SP-MC-SP requires an additional picosecond relaxation time (Sec. 5.6.2). In a second experiment, the questions dealing with isomerization are discussed. Hot merocyanine in S_1 is resonantly excited into higher-lying excited states, trying to generate a measurable isomerization or an increased ring-closure yield. However, the formation of a radical cation is observed. Yet, the ionized merocyanine isomer can only be inferred (Sec. 5.6.3).

5.6.1 Pump–Repump–Probe Spectroscopy: Implementation and Data Analysis

For all three-color pump–repump–probe experiments the transient-absorption setup described in Sec. 3.2.3 is used as the experimental backbone, providing all three required pulses. However, in contrast to regular pump–probe experiments, both pump lines were used simultaneously: One delivering the pump pulses (P), the other one the repump pulses (R), which either dump [50,275–278] or re-excite [17,203,279] the intermediate generated by the pump puls. The used wavelengths depend on the specific measurement, arbitrarily selectable from the light sources within the laboratory: Two different NOPAs, the laser fundamental (800 nm) or higher-order harmonics of the fundamental (SHG: 400 nm, THG: 267 nm) are available. The supercontinuum probe (Pr), covering the visible spectral range, recorded by a shot-to-shot detection

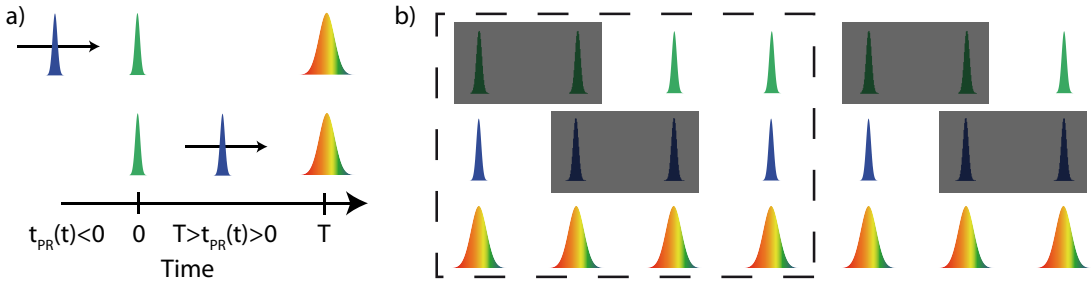

Figure 5.17: a) Pulse ordering in a pump–repump–probe scheme. While the pump (green, 0) and the probe (spectrum, T) remain fixed, the repump is scanned (blue, t_{PR} from negative (top) to positive (bottom) times. b) Pump–repump–probe scheme with two choppers operating at a quarter of the laser frequency. Every chopper blocks, phase-shifted, two consecutive pulses resulting in four different probe signals. Black boxes symbolize blocked pulses and the dashed box a complete cycle of possible pulse combinations.

scheme is identical compared to previous experiments. Thus, a wide array of photoprocesses can be initiated (P, R) and detected (Pr) by employing various pulse combinations.

For pump–repump–probe measurements, the transient signal depends on the ordering and relative delay of all three participating pulses. In this work the following convention is used. The pump pulse is always fixed at time zero. The probe pulse arrives after a certain, but again always fixed, positive waiting time T. In all experiments the waiting time T is larger than $T > 1000$ ps. Thus, only permanent photoproducts or highly stable intermediates will be detected. The repump pulse is scanned by t_{PR} relative to the pump pulse as visualized in Fig. 5.17a) with a green pump, a blue repump and a continuum probe pulse. The black arrow within the blue pulse indicates that this pulse is scanned over the course of the experiment in time. If $t_{\mathrm{PR}} < 0$ then the repump pulse pre-excites the sample before pump interaction (top panel). Accordingly, $t_{\mathrm{PR}} = 0$ corresponds to simultaneous excitation and $t_{\mathrm{PR}} > 0$ is the most interesting case with the ordering pump, repump, probe pulse (bottom panel). If $t_{\mathrm{PR}} > T$ is valid the repump arrives after the probe pulse. Hence, the measurement is similar to a pump–probe experiment, because the changes induced by the repump are not detected by the probe pulse.

Both excitation pulses are separately chopped at 250 Hz (a quarter of the laser's repetition rate) in contrast to half the repetition rate in a pump–probe measurement. This is accomplished by using two synchronized choppers wheels, which are frequency-locked to the laser repetition rate, in addition to being phase-stable relative to each other. Hence, by using 250 Hz, two subsequent pulses are either blocked or pass, contrary to the 500 Hz clock rate, where every second consecutive pulse is blocked. In addition to the reduced frequency, a relative phase shift of $\pi/2$, corresponding to an one-pulse difference, is introduced between the two choppers wheels. Therefore, recording of four different probe intensities is enabled, as visualized in

Fig. 5.17b). The respective probe intensity values

1. I_{PRPr}, induced by pump and repump (5.6)
2. I_{PPr}, induced by pump only (5.7)
3. I_{RPr}, induced by repump only, and (5.8)
4. I_{Pr}, as the probe intensity (5.9)

are subsequently used to calculate three different optical absorption changes, induced by either I_{PPr}, or I_{RPr}, or I_{PRPr} compared to the probe only case I_{Pr}, resulting in:

$$\Delta\mathrm{Abs}_{\mathrm{PPr}} = -\lg \frac{I_{\mathrm{PPr}}}{I_{\mathrm{Pr}}}, \tag{5.10}$$

$$\Delta\mathrm{Abs}_{\mathrm{RPr}} = -\lg \frac{I_{\mathrm{RPr}}}{I_{\mathrm{Pr}}}, \tag{5.11}$$

$$\Delta\mathrm{Abs}_{\mathrm{PRPr}} = -\lg \frac{I_{\mathrm{PRPr}}}{I_{\mathrm{Pr}}}. \tag{5.12}$$

Finally, the additional absorption change $\Delta\mathrm{Abs}_{\mathrm{diff}}$, induced by the combination of pump and repump, compared to either pump, or repump only excitation, $\Delta\mathrm{Abs}_{\mathrm{diff}}$ is obtained. Therefore, subtracting both two-color measurements pump–probe ($\Delta\mathrm{Abs}_{\mathrm{PPr}}$) and repump–probe ($\Delta\mathrm{Abs}_{\mathrm{RPr}}$) from the complete three-color pump–repump–probe signal $\Delta\mathrm{Abs}_{\mathrm{PRPr}}$, results in

$$\Delta\mathrm{Abs}_{\mathrm{diff}} = \Delta\mathrm{Abs}_{\mathrm{PRPr}} - \Delta\mathrm{Abs}_{\mathrm{PPr}} - \Delta\mathrm{Abs}_{\mathrm{RPr}}. \tag{5.13}$$

This signal $\Delta\mathrm{Abs}_{\mathrm{diff}}$ corresponds to additional photochemical contributions only obtained by the interaction of both pump and repump pulse with the sample and cannot be found by a two-color transient-absorption measurement. An example is direct excitation into S_1 by the pump pulse, followed directly by the repump pulse, which excites resonantly into an excited-state absorption. Afterwards, a new photoproduct is measured, which is caused by the presence of excess energy or the fact that the system is in an electronically higher-excited state, where different reaction mechanisms are possible. Therefore, this mechanism could also be used to cross energetic barriers within S_1, proposed to exist for merocyanines in the previous section.

It has been previously reported that the highest correlation between two laser shots is obtained for consecutive pulses. Hence, induced absorption changes possess the highest signal-to-noise ratio when obtained by shot-to-shot detection, followed by a direct calculation of ΔAbs for only two pulses [280]. This was verified by calculations and measurements from S. Keiber within her master thesis for the laser systems used in this thesis [281]. For the calculation of $\Delta\mathrm{Abs}_{\mathrm{diff}}$, however, four consecutive laser pulses have to be taken into account, resulting in a higher noise level. Even the two-color signals have slightly more noise when compared to the experiments in Sec. 5.4, because of the reduced grade of correlation. However, the 250 Hz acquisition rate is still preferable in comparison to no shot-to-shot detection at all, when

compared to the usage of a separate reference beam and an averaging mechanism, which detects the induced changes over many pulses. Combining shot-to-shot detection with an additional reference beam results in the best possible signal quality in pump–repump–probe experiments, however two independent spectrometers are needed [282]. The signal quality is very important in this kind of experiment because the change of an optical density change is measured. Thus, the signal strength is more than one order of magnitude lower as in common pump–probe experiments. This results from the necessity to work in a linear excitation regime. Hence, only a small percentage of molecules in solution is excited and of them again only a small percentage is repumped, resulting in a weak signal strength.

5.6.2 Resolution of Two Ultrafast Subsequent Electrocyclic Reactions

The following section traces the photochemistry of the product generated after photoexcitation of either merocyanine or spiropyran. As shown previously, merocyanine performs an electrocyclic ring-closure reaction after photoexcitation, forming spiropyran (Sec. 5.4.3, Ref. [20,217]). For the BIPS family it is well known that the other direction is also possible [206, 255]. In BIPS itself this pathway was identified and analyzed in Ref. [20,58,71]. In order to demonstrate that 6,8-dinitro BIPS possesses dominant singlet reaction pathways, both merocyanine and spiropyran will be exposed to two subsequent excitation pulses in order to induce a second electrocyclic reaction on a picosecond time-scale. Thus, the reaction product generated from the first pulse is used as the reactant for a second excitation and has, in regard to thermal reaction dynamics, no time to relax. The following results have already been published in Ref. [20].

Experimental Parameters

To resolve the full photocycle (closing–opening–closing and vice versa) of 6,8-dinitro BIPS, the thermally stable merocyanine is bleached with an array of high-powered green and orange LEDs. This illumination results in a high spiropyran concentration, as proven by the optical transparency in the visible spectral range shown in the absorption spectra in Fig. 5.4 (black, dashed). This molecular mixture, consisting of a large spiropyran and a low merocyanine concentration, is then subjected to a series of pump and repump pulses.

For this pump–repump–probe experiment, pump pulses centered at 267 nm, fixed at time zero, generated via THG are used. The repump pulses, generated from a NOPA (TOPAS White), is centered at 560 nm and excites predominantly merocyanine (mainly the TTC isomer). The repump pulse is varied in time by t_{PR} in relation to the pump pulse. The supercontinuum probe is fixed at $T \approx 1400$ ps. Accordingly, only permanent changes in the effective reactant and product concentrations are detected, as long as t_{PR} does not approach T. Furthermore, this combination of

pump and repump wavelengths enables a nearly selective excitation of the ring-closed spiropyran by the pump and the ring-open merocyanine by the repump in their corresponding ground states. The supercontinuum probe pulse monitors changes in the merocyanine concentration, as well as excited-state features like SE and ESA, similar to the transient-absorption experiments in Sec. 5.4. However, the amount of ground-state bleach at 560 nm yields the most important information. A positive absorption means the equilibrium of the sample has changed to an increased amount of merocyanine (and less spiropyran) after twofold excitation. A negative signal at 560 nm corresponds to more spiropyran and less merocyanine.

Fig. 5.18 visualizes the experimental results in a spectrally resolved [Fig. 5.18a)] and a transient manner [Fig. 5.18b)]. At first the spectral behavior will be commented on, which identifies participating reactants and products. However, no information about the reaction speed is retrieved. Therefore, Fig. 5.18b) visualizes the transient behavior at $\lambda_{\mathrm{pr}} = 560$ nm, allowing to deduce temporal information about the TTC concentration. The top panel shows an effective delay of 3.6 ns ranging from -1600 ps $< t_{\mathrm{PR}} < 2000$ ps, while the bottom panel zooms in to times $t_{\mathrm{PR}} \approx 0$.

Fig. 5.18a) shows normalized difference spectra for three delay times t_{PR}. Positive values denote an increased absorption after $T = 1.4$ ns and negative values a decreased one. Solid lines represent additional photochemical changes $\Delta\mathrm{Abs}_{\mathrm{diff}}$ purely caused by the combination of pump and repump. Dashed lines correspond to either pump or repump only data. They are additionally shown to enable a comparison with $\Delta\mathrm{Abs}_{\mathrm{diff}}$ and to identify observed features. Each specific pump–repump delay is denoted by a certain color. It is important to keep in mind that the effective signal strength of the pump–repump–probe signals (~ 0.1 mOD) is much weaker than the (re)pump–probe signals (~ 10 mOD), explaining the different noise levels.

Tracking a Closing–Opening Cycle

The first discussed spectra are for $t_{\mathrm{PR}} < 0$ (green). Thus, the repump pulse precedes the pump pulse as shown in Fig. 5.17a). Looking first at the dashed spectrum, corresponding to 267 nm excitation only, a positive absorption centered at ≈ 560 nm is evident. When comparing the spectral shape with the permanent GSB after 560 nm excitation and the steady-state absorption spectra [both: Fig. 5.9a)] they are virtually identical. In addition, for $\lambda_{\mathrm{Pr}} < 450$ nm a positive signal, attributed to the S_2 absorption band is seen. Hence, excitation of spiropyran with 267 nm generates merocyanine, more specifically the TTC isomer. This reaction proceeds on a picosecond time-scale and is analyzed in more detail in Ref. [20, 58, 71] for 6,8-dinitro BIPS, resulting in the same conclusion. Furthermore, electrocyclic ring-opening reactions for other BIPS molecules are quite well studied in literature as described in Sec. 5.2.3. For example, BIPS itself performs a fast ring-opening reaction via singlet states within picoseconds [206, 233]. In 6-nitro BIPS the ring opening is also evident but proceeds at least partially over triplet states [255]. Looking at $\Delta\mathrm{Abs}_{\mathrm{diff}}$ (solid) the spectral shape corresponds very well with the spectrum obtained after UV excitati-

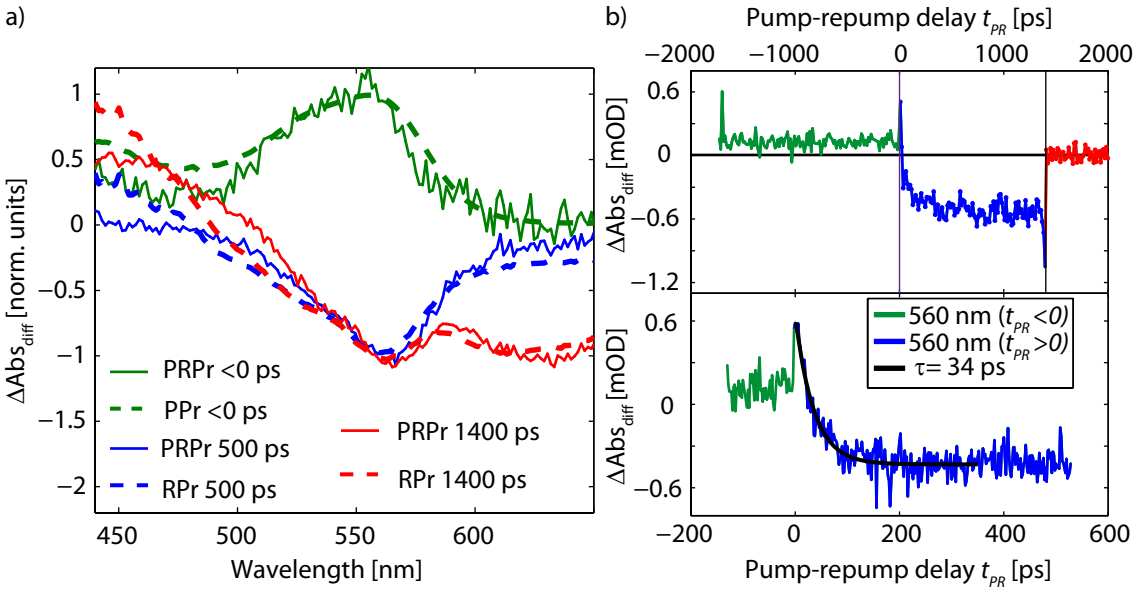

Figure 5.18: a) Normalized difference spectra $\Delta\text{Abs}_{\text{diff}}$ for $t_{\text{PR}} < 0$ ps (green, solid), together with $\Delta\text{Abs}_{\text{PPr}}$ (green, dashed), for $t_{\text{PR}} = 500$ ps (blue) together with $\Delta\text{Abs}_{\text{RPr}}$, and for $t_{\text{PR}} = 1400$ ps (red) together with ΔOD_{RPr} [20]. b) top: Transient behavior of $\Delta\text{Abs}_{\text{diff}}$ for 560 nm with the pump at 267 nm and the repump at 560 nm. For $t_{\text{PR}} < 0$ (green) additional TTC is probed while $t_{\text{PR}} > 0$ ps (blue) has decreased TTC absorption. For $t_{\text{PR}} > T$ no signal is observed (red). bottom: Resolution of $t_{\text{PR}} \approx 0$ combined with a mono-exponential fit with a lifetime of 34 ps (black).

on, i.e., additional merocyanine absorption is observed in the pump–repump–probe experiment for $t_{\text{PR}} < 0$.

Examining the temporal evolution in Fig. 5.18b) for -1600 ps $< t_{\text{PR}} < 0$ ps (green), e.g., the repump precedes the pump pulse, a constant positive offset is seen, ranging over the entire measured time delay. Thus, two conclusions can be drawn. First, since no decay or rise is associated with the reaction, especially with t_{PR} approaching zero, it has to be a concerted reaction scheme involving no intermediate states living on a ps time-scale. This means, the intermediate generated by exciting 6,8-dinitro BIPS with 560 nm pulses is without relaxation able to absorb 267 nm photons. After absorption of this UV photon the behavior at 560 nm changes again. Second, this intermediate is stable in time, when not subjected to excitation, and is already completely relaxed. This conclusion can be drawn from the fact that the effective signal strength at 560 nm does not change with time; the value at a short picosecond time delays is identical to the signal strength at $t_{\text{PR}} \approx -1500$ ps.

After combining all information, e.g. the pump excites spiropyran, the repump pulse excites merocyanine, a constant positive offset at 560 nm is present for all measured negative pump–repump delays, which in addition possesses the same spectral shape as the TTC ground-state absorption, the following explanation is proposed: 6,8-dinitro BIPS is able to perform two electrocyclic reactions via singlet states only, one opening and one closing step proceeding on an ultrafast time-scale and without

the involvement of long-living intermediates. In more detail, the remaining merocyanine in the sample, where the equilibrium was shifted more towards the spiropyran isomer, is excited by the green repump pulse. Accordingly, additional spiropyran with a quantum yield of $\approx 40\%$ for TTC is generated as discussed in detail in the transient-absorption experiments analyzed in Sec. 5.4.3. Since the UV pump pulse is able to initiate a ring-opening reaction, as indicated by the green, dashed difference spectrum in Fig. 5.17a), this newly generated spiropyran together with the already present concentration is then (partially) switched back to merocyanine. As a result of the effectively higher spiropyran concentration in the three-color experiment compared to the two-color case, more TTC is generated, resulting in a positive product absorption band around 560 nm. Hence, the green repump pulse induces a ring closure from merocyanine to spiropyran. This ring-closed stable intermediate is afterwards re-opened by the UV pump pulse enabling the (green part of the) probe to detect additional merocyanine, which was switched back and forth.

This entire mechanism proceeds within the time resolution of the experiment ($<$ 6 ps). Thus, after the merocyanine is excited, spiropyran is immediately formed, most probably via a theoretically proposed and calculated conical intersection [208, 252]. Afterwards, this photochemically generated spiropyran can be switched back directly without a measurable cooling period. The SP S_1 is either not participating in the reaction, because the conical intersection connects TTC S_1 with the SP S_0 state, or the participation is too short-lived to be detected. The existence of a conical intersection in S_1 for spiropyran-based photoswitches is quite common, e.g. Lanzani and coworkers found one for spirooxazines leading to an excited-state relaxation within 300 fs [283]. The minimal step size in the experiments shown here was 6 ps, allowing a deduced reaction speed of $<$ 6 ps for a full switching cycle starting at the merocyanine isomer because at $t_{PR} \approx 0$ ps the change in the behavior occurs within a single time-step and without any exponential rises or decays. In addition, the newly generated spiropyran by the first pulse is stable for at least 1.5 ns, since the yield of the bidirectional switching is not influenced by the effective delay between all three pulses. This confirms that the first reaction step (electrocyclic ring closure) is not only fast but also results in a stable product. Further reactions are only observed after an additional light-matter interaction within the maximal time delay. This longevity is one of the important necessary attributes for a molecular switch [19].

Tracking an Opening–Closing Cycle

After accessing one of the two possible switching directions, the pulse ordering is now reversed, thus, $t_{PR} > 0$. Accordingly, the 267 nm pump pulse, exciting spiropyran, precedes the 560 nm repump pulse, exciting merocyanine, as visualized in Fig. 5.17a). The spectral response for $t_{PR} \approx 500$ ps is shown in blue in Fig. 5.18a).

The dashed spectrum, corresponding to 560 nm excitation only, results in a permanent bleach centered at 560 nm, whose shape is reminiscent of the merocyanine steady-state absorption. In addition, both the green and blue dashed spectra correspond well to each other, only the sign is inverted. As discussed in Sec. 5.4.3 the

shape corresponds to GSA of TTC and the negative sign to a permanent bleach. Hence, a reduced TTC concentration is observed after excitation into S_1. As it is expected nearly no SE and ESA are seen, because t_{PR} is $\approx 5 \cdot \tau_{TTC}$. Again, the ΔAbs_{diff} spectrum looks virtually identical. Thus, the pump–repump combination shifts the equilibrium after two light-matter interactions towards spiropyran for $t_{PR} \approx 500$ ps.

This inference is further strengthened by the third solid spectrum (red) representing $t_{PR} \approx 1400$ps $\approx T$. Pulse ordering is identical to the pump–repump case discussed above for $t_{PR} \approx 500$ ps. Hereby, a similar spectral behavior is expected after normalization. However, looking at the difference spectrum for ΔAbs_{RPr} (corresponding to 560 nm excitation only) negative SE (620 nm) and positive ESA (445 nm) are visible, in addition to GSB (559 nm). This agrees well with the transient-absorption data shown in Fig. 5.5 for short waiting times. There, these signals are assigned to relaxation from S_1 into S_0. The ESA measures the excited-state population directly, while the decreasing SE and GSB indicate that S_0 is repopulated (Sec. 5.4.3). Since in principle $T \approx 1400$ ps is a long waiting time, neither SE nor ESA are expected. However, t_{PR} approaches the waiting time T. Hence, the photoprocesses initiated by the repump pulse are not finished at the arrival time of the probe pulse. Thus, the time-resolved behavior is mirrored, albeit, seemingly with reversed time-ordering. The more t_{PR} is increased, the closer it gets relative to the probe pulse, explaining the inversed ordering.

Again the spectral shape of the extracted pump–repump–probe signal corresponds well to one-color excitation data, showing analogous ESA, GSB, and SE features. Whereas the permanent GSB is explained by increased spiropyran and decreased merocyanine concentration, the other signals are also intuitively explicable. The reason for the observed ESA and SE in ΔAbs_{diff} is that excited merocyanine performs a ring-closure reaction with a yield of $\Phi_{o-c} \approx 40\%$ only. The remaining fraction of excited molecules remains in S_1 and radiatively relaxes, while the effective population is monitored via ESA. All three signals are visible because TTC has a lifetime of 95 ps. Hence, a high percentage of molecules is still in S_1 at $t_{PR} \approx 1400$ ps $\approx T$. Thus, not only permanent products are monitored in this direction, but also non-finished relaxation has to be considered. However, the behavior of both discussed spectra for this pump–repump ordering confirms additional merocyanine bleach is induced by this pulse combination. Therefore, the equilibrium is shifted towards spiropyran.

This shift towards lower merocyanine and higher spiropyran concentration, caused by the 267 nm-pump followed by 560 nm-repump excitation, can be explained by the following bidirectional switching scheme: The UV pump excites the high spiropyran concentration, leading to a higher merocyanine ground-state concentration at the time when the repump interacts with the sample. This increased concentration is then excited and partially switched to spiropyran by the repump pulse. Hence, a slightly larger amount of merocyanine is bleached as compared to the case without the pump pulse being present. Therefore, the probe pulse measures a negative absorption change ΔAbs_{diff}, because less TTC is present. Hence, 6,8-dinitro BIPS is also switchable in the direction ring-closed SP to ring-open MC and back to SP with at least 500 ps. A better estimation of the speed is given below.

While the spectral behavior at two different pump–repump delays explain the principal mechanism, the reaction speed for a full switching cycle SP-MC-SP is deduced from the blue transient (specified by $0 < t_{\mathrm{PR}} < 1400$ ps) in Fig. 5.18b) (top). Here, a constant negative signal is identified for long times, as discussed in the corresponding difference spectra. Contrary to the inverse pulse ordering, the change is not instantaneous but increases in value on a picosecond time-scale. Therefore, upon excitation with the 267 nm pump pulse, the reaction has to proceed over an intermediate state, which is not capable of ring-closure, before the 560 nm repump can successfully reclose the now relaxed molecules. The lower panel shows an inset for short pump-repump delays $t_{\mathrm{PR}} < 500$ ps combined with an exponential fit. The additional merocyanine bleach increases with $\tau = 34$ ps until it reaches a constant level. As far as the reaction intermediate goes, several possibilities exist. Wohl and Kuciauskas reported for 6-nitro BIPS the formation of various isomers, which interconvert on a picosecond time-scale. Accordingly, this would be the necessary time until an equilibrium is reached, which can be switched back [254]. In addition, the presence of a cisoid species, resembling a spiropyran but with an already broken CO bond, absorbing in the visible [255], could be a precursor of the finally thermally stable TTC. Merocyanine triplet states are reported to live in the microsecond domain [253, 265, 284]. Hence, they proceed on a completely different time-scale.

In conclusion, a reaction speed of $\tau \approx 34$ ps is identified for the closed-open-closed cycle. The second reaction step is the time-limiting one and it proceeds via an unknown merocyanine intermediate. The short lifetime of the intermediate allows exclusion of strong triplet state participation in the electrocyclic ring closure and opening reaction, confirming a concerted reaction process.

In addition, there is a clear positive spike, and, accordingly, a positive offset over the entire remaining time t_{PR}, when the pulse ordering is changed. This offset cannot be related to any kind of coherent artifact because it is detected after the long waiting time $T \approx 1.4$ ns. Hence, a permanent, positive absorption is generated, overlaid with the additional TTC bleach. This signal most probably results from a slight underestimation of the signal strength when calculating $\Delta\mathrm{Abs}_{\mathrm{diff}}$. As shown in Equation 5.13 $\Delta\mathrm{Abs}_{\mathrm{RPr}}$, corresponding to a permanent merocyanine bleach, is subtracted from $\Delta\mathrm{Abs}_{\mathrm{PRPr}}$ in order to extract the pure three-color signal. However, the excited amount of merocyanine is lower in the pump–repump–probe measurement, because the repump pulse excites also hot, non-switchable, molecules, generated by the pump, effectively reducing the observable bleach. Thus, during relaxation of hot merocyanine, $|\Delta\mathrm{Abs}_{\mathrm{PRPr}}| > |\Delta\mathrm{Abs}_{\mathrm{RPr}}|$ is valid, resulting in a seemingly positive new absorption band when calculating $\Delta\mathrm{Abs}_{\mathrm{PRPr}} - \Delta\mathrm{Abs}_{\mathrm{RPr}}$. Albeit, without any pulse combination effect, these two signals should be identical.

At last, for $t_{\mathrm{PR}} > 1400$ ps (red in Fig 5.18) $\Delta\mathrm{Abs}_{\mathrm{diff}} = 0$ is measured. There, the repump pulse excites the sample after the probe pulse detects the photochemical changes. Hence, no influence from the repump is measurable. The pump–repump–probe data should correspond to the pump–probe data and after subtraction the effective signal strength is zero. This actually confirms that the experimental scheme works reliably as explained in Sec 5.6.1.

Concluding this section, pump–repump–probe experiments serve a twofold purpose. On the one hand, the sensitivity of the employed transient-absorption setup is visualized. It is possible to measure the change in an absorption change, a signal which is 10-100 times smaller, with sufficient resolution. Hence, there is no technical obstacle to introduce triggered exchange 2D, explained in the introduction of this section, also in the visible spectral range and not only on the NIR. On the other hand, new photochemical insight about the excited-state behavior of 6,8-dinitro BIPS is shown. The molecule is capable of switching in both directions, from merocyanine to spiropyran to merocyanine and the other way around, a unique property for merocyanines. To my knowledge only one other merocyanine dye has shown this property, a water soluble Py-BIPS [212]. Most other BIPS systems only perform isomerization [285]. However it is important to note that one direction is direct and fast within 6 ps, while in the other direction hot merocyanine needs to relax, limiting the ring-closure direction to $\tau \approx 34$ ps.

5.6.3 Assessing Reaction Pathways Originating from Excited States Only

The following section analyzes the properties of excited merocyanine. Hence, the behavior of molecules who do not perform an electrocyclic reaction (explained in the previous section) is discussed now. Transient absorption (Sec. 5.4) and 2D measurements (Sec. 5.5) showed that the excited molecules after excitation into S_1 relax radiatively. However, the question of what happens after re-excitation cannot be addressed without a further light-matter interaction. This is a topic of interest because energetic barriers in merocyanine [208] could be circumvented. Therefore, ring closure quantum yields or isomerization efficiency could possibly be enhanced.

To this end, the same pump–repump–probe technique as for bidirectional switching is used, however, with a different wavelength combination of pump and repump pulses. The results will be explained in the following section and have been published in Ref. [219].

Spectro–Temporal Pump–Repump–Probe Results

To analyze the excited-state behavior of 6,8-dinitro BIPS, the merocyanine configuration is used. Photoexcitation is performed with a 600 nm pump pulse ($E_P \approx 40$ nJ), generated from the home-built NOPA system and additionally with a 440 nm repump pulse ($E_R \approx 150$ nJ), obtained by using the second harmonic from the commercial NOPA system (TOPAS White). All pulses possess parallel polarization with respect to each other. The wavelength of the pump pulse allows for an effective excitation of both TTC and TTT merocyanine into S_1 (GSA_{TTC}: 559 nm, GSA_{TTT}: 600 nm), while the repump is resonant with the ESA of both isomers (ESA_{TTC}: 445 nm, ESA_{TTT}: 460 nm). The waiting time T between pump and supercontinuum probe was adjusted to $T \approx 2000$ ps. Thus, only the long-living permanent bleach

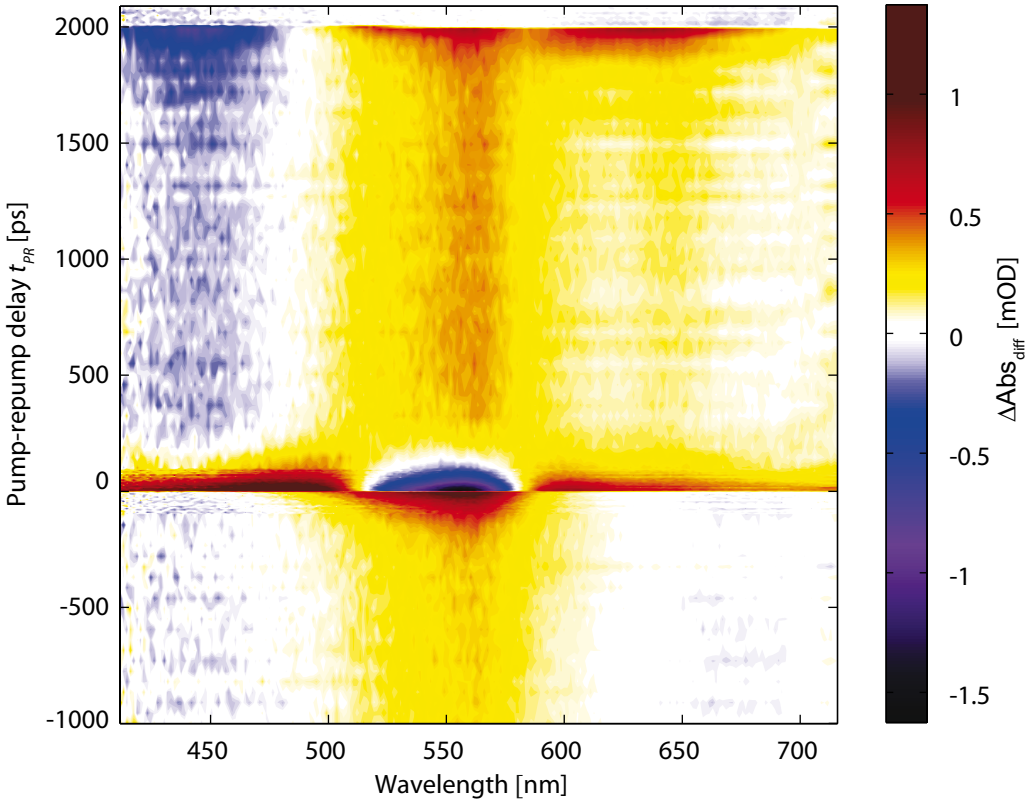

Figure 5.19: Spectrally resolved pump–repump–probe contour plot for $T = 2000$ ps after resonant excitation into S_1 combined by a 440 nm repump pulse. Additional photobleaching (negative) and product formation (positive) is observed for $0 < t_{PR} < 250$ ps overlaid by a signal overestimation for nearly all other delays [219].

of TTC and TTT is detected when the visible pump pulse is present (compare difference spectrum after 3 ns in Fig. 5.9 for excitation of both TTC and TTT).

Fig. 5.19 shows a contour plot of pump–repump–probe data $\Delta\text{Abs}_{\text{diff}}$ depending on λ_{Pr} and pump–repump delay t_{PR}. The repump was scanned from $t_{\text{PR}} = -1000$ ps up to 2100 ps, crossing the pump at $t_{\text{PR}} = 0$, and finally the probe at $t_{\text{PR}} = 2000$ ps. Positive values for $\Delta\text{Abs}_{\text{diff}}$, resulting in increased absorption, are shown in reddish and negative ones, indicating a decrease when compared to common pump–probe measurements, in bluish colors. Again, the depicted response $\Delta\text{Abs}_{\text{diff}}$ is purely caused by the interaction of both pulses and not by a single (re)pump pulse [219].

The signal can be divided into different contributions. The most prominent, and also most interesting, signal is obtained for $0 < t_{\text{PR}} < 250$ ps. There, resonant excitation into S_1 for both isomers occurs via pump-pulse excitation, followed by resonant excitation via ESA around 440 nm into highly excited states of merocyanine. A strong negative signal, centered at the TTC absorption wavelengths of 559 nm, is observed corresponding to an increase of the absolute value of the observed bleach after 2 ns. Thus, the TTC ground-state concentration is permanently reduced by the three-color experiment. This bleach is accompanied by two strong positive ab-

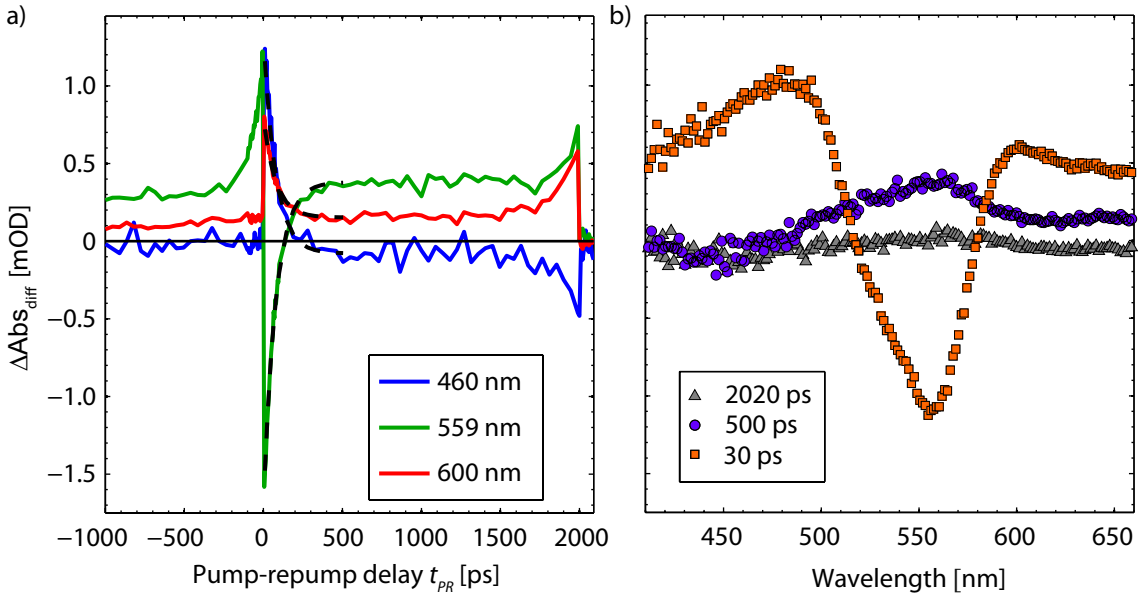

Figure 5.20: a) Transient behavior of $\Delta\text{Abs}_{\text{diff}}$ for 460 nm (blue), 559 nm (green), and 600 nm (red) combined with a global fitting routine (black). b) Difference spectra for $t_{\text{PR}} = 30$ ps (orange, squares) highlighting additional bleaching and product generation, 500 ps (violet, circles) visualizing the inverted transient-absorption data, and 2020 ps (white, triangles) corresponding to pump-only excitation [219].

sorption bands, one between 400 to 500 nm, and the second one ranging from 600 to 700 nm. The latter band strongly overlaps with the TTT GSA. Both of these bands indicate the formation of a new long-living species since they last over 2 ns.

The temporal behavior of these three bands is presented in Fig. 5.20a) by transient cuts of the data shown in Fig. 5.19. A global fitting routine results in monoexponential decay with 80 ps and a permanent offset as visualized in black for both product bands (blue:460 nm, red: 600 nm) and the GSB (green:559 nm). However, only the first 500 ps are taken into account. This was done in order to avoid any contributions which originate from t_{PR} approaching the continuum probe at T. This time constant of 80 ps corresponds well to the observed S_1 lifetime of 95 ps of TTC in the previous transient-absorption experiments in Sec. 5.4. This strongly indicates that the additional photoproduct, generated by accessing reaction pathways, which involve higher-lying electronic states, originates from the TTC S_1 state. In addition to transient cuts, Fig. 5.20b) shows difference spectra for three delays t_{PR}, namely 30 ps (orange, squares), 500 ps (blue, circles), and 2020 ps (gray, triangles) highlighting the spectral behavior for the most interesting pump–repump delays.

At longer times $250 < t_{\text{PR}} < 2000$ ps all three bands vanish. Instead, a positive signal emerges for wavelengths $\lambda_{\text{Pr}} > 500$ nm and a very weak negative one to the blue side with $\lambda_{\text{Pr}} < 500$ nm. The signal strength remains constant up to $t_{\text{PR}} = 1500$ ps. Therefore, neither the S_1 lifetime of TTC (95 ps), nor of TTT (800 ps) can be responsible because in the transient cuts shown in Fig. 5.20a) no change is observed with these time constants. The difference spectrum in Fig. 5.20b) for

$t_{PR} = 500$ ps (blue, circles) has the same spectral shape but opposite sign as the black DADS obtained upon 560 nm excitation, associated with the permanent bleaching of merocyanine. Accordingly, this signal is interpreted as an overestimation of the effective pump–repump signal when calculating ΔAbs_{diff} using Equation 5.13. Both two-color measurements with either pump (ΔAbs_{PPr}) or repump (ΔAbs_{RPr}) only, excite a fresh sample with a well-known optical density, provided by usage of a flow cell. However, in the pump–repump–probe measurement, after the pump has excited the sample, the repump pulse acts on a lower concentration of merocyanine molecules in the ground state, because $\approx 40\%$ of the excited molecules have formed spiropyran. Hence, a slightly lower signal is obtained for ΔAbs_{PRPr}. This concentration change corresponds to a very small bleach (< 200 µOD), as compared to a signal strength around 10 mOD in the pump–probe experiment. The same effect occurs if the pulse ordering is reversed. While the absorption of both merocyanine isomers at 440 nm is minimal as shown in Fig. 5.4a), excitation is evident. It is important to note that this overestimation of the signal is not an error in the measurement, because the concentration change for TTC is a real effect, caused by the multipulse combination.

The explanation above is actually strengthened when looking at the signal development for pump–repump delays of $1750 < t_{PR} < 2000$ ps. The value of overestimation increases with increasing time t_{PR} because as the repump approaches the probe, an increased percentage of excited molecules still remains in S_1 and has not relaxed to the ground state. This results in signals for ESA (440 nm), GSB (559 nm) and SE (600 nm) similar to the transient-absorption results. This is actually the same effect as already discussed in Sec 5.6.2. A related explanation is valid for the increasing signal ΔAbs_{diff} for $t_{PR} < 0$. Here, the repump precedes the pump and, thus, the pump pulse excites a lower merocyanine concentration. This concentration reduces even more when the repump approaches the pump because molecules still remain in S_1 and, hence, cannot be excited. The temporal behavior mirrors the 80 ps dynamics observed for the TTC relaxation confirming this interpretation as shown for 559 nm (green line) in Fig. 5.20a). Looking at the spectral behavior in Fig. 5.19 for $t_{PR} < 0$, no ESA at 440 nm is observed because it has decayed within a probe delay of 2 ns but a weak (positive) signal at 600 nm is seen, corresponding to an effective bleach of the TTT isomer, confirming that both isomers are excited partially.

Finally, $\Delta Abs_{diff} = 0$ for time delays $t_{PR} > 2000$ ps, as shown in the black difference spectrum for 2020 ps. Since for these long delays the repump interacts with the sample after the probe pulse, no influence is detectable. In addition, the probed concentration for both pump and repump excitation, when compared to the pump only measurement is now identical, no overestimation occurs (compare Sec. 5.6.2).

Validating Cation Formation after Twofold Excitation

The pump–repump–probe scheme allows unraveling of reaction pathways occurring after re-excitation of an electronically excited state. The results shown in Figures 5.19 and 5.20 correspond to excitation of both TTC and TTT merocyanine into S_1, followed by a resonant repump pulse exciting the molecules into even higher elec-

tronic states for $0 < t_{\mathrm{PR}} < 250$ ps. The shape of the observable bleach is reminiscent of the TTC absorption shown in Fig. 5.9 centered at 559 nm. In addition, both the amount of bleach and the new observable photoproduct seen for $T = 2000$ ps reduces exponentially with a time constant of 80 ps for positive t_{PR}. However, spectral TTT contributions cannot be ruled out completely because they might be hidden under the positive absorption peak, which is lower for $\lambda_{\mathrm{Pr}} = 600$ nm, as compared to $\lambda_{\mathrm{Pr}} = 490$ nm. The identification of the formed product is challenging as well. In the following, the most probable assignments will be discussed [219].

First, isomerization could occur between TTC and TTT. It was determined to be an insignificant reaction pathway after excitation into S_1 via 2D spectroscopy in Sec. 5.5.4. This statement may not hold true upon excitation into even higher states because of the access to higher-lying potential energy surfaces, possibly characterized by different relaxation pathways. Moreover, the additional energy might be enough to overcome the barrier between the multidimensional potential curves estimated in Ref. [208]. In this reference a simplified photosystem is used to verify theoretically the ring-closure and ring-opening reaction proposed for 6,8-dinitro BIPS [58]. Looking at the difference spectrum for $t_{\mathrm{PR}} = 30$ ps (orange squares) in Fig. 5.20b) one positive absorption band is centered at $\lambda_{\mathrm{Pr}} = 600$ nm corresponding well to the TTT absorption maximum. However, the TTT absorption is nearly zero for $\lambda_{\mathrm{Pr}} = 650$ nm as seen in the black offset in Fig. 5.9b), which is not the case for the pump–repump–probe data. In addition, while TTT possesses positive ESAs for $\lambda_{\mathrm{Pr}} < 580$ nm their spectral shape does not match at all. The ESA is twofold, centered at 460 and 550 nm compared to the single peak centered at ≈ 585 nm seen here. Thus, isomerization between the two known isomers can again be excluded to be a significant pathway. While in principle isomerization into another merocyanine isomer is possible — the theoretical existence of eight isomers is visualized in Fig. 5.10b) and at least four of them should be stable in principle — a blue-shifted photostable isomer was never observed in literature. In addition, it seems plausible from a thermodynamic point of view that the most stable isomer has the highest energetic transition into S_1. Thus, this possibility seems also highly unlikely. However, at least the existence of three different isomers was proposed for 6-nitro BIPS [254], but as previously shown the photochemistry of 6,8-dinitro BIPS and 6-nitro BIPS differs seriously.

Second, the excited molecules could pass a conical intersection, most probable for the ring-closure reaction [20, 208], when relaxing via IVR. This would result in an increased amount of ring-closed molecules. On the one hand, this explains the observed photobleach. On the other hand, spiropyran possesses no absorption band in the visible spectral range. Hence, the positive bands are unexplainable. So, this assumption is also discarded for the majority of repumped molecules.

Third, a participation of long-living triplet states populated by the repump would be possible. For this explanation the observed bands would be ESA and not product bands because of the µs lifetime of triplet states, which cannot be resolved here. While for 6-nitro BIPS the participation of triplet states to the photochemical behavior was suggested [255], nothing similar was seen in the transient-absorption data of 6,8-dinitro BIPS in Sec. 5.4. Moreover, transient absorption with detection in the

mid infrared, previously performed in this group, also found no evidence of strong triplet state contributions in the photochemistry of 6,8-dinitro BIPS [58]. Further evidence for a singlet pathway dominating merocyanine reactions are derived from Ref. [286], where a merocyanine dye was analyzed with and without the presence of oxygen serving as a triplet quencher. No effect was observed on the photochemistry, thus, triplet pathways were excluded.

After discussion and subsequent elimination of the most obvious reaction channels, other possibilities have to be taken into account. The combined excitation energy of pump and repump pulses corresponds to an effective excitation with 5 eV. The ionization energies for both indole [287] and [2H-1]-benzopyran [288], the building blocks of a spiropyran, were determined to be ≈ 8 eV in literature. While these two values exceed the excitation energy, the effect of the π-electron system has to be considered, when the two units are linked. A completely new absorption band in the visible spectral range is generated. Hence, the linked chromophore absorbs at much lower energies. If the ionization energy is also lowered, this reaction pathway has to be considered. Ionization yields a free electron that is released to the solvent. Solvated electrons give rise to broadband signals, which interfere with the measurements. However, chloroform is used as a solvent, which prevents the solvation but reacts with the free electrons in a dissociative process, which does not yield any signals in the visible regime [289]. Ionization results in the formation of a new radical cation $MC^{+\bullet}$, which could explain the new product absorption. According to literature an ionized merocyanine dye is characterized by the formation of a high- and low-energy band when compared to the ground-state absorption mirroring the findings here [286]. In addition, 308 nm (≈ 4 eV) excitation proved sufficient for ionization. These considerations are transferred to 6,8-dinitro BIPS. After the first pulse generates a population in S_1, the repump pulse is used as an ionization beam, explaining the new absorption bands. Thus, pump–repump–probe spectroscopy accesses a two-step ionization pathway. The effectiveness of this pathway can be controlled by the pulse separation t_{PR} effectively scanning the excited-state population.

5.6.4 Conclusion

Taking both experiments performed in this section into account, the reactions proceeding after the first excitation pulse are uncovered for 6,8-dinitro BIPS. Either spiropyran is generated or radiative relaxation occurs from the merocyanine S_1 state. On the one hand, pump–repump–probe spectroscopy is used to track the ultrafast electrocyclic ring-closure to spiropyran. The measurements unambiguously show that both conformations are connected via singlet pathways. On the other hand, molecules, which were not switched, were ionized in a second experiment, clearly showing that ground-state excitation and excited-state excitation differ. Hence, pump–repump–probe spectroscopy is an extension of common pump–probe spectroscopy, which is especially suited for tracking multi-step and excited-state reactions by using an additional laser pulse for an additional light-matter interaction.

5.7 Tracing Multi-Step Photoreactions of Two Isomeric Species at Once

Femtosecond time-resolved spectroscopy was used in the previous sections to characterize photoexcited 6,8-dinitro BIPS via direct resolution of the participating processes. The capability of directly accessing reaction mechanisms in real time is one of the most crucial benefits of time-resolved optical techniques [8–10]. In the following pump–repump–probe spectroscopy (introduced in Sec. 5.6) is combined with coherent electronic 2D spectroscopy (introduced in Sec. 5.5). This combination is called coherent triggered-exchange 2D (TE2D) spectroscopy and directly correlates the absorbing characteristics of an unknown sample before and after an additional light-matter interaction. The pulse sequence is shown Fig. 5.1d) in the introduction. Until now, this technique has only been demonstrated for 2D experiments in the mid-infrared spectral range probing purely vibrational changes [225, 226], but not for electronic transitions induced by the 2D pump pulse sequence. In the following example, a reactant, defined via the S_1-S_0 transition frequency, will be connected to a photoproduct formed after repump-interaction between pump and probe pulse. This enables an unambiguous identification of the isomer of 6,8-dinitro BIPS, which is responsible for the formation of the radical cation observed in the pump–repump–probe measurements presented in Sec. 5.6. The experimental data and results of this section have already been published in Ref. [219].

5.7.1 Triggered-Exchange 2D Spectroscopy

TE2D spectroscopy is realized similar to the 2D measurements described in Sec. 5.5 using a phase-locked pump pulse pair generated with a pulse shaper and separated by coherence time τ. Furthermore, all three beam lines from the transient-absorption spectrometer, explained in detail in Sec. 3.2, are in use. Basically, a common 2D experiment is combined with a repump pulse, which re-excites the transient population and the data is treated in a similar way as in the experiments described in Sec. 5.6.1 for the analysis of pump–repump–probe data. Both, pump as well as repump, pulses are generated by two independent NOPAS. The pump pulses are centered at $\lambda_P = 590$ nm and compressed down to 17 fs. Thus, they have sufficient bandwidth to excite both isomers of 6,8-dinitro BIPS. After compression, the pulse shaper generates phase-stable pulse pairs with an adjustable coherence time delay τ by applying the phase mask in Eqn. 5.1. The repump pulses are centered at $\lambda_R = 435$ nm with ≈ 40 fs duration, again covering both the ESA of TTC (445 nm) as well as the ESA of TTT (460 nm) to a sufficient degree. The use of a continuum probe pulse enables detection of the features described in the previous sections. All pulses were adjusted to possess parallel polarization relative to each other.

By employing the same chopper configuration, two phase-locked chopper wheels, placed in the pump and repump beams, respectively, as described in Sec. 5.6.1, again three different optical density values [ΔAbs_{PRPr} (blue), ΔAbs_{PPr} (red), and ΔAbs_{RPr}

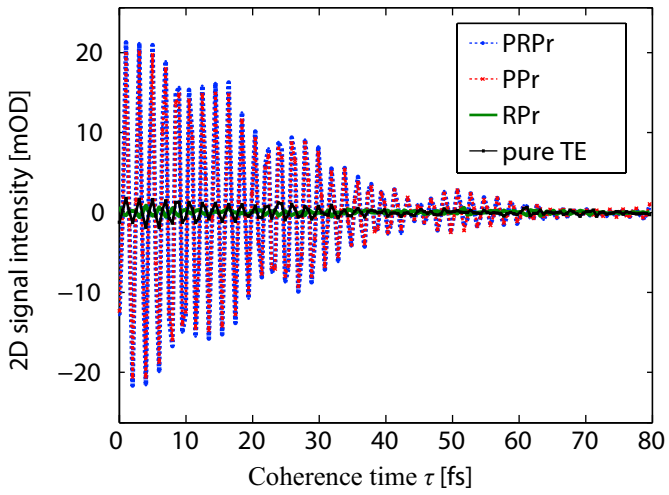

Figure 5.21: Transient cuts for $\lambda_{Pr} = 585$ nm exemplifying extraction of a TE2D signal in the time domain. From the signal of dual excitation S_{PRPr} (blue), the single cases S_{PPr} (red) and S_{RPr} (green) are subtracted leading to the TE signal (black). Note the small differences in S_{PPr} and S_{PRPr} (blue) and the low signal-to-noise ratio of the final TE signal.

(green)] are obtained. The colors denote to Fig. 5.21. This chopper configuration is necessary to provide shot-to-shot signal detection. Additionally, for each fixed population time T and pump–repump delay t_{PR}, the coherence time τ is scanned and a four-step phase-cycling scheme applied (see Sec. 5.5.1).

Figure 5.21 shows the corresponding oscillating transient cuts S_x obtained for different pulse combinations. Resulting from the used phase-cycling scheme, the shown data only contains the phase-sensitive contributions, enabling extraction of the corresponding 2D spectra. Both, S_{PRPr} (blue) and S_{PPr} (red), possess a strong, phase-sensitive signal which decays over a coherence time of 80 fs. By contrast, S_{RPr} (green), which does not depend on the coherence time τ, has (nearly) zero signal strength as expected. The effective triggered-exchange signal S_{TE} is obtained by calculating

$$S_{TE} = S_{PRPr} - S_{PPr} - S_{RPr} \tag{5.14}$$

for every value of τ and λ_{Pr}, while retaining T and t_{PR}. Resulting from the large similarities between S_{PRPr} and S_{PPr}, only the very weak, but oscillating, triggered exchange signal S_{TE} (black) is obtained. This phase-sensitive coherent signal decays within 60 fs at most. After performing Fourier transformation over τ and taking the real part, the absorptive, intrinsically phased, TE2D spectrum is obtained with the signal spread along an additional spectrally resolved pump-axis.

For the measurements τ was scanned up to 60 fs in steps of 0.5 fs and no rotating frame was chosen ($\gamma = 1$), thus, the 2D signal was not undersampled but completely resolved within the Nyquist limit. In order to obtain smoother spectra the effective coherence time was increased to 360 fs using zero padding, i.e., the signal was assumed to be completely zero after 60 fs and no coherent signals were observed anymore. The four-step phase cycling scheme was repeated four times reducing

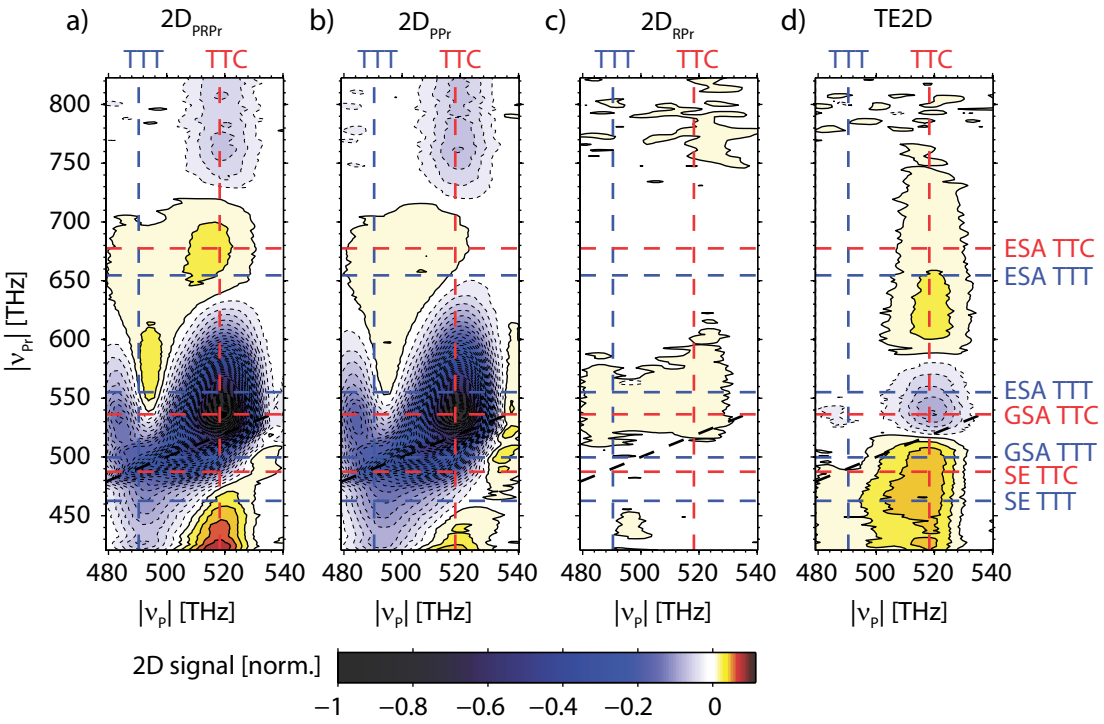

Figure 5.22: Visualization of a TE2D spectrum for $t_{PR} = 0.5$ ps and $T = 2000$ ps. a) $2D_{PRPr}$ spectrum containing sample interaction with all pulses b) $2D_{PPr}$ spectrum obtained after excitation with a pump pulse pair c) $2D_{RPr}$ spectrum after pure repump interaction d) Extracted TE2D spectrum showing TTC bleach and product formation [219].

long-term noise while short-term noise was limited by averaging over 500 ΔAbs calculation (resulting from 2000 shots) to obtain all three signal contributions. No sample degradation was observed over the course of the measurement.

5.7.2 Results of Triggered-Exchange 2D Spectroscopy

An exemplary TE2D spectrum, together with the measured 2D spectra for different excitation configurations, is shown in Fig. 5.22 for 6,8-dinitro BIPS in chloroform. The pump–repump delay was fixed at $t_{PR} = 0.5$ ps and the population time adjusted to $T = 2000$ ps. Hence, the 440 nm repump pulse excites a large amount of merocyanine molecules in the S_1 state of both isomers, while the probe only detects photoproducts stable for at least 2 ns. In Figures 5.22a)-d) vertical red/blue lines denote the TTC/TTT absorption frequency obtained by multiplying the GSA absorption of both isomers with the excitation spectra. Moreover, horizontal lines denote absorption and emission frequencies obtained in Sec. 5.4 for both isomers, again TTC is shown in red and TTT in blue. However, these frequencies are unaltered, as probe frequencies in a pump–probe based 2D approach are intrinsically normalized to the relative changes in the continuum probe. The color code is similar to previous experiments with yellow/red denoting increased absorption and blue/violet/black decreased absorption change [219].

Figure 5.22a) shows the 2D spectrum $2D_{PRPr}$ obtained after excitation with a pump pulse pair and an additional repump. At first glance it appears quite similar to the $2D_{PPr}$ spectrum in Fig. 5.22b) obtained by pump pulse excitation only. Both spectra have distinct absorption and emission frequencies centered on the vertical lines denoting the two isomers. Hence, both TTC and TTT are sufficiently excited to disentangle their respective relaxation. When compared to the 2D spectra shown in Fig. 5.15, the data matches very well the 2D spectrum measured for $T = 1000$ ps. GSB (550 THz), SE (490 THz) and ESA (680 THz) are clearly identified in both $2D_{PRPr}$ and $2D_{PPr}$ alongside the effective TTC absorption frequency at $|\nu_P| \approx 520$ THz. Likewise, all previously known contributions, GSB (500 THz), SE (460 THz), and ESA (550 THz, 650 THz) are identified for TTT at $|\nu_P| \approx 495$ THz. Additionally, in the $2D_{PRPr}$ spectrum a positive signal, absorbing at TTC pump frequencies, extends beyond 450 THz hinting at an additional contribution caused by the presence of the repump. The last measured spectrum $2D_{RPr}$ corresponds to repump interaction only, shown in Figure 5.22c), and possesses only very weak noise around the TTC ground-state absorption. The non-occurrence of a 2D signal is in line with the expectation, since the pump pulse pair is blocked.

Combining the measured data sets as explained in Sec. 5.7.1 and taking the real-valued signal contributions after Fourier transformation yields the TE2D spectrum shown in Fig. 5.22d). Similar to pump–repump–probe measurements the additional effects of the multipulse combination are visualized. Thus, the TE2D spectrum can be considered as the change in the conventional electronic 2D spectrum due to the interaction of excited molecules with the repump pulse. However, by generating an excitation frequency axis corresponding to the pump pulse frequencies, the molecular ground state, from where the photochemical reaction pathway sets in, is resolved. Thus, TE2D directly visualizes the correlations between the spectral signatures of the precursor molecule and the response of the repump-induced photoproduct.

Looking at the spectrum along $|\nu_P| = 495$ THz, corresponding to TTT excitation, nearly no TE2D signal is seen. Moreover, no negative contribution is identified. This means, the repump pulse does not induce any additional TTT bleach. Thus, every TTT molecule in S_1 that undergoes excitation into even higher electronically-excited states, relaxes back to S_1 via non-radiative mechanism like internal conversion combined with vibrational relaxation. From here on, the known fluorescence pathway with a lifetime of $\tau_{TTT} \approx 800$ ps sets in. This statement can be made because after subtraction of both $2D_{PPr}$ and $2D_{RPr}$ nothing additional remains. Therefore, the photochemical behavior is identical after excitation into S_1 or S_n. Perhaps a slight positive signal, weakly above the noise amplitude, is identified at $|\nu_{Pr}| = (400 - 520)$ THz. This results from the fact that the TTT bleaching strength is overestimated by the measurement and data analysis procedure, similar to the pump–repump–probe experiments (Sec. 5.6), and bears no additional information. Mainly, it can be seen as an indication that the measurement procedure is working well.

As far as strong signals are concerned, a distinct GSB ranging from $|\nu_{Pr}| = (520 - 570)$ THz (or $\lambda_{Pr} \approx (520 - 580)$ nm) and two new positive product bands are identified. One absorbs between $|\nu_{Pr}| = (400 - 520)$ THz (or $\lambda_{Pr} \approx (580 - 750)$ nm)

and the other band at $|\nu_{\mathrm{Pr}}| = (590 - 750)$ THz (or $\lambda_{\mathrm{Pr}} \approx (400 - 750)$ nm). These three features are virtually identical to those observed in the pump-repump-probe experiment analyzed in 5.6.3 and shown in the orange difference spectrum in Fig. 5.20b) for $t_{\mathrm{PR}} = 30$ ps. Hence, the formation of a radical cation $MC^{+\bullet}$ is the most logical conclusion, confirming the previous experiments. However, as a result of the new excitation frequency axis, the sole absorption frequency $|\nu_{\mathrm{P}}| = 510 - 530$ THz, causing the formation of $MC^{+\bullet}$, is identified. This absorption range corresponds well to the TTC S_1 absorption (red dashed line in Fig. 5.22). Thus, the S_1 absorption state of TTC is identified as the chemical precursor of the $MC^{+\bullet}$ generation. This information was not directly available in the pump–repump–probe measurements, which could only resolve the final state.

Therefore, TE2D measurements, which are an extension of both 2D and pump–repump–probe, offer a highly sensitive tool, enabling the analysis of excite-state photochemistry. This is important, because two-color measurements, like, e.g., transient absorption or fluorescence upconversion, often only cover the ground and the first excited state directly by absorption and detection of one photon each. Coherent 2D spectroscopy offers more information by resolution of the pump-frequency axis but again only the population change induced by the first pump pulse pair is traced. By contrast, three-color techniques (pump–repump/dump–probe) force the absorption of two photons allowing excitation into higher states and the subsequent resolution of the population relaxation of these excited states. However, if molecular mixtures are present, no discrimination between molecules absorbing at different wavelengths is possible. Accordingly, TE2D closes the gap between these two techniques by spectrally resolving the pump axis while keeping the twofold excitation. It is important to note that if both, 2D and pump–repump–probe spectroscopy, are known, the bridge to TE2D spectroscopy can be crossed in an intuitive way. In fact, the experimental conditions, the data analysis and interpretation are straightforward, and very similar to the two techniques TE2D is based on. Hence, TE2D offers a powerful technique, which enables the analysis of excited-state photochemistry.

5.8 Combining All Results into a Reaction Scheme

Within this chapter different time-resolved methods were used (TA: Sec. 5.4), adapted (two-color 2D: Sec. 5.5; pump–repump–probe: Sec. 5.6) and newly developed (TE2D: Sec. 5.7) to examine the photochemical behavior of the molecular switch 6,8-dinitro BIPS, resulting in a comprehensive reaction scheme. This is visualized in Fig. 5.23 and every contribution identified will be shortly reviewed here.

Transient-absorption experiments with two excitation wavelengths [green arrow (560 nm); orange arrow (620 nm)] unambiguously verified the presence of two merocyanine isomers in solution (Sec. 5.4). Previous NMR measurements by Hobley *et al.* identified TTC (dominant, left side) and TTT (minor contributions, right side) as the most stable isomers in solution. Thus, this assignment was transferred here [216, 290]. A separation of the two isomers was possible because TTC relaxes with

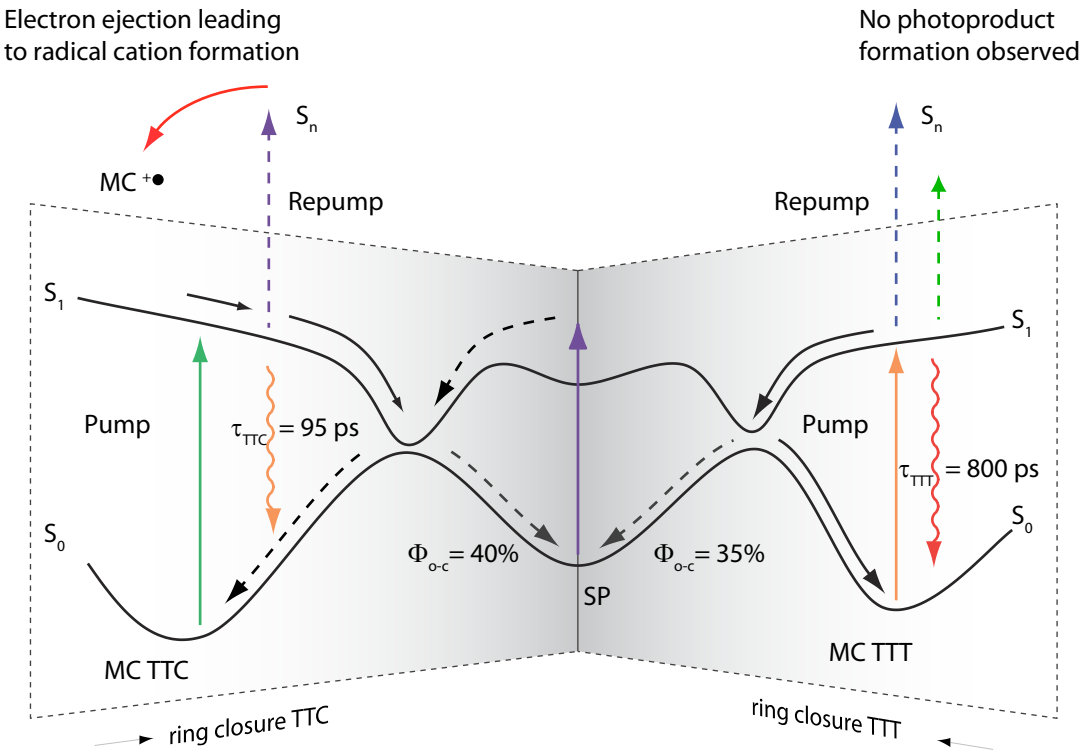

Figure 5.23: Comprehensive reaction scheme of 6,8-dinitro BIPS. Both MC isomers, predominant TTC (left) and blended TTT (right) perform efficient ring closure to SP via a conical intersection (gray, dashed), and SP forms at least TTC via a singlet ring opening (black, dashed). The remaining excited merocyanine molecules relax via fluorescence (undulated arrow) on a picosecond time-scale. Hot TTC forms after resonant excitation $MC^{+\bullet}$ while only IVR is observed for TTT. The arrow color denotes the excitation or emission wavelength while black/gray arrows denote non-radiative transitions.

$\tau_{TTC} \approx 95$ ps and TTT roughly 10 times slower with $\tau_{TTT} \approx 800$ ps. Every TTT band is red-shifted when compared to TTC, both showing stimulated emission (undulated arrows; TTC: orange, 610 nm; TTT: red, 650 nm) and an excited-state absorption at ≈ 450 nm (dashed arrows; TTC: violet, 445 nm; TTT: blue, 460 nm). For TTT an additional ESA in the visible spectral range is identified at 550 nm (dashed, green). Both isomers show a permanent bleach, indicating a loss channel with high yield ($\Phi_{o-c} \approx 40\%$ for TTC and $\Phi_{o-c} \approx 35\%$ for TTT) (gray dashed). While Hobley *et al.* speculated [217], in previous work in this group the photoproduct was identified as spiropyran (middle) by using transient mid-infrared spectroscopy [20, 58, 71]. The black, curved arrows denote ultrafast, non-radiative relaxation.

This electrocyclic ring-closure reaction was confirmed by pump–repump–probe spectroscopy, which excited merocyanine first and then re-excited photochemically generated spiropyran (violet arrow, 267 nm) resulting in newly formed merocyanine. This measurement was also performed vice versa. Thus, 6,8-dinitro BIPS really performs a complete and effective photocycle starting from all possible isomers (TTC, TTT, and SP) (Sec. 5.6.2). This efficiency compares well to a previous reported

full switching cycle of fulgides [196] demonstrating the potential of merocyanine in further electronic applications.

Furthermore, 2D electronic spectroscopy was implemented using an approach in pump–probe geometry as proposed by Jonas [75] (Sec. 5.5). More precisely, pulse-shaper generated double pulses were combined with a supercontinuum probe as first realized by Ogilvie and coworkers in the visible spectral range [220]. In the presented approach a LCD-based shaper was used to generate the phase-stable pulse pairs as compared to an acousto-optical modulator there. The identified merocyanine isomers in solution feature differing relaxation characteristics, which are directly evident in the 2D spectra. The probe pulse, covering the visible spectral range, allowed to simultaneously monitor the temporal changes over a broad spectral region. A considerable frequency shift in the ESA could be identified, due to the different time constants of the two isomers. Whereas the linear spectra corresponding to GSA and SE of both isomers overlap, the corresponding peaks in the 2D spectra could be clearly distinguished. The absence of cross peaks connecting TTC and TTT in the spectra corroborates that cis/trans photoisomerization is a negligible reaction channel. Hence, by means of broadband coherent two-dimensional electronic spectroscopy it is possible to directly visualize the excited-state and relaxation dynamics of a complex photoreactive molecular system.

Conventional pump–probe spectroscopy on multichannel reactive systems [20, 27] may require tedious and elaborate data analysis of many different data sets and combination of those results to retrieve information about the relevant pathways in an indirect procedure. If spectroscopic signatures from the involved species overlap significantly in transient spectra, it may even not be possible at all to disentangle the respective channels and to arrive at conclusive evidence. On the other hand, with 2D spectroscopy the different contributions are separated due to the second frequency axis, and, thus, one can directly read off the relevant photochemistry from the experimental 2D traces. Thus, the (qualitative) analysis is greatly simplified even though three rather than two pulses have to be employed in the experiment. Hence, coherent 2D electronic spectroscopy holds great promise not only for analyzing photophysical processes such as energy transport, but also for providing new insights into photochemical reactions with many (interconnected) pathways [78].

A second pump–repump–probe measurement clearly demonstrates the importance of reaction pathways not originating from the electronic ground state (Sec. 5.6.3). Here both isomers were excited into S_1, followed by a repump resonant with ESA, hence, highly excited states were reached. Via relaxation from these states previously insurmountable barriers may be crossed or other conical intersections become accessible. These processes possibly widen the array of available reaction pathways. Here, excitation of 6,8-dinitro BIPS resulted in the formation of a radical cation $MC^{+\bullet}$ (curved, red arrow) and not in an increased ring-closure or isomerization yield.

By combining electronic 2D spectroscopy with a subsequent repump pulse, electronic TE2D spectroscopy was realized for the first time (Sec. 5.7). This exemplary TE2D measurement clearly identified that excited TTC is responsible for generating $MC^{+\bullet}$,

while TTT just relaxes non-radiatively into S_1. The intrinsically preserved origin of the excited-state physics resolved via TE2D allows disentanglement of complicated systems consisting of more than one molecule, which even share combined excited states. This could allow the study of molecules relevant for photovoltaics, especially when multipulse-induced charge separation is observed [291] or when searching for (multi)photon reaction channels in heterogeneous electron transfer of dye-sensitized devices [292]. In addition, tracing a reaction path could also be beneficial for bond-forming dynamics of molecules adsorbed on surfaces [293–295] or for switching events in envisaged ultrafast data storage [196, 214].

In conclusion, all experiments described in this chapter clearly demonstrate that transient-absorption measurements only result in a partial photochemical picture of 6,8-dinitro BIPS because reaction pathways happening in excited states are not detected sufficiently. This assessment is in-line with the previous chapter about $(ZnTPP)_2$, where also additional measurements were necessary. With coherent 2D spectroscopy isomerization between two merocyanines isomers was shown to be a negligible reaction path. Pump–repump–probe measurements clearly identified two photoproducts (spiropyran and the radical cation $MC^{+\bullet}$), which are not detectable otherwise. Finally, TE2D spectroscopy identifies for which isomer in a molecular mixture twofold excitation leads to different pathways. Thus, accessing excited-state photochemistry is not only beneficial but also necessary for generating a comprehensive photochemical reaction scheme.

Chapter 6

Summary and Outlook

Light-induced excitation of matter, especially of atoms and molecules, proceeds commonly within femtoseconds, resulting in excited states. Originating from these states many interconnecting reaction pathways may set in and chemical reaction mechanisms, like isomerization or bond-breaking and formation are possible, resulting in photoproducts that are detectable by optical means. In addition, photophysical mechanisms like energy distribution and excitonic delocalization occur, often combined with radiative relaxation via fluorescence. Thus, the reaction scheme has to be disentangled by assessing the existence or importance of each process. Spectroscopic methods based on femtosecond laser pulses have emerged as a versatile tool to study photochromic reactions. Most commonly one pulse excites the sample, while a second one, variably delayed, detects changes in the effective absorption.

Within this thesis time-resolved experiments with femtosecond laser pulses on various molecular systems were performed. However, the presented work had two foci. On the one hand, novel photosystems, with possible applications ranging from ultrathin molecular wires to molecular switching devices, were extensively photochemically and -physically characterized. On the other hand, time-resolved broadband spectroscopic methods had to be newly developed, in order to resolve the complex kinetics of the investigated systems. This combined approach, i.e., tailoring new techniques to answer specific questions in unexplored photosystems, resulted in spectroscopic techniques which can easily be transferred to other scientific studies.

By combining an excitation pulse pair with an additional laser pulse, all in the visible spectral range, and a continuum probe electronic triggered-exchange two-dimensional spectroscopy (TE2D) was demonstrated for the first time. This goal was accomplished by first combining a transient-absorption setup with pump–repump–probe capability with a pulse shaper, capable of amplitude and phase shaping in the visible spectral range. Hence, 2D spectroscopy with a continuum probe was implemented similar to previous setups in different research groups, covering the ultraviolet (UV) [84], visible (VIS) [220], and mid/near-infrared (NIR) spectral range [94]. Via the continuum probe a much wider detection axis is generated compared to 2D spectroscopy with degenerate pulses.

Using the described methods two different molecular systems in solution were studied and characterized in a comprehensive manner in this thesis. A bisporphyrin, namely a directly β,β'-linked Zn-metallated tetraphenylporphyrin dimer, $(ZnTPP)_2$, and a representative of the spiropyran–merocyanine photosystem, 6,8-dinitro BIPS, were characterized for their possible future use in applications. $(ZnTPP)_2$ is a homodimer, featuring strong excitonic effects. These effects manifest themselves in twofold splitting of the Soret band (S_2) absorption spectrum. Interestingly, no splitting is seen for the Q band (S_1). Like $(ZnTPP)_2$, 6,8-dinitro BIPS is also constructed using two, this time differing, subunits. However, they are not similar enough to warrant a treatment as a heterodimer. The two chromophores are a benzopyran and an indole moiety, connected by a common carbon atom. 6,8-Dinitro BIPS itself exists in one of two possible conformations. The ring closed spiropyran absorbs only in the UV, by contrast the ring open merocyanine has a strong absorption in the visible spectral range. For both molecular systems photodynamics upon illumination were in a first step monitored using transient-absorption spectroscopy. However, the results of these experiments were ambiguous because of the multitude of obtained signals, necessitating more complex methods, which were subsequently employed.

In the case of $(ZnTPP)_2$ first the monomeric building block, ZnTPP itself, was characterized by transient absorption combined with elaborate global fitting routines. According to the results, population transfer from the S_2 state into S_1 within picoseconds was identified ($\tau(S_2) \approx 2$ ps). Afterwards, intersystem crossing into T_1 proceeds within nanoseconds ($\tau(S_1) \approx 2$ ns).

For $(ZnTPP)_2$ in principle the same pathways were found after excitation into the Soret and Q band, albeit the afterwards observed relaxation is faster. In addition, intersystem crossing was not only indirectly deduced but directly measured by probing in the NIR spectral range. There, singlet and triplet states were completely separable and the transfer proceeds with $\tau(S_1) \approx 1.5$ ns. The influence of excitons in this bisporphyrin was investigated by coherent 2D spectroscopy exciting and detecting the Soret band. Energy and population transfer within S_2 was directly visualized on a time-scale of ≈ 100 fs. This population transfer proceeds in combination with relaxation into S_1. The latter was estimated to be on the same time-scale making it impossible to extract the coupling without 2D measurements. Calculation of the 2D spectra of a simple homodimer confirmed the results. After the presented analysis of the distinct excitonic character, this molecule may serve as a unique building block for larger porphyrin arrays with applications ranging from asymmetric catalysis over biomimicry of electron-transfer to organic optical devices in the future [115]. The pronounced axial chirality, caused by the molecular frame, was not exploited as a racemic mixture was studied. Methods like time-resolved circular dichroism [296, 297] could allow the determination of chiral properties in future experiments.

The second studied photosystem was the molecular switch 6,8-dinitro BIPS, existing in two conformations. Merocyanine is the more stable form in thermal equilibrium. Transient-absorption measurements uncovered that the sample consisted of a molecular mixture of two different merocyanine isomers, referred to as TTC and TTT and defined by the respective cis (C) or trans (T) configurations in the methine bridge.

However, both isomers are capable of electrocyclic ring-closure with a quantum yield $\Phi_{o-c} > 35\%$, forming the spiropyran configuration. The remaining excited molecules return to the corresponding ground state radiatively ($\tau_{TTC} \approx 95$ ps, $\tau_{TTT} \approx 800$ ps). Conducting 2D measurements utilizing a continuum probe the differing photochemistry of both isomers was examined in a single measurement. No isomerization between these two conformations was detected, neither via a conical intersection nor in the excited state. Therefore, 6,8-dinitro BIPS performs a concerted switching with the single loss channel being fluorescence, despite the presence of two reactants. This direct switching without long-living intermediates was confirmed by utilizing a pump–repump–probe approach. 6,8-Dinitro BIPS can be closed by visible and opened by UV pulses using subsequent pulses. This mechanism via singlet pathways satisfies an important criterion for an unimolecular switching device [19]. The reversed direction was also successfully measured. A second pump–repump–probe experiment showed that the sample is ionized, resulting in a merocyanine radical cation, when the first excited state is resonantly excited into higher electronic states. Furthermore, by implementing triggered-exchange 2D spectroscopy, it was elucidated that only one isomer (TTC) was ionized, while the second one (TTT) exclusively relaxes back into the ground state by fluorescence originating from S_1.

Taking all this into account this thesis clearly showed that focusing both on the development of new techniques and characterizing new molecular systems yields progress in both areas at once. Deeper insight into the photodynamics of both $(ZnTPP)_2$, a bisporphyrin, and 6,8-dinitro BIPS, a spiropyran–merocyanine switching system, was gained by adapting transient absorption in the NIR spectral range, constructing a novel 2D setup in pump–probe geometry with a continuum probe, and combining it with multipulse excitation to coherent electronic triggered-exchange 2D spectroscopy. All techniques solved the questions for which they were constructed, but they are not limited to these cases. Especially TE2D opens new roads in photochemistry. By connecting reactant, product and the corresponding intermediates, a chemical reaction can be tracked through all stages, making unambiguous identification of the reactive states feasible. Thus, fundamental insight into the photochemistry of molecular compounds is gained.

Zusammenfassung

Nach Anregung mit Licht gelangen Atome und Moleküle innerhalb weniger Femtosekunden aus dem Grundzustand in angeregte Zustände. Aus diesen können verschiedene photochemische Reaktionspfade, wie Isomerisierung oder Bindungsbrüche und -verknüpfungen, einsetzen. Die hierdurch erzeugten Photoprodukte lassen sich oft über optische Methoden nachweisen. Neben diesen photochemischen Prozessen treten oft auch photophysikalische Effekte wie zum Beispiel die Umverteilung der Anregungsenergie und exzitonische Delokalisierungen auf. Daher ist es essentiell, die Existenz oder Bedeutung von möglichst vielen denkbaren Relaxationspfaden festzustellen um das Reaktionsschema des untersuchten Systems zu erhalten. Hierzu hat sich Ultrakurzzeitspektroskopie mit Femtosekundenlaserpulsen als vielfältiges Werkzeug herausgestellt um lichtinduzierte Reaktionen auf ihrer intrinsischen Zeitskala zu studieren. Dazu werden verschiedene Pulssequenzen genutzt. Beispielsweise kann ein erster Puls die Probe anregen, während ein zweiter durch Variation des relativen Pulsabstandes zeitaufgelöst Änderungen im Absorptionsverhalten misst.

Im Rahmen dieser Arbeit sind zeitaufgelöste Experimente mit Femtosekundenlaserpulsen an unterschiedlichen Verbindungen durchgeführt worden. Einerseits war der Schwerpunkt neuartige Molekülklassen, deren denkbare Anwendungen von ultradünnen Drähten bis hin zu molekularen Schaltern reichen, umfassend photodynamisch zu untersuchen. Andererseits sind neue breitbandige, zeitaufgelöste Spektroskopiemethoden entwickelt worden. Diese kombinierte Vorgehensweise – also das Maßschneidern neuer Techniken zur Aufklärung offener Fragestellungen an einem neuartigen Photosystem – resultierte in neuen spektroskopischen Methoden, die intuitiv auf andere wissenschaftliche Herausforderungen transferiert werden können.

Durch die Kombination eines Anregungspulspaars mit einem weiteren Laserpuls sowie einem Weißlichtkontinuum wurde zum ersten Mal elektronische zweidimensionale Spektroskopie mit ausgelöster Umwandlung („triggered-exchange 2D“, TE2D) demonstriert. Dies war durch die Implementierung eines Pulsformers in ein transientes Absorptionsspektrometer möglich. Eine wichtige Voraussetzung hierfür war die Möglichkeit zwei Anregepulse gleichzeitig nutzen zu können, was zusätzlich Anrege-Wiederanrege-Abfrage-Experimente ermöglichte. In einem ersten Experiment wurde die prinzipielle Eignung des Aufbaus dadurch getestet, dass 2D Spektroskopie mit Weißlichtabfrage implementiert wurde. Hierzu war die Vorgehensweise ähnlich zu bereits literaturbekannten Experimenten im ultravioletten [84], im sichtbaren [220] und infraroten Spektralbereich [94]. Der Vorteil der Verwendung eines Weißlichtkon-

tinuums als Abfragepuls ist die spektral breitere Abfrageachse verglichen mit der 2D Spektroskopie in der sogenannten Boxgeometrie und entarteten Pulsen.

In flüssiger Phase wurden diese Methoden dazu genutzt zwei verschiedene Verbindungsklassen zu untersuchen. Ein Bisporphyrin, das direkt β,β'-verknüpfte Zn-metallierte Tetraphenylporphyrindimer [$(ZnTPP)_2$] und ein dinitro-substituierter Spiropyran-Merocyanin Photoschalter (6,8-dinitro BIPS) wurden im Hinblick auf zukünftige Anwendungen charakterisiert. $(ZnTPP)_2$ ist ein Homodimer, in welchem sich starke exzitonische Einflüsse zeigen, z. B. durch das Aufspalten der Soret-Bande (S_2) im Absorptionsspektrum. Interessanterweise zeigt sich kein ähnliches Verhalten im Q-Band (S_1). Ähnlich zu $(ZnTPP)_2$ ist 6,8-dinitro BIPS auch aus zwei einzelnen, allerdings unterschiedlichen, Chromophoren zusammengesetzt. 6,8-Dinitro BIPS besteht aus zwei Konformeren. Zum einen liegt das stark im ultravioletten Spektralbereich absorbierende Spiropyran vor, welches über einen geschlossenen Pyranrest verfügt. Das zweite Konformer ist das planare Merocyanin, in welchem das Pyran geöffnet wurde. Auf Grund der geänderten Elektronendichteverteilung absorbiert Merocyanin zusätzlich im sichtbaren Spektralbereich. In einem ersten Schritt ist die Relaxationsdynamik nach Lichtanregung für beide Moleküle, 6,8-dinitro BIPS und $(ZnTPP)_2$ mittels transienter Absorptionsspektroskopie untersucht worden. Allerdings waren die Resultate auf Grund der vielen Signalbeiträge nicht eindeutig, so dass im Anschluss komplexere Messmethoden angewandt und entwickelt wurden.

Für das Studium des Bisporphyrins $(ZnTPP)_2$ wurde zuerst das zugrundeliegende Monomer ZnTPP transient untersucht und über eine globale Analyse wichtige Signalbeiträge extrahiert: Nach Lichtanregung relaxiert die angeregte Population aus dem S_2 in den S_1 Zustand auf einer Pikosekunden-Zeitskala ($\tau(S_2) \approx 2$ ps). Daran anschließend tritt Intersystem Crossing in T_1 ein ($\tau(S_1) \approx 2$ ns).

Für das Dimer selbst ergaben sich prinzipiell die gleichen Reaktionswege, allerdings mit höherer Reaktionsgeschwindigkeit. Dies ist sowohl durch Anregung direkt in die Soret- als auch in die Q-Bande überprüft worden. Das Intersystem Crossing mit $\tau(S_1) \approx 1.5$ ns wurde nicht nur indirekt abgeleitet, sondern durch Abfrage im nahinfraroten Spektalbereich direkt gemessen. Der Einfluss der Exzitonen auf das Bisporphyrin wurde durch kohärente 2D Spektroskopie innerhalb der Soret-Bande untersucht. Dies ermöglichte die Visualizierung von Energie- und Populationstransfer auf einer Zeitskala von ≈ 100 fs. Da dieser Populationstransfer mit Relaxierung in den S_1 Zustand verknüpft ist, konnten diese Prozesse alleine durch transiente Absorptionsmessungen nicht getrennt werden. Eine zusätzlich durchgeführte Berechnung der 2D Spektren eines einfachen Homodimers unterstützte die Resultate. Indem die hier vorgestellten Ergebnisse bezüglich der exzitonischen Eigenschaften gezielt ausgenützt werden, könnte $(ZnTPP)_2$ als Baustein für größere Porphyrinsysteme dienen. Deren denkbare zukünftige Anwendungen reichen von asymmetrischer Katalyse über die Nachahmung von biologischem Elektronentransfer hinzu organo-optischen Geräten [115]. Die betonte axiale Chiralität des Systems wurde in den vorgestellten Experimenten nicht ausgenutzt, da eine racemische Lösung vorlag. Daher könnten Methoden wie die zeitaufgelöste Messung des Circulardichroismus [296, 297] noch zusätzlich die chiralen Eigenschaften analysieren.

Das zweite untersuchte System war der molekulare Schalter 6,8-dinitro BIPS, bestehend aus zwei Konformeren. Hierbei ist im thermischen Gleichgewicht Merocyanin die stabile Form. Transiente Absorptionsmessungen deckten auf, dass die Lösung zusätzlich aus zwei Merocyanin-Isomeren besteht, die gemäß der Cis (C) oder Trans (T) Konfiguration innerhalb der Methinbrücke als TTC oder TTT bezeichnet werden. Im gleichen Experiment ergab sich, dass beide Isomere fähig sind eine elektrozyklische Ringschlussreaktion mit einer Effizienz von $\Phi_{o-c} > 35\%$ zum Spiropyran durchzuführen. Der verbleibende Anteil der angeregten Population kehrt über Fluoreszenz in den Grundzustand zurück ($\tau_{TTC} \approx 95$ ps, $\tau_{TTT} \approx 800$ ps). Mit Hilfe eines kohärenten 2D Spektrums konnte die sich unterscheidente Photochemie beider Isomere innerhalb einer einzigen Messung aufgezeigt werden. Zusätzlich wurde keine Isomerisierung zwischen ihnen beobachtet, weder durch eine konische Durchschneidung, noch direkt im angeregten Zustand. Damit steht fest, dass 6,8-dinitro BIPS entweder eine konzertierte Reaktion zum Spiropyran durchführt oder über Fluoreszenz komplett relaxiert, obwohl zwei Edukte vorliegen, die im identischen Produkt enden können. Der direkte Schaltvorgang ohne langlebige Zwischenprodukte wurde eindeutig über Anrege–Wiederanrege–Abfrage Spektroskopie nachgewiesen. Hierfür wurde 6,8-dinitro BIPS in der Meroform zuerst mit sichtbarem Licht geschlossen und anschließend mit ultraviolettem Licht wieder geöffnet. Dieser schnelle Schaltvorang, der über Singulett-Zustände abläuft und auch für die Rückrichtung gezeigt wurde, ist ein wichtiges Kriterium für einen funktionierenden molekularen Photoschalter [19]. Ein zweites, ähnliches Experiment zeigte, dass 6,8-dinitro BIPS zusätzlich ionisiert werden kann, wenn die Population im angeregten Zustand resonant wiederangeregt wird. Das neugebildete langlebige Produkt konnte einem Merocyaninkation zugeordnet werden. Zusätzlich durch die Verwendung der neuen elektronischen TE2D Methode ist aufgezeigt worden, dass lediglich das TTC Isomer ionisiert werden kann, wohingegen das zweite Isomer (TTT) strahlend in den Grundzustand zurückkehrt.

Zusammengefasst gilt, dass durch die gleichzeitige Fokussierung auf die Methodenentwicklung und die Charakterisierung von unerforschten Verbindungen Fortschritte in beiden Gebieten erzielt wurden. Ein tieferes Verständnis über die Dynamiken des Porphyrindimers $(ZnTPP)_2$ und die des molekularen Schalters 6,8-dinitro BIPS wurden durch Erweiterungen an einem transienten Absorptionsspektrometers, den Aufbau eines kohärenten 2D Spektrometers in Anrege-Abfrage-Geometrie und durch die Kombination von letzterem mit Mehrfachpulsanregung zu TE2D Spektroskopie gewonnen. Insbesondere letzteres eröffnet neue Möglichkeiten in der Photochemie, da Edukte, Produkte und die zugehörigen Zwischenzuständen miteinander verknüpft werden, wodurch lichtinduzierte Reaktionen schrittweise nachvollzogen werden können.

List of Abbreviations

$(ZnTPP)_2$ bis[tetraphenylporphyrinato-zinc(II)]

2D two-dimensional

Ag silver

Al aluminum

BBO β-barium-borat

BIPS 1',3',3'-trimethylspiro[2H-1-benzopyran-2,2'-indoline]

CaF_2 calciumfluoride

CI conical intersection

DADS decay-associated difference spectrum

DFG difference frequency generation

DFT density functional theory

DS difference spectra

EADS evolution-associated difference spectrum

ESA excited-state absorption

FROG frequency-resolved optical gating

FT Fourier transform/transformation

GSA ground-state absorption

GSB ground-state bleach

HOMO highest occupied molecular orbital

IC internal conversion

IRF instrument response function

ISC intersystem crossing

IVR intramolecular vibrational relaxation

lg decadic logarithm

LUMO lowest unoccupied molecular orbital

MC merocyanine

ND neutral density

NIR near-infrared (spectral range)

NOPA non-collinear optical parametric amplification

OPA optical parametric amplification

P pump pulse

PA product absorption

Pr probe pulse

R repump pulse

SCG super continuum generation

SE stimulated emission

SFG sum frequency generation

SHG second harmonic generation

SVEA slowly-varying envelope approximation

SP spiropyran

TA transient-absorption (spectroscopy)

TE2D triggered-exchange two-dimensional spectroscopy

THG third harmonic generation

UV ultraviolet (spectral range)

VIS visible (spectral range)

ZnTPP 5,10,15,20-tetraphenylporphyrin

(ZnTPP)$_2$ β,β'-linked ZnTPP dimer

Bibliography

[1] V. Smil.
Detonator of the Population Explosion.
Nature **400**, 415–415 (1999).

[2] G. Ertl.
Reactions at Surfaces: From Atoms to Complexity (Nobel Lecture).
Angew. Chem. Int. Ed. **47**, 3524–3535 (2008).

[3] V. V. Krongauz and A. D. Trifunac.
Processes in Photoreactive Polymers.
Springer (1995).

[4] P. Rudolf, J. Buback, J. Aulbach, P. Nuernberger, and T. Brixner.
Ultrafast Multisequential Photochemistry of 5-Diazo Meldrum's Acid.
J. Am. Chem. Soc. **132**, 15213–15222 (2010).

[5] R. Trebino.
Frequency-Resolved Optical Gating: The Measurement of Ultrashort Laser Pulses.
Har/Cdr edition. Springer Netherlands (2002).

[6] G. Wedler.
Lehrbuch der Physikalischen Chemie.
Fifth edition. Wiley-VCH Verlag GmbH & Co. KGaA (2004).

[7] U. Keller, G. W. t'Hooft, W. H. Knox, and J. E. Cunningham.
Femtosecond Pulses from a Continuously Self-Starting Passively Mode-Locked Ti:Sapphire Laser.
Opt. Lett. **16**, 1022–1024 (1991).

[8] S. Mukamel.
Principles of Nonlinear Optical Spectroscopy.
First edition. Oxford University Press, New York (1999).

[9] D. Tannor.
Introduction to Quantum Mechanics: A Time-Dependent Perspective.
University Science Books, Sausalito (2007).

[10] A. H. Zewail.
Femtochemistry: Atomic-Scale Dynamics of the Chemical Bond.
J. Phys. Chem. A **104**, 5660–5694 (2000).

[11] W. P. Aue, E. Bartholdi, and R. R. Ernst.
Two-dimensional spectroscopy. Application to nuclear magnetic resonance.
J. Chem. Phys. **64**, 2229–2246 (1976).

[12] J. Jeener, B. H. Meier, P. Bachmann, and R. R. Ernst.
Investigation of exchange processes by two-dimensional NMR spectroscopy.
J. Chem. Phys. **71**, 4546–4553 (1979).

[13] J. D. Hybl, A. W. Albrecht, S. M. G. Faeder, and D. M. Jonas.
Two-Dimensional Electronic Spectroscopy.
Chem. Phys. Lett. **297**, 307–313 (1998).

[14] L. Lepetit and M. Joffre.
Two-dimensional nonlinear optics using Fourier-transform spectral interferometry.
Opt. Lett. **21**, 564–566 (1996).

[15] T. Brixner, J. Stenger, H. M. Vaswani, M. Cho, R. E. Blankenship, and G. R. Fleming.
Two-Dimensional Spectroscopy of Electronic Couplings in Photosynthesis.
Nature **434**, 625–628 (2005).

[16] M. Diekmann.
Kohärente multidimensionale Spektroskopie an Merocyanin-Isomeren.
Diplomarbeit, Universität Würzburg (2012).

[17] S. L. Logunov, V. V. Volkov, M. Braun, and M. A. El-Sayed.
The Relaxation Dynamics of the Excited Electronic States of Retinal in Bacteriorhodopsin by Two-Pump-Probe Femtosecond Studies.
Proc. Nat. Acad. Sci. U.S.A. **98**, 8475 –8479 (2001).

[18] L. R. Milgrom.
The Colours of Life: An Introduction to the Chemistry of Porphyrins and Related Compounds.
Oxford University Press (1997).

[19] B. L. Feringa.
Molecular Switches.
Wiley-VCH Verlag GmbH, Berlin (2001).

[20] J. Buback, M. Kullmann, F. Langhojer, P. Nuernberger, R. Schmidt, F. Würthner, and T. Brixner.
Ultrafast Bidirectional Photoswitching of a Spiropyran.
J. Am. Chem. Soc. **132**, 16510–16519 (2010).

[21] H. Dürr and H. Bouas-Laurent.
Photochromism: Molecules and Systems.
Elsevier, Amsterdam (2003).

[22] R. W. Boyd.
Nonlinear Optics.
Third edition. Academic Press, Burlington (2008).

[23] A. E. Siegman.
Lasers.
University Science Books, Sausalito (1986).

[24] J. Diels and W. Rudolph.
Ultrashort Laser Pulse Phenomena: Fundamentals, Techniques, and Applications on a Femtosecond Time Scale (Optics and Photonics Series).
Second edition. Academic Press Inc (2006).

[25] M. Wollenhaupt, A. Assion, and T. Baumert.
Femtosecond Laser Pulses: Linear Properties, Manipulation, Generation and Measurement.
In *Springer Handbook of Lasers and Optics*, pp. 937–983. Springer Science+Business Media, New York (2007).

[26] U. Megerle, I. Pugliesi, C. Schriever, C. Sailer, and E. Riedle.
Sub-50 fs Broadband Absorption Spectroscopy with Tunable Excitation: Putting the Analysis of Ultrafast Molecular Dynamics on Solid Ground.
Appl. Phys. B **96**, 215–231 (2009).

[27] J. Buback, P. Nuernberger, M. Kullmann, F. Langhojer, R. Schmidt, F. Würthner, and T. Brixner.
Ring-Closure and Isomerization Capabilities of Spiropyran-Derived Merocyanine Isomers.
J. Phys. Chem. A **115**, 3924–3935 (2011).

[28] J. Eichler, L. Dünkel, and B. Eppich.
Die Strahlqualität von Lasern.

Laser Journal **1**, 63–66 (2004).

[29] P. A. Franken, A. E. Hill, C. W. Peters, and G. Weinreich.
Generation of Optical Harmonics.
Phys. Rev. Lett. **7**, 118 (1961).

[30] G. Cerullo and S. D. Silvestri.
Ultrafast Optical Parametric Amplifiers.
Rev. Sci. Instrum. **74**, 1–18 (2003).

[31] R. R. Alfano and S. L. Shapiro.
Emission in the Region 4000 to 7000 Å Via Four-Photon Coupling in Glass.
Phys. Rev. Lett. **24**, 584 – 587 (1970).

[32] I. Buchvarov, A. Trifonov, and T. Fiebig.
Toward an Understanding of White-Light Generation in Cubic Media - Polarization Properties Across the Entire Spectral Range.
Opt. Lett. **32**, 1539–1541 (2007).

[33] W. Wadsworth, A. Ortigosa-Blanch, J. Knight, T. Birks, T. Man, and P. Russell.
Supercontinuum Generation in Photonic Crystal Fibers and Optical Fiber Tapers: a Novel Light Source.
J. Opt. Soc. Am. B **19**, 2148–2155 (2002).

[34] M. Förster.
Design and Implementation of Four-Wave-Mixing Setups in the Ultraviolet Regime.
Masterarbeit, Würzburg (2011).

[35] R. Trebino, K. W. DeLong, D. N. Fittinghoff, J. N. Sweetser, M. A. Krumbügel, B. A. Richman, and D. J. Kane.
Measuring Ultrashort Laser Pulses in the Time-Frequency Domain Using Frequency-Resolved Optical Gating.
Rev. Sci. Instrum. **68**, 3277–3295 (1997).

[36] L. Lepetit, G. Chériaux, and M. Joffre.
Linear Techniques of Phase Measurement by Femtosecond Spectral Interferometry for Applications in Spectroscopy.
J. Opt. Soc. Am. B **12**, 2467–2474 (1995).

[37] C. Dorrer and I. A. Walmsley.
Accuracy Criterion for Ultrashort Pulse Characterization Techniques: Application to Spectral Phase Interferometry for Direct Electric Field Reconstruction.
J. Opt. Soc. Am. B **19**, 1019–1029 (2002).

[38] P. Baum, S. Lochbrunner, and E. Riedle.
Zero-Additional-Phase SPIDER: Full Characterization of Visible and Sub-20-fs Ultraviolet Pulses.
Opt. Lett. **29**, 210–212 (2004).

[39] I. Amat-Roldán, I. Cormack, P. Loza-Alvarez, E. Gualda, and D. Artigas.
Ultrashort Pulse Characterisation with SHG Collinear-FROG.
Opt. Express **12**, 1169–1178 (2004).

[40] A. Galler and T. Feurer.
Pulse Shaper Assisted Short Laser Pulse Characterization.
Appl. Phys. B **90**, 427–430 (2008).

[41] F. Schwabl.
Quantenmechanik.
6th edition. Springer, Berlin (2007).

[42] W. Demtröder.
Experimentalphysik, Bd. 3. Atome, Moleküle und Festkörper.
Third edition. Springer, Berlin (2005).

[43] F. Bernardi, M. Olivucci, and M. A. Robb.
Potential Energy Surface Crossings in Organic Photochemistry.
Chem. Soc. Rev. **25**, 321–328 (1996).

[44] K. K. Rohatgi-Mukherjee.
Fundamentals of Photochemistry.
John Wiley & Sons (Asia) Pte Ltd (1978).

[45] H. G. O. Becker.
Einführung in die Photochemie.
Second edition. Thieme Georg Verlag (1989).

[46] R. Schoenlein, L. Peteanu, R. Mathies, and C. Shank.
The First Step in Vision: Femtosecond Isomerization of Rhodopsin.
Science **254**, 412–415 (1991).

[47] Q. Wang, R. W. Schoenlein, L. A. Peteanu, R. A. Mathies, and C. V. Shank.
Vibrationally Coherent Photochemistry in the Femtosecond Primary Event of Vision.
Science **266**, 422–424 (1994).

[48] J. Briand, O. Bräm, J. Réhault, J. Léonard, A. Cannizzo, M. Chergui, V. Zanirato, M. Olivucci, J. Helbing, and S. Haacke.
Coherent Ultrafast Torsional Motion and Isomerization of a Biomimetic Dipolar Photoswitch.
Phys. Chem. Chem. Phys. **12**, 3178 (2010).

[49] D. R. Yarkony.
Diabolical Conical Intersections.
Rev. Mod. Phys. **68**, 985 (1996).

[50] G. Vogt, P. Nuernberger, T. Brixner, and G. Gerber.
Femtosecond Pump-Shaped-Dump Quantum Control of Retinal Isomerization in Bacteriorhodopsin.
Chem. Phys. Lett. **433**, 211–215 (2006).

[51] W. Domcke, D. R. Yarkony, and H. Koppel.
Conical Intersections: Electronic Structure, Dynamics and Spectroscopy.
World Scientific Publishing (2004).

[52] P. Maine, D. Strickland, P. Bado, M. Pessot, and G. Mourou.
Generation of Ultrahigh Peak Power Pulses by Chirped Pulse Amplification.
IEEE J. Quantum Electron. **24**, 398–403 (1988).

[53] L. C. Ltd.
TOPAS White - Data Sheet.

[54] F. Langhojer.
New Techniques in Liquid-Phase Ultrafast Spectroscopy.
Dissertation, Universität Würzburg (2009).

[55] D. V. O'Connor and D. Phillips.
Time-Correlated Single Photon Counting.
Academic Pr (1984).

[56] C. Min, T. Joo, M. Yoon, C. M. Kim, Y. N. Hwang, D. Kim, N. Aratani, N. Yoshida, and A. Osuka.
Transient Absorption Anisotropy Study of Ultrafast Energy Transfer in Porphyrin Monomer, its Direct Meso–Meso Coupled Dimer and Trimer.
J. Chem. Phys. **114**, 6750–6758 (2001).

[57] H. E. Lessing and A. V. Jena.
Separation of Rotational Diffusion and Level Kinetics in Transient Absorption Spectroscopy.
Chem. Phys. Lett. **42**, 213–217 (1976).

[58] J. Buback.
Femtochemistry of Pericyclic Reactions and Advances towards Chiral Control.

Dissertation, Universität Würzburg (2011).

[59] S. A. Kovalenko, A. L. Dobryakov, J. Ruthmann, and N. P. Ernsting.
Femtosecond Spectroscopy of Condensed Phases with Chirped Supercontinuum Probing.
Phys. Rev. A **59**, 2369–2384 (1999).

[60] K. Ekvall, P. van der Meulen, C. Dhollande, L. Berg, S. Pommeret, R. Naskrecki, and J. Mialocq.
Cross Phase Modulation Artifact in Liquid Phase Transient Absorption Spectroscopy.
J. Appl. Phys. **87**, 2340 (2000).

[61] M. Lorenc, M. Ziolek, R. Naskrecki, J. Karolczak, J. Kubicki, and A. Maciejewski.
Artifacts in Femtosecond Transient Absorption Spectroscopy.
Appl. Phys. B **74**, 19–27 (2002).

[62] M. Rasmusson, A. N. Tarnovsky, E. Åkesson, and V. Sundström.
On the Use of Two-Photon Absorption for Determination of Femtosecond Pump-Probe Cross-Correlation Functions.
Chem. Phys. Lett. **335**, 201–208 (2001).

[63] G. S. Vogt.
Adaptive Femtosekunden-Quantenkontrolle komplexer Moleküle in kondensierter Phase.
Dissertation, Universität Würzburg (2006).

[64] I. H. M. van Stokkum, D. S. Larsen, and R. van Grondelle.
Global and Target Analysis of Time-Resolved Spectra.
Biochim. Biophys. Acta, Bioenerg. **1657**, 82–104 (2004).

[65] J. J. Snellenburg, S. P. Laptenok, R. Seger, K. M. Mullen, and I. H. M. van Stokkum.
Glotaran: a Java-Based Graphical User Interface for the R-Package TIMP.
J. Stat. Softw. **49** (2012).

[66] K. M. Mullen and I. H. M. van Stokkum.
TIMP: An R Package for Modeling Multi-way Spectroscopic Measurements.
J. Stat. Softw. **18**, 1–46 (2007).

[67] F. Milota, V. I. Prokhorenko, T. Mančal, H. von Berlepsch, O. Bixner, H. F. Kauffmann, and J. Hauer.
Vibronic and Vibrational Coherences in Two-Dimensional Electronic Spectra of Supramolecular J-Aggregates.
J. Phys. Chem. A (2013).

[68] J. A. Myers, K. L. M. Lewis, F. D. Fuller, P. F. Tekavec, C. F. Yocum, and J. P. Ogilvie.
Two-Dimensional Electronic Spectroscopy of the D1-D2-cyt b559 Photosystem II Reaction Center Complex.
J. Phys. Chem. Lett. **1**, 2774–2780 (2010).

[69] C. Consani, G. Auböck, F. van Mourik, and M. Chergui.
Ultrafast Tryptophan-to-Heme Electron Transfer in Myoglobins Revealed by UV 2D Spectroscopy.
Science **339**, 1586–1589 (2013).

[70] O. A. Sytina, I. H. M. van Stokkum, R. van Grondelle, and M. L. Groot.
Single and Multi-Exciton Dynamics in Aqueous Protochlorophyllide Aggregates.
J. Phys. Chem. A **115**, 3936–3946 (2011).

[71] M. Kullmann.
Transiente Absorptionsspektroskopie an einem molekularen Schalter auf Spiropyranbasis.
Diplomarbeit, Universität Würzburg (2009).

[72] D. Reitzenstein, T. Quast, F. Kanal, M. Kullmann, S. Ruetzel, M. S. Hammer, C. Deibel, V. Dyakonov, T. Brixner, and C. Lambert.
Synthesis and Electron Transfer Characteristics of a Neutral, Low-Band-Gap, Mixed-Valence Polyradical.
Chem. Mater. **22**, 6641–6655 (2010).

[73] T. Quast.
Spectroscopic Investigations of Charge-Transfer Processes and Polarisation Pulse Shaping in the Visible Spectral Range.
Dissertation, Universität Würzburg (2012).

[74] S. Mukamel.
Multidimensional Femtosecond Correlation Spectroscopies of Electronic and Vibrational Excitations.
Annu. Rev. Phys. Chem. **51**, 691–729 (2000).

[75] D. M. Jonas.
Two-Dimensional Femtosecond Spectroscopy.
Annu. Rev. Phys. Chem. **54**, 425–463 (2003).

[76] M. Cho.
Two-Dimensional Optical Spectroscopy.
CRC Press, Boca Raton, FL (2009).

[77] J. P. Ogilvie, K. J. Kubarych, P. R. Berman, and C. C. L. E. Arimondo.
Multidimensional Electronic and Vibrational Spectroscopy: An Ultrafast Probe of Molecular Relaxation and Reaction Dynamics (Chapter 5).
Adv. At. Mol. Opt. Phys. **57**, 249–321 (2009).

[78] M. Kullmann, S. Ruetzel, J. Buback, P. Nuernberger, and T. Brixner.
Reaction Dynamics of a Molecular Switch Unveiled by Coherent Two-Dimensional Electronic Spectroscopy.
J. Am. Chem. Soc. **133**, 13074–13080 (2011).

[79] P. Hamm, M. Lim, and R. M. Hochstrasser.
Structure of the Amide I Band of Peptides Measured by Femtosecond Nonlinear-Infrared Spectroscopy.
J. Phys. Chem. B **102**, 6123–6138 (1998).

[80] O. Golonzka, M. Khalil, N. Demirdöven, and A. Tokmakoff.
Vibrational Anharmonicities Revealed by Coherent Two-Dimensional Infrared Spectroscopy.
Phys. Rev. Lett. **86**, 2154–2157 (2001).

[81] T. Brixner, I. V. Stiopkin, and G. R. Fleming.
Tunable Two-Dimensional Femtosecond Spectroscopy.
Opt. Lett. **29**, 884–886 (2004).

[82] M. L. Cowan, J. P. Ogilvie, and R. J. D. Miller.
Two-dimensional Spectroscopy Using Diffractive Optics Based Phased-Locked Photon Echoes.
Chem. Phys. Lett. **386**, 184–189 (2004).

[83] U. Selig, F. Langhojer, F. Dimler, T. Löhrig, C. Schwarz, B. Gieseking, and T. Brixner.
Inherently Phase-Stable Coherent Two-Dimensional Spectroscopy Using only Conventional Optics.
Opt. Lett. **33**, 2851–2853 (2008).

[84] C. Tseng, S. Matsika, and T. C. Weinacht.
Two-Dimensional Ultrafast Fourier Transform Spectroscopy in the Deep Ultraviolet.
Opt. Express **17**, 18788–18793 (2009).

[85] U. Selig, C. Schleussner, M. Foerster, F. Langhojer, P. Nuernberger, and T. Brixner.
Coherent Two-Dimensional Ultraviolet Spectroscopy in Fully Noncollinear Geometry.
Opt. Lett. **35**, 4178–4180 (2010).

[86] B. A. West and A. M. Moran.
Two-Dimensional Electronic Spectroscopy in the Ultraviolet Wavelength Range.
J. Phys. Chem. Lett. **3**, 2575–2581 (2012).

[87] P. Hamm, J. Helbing, and J. Bredenbeck.
Two-Dimensional Infrared Spectroscopy of Photoswitchable Peptides.
Annu. Rev. Phys. Chem. **59**, 291–317 (2008).

[88] T. Brixner, T. Mančal, I. V. Stiopkin, and G. R. Fleming.
Phase-Stabilized Two-Dimensional Electronic Spectroscopy.
J. Chem. Phys. **121**, 4221–4236 (2004).

[89] J. A. Myers, K. L. Lewis, P. F. Tekavec, and J. P. Ogilvie.
Two-Color Two-Dimensional Fourier Transform Electronic Spectroscopy with a Pulse-Shaper.
Opt. Express **16**, 17420–17428 (2008).

[90] H. Tan.
Theory and Phase-Cycling Scheme Selection Principles of Collinear Phase Coherent Multi-Dimensional Optical Spectroscopy.
J. Chem. Phys. **129**, 124501 (2008).

[91] M. Motzkus, S. Pedersen, and A. H. Zewail.
Femtosecond Real-Time Probing of Reactions. 19. Nonlinear (DFWM) Techniques for Probing Transition States of Uni- and Bimolecular Reactions.
J. Phys. Chem. **100**, 5620–5633 (1996).

[92] U. Selig-Parthey.
Methods of Nonlinear Femtosecond Spectroscopy in the Visible and Ultraviolet Regime and their Application to Coupled Multichromophore Systems.
Dissertation, Universität Würzburg (2012).

[93] V. Volkov, R. Schanz, and P. Hamm.
Active phase stabilization in Fourier-transform two-dimensional infrared spectroscopy.
Opt. Lett. **30**, 2010–2012 (2005).

[94] S. Shim and M. T. Zanni.
How to Turn Your Pump–Probe Instrument into a Multidimensional Spectrometer: 2D IR and VIS Spectroscopies via Pulse Shaping.
Phys. Chem. Chem. Phys. **11**, 748–761 (2009).

[95] C. Schleussner.
Design and Implementation of a Coherent Two-Dimensional Spectroscopy Setup for the Ultraviolet.
Masterarbeit, Universität Würzburg (2009).

[96] U. Selig.
Kohärente 2D Spektroskopie bei breitbandiger Anregung im sichtbaren Spektralbereich.
Diplomarbeit, Universität Würzburg (2007).

[97] J. L. Martin and M. H. Vos.
Femtosecond Biology.
Annu. Rev. Biophys. **21**, 199–222 (1992).

[98] V. Sundström.
Femtobiology.
Annu. Rev. Phys. Chem. **59**, 53–77 (2008).

[99] S. A. Priola, A. Raines, and W. S. Caughey.
Porphyrin and Phthalocyanine Antiscrapie Compounds.
Science **287**, 1503–1506 (2000).

[100] E. D. Sternberg, D. Dolphin, and C. Brückner.
Porphyrin-Based Photosensitizers for Use in Photodynamic Therapy.
Tetrahedron **54**, 4151–4202 (1998).

[101] C. A. Mirkin and M. A. Ratner.
Molecular Electronics.
Annu. Rev. Phys. Chem. **43**, 719–754 (1992).

[102] R. K. Lammi, A. Ambroise, T. Balasubramanian, R. W. Wagner, D. F. Bocian, D. Holten, and J. S. Lindsey.

Structural Control of Photoinduced Energy Transfer between Adjacent and Distant Sites in Multiporphyrin Arrays.
J. Am. Chem. Soc. **122**, 7579–7591 (2000).

[103] P. G. van Patten, A. P. Shreve, J. S. Lindsey, and R. J. Donohoe.
Energy-Transfer Modeling for the Rational Design of Multiporphyrin Light-Harvesting Arrays.
J. Phys. Chem. B **102**, 4209–4216 (1998).

[104] M. Andersson, J. Davidsson, L. Hammarström, J. Korppi-Tommola, and T. Peltola.
Photoinduced Electron Transfer Reactions in a Porphyrin-Viologen Complex: Observation of S2 to S1 Relaxation and Electron Transfer from the S2 State.
J. Phys. Chem. B **103**, 3258–3262 (1999).

[105] J. Petersson, M. Eklund, J. Davidsson, and L. Hammarström.
Ultrafast Electron Transfer Dynamics of a Zn(II)porphyrin-Viologen Complex Revisited: S2 vs S1 Reactions and Survival of Excess Excitation Energy.
J. Phys. Chem. B **114**, 14329–14338 (2010).

[106] H. Imahori, S. Kang, H. Hayashi, M. Haruta, H. Kurata, S. Isoda, S. E. Canton, Y. Infahsaeng, A. Kathiravan, T. Pascher, P. Chábera, A. P. Yartsev, and V. Sundström.
Photoinduced Charge Carrier Dynamics of Zn-Porphyrin-TiO2 Electrodes: The Key Role of Charge Recombination for Solar Cell Performance.
J. Phys. Chem. A **115**, 3679–3690 (2011).

[107] M. Yoon, D. H. Jeong, S. Cho, D. Kim, H. Rhee, and T. Joo.
Ultrafast Transient Dynamics of Zn(II) Porphyrins: Observation of Vibrational Coherence by Controlling Chirp of Femtosecond Pulses.
J. Chem. Phys. **118**, 164 (2003).

[108] R. Kumble, S. Palese, V. S. Lin, M. J. Therien, and R. M. Hochstrasser.
Ultrafast Dynamics of Highly Conjugated Porphyrin Arrays.
J. Am. Chem. Soc. **120**, 11489–11498 (1998).

[109] D. Kim and A. Osuka.
Photophysical Properties of Directly Linked Linear Porphyrin Arrays.
J. Phys. Chem. A **107**, 8791–8816 (2003).

[110] J. S. Baskin, H. Yu, and A. H. Zewail.
Ultrafast Dynamics of Porphyrins in the Condensed Phase: I. Free Base Tetraphenylporphyrin.
J. Phys. Chem. A **106**, 9837–9844 (2002).

[111] G. A. Lott, A. Perdomo-Ortiz, J. K. Utterback, J. R. Widom, A. Aspuru-Guzik, and A. H. Marcus.
Conformation of Self-Assembled Porphyrin Dimers in Liposome Vesicles by Phase-Modulation 2D Fluorescence Spectroscopy.
Proc. Natl. Acad. Sci. U.S.A. **108**, 16521–16526 (2011).

[112] A. Perdomo-Ortiz, J. R. Widom, G. A. Lott, A. Aspuru-Guzik, and A. H. Marcus.
Conformation and Electronic Population Transfer in Membrane-Supported Self-Assembled Porphyrin Dimers by 2D Fluorescence Spectroscopy.
J. Phys. Chem. B **116**, 10757–10770 (2012).

[113] M. Yoon, S. Lee, S. Tokuji, H. Yorimitsu, A. Osuka, and D. Kim.
Homoconjugation in Diporphyrins: Excitonic Behaviors in Singly and Doubly Linked Zn(II)porphyrin Dimers.
Chem. Sci. **4**, 1756–1764 (2013).

[114] G. Bringmann, S. Rüdenauer, D. C. G. Götz, T. A. M. Gulder, and M. Reichert.
Axially Chiral Directly beta,beta'-Linked Bisporphyrins: Synthesis and Stereostructure.
Org. Lett. **8**, 4743–4746 (2006).

[115] G. Bringmann, D. C. G. Götz, T. A. M. Gulder, T. H. Gehrke, T. Bruhn, T. Kupfer, K. Radacki, H. Braunschweig, A. Heckmann, and C. Lambert.
Axially Chiral beta,beta'-Bisporphyrins: Synthesis and Configurational Stability Tuned by the Central Metals.
J. Am. Chem. Soc. **130**, 17812–17825 (2008).

[116] M. Kullmann, A. Hipke, P. Nuernberger, T. Bruhn, D. C. G. Götz, M. Sekita, D. M. Guldi, G. Bringmann, and T. Brixner.
Ultrafast Exciton Dynamics after Soret- or Q-Band Excitation of a Directly beta,beta'-Linked Bisporphyrin.
Phys. Chem. Chem. Phys. **14**, 8038–8050 (2012).

[117] F. Koch, M. Kullmann, U. Selig, P. Nuernberger, D. C. G. Götz, G. Bringmann, and T. Brixner.
Coherent Two-Dimensional Electronic Spectroscopy in the Soret Band of a Chiral Porphyrin Dimer.
New J. Phys. **15**, 025006 (2013).

[118] Y. Nakamura, I. Hwang, N. Aratani, T. K. Ahn, D. M. Ko, A. Takagi, T. Kawai, T. Matsumoto, D. Kim, and A. Osuka.
Directly meso-meso Linked Porphyrin Rings: Synthesis, Characterization, and Efficient Excitation Energy Hopping.
J. Am. Chem. Soc. **127**, 236–246 (2005).

[119] N. Yoshida and A. Osuka.
First Optical Resolution of meso-meso Linked Diporphyrin.
Tetrahedron Lett. **41**, 9287–9291 (2000).

[120] H. S. Cho, N. W. Song, Y. H. Kim, S. C. Jeoung, S. Hahn, D. Kim, S. K. Kim, N. Yoshida, and A. Osuka.
Ultrafast Energy Relaxation Dynamics of Directly Linked Porphyrin Arrays.
J. Phys. Chem. A **104**, 3287–3298 (2000).

[121] M. Biesaga, K. Pyrzyńska, and M. Trojanowicz.
Porphyrins in Analytical Chemistry. A Review.
Talanta **51**, 209–224 (2000).

[122] K. M. Kadish, R. Guilard, and K. M. Smith.
Handbook of Porphyrin Science: With Applications to Chemistry, Physics, Materials Science, Engineering, Biology and Medicine, volume 1.
First edition. World Scientific Publishing Company (2010).

[123] H. Rzepa.
The Aromaticity of Pericyclic Reaction Transition States.
J. Chem. Educ. **84**, 1535–1540 (2007).

[124] E. Rabinowitch.
Spectra of Porphyrins and Chlorophyll.
Rev. Mod. Phys. **16**, 226–235 (1944).

[125] M. Gouterman.
Spectra of Porphyrins: Part I.
J. Mol. Spectrosc. **6**, 138–163 (1961).

[126] D. Dolphin.
The Porphyrins, volume 3.
Academic Press Inc, New York (1978).

[127] M. Gouterman, G. H. Wagnière, and L. C. Snyder.
Spectra of Porphyrins: Part II. Four Orbital Model.
J. Mol. Spectrosc. **11**, 108–127 (1963).

[128] F. P. Miller, A. F. Vandome, and J. McBrewster.
Configuration Interaction.
VDM Publishing House Ltd. (2010).

[129] J. Frenkel.
On the Transformation of Light into Heat in Solids. I.
Phys. Rev. **37**, 17–44 (1931).

[130] M. Kasha, H. R. Rawls, and M. A. El-Bayoumi.
The Exciton Model in Molecular Spectroscopy.
Pure Appl. Chem. **11**, 371–392 (1965).

[131] M. Kasha.
Relation between Exciton Bands and Conduction Bands in Molecular Lamellar Systems.
Rev. Mod. Phys. **31**, 162–169 (1959).

[132] H. van Amerongen, L. Valkunas, and R. van Grondelle.
Photosynthetic Excitons.
World Scientific Publishing Co. Pte. Ltd. (2000).

[133] C. Hettich, C. Schmitt, J. Zitzmann, S. Kühn, I. Gerhardt, and V. Sandoghdar.
Nanometer Resolution and Coherent Optical Dipole Coupling of Two Individual Molecules.
Science **298**, 385–389 (2002).

[134] S. Zottnick.
Transiente Absorption im Nahinfraroten.
Bachelor thesis, Universität Würzburg (2011).

[135] O. Schalk, H. Brands, T. S. Balaban, and A. Unterreiner.
Near-Infrared Excitation of the Q Band in Free Base and Zinc Tetratolyl-porphyrins.
J. Phys. Chem. A **112**, 1719–1729 (2008).

[136] C. Nagura, A. Suda, H. Kawano, M. Obara, and K. Midorikawa.
Generation and Characterization of Ultrafast White-Light Continuum in Condensed Media.
Appl. Opt. **41**, 3735–3742 (2002).

[137] U. Brackmann.
Lambdachrome Laser Dyes.
Third edition. Lambda Physik AG, Goettingen (2000).

[138] D. Wang, H. Jiang, H. Yang, C. Liu, Q. Gong, J. Xiang, and G. Xu.
Investigation on Photoexcited Dynamics of IR-140 Dye in Ethanol by Femtosecond Supercontinuum-Probing Technique.
J. Opt. A: Pure Appl. Opt. **4**, 155–159 (2002).

[139] D. Wang, H. Jiang, S. Wu, H. Yang, Q. Gong, J. Xiang, and G. Xu.
An Investigation of Solvent Effects on the Optical Properties of Dye IR-140 Using the Pump Supercontinuum-Probing Technique.
J. Opt. A: Pure Appl. Opt. **5**, 515–519 (2003).

[140] M. J. Frisch, G. W. Trucks, H. B. Schlegel, G. E. Scuseria, M. A. Robb, J. R. Cheeseman, G. Scalmani, V. Barone, B. Mennucci, G. A. Petersson, H. Nakatsuji, M. Caricato, X. Li, H. P. Hratchian, A. F. Izmaylov, J. Bloino, G. Zheng, J. L. Sonnenberg, M. Hada, M. Ehara, K. Toyota, R. Fukuda, J. Hasegawa, M. Ishida, T. Nakajima, Y. Honda, O. Kitao, H. Nakai, T. Vreven, J. J. A. Montgomery, J. E. Peralta, F. Ogliaro, M. Bearpark, J. J. Heyd, E. Brothers, K. N. Kudin, V. N. Staroverov, R. Kobayashi, J. Normand, K. Raghavachari, A. Rendell, J. C. Burant, S. S. Iyengar, J. Tomasi, M. Cossi, N. Rega, J. M. Millam, M. Klene, J. E. Knox, J. B. Cross, V. Bakken, C. Adamo, J. Jaramillo, R. Gomperts, R. E. Stratmann, O. Yazyev, A. J. Austin, R. Cammi, C. Pomelli, J. W. Ochterski, R. L. Martin, K. Morokuma, V. G. Zakrzewski, G. A. Voth, P. Salvador, J. J. Dannenberg, S. Dapprich, A. D. Daniels, O. Farkas, J. B. Foresman, J. V. Ortiz, J. Cioslowski, and D. J. Fox.
Gaussian 09 Revision A.1 (2009).

[141] J. Chai and M. Head-Gordon.
Long-Range Corrected Hybrid Density Functionals with Damped Atom–Atom Dispersion Corrections.
Phys. Chem. Chem. Phys. **10**, 6615–6620 (2008).

[142] T. Yanai, D. P. Tew, and N. C. Handy.
A New Hybrid Exchange–Correlation Functional Using the Coulomb-Attenuating Method (CAM-B3LYP).
Chem. Phys. Lett. **393**, 51–57 (2004).

[143] W. J. Hehre, R. Ditchfield, and J. A. Pople.
Self—Consistent Molecular Orbital Methods. XII. Further Extensions of Gaussian—Type Basis Sets for Use in Molecular Orbital Studies of Organic Molecules.
J. Chem. Phys. **56**, 2257–2261 (1972).

[144] P. C. Hariharan and J. A. Pople.
The Influence of Polarization Functions on Molecular Orbital Hydrogenation Energies.
Theor. Chim. Acta **28**, 213–222 (1973).

[145] A. J. H. Wachters.
Gaussian Basis Set for Molecular Wavefunctions Containing Third-Row Atoms.
J. Chem. Phys. **52**, 1033–1036 (1970).

[146] P. J. Hay.
Gaussian Basis Sets for Molecular Calculations. The Representation of 3d Orbitals in Transition-Metal Atoms.
J. Chem. Phys. **66**, 4377–4384 (1977).

[147] M. Cossi, N. Rega, G. Scalmani, and V. Barone.
Energies, Structures, and Electronic Properties of Molecules in Solution with the C-PCM Solvation Model.
J. Comput. Chem. **24**, 669–681 (2003).

[148] T. Bruhn, Y. Hemberger, A. Schaumlöffel, and G. Bringmann.
SpecDis (2011).

[149] T. Bruhn, A. Schaumlöffel, Y. Hemberger, and G. Bringmann.
SpecDis: Quantifying the Comparison of Calculated and Experimental Electronic Circular Dichroism Spectra.
Chirality **25**, 243–249 (2013).

[150] Y. Hua-Zhong, J. S. Baskin, and A. H. Zewail.
Ultrafast Dynamics of Porphyrins in the Condensed Phase: II. Zinc Tetraphenylporphyrin.
J. Phys. Chem. A **106**, 9845–9854 (2002).

[151] U. Tripathy and R. P. Steer.
The Photophysics of Metalloporphyrins Excited in their Soret and Higher Energy UV Absorption Bands.
J. Porphyrins Phthalocyanines **11**, 228 (2007).

[152] A. Lukaszewicz, J. Karolczak, D. Kowalska, A. Maciejewski, M. Ziolek, and R. P. Steer.
Photophysical Processes in Electronic States of Zinc Tetraphenyl Porphyrin Accessed on One- and Two-Photon Excitation in the Soret Region.
Chem. Phys. **331**, 359–372 (2007).

[153] U. Tripathy, D. Kowalska, X. Liu, S. Velate, and R. P. Steer.
Photophysics of Soret-Excited Tetrapyrroles in Solution. I. Metalloporphyrins: MgTPP, ZnTPP, and CdTPP.
J. Phys. Chem. A **112**, 5824–5833 (2008).

[154] X. Liu, U. Tripathy, S. V. Bhosale, S. J. Langford, and R. P. Steer.
Photophysics of Soret-Excited Tetrapyrroles in Solution. II. Effects of Perdeuteration, Substituent Nature and Position, and Macrocycle Structure and Conformation in Zinc(II) Porphyrins.
J. Phys. Chem. A **112**, 8986–8998 (2008).

[155] O. Ohno, Y. Kaizu, and H. Kobayashi.
Luminescence of Some Metalloporphins Including the Complexes of the IIIb Metal Group.
J. Chem. Phys. **82**, 1779–1787 (1985).

[156] S. Tobita, Y. Kaizu, H. Kobayashi, and I. Tanaka.
Study of Higher Excited Singlet States of Zinc(II)-Tetraphenylporphin.
J. Chem. Phys. **81**, 2962–2969 (1984).

[157] M. I. S. Röhr, J. Petersen, M. Wohlgemuth, V. Bonačić-Koutecký, and R. Mitrić.
Nonlinear Absorption Dynamics Using Field-Induced Surface Hopping: Zinc Porphyrin in Water.
ChemPhysChem **14**, 1377–1386 (2013).

[158] G. G. Gurzadyan, T. Tran-Thi, and T. Gustavsson.
Time-Resolved Fluorescence Spectroscopy of High-Lying Electronic States of Zn-Tetraphenylporphyrin.
J. Chem. Phys. **108**, 385–388 (1997).

[159] M. Enescu, K. Steenkeste, F. Tfibel, and M. Fontaine-Aupart.
Femtosecond Relaxation Processes from Upper Excited States of Tetrakis(N-methyl-4-pyridyl)porphyrins Studied by Transient Absorption Spectroscopy.
Phys. Chem. Chem. Phys. **4**, 6092–6099 (2002).

[160] U. Even, J. Magen, J. Jortner, J. Friedman, and H. Levanon.
Isolated Ultracold Porphyrins in Supersonic Expansions. I. Free-Base Tetraphenylporphyrin and Zn-Tetraphenylporphyrin.
J. Chem. Phys. **77**, 4374 (1982).

[161] A. Hipke.
Ultrafast Dynamics of the Novel, Intrinsically Chiral Model Bisporphyrin beta,beta' Linked Bis[Tetraphenylporphyrinato-Zinc(II)].
Masterarbeit, Universität Würzburg (2011).

[162] D. R. Tackley, G. Dent, and W. E. Smith.
IR and Raman Assignments for Zinc Phthalocyanine from DFT Calculations.
Phys. Chem. Chem. Phys. **2**, 3949–3955 (2000).

[163] M. Atamian, R. J. Donohoe, J. S. Lindsey, and D. F. Bocian.
Resonance Raman Spectra and Normal-Coordinate Analysis of Reduced Porphyrins. 1. Zinc(II) Tetraphenylporphyrin Anion.
J. Phys. Chem. **93**, 2236–2243 (1989).

[164] G. W. Canters, J. van Egmond, J. H. Schaafsma, and T. J. van der Waals.
Optical and Zeeman Studies of the First Excited Singlet State of Zinc Porphin in a Single Crystal of n-Octane: Evidence for Jahn-Teller Instability.
Mol. Phys. **24**, 1203–1215 (1972).

[165] J. Karolczak, D. Kowalska, A. Lukaszewicz, A. Maciejewski, and R. P. Steer.
Photophysical Studies of Porphyrins and Metalloporphyrins: Accurate Measurements of Fluorescence Spectra and Fluorescence Quantum Yields for Soret Band Excitation of Zinc Tetraphenylporphyrin.
J. Phys. Chem. A **108**, 4570–4575 (2004).

[166] R. Maksimenka, M. Margraf, J. Köhler, A. Heckmann, C. Lambert, and I. Fischer.
Femtosecond Dynamics of Electron Transfer in a Neutral Organic Mixed-Valence Compound.
Chem. Phys. **347**, 436–445 (2008).

[167] V. S. Lin, S. G. DiMagno, and M. J. Therien.
Highly Conjugated, Acetylenyl Bridged Porphyrins: New Models for Light-Harvesting Antenna Systems.
Science **264**, 1105–1111 (1994).

[168] A. Osuka and H. Shimidzu.
meso, meso-Linked Porphyrin Arrays.
Angew. Chem. Int. Ed. (English) **36**, 135–137 (1997).

[169] A. Tsuda and A. Osuka.

Fully Conjugated Porphyrin Tapes with Electronic Absorption Bands That Reach into Infrared.
Science **293**, 79–82 (2001).

[170] C. Liu, H. Pan, M. A. Fox, and A. J. Bard.
High-Density Nanosecond Charge Trapping in Thin Films of the Photoconductor ZnODEP.
Science **261**, 897–899 (1993).

[171] I. Hwang, T. Kamada, T. K. Ahn, D. M. Ko, T. Nakamura, A. Tsuda, A. Osuka, and D. Kim.
Porphyrin Boxes Constructed by Homochiral Self-Sorting Assembly: Optical Separation, Exciton Coupling, and Efficient Excitation Energy Migration.
J. Am. Chem. Soc. **126**, 16187–16198 (2004).

[172] I. Hwang, H. S. Cho, D. H. Jeong, and D. Kim.
Photophysical Properties of a Three-Dimensional Zinc(II) Porphyrin Box.
J. Phys. Chem. B **107**, 9977–9988 (2003).

[173] S. Cho, M. Yoon, J. M. Lim, P. Kim, N. Aratani, Y. Nakamura, T. Ikeda, A. Osuka, and D. Kim.
Structural Factors Determining Photophysical Properties of Directly Linked Zinc(II) Porphyrin Dimers: Linking Position, Dihedral Angle, and Linkage Length.
J. Phys. Chem. B **113**, 10619–10627 (2009).

[174] P. Hamm.
Coherent Effects in Femtosecond Infrared Spectroscopy.
Chem. Phys. **200**, 415–429 (1995).

[175] H. Kano, T. Saito, and T. Kobayashi.
Dynamic Intensity Borrowing in Porphyrin J-Aggregates Revealed by Sub-5-fs Spectroscopy.
J. Phys. Chem. B **105**, 413–419 (2001).

[176] I. Coddington, W. C. Swann, and N. R. Newbury.
Time-Domain Spectroscopy of Molecular Free-Induction Decay in the Infrared.
Opt. Lett. **35**, 1395–1397 (2010).

[177] Z. Cai, M. J. Crossley, J. R. Reimers, R. Kobayashi, and R. D. Amos.
Density Functional Theory for Charge Transfer: The Nature of the N-Bands of Porphyrins and Chlorophylls Revealed through CAM-B3LYP, CASPT2, and SAC-CI Calculations.
J. Phys. Chem. B **110**, 15624–15632 (2006).

[178] R. Improta, C. Ferrante, R. Bozio, and V. Barone.
The Polarizability in Solution of Tetra-Phenyl-Porphyrin Derivatives in their Excited Electronic States: a PCM/TD-DFT Study.
Phys. Chem. Chem. Phys. **11**, 4664–4673 (2009).

[179] M. Lippitz, C. G. Huebner, T. Christ, H. Eichner, P. Bordat, A. Herrmann, K. Müllen, and T. Basché.
Coherent Electronic Coupling versus Localization in Individual Molecular Dimers.
Phys. Rev. Lett. **92**, 103001–103004 (2004).

[180] D. Smith, R. Mead, and A. Zewail.
Anderson's Localization of Molecular Excitons in Substitutionally Disordered Systems.
Chem. Phys. Lett. **50**, 358–363 (1977).

[181] X. Yang, T. E. Dykstra, and G. D. Scholes.
Photon-Echo Studies of Collective Absorption and Dynamic Localization of Excitation in Conjugated Polymers and Oligomers.
Phys. Rev. B **71**, 045203–045203–15 (2005).

[182] J. J. Piet, P. N. Taylor, H. L. Anderson, A. Osuka, and J. M. Warman.
Excitonic Interactions in the Singlet and Triplet Excited States of Covalently Linked Zinc Porphyrin Dimers.
J. Am. Chem. Soc. **122**, 1749–1757 (2000).

[183] C. She, J. E. McGarrah, S. J. Lee, J. L. Goodman, S. T. Nguyen, J. A. G. Williams, and J. T. Hupp.
Probing Exciton Localization/Delocalization: Transient dc Photoconductivity Studies of Excited States of Symmetrical Porphyrin Monomers, Oligomers, and Supramolecular Assemblies.
J. Phys. Chem. A **113**, 8182–8186 (2009).

[184] Y. H. Kim, D. H. Jeong, D. Kim, S. C. Jeoung, H. S. Cho, S. K. Kim, N. Aratani, and A. Osuka.
Photophysical Properties of Long Rodlike meso-meso-Linked Zinc(II) Porphyrins Investigated by Time-Resolved Laser Spectroscopic Methods.
J. Am. Chem. Soc. **123**, 76–86 (2001).

[185] M. Sekita.
Photophysical Characterization of Multichromophoric Porphyrin Systems.
Master thesis, Friedrich-Alexander-Universität Erlangen-Nürnberg (2011).

[186] J. R. Widom, W. Lee, A. Perdomo-Ortiz, D. Rappoport, T. F. Molinski, A. Aspuru-Guzik, and A. H. Marcus.
Temperature-Dependent Conformations of a Membrane Supported Zinc Porphyrin Tweezer by 2D Fluorescence Spectroscopy.
J. Phys. Chem. A (2013).

[187] S. M. G. Faeder and D. M. Jonas.
Two-Dimensional Electronic Correlation and Relaxation Spectra: Theory and Model Calculations.
J. Phys. Chem. A **103**, 10489–10505 (1999).

[188] F. Koch.
Kohärente zweidimensionale Spektroskopie am direkt beta,beta'-verknüpften Bis[Tetraphenylporphyrinato-Zinc(II)].
Master thesis, Universität Würzburg (2012).

[189] A. Nemeth, F. Milota, T. Mančal, V. Lukeš, J. Hauer, H. F. Kauffmann, and J. Sperling.
Vibrational Wave Packet Induced Oscillations in Two-Dimensional Electronic Spectra. I. Experiments.
J. Chem. Phys. **132**, 184514 (2010).

[190] T. Mančal, A. Nemeth, F. Milota, V. Lukeš, H. F. Kauffmann, and J. Sperling.
Vibrational Wave Packet Induced Oscillations in Two-Dimensional Electronic Spectra. II. Theory.
J. Chem. Phys. **132**, 184515–184515–12 (2010).

[191] M. Joffre.
Coherent Effects in Femtosecond Spectroscopy: A Simple Picture Using the Bloch Equation.
In C. Rullière (Ed.), *Femtosecond Laser Pulses: Principles and Experiments*, p. 283–308. Springer, Berlin (1998).

[192] P. Kjellberg, B. Brüggemann, and T. Pullerits.
Two-Dimensional Electronic Spectroscopy of an Excitonically Coupled Dimer.
Phys. Rev. B **74** (2006).

[193] V. Szöcs, T. Pálszegi, V. Lukeš, J. Sperling, F. Milota, W. Jakubetz, and H. F. Kauffmann.
Two-Dimensional Electronic Spectra of Symmetric Dimers: Intermolecular Coupling and Conformational States.
J. Chem. Phys. **124**, 124511–10 (2006).

[194] D. V. Voronine, D. Abramavicius, and S. Mukamel.
Coherent Control of Cross-Peaks in Chirality-Induced Two-Dimensional Optical Signals of Excitons.
J. Chem. Phys. **125**, 224504 (2006).

[195] B. L. Feringa, W. F. Jager, and B. de Lange.
Organic Materials for Reversible Optical Data Storage.
Tetrahedron **49**, 8267–8310 (1993).

[196] S. Malkmus, F. O. Koller, S. Draxler, T. E. Schrader, W. J. Schreier, T. Brust, J. A. DiGirolamo, W. J. Lees, W. Zinth, and M. Braun.
All-Optical Operation Cycle on Molecular Bits with 250-GHz Clock-Rate Based on Photochromic Fulgides.
Adv. Funct. Mater. **17**, 3657–3662 (2007).

[197] A. Sinicropi, E. Martin, M. Ryazantsev, J. Helbing, J. Briand, D. Sharma, J. Léonard, S. Haacke, A. Cannizzo, M. Chergui, V. Zanirato, S. Fusi, F. Santoro, R. Basosi, N. Ferré, and M. Olivucci.
An Artificial Molecular Switch that Mimics the Visual Pigment and Completes its Photocycle in Picoseconds.
Proc. Natl. Acad. Sci. U.S.A. **105**, 17642–17647 (2008).

[198] M. Irie.
Diarylethenes for Memories and Switches.
Chem. Rev. **100**, 1685–1716 (2000).

[199] K. Mori, Y. Ishibashi, H. Matsuda, S. Ito, Y. Nagasawa, H. Nakagawa, K. Uchida, S. Yokojima, S. Nakamura, M. Irie, and H. Miyasaka.
One-Color Reversible Control of Photochromic Reactions in a Diarylethene Derivative: Three-Photon Cyclization and Two-Photon Cycloreversion by a Near-Infrared Femtosecond Laser Pulse at 1.28 microm.
J. Am. Chem. Soc. **133**, 2621–2625 (2011).

[200] T. Fukaminato, T. Doi, N. Tamaoki, K. Okuno, Y. Ishibashi, H. Miyasaka, and M. Irie.
Single-Molecule Fluorescence Photoswitching of a Diarylethene-Perylenebisimide Dyad: Non-destructive Fluorescence Readout.
J. Am. Chem. Soc. **133**, 4984–4990 (2011).

[201] Y. Yokoyama.
Fulgides for Memories and Switches.
Chem. Rev. **100**, 1717–1740 (2000).

[202] A. Nenov, W. J. Schreier, F. O. Koller, M. Braun, R. de Vivie-Riedle, W. Zinth, and I. Pugliesi.
Molecular Model of the Ring-Opening and Ring-Closure Reaction of a Fluorinated Indolylfulgide.
J. Phys. Chem. A **116**, 10518–10528 (2012).

[203] S. Draxler, T. Brust, S. Malkmus, J. A. DiGirolamo, W. J. Lees, W. Zinth, and M. Braun.
Ring-Opening Reaction of a Trifluorinated Indolylfulgide: Mode-Specific Photochemistry after Pre-Excitation.
Phys. Chem. Chem. Phys. **11**, 5019–5027 (2009).

[204] M. A. Wolak, C. J. Thomas, N. B. Gillespie, R. R. Birge, and W. J. Lees.
Tuning the Optical Properties of Fluorinated Indolylfulgimides.
J. Org. Chem. **68**, 319–326 (2003).

[205] G. Berkovic, V. Krongauz, and V. Weiss.
Spiropyrans and Spirooxazines for Memories and Switches.
Chem. Rev. **100**, 1741–1754 (2000).

[206] N. P. Ernsting.
Transient Optical Absorption Spectroscopy of the Photochemical Spiropyran-Merocyanine Conversion.
Chem. Phys. Lett. **159**, 526–531 (1989).

[207] N. Ernsting and T. Arthenengeland.
Photochemical Ring-Opening Reaction of Indolinospyropyrans Studied by Subpicosecond Transient Absorption.
J. Phys. Chem. **95**, 5502–5509 (1991).

[208] M. Sanchez-Lozano, C. M. Estévez, J. Hermida-Ramón, and L. Serrano-Andres.

Ultrafast Ring-Opening/Closing and Deactivation Channels for a Model Spiropyran–Merocyanine System.
J. Phys. Chem. A **115**, 9128–9138 (2011).

[209] J. Z. Zhang, B. J. Schwartz, J. C. King, and C. B. Harris.
Ultrafast Studies of Photochromic Spiropyrans in Solution.
J. Am. Chem. Soc. **114**, 10921–10927 (1992).

[210] M. Maafi.
Useful Spectrokinetic Methods for the Investigation of Photochromic and Thermo-Photochromic Spiropyrans.
Molecules **13**, 2260–2302 (2008).

[211] R. Siewertsen, F. Strübe, J. Mattay, F. Renth, and F. Temps.
Tuning of Switching Properties and Excited-State Dynamics of Fulgides by Structural Modifications.
Phys. Chem. Chem. Phys. **13**, 3800–3808 (2011).

[212] J. Kohl-Landgraf, M. Braun, C. Özçoban, D. P. N. Gonçalves, A. Heckel, and J. Wachtveitl.
Ultrafast Dynamics of a Spiropyran in Water.
J. Am. Chem. Soc. **134**, 14070–14077 (2012).

[213] D. Parthenopoulos and P. Rentzepis.
Three-Dimensional Optical Storage Memory.
Science **245**, 843–845 (1989).

[214] A. S. Dvornikov, Y. Liang, C. S. Cruse, and P. M. Rentzepis.
Spectroscopy and Kinetics of a Molecular Memory with Nondestructive Readout for Use in 2D and 3D Storage Systems.
J. Phys. Chem. B **108**, 8652–8658 (2004).

[215] A. S. Dvornikov, E. P. Walker, and P. M. Rentzepis.
Two-Photon Three-Dimensional Optical Storage Memory.
J. Phys. Chem. A **113**, 13633–13644 (2009).

[216] J. Hobley, V. Malatesta, R. Millini, L. Montanari, and W. O. Parker.
Proton Exchange and Isomerisation Reactions of Photochromic and Reverse Photochromic Spiro-Pyrans and their Merocyanine Forms.
Phys. Chem. Chem. Phys. **1**, 3259–3267 (1999).

[217] J. Hobley, U. Pfeifer-Fukumura, M. Bletz, T. Asahi, H. Masuhara, and H. Fukumura.
Ultrafast Photo-Dynamics of a Reversible Photochromic Spiropyran.
J. Phys. Chem. A **106**, 2265–2270 (2002).

[218] R. Siewertsen, F. Renth, F. Temps, and F. Sonnichsen.
Parallel Ultrafast E-C Ring Closure and E-Z Isomerisation in a Photochromic Furylfulgide Studied by Femtosecond Time-Resolved Spectroscopy.
Phys. Chem. Chem. Phys. **11**, 5952–5961 (2009).

[219] S. Ruetzel, M. Kullmann, J. Buback, P. Nuernberger, and T. Brixner.
Tracing the Steps of Photoinduced Chemical Reactions in Organic Molecules by Coherent Two-Dimensional Electronic Spectroscopy Using Triggered Exchange.
Phys. Rev. Lett. **110**, 148305 (2013).

[220] P. F. Tekavec, J. A. Myers, K. L. M. Lewis, and J. P. Ogilvie.
Two-Dimensional Electronic Spectroscopy with a Continuum Probe.
Opt. Lett. **34**, 1390–1392 (2009).

[221] P. A. Tekavec, K. L. Lewis, F. D. Fuller, J. A. Myers, and J. P. Ogilvie.
Toward Broad Bandwidth 2-D Electronic Spectroscopy: Correction of Chirp From a Continuum Probe.
IEEE J. Sel. Top. Quantum Electron. **18**, 210–217 (2012).

[222] A. Nemeth, V. Lukes, J. Sperling, F. Milota, H. F. Kauffmann, and T. Mančal.

Two-Dimensional Electronic Spectra of an Aggregating Dye: Simultaneous Measurement of Monomeric and Dimeric Line-Shapes.
Phys. Chem. Chem. Phys. **11**, 5986–5997 (2009).

[223] J. Bredenbeck, J. Helbing, R. Behrendt, C. Renner, L. Moroder, J. Wachtveitl, and P. Hamm.
Transient 2D-IR Spectroscopy: Snapshots of the Nonequilibrium Ensemble during the Picosecond Conformational Transition of a Small Peptide.
J. Phys. Chem. B **107**, 8654–8660 (2003).

[224] H. S. Chung, Z. Ganim, K. C. Jones, and A. Tokmakoff.
Transient 2D IR Spectroscopy of Ubiquitin Unfolding Dynamics.
Proc. Natl. Acad. Sci. U.S.A. **104**, 14237 –14242 (2007).

[225] J. Bredenbeck, J. Helbing, C. Kolano, and P. Hamm.
Ultrafast 2D–IR Spectroscopy of Transient Species.
ChemPhysChem **8**, 1747–1756 (2007).

[226] C. R. Baiz, M. J. Nee, R. McCanne, and K. J. Kubarych.
Ultrafast Nonequilibrium Fourier-Transform Two-Dimensional Infrared Spectroscopy.
Opt. Lett. **33**, 2533–2535 (2008).

[227] J. Zheng, K. Kwak, J. Asbury, X. Chen, I. R. Piletic, and M. D. Fayer.
Ultrafast Dynamics of Solute-Solvent Complexation Observed at Thermal Equilibrium in Real Time.
Science **309**, 1338–1343 (2005).

[228] Y. S. Kim and R. M. Hochstrasser.
Chemical Exchange 2D IR of Hydrogen-Bond Making and Breaking.
Proc. Natl. Acad. Sci. U.S.A. **102**, 11185 –11190 (2005).

[229] S. Woutersen, Y. Mu, G. Stock, and P. Hamm.
Hydrogen-Bond Lifetime Measured by Time-Resolved 2D-IR Spectroscopy: N-Methylacetamide in Methanol.
Chem. Phys. **266**, 137–147 (2001).

[230] J. M. Anna, M. R. Ross, and K. J. Kubarych.
Dissecting Enthalpic and Entropic Barriers to Ultrafast Equilibrium Isomerization of a Flexible Molecule Using 2DIR Chemical Exchange Spectroscopy.
J. Phys. Chem. A **113**, 6544–6547 (2009).

[231] M. Olschewski, S. Knop, J. Seehusen, J. Lindner, and P. Vöhringer.
Ultrafast Internal Dynamics of Flexible Hydrogen-Bonded Supramolecular Complexes.
J. Phys. Chem. A **115**, 1210–1221 (2011).

[232] R. Kießwetter, N. Pustet, F. Brandl, and A. Mannschreck.
1',3',3'-Trimethyl-6-nitrospiro[2H-1-benzopyran-2,2'-indoline]: Its Thermal Enantiomerization and the Equilibration with Its Merocyanine.
Tetrahedron: Asymmetry **10**, 4677–4687 (1999).

[233] M. Rini, A. Holm, E. T. J. Nibbering, and H. Fidder.
Ultrafast UV-mid-IR Investigation of the Ring Opening Reaction of a Photochromic Spiropyran.
J. Am. Chem. Soc. **125**, 3028–3034 (2003).

[234] H. Satzger, C. Root, and M. Braun.
Excited-State Dynamics of trans- and cis-Azobenzene after UV Excitation in the pp Band.*
J. Phys. Chem. A **108**, 6265–6271 (2004).

[235] R. Siewertsen, H. Neumann, B. Buchheim-Stehn, R. Herges, C. Näther, F. Renth, and F. Temps.
Highly Efficient Reversible Z-E Photoisomerization of a Bridged Azobenzene with Visible Light through Resolved S1(np) Absorption Bands.*
J. Am. Chem. Soc. **131**, 15594–15595 (2009).

[236] M. L. Bossi, J. B. Rodríguez, and P. F. Aramendía.
Photoinduced Changes of Absorption and Circular Dichroism in a Chiral Nematic Phase Containing a Photochromic Fulgide.
J. Photochem. Photobiol., A **179**, 35–41 (2006).

[237] S. Malkmus, F. Koller, B. Heinz, W. Schreier, T. Schrader, W. Zinth, C. Schulz, S. Dietrich, K. Rück-Braun, and M. Braun.
Ultrafast Ring Opening Reaction of a Photochromic Indolyl-Fulgimide.
Chem. Phys. Lett. **417**, 266–271 (2006).

[238] T. Cordes, S. Malkmus, J. A. DiGirolamo, W. J. Lees, A. Nenov, R. de Vivie-Riedle, M. Braun, and W. Zinth.
Accelerated and Efficient Photochemistry from Higher Excited Electronic States in Fulgide Molecules.
J. Phys. Chem. A **112**, 13364–13371 (2008).

[239] M. Murakami, H. Miyasaka, T. Okada, S. Kobatake, and M. Irie.
Dynamics and Mechanisms of the Multiphoton Gated Photochromic Reaction of Diarylethene Derivatives.
J. Am. Chem. Soc. **126**, 14764–14772 (2004).

[240] R. Siewertsen.
Ultrafast Photochromic Reactions of Structurally Modified Furylfulgides and a Bridged Azobenzene.
Dissertation, Universität Kiel (2011).

[241] G. Cottone, R. Noto, and G. L. Manna.
Density Functional Theory Study of the Trans-Trans-Cis (TTC)-> Trans-Trans-Trans (TTT) Isomerization of a Photochromic Spiropyran Merocyanine.
Molecules **13**, 1246–1252 (2008).

[242] K. C. Nicolaou, S. A. Snyder, T. Montagnon, and G. Vassilikogiannakis.
The Diels-Alder Reaction in Total Synthesis.
Angew. Chem. Int. Ed. **41**, 1668–1698 (2002).

[243] P. Celani, S. Ottani, M. Olivucci, F. Bernardi, and M. A. Robb.
What Happens during the Picosecond Lifetime of 2A1 Cyclohexa-1,3-diene? A CAS-SCF Study of the Cyclohexadiene/Hexatriene Photochemical Interconversion.
J. Am. Chem. Soc. **116**, 10141–10151 (1994).

[244] M. Kotur, T. Weinacht, B. J. Pearson, and S. Matsika.
Closed-Loop Learning Control of Isomerization Using Shaped Ultrafast Laser Pulses in the Deep Ultraviolet.
J. Chem. Phys. **130**, 134311–5 (2009).

[245] B. A. West, B. P. Molesky, N. P. Montoni, and A. M. Moran.
Nonlinear Optical Signatures of Ultraviolet Light-Induced Ring Opening in alpha-Terpinene.
New J. Phys. **15**, 025007 (2013).

[246] S. H. Pullen, N. A. Anderson, L. A. Walker, and R. J. Sension.
The Ultrafast Photochemical Ring-Opening Reaction of 1,3-Cyclohexadiene in Cyclohexane.
J. Chem. Phys. **108**, 556–563 (1998).

[247] I. Fleming.
Frontier Orbitals and Organic Chemical Reactions.
First edition. Wiley (1976).

[248] I. Fleming.
Grenzorbitale und Reaktionen organischer Verbindungen.
Wiley-VCH (1990).

[249] S. H. Pullen, N. A. Anderson, L. A. Walker, and R. J. Sension.
The Ultrafast Ground and Excited State Dynamics of Cis-Hexatriene in Cyclohexane.
J. Chem. Phys. **107**, 4985 (1997).

[250] Y. Hirshberg and E. Fischer.
Low-Temperature Photochromism and Its Relation to Thermochromism.
J. Chem. Soc. pp. 629–636 (1953).

[251] I. Fleming.
Molekülorbitale und Reaktionen organischer Verbindungen.
First edition. Wiley-VCH Verlag GmbH & Co. KGaA (2012).

[252] I. Gómez, M. Reguero, and M. A. Robb.
Efficient Photochemical Merocyanine-to-Spiropyran Ring Closure Mechanism through an Extended Conical Intersection Seam. A Model CASSCF/CASPT2 Study.
J. Phys. Chem. A **110**, 3986–3991 (2006).

[253] A. K. Chibisov and H. Görner.
Photoprocesses in Spiropyran-Derived Merocyanines.
J. Phys. Chem. A **101**, 4305–4312 (1997).

[254] C. J. Wohl and D. Kuciauskas.
Excited-State Dynamics of Spiropyran-Derived Merocyanine Isomers.
J. Phys. Chem. B **109**, 22186–22191 (2005).

[255] A. Holm, O. F. Mohammed, M. Rini, E. Mukhtar, E. T. J. Nibbering, and H. Fidder.
Sequential Merocyanine Product Isomerization Following Femtosecond UV Excitation of a Spiropyran.
J. Phys. Chem. A **109**, 8962–8968 (2005).

[256] L. Poisson, K. D. Raffael, B. Soep, J. Mestdagh, and G. Buntinx.
Gas-Phase Dynamics of Spiropyran and Spirooxazine Molecules.
J. Am. Chem. Soc. **128**, 3169–3178 (2006).

[257] C. J. Wohl and D. Kuciauskas.
Isomerization Dynamics of Photochromic Spiropyran Molecular Switches in Phospholipid Bilayers.
J. Phys. Chem. B **109**, 21893–21899 (2005).

[258] S. Konorov, D. Sidorov-Biryukov, I. Bugar, D. Chorvat, D. Chorvat, and A. Zheltikov.
Quantum-Controlled Color: Chirp- and Polarization-Sensitive Two-Photon Photochromism of Spiropyrans in the Solid Phase.
Chem. Phys. Lett. **381**, 572–578 (2003).

[259] S. O. Konorov, D. A. Sidorov-Biryukov, I. Bugar, D. Chorvat, D. Chorvat, and A. M. Zheltikov.
Femtosecond Two-Photon-Absorption-Resonant Four-Wave Mixing for Time-Resolved Studies of Photochromism in Three Dimensions.
Chem. Phys. Lett. **378**, 630–637 (2003).

[260] S. O. Konorov, D. A. Sidorov-Biryukov, I. Bugar, D. Chorvat, D. Chorvat, and A. M. Zheltikov.
Quantum Control of Two-Photon Photochromism in the Solid Phase.
JETP Letters **78**, 246–249 (2003).

[261] M. S. Bugayova and A. S. Vetchinkin.
Quantum Control Over Isomerization of Spiropyran (Model Potential).
Russ. J. Phys. Chem. B **3**, 191–194 (2009).

[262] A. Gahlmann, I. Lee, and A. H. Zewail.
Direct Structural Determination of Conformations of Photoswitchable Molecules by Laser Desorption-Electron Diffraction.
Angew. Chem. Int. Ed. **49**, 6524–6527 (2010).

[263] M. Minami and N. Taguchi.
Effects of Substituents on the Indoline Ring on the Negative Photochromic Properties of Spirobenzopyran Derivatives.
Chem. Lett. **25**, 429–430 (1996).

[264] J. Takeda, Y. Ikeda, D. Mihara, S. Kurita, A. Sawada, and Y. Yokoyama.
Transient Absorption Spectroscopy for Photochemical Reactions of a Negative Photochromic Spiropyran.
Mol. Cryst. Liq. Cryst. Sci. Technol., Sect. A **345**, 191 (2000).

[265] B. Siebenhofer, S. Gorelik, M. J. Lear, H. Y. Song, C. Nowak, and J. Hobley.
Transient absorption spectroscopy on spiropyran monolayers using nanosecond pump–probe Brewster angle reflectometry.
Photochem. Photobiol. Sci. **12**, 848–853 (2013).

[266] Y. Futami, M. L. S. Chin, S. Kudoh, M. Takayanagi, and M. Nakata.
Conformations of Nitro-Substituted Spiropyran and Merocyanine Studied by Low-Temperature Matrix-Isolation Infrared Spectroscopy and Density-Functional-Theory Calculation.
Chem. Phys. Lett. **370**, 460–468 (2003).

[267] E. M. Grumstrup, S. Shim, M. A. Montgomery, N. H. Damrauer, and M. T. Zanni.
Facile Collection of Two-Dimensional Electronic Spectra Using Femtosecond Pulse-Shaping Technology.
Opt. Express **15**, 16681–16689 (2007).

[268] S. Shim, D. B. Strasfeld, Y. L. Ling, and M. T. Zanni.
Automated 2D IR Spectroscopy Using a Mid-IR Pulse Shaper and Application of This Technology to the Human Islet Amyloid Polypeptide.
Proc. Natl. Acad. Sci. U.S.A. **104**, 14197–14202 (2007).

[269] T. Löhrig.
Planung und Realisierung eines Aufbaus zur Formung ultrabreitbandier fs-Laserpulse im sichtbaren Spektralbereich.
Diplomarbeit, Universität Würzburg (2007).

[270] J. Koehler, M. Wollenhaupt, T. Bayer, C. Sarpe, and T. Baumert.
Zeptosecond Precision Pulse Shaping.
Opt. Express **19**, 11638–11653 (2011).

[271] S. Ruhman, A. G. Joly, and K. A. Nelson.
Time-Resolved Observations of Coherent Molecular Vibrational Motion and the General Occurrence of Impulsive Stimulated Scattering.
J. Chem. Phys. **86**, 6563–6565 (1987).

[272] P. F. Tekavec, J. A. Myers, K. L. M. Lewis, F. D. Fuller, and J. P. Ogilvie.
Effects of Chirp on Two-Dimensional Fourier Transform Electronic Spectra.
Opt. Express **18**, 11015–11024 (2010).

[273] I. Baraldi, F. Momicchioli, G. Ponterini, A. S. Tatikolov, and D. Vanossi.
Photoisomerization of Simple Merocyanines: a Theoretical and Experimental Comparison with Polyenes and Symmetric Cyanines.
Phys. Chem. Chem. Phys. **5**, 979–987 (2003).

[274] N. Krebs, I. Pugliesi, and E. Riedle.
Pulse Compression of Ultrashort UV Pulses by Self-Phase Modulation in Bulk Material.
Applied Sciences **3**, 153–167 (2013).

[275] D. J. Tannor and S. A. Rice.
Control of Selectivity of Chemical Reaction via Control of Wave Packet Evolution.
J. Chem. Phys. **83**, 5013–5018 (1985).

[276] F. Gai, J. C. McDonald, and P. A. Anfinrud.
Pump–Dump–Probe Spectroscopy of Bacteriorhodosin: Evidence for a Near-IR Excited State Absorbance.
J. Am. Chem. Soc. **119**, 6201–6202 (1997).

[277] S. Ruhman, B. Hou, N. Friedman, M. Ottolenghi, and M. Sheves.

Following Evolution of Bacteriorhodopsin in Its Reactive Excited State via Stimulated Emission Pumping.
J. Am. Chem. Soc. **124**, 8854–8858 (2002).

[278] D. S. Larsen, I. H. van Stokkum, M. Vengris, M. A. van der Horst, F. L. de Weerd, K. J. Hellingwerf, and R. van Grondelle.
Incoherent Manipulation of the Photoactive Yellow Protein Photocycle with Dispersed Pump-Dump-Probe Spectroscopy.
Biophys. J. **87**, 1858–1872 (2004).

[279] D. S. Larsen, E. Papagiannakis, I. H. M. van Stokkum, M. Vengris, J. T. M. Kennis, and R. van Grondelle.
Excited State Dynamics of beta-Carotene Explored with Dispersed Multi-Pulse Transient Absorption.
Chem. Phys. Lett. **381**, 733–742 (2003).

[280] C. Schriever, S. Lochbrunner, E. Riedle, and D. J. Nesbitt.
Ultrasensitive Ultraviolet-Visible 20 fs Absorption Spectroscopy of Low Vapor Pressure Molecules in the Gas Phase.
Rev. Sci. Instrum. **79**, 013107 (2008).

[281] S. Keiber.
Investigation of the Electron Transfer Properties of a Neutral Mixed-Valence Polymer and Introduction of a Shot-to-Shot Readout Mechanism for High Repitition Rates.
Masterarbeit, Würzburg (2011).

[282] S. Draxler, T. Brust, J. Eicher, W. Zinth, and M. Braun.
Novel Detection Scheme for Application in Pump-Pepump-Probe Spectroscopy.
Opt. Commun. **283**, 1050–1054 (2010).

[283] R. S. S. Kumar, L. Lüer, D. Polli, M. Garbugli, and G. Lanzani.
Primary Photo-Events in a Metastable Photomerocyanine of Spirooxazines.
Opt. Mater. Express **1**, 293–304 (2011).

[284] A. K. Chibisov and H. Görner.
Photochromism of Spirobenzopyranindolines and Spironaphthopyranindolines.
Phys. Chem. Chem. Phys. **3**, 424–431 (2001).

[285] H. Görner.
Photochromism of Nitrospiropyrans: Effects of Structure, Solvent and Temperature.
Phys. Chem. Chem. Phys. **3**, 416–423 (2001).

[286] S. Yang, H. Tian, H. Xiao, X. Shang, X. Gong, S. Yao, and K. Chen.
Photodegradation of Cyanine and Merocyanine Dyes.
Dyes Pigments **49**, 93–101 (2001).

[287] J. Dewar, A. Harget, N. Trinajstić, and S. Worley.
Ground States of Conjugated Molecules–XXI : Benzofurans and Benzopyrroles.
Tetrahedron **26**, 4505–4516 (1970).

[288] J. Behan, F. Dean, and R. Johnstone.
Photoelectron Spectra of Cyclic Aromatic Ethers : The Question of the Mills-Nixon Effect.
Tetrahedron **32**, 167–171 (1976).

[289] C. Xia, J. Peon, and B. Kohler.
Femtosecond Electron Ejection in Liquid Acetonitrile: Evidence for Cavity Electrons and Solvent Anions.
J. Chem. Phys. **117**, 8855–8866 (2002).

[290] J. Hobley and V. Malatesta.
Energy Barrier to TTC–TTT Isomerisation for the Merocyanine of a Photochromic Spiropyran.
Phys. Chem. Chem. Phys. **2**, 57–59 (2000).

[291] A. A. Bakulin, A. Rao, V. G. Pavelyev, P. H. M. van Loosdrecht, M. S. Pshenichnikov, D. Niedzialek, J. Cornil, D. Beljonne, and R. H. Friend.
The Role of Driving Energy and Delocalized States for Charge Separation in Organic Semiconductors.
Science **335**, 1340–1344 (2012).

[292] G. Benkö, J. Kallioinen, J. E. I. Korppi-Tommola, A. P. Yartsev, and V. Sundström.
Photoinduced Ultrafast Dye-to-Semiconductor Electron Injection from Nonthermalized and Thermalized Donor States.
J. Am. Chem. Soc. **124**, 489–493 (2002).

[293] M. Bonn, S. Funk, C. Hess, D. N. Denzler, C. Stampfl, M. Scheffler, M. Wolf, and G. Ertl.
Phonon- Versus Electron-Mediated Desorption and Oxidation of CO on Ru(0001).
Science **285**, 1042–1045 (1999).

[294] P. Nuernberger, D. Wolpert, H. Weiss, and G. Gerber.
Femtosecond Quantum Control of Molecular Bond Formation.
Proc. Natl. Acad. Sci. U.S.A. **107**, 10366 –10370 (2010).

[295] M. E. Vaida and T. M. Bernhardt.
Surface-Aligned Femtochemistry: Photoinduced Reaction Dynamics of CH3I and CH3Br on MgO(100).
Faraday Discuss. **157**, 437–449 (2012).

[296] A. Steinbacher, J. Buback, P. Nuernberger, and T. Brixner.
Precise and Rapid Detection of Optical Activity for Accumulative Femtosecond Spectroscopy.
Opt. Express **20**, 11838–11854 (2012).

[297] A. Steinbacher, J. Buback, P. Nuernberger, and T. Brixner.
Precise and Rapid Detection of Optical Activity for Accumulative Femtosecond Spectroscopy.
EPJ Web of Conferences **41**, 12011 (2013).

Acknowledgments

Scientific progress always depends upon teamwork between colleagues, cooperation partners and supporters because a combined effort results in higher output than the sum of every single contribution. All persons mentioned in the following contributed in important ways to the research presented within this thesis. I am very grateful to all of them and hope that they receive as much as they give and share.

Therefore, I would like to thank explicitly:

- First, and above all, my supervisor **Prof. Dr. Tobias Brixner** for envisioning the presented experiments and providing the best possible working environment combined with the encouragement to trust ones own ideas.

- **Prof. Dr. Dr. h.c. mult. Gerhard Bringmann** and his staff (**Dr. Torsten Bruhn**, **Dr. Daniel Götz**, **Franziska Witterauf**) for the synthesis, NMR characterization, and theoretical support within the bisporphyrin project.

- **Prof. Dr. Frank Würthner** and **Dr. Ralf Schmidt** for the synthesis and the collaboration within the 6,8-dinitro BIPS project.

- **Dr. Patrick Nuernberger** for always having an insightful suggestion after having been asked a question. Especially his knowledge of literature is nearly limitless, thus, enabling the comprehensive discussion of all investigated compounds.

- **Dr. Johannes Buback** for his fundamental and excellent work on 6,8-dinitro BIPS, the transient-absorption setup in Lab 2 and the corresponding software. Also for teaching me the importance of patience and endurance when working in a lab.

- **Stefan Ruetzel** for sharing lots of lab time with me and for his extensive knowledge about pulse shaping. Furthermore, for his unbroken motivation within the 6,8-dinitro BIPS project, no matter how slow the progress was at times.

- My former master and bachelor students **Arthur Hipke**, **Federico Koch** and **Sven Zottnick** for their help within the porphyrin experiments. Hopefully, they are supervising students as curious and capable as they have been.

- **Dr. Ulrike Selig** for setting up Lab 5 and constructing the 2D setup in box geometry together with **Michael Förster** and **Carl-Friedrich Schleußner**.

- All employees of the workshops for providing fast solutions for unique challenges. The technical staff (**Belinda Böhm**, **Sabine Fuchs**, **Gudrun Mühlrath**) and secretary **Andrea Gehring** for their help with everyday problems. All of them often remain in the background, however, their support is extremely valuable.

- **Dr. Cristina Consani**, **Arthur Hipke**, **Florian Kanal**, **Federico Koch**, **Dr. Patrick Nuernberger**, **Stefan Ruetzel**, and **Sebastian Schott** for carefully proof reading parts of this thesis. Hopefully, all their comments have been addressed.

- My colleagues in office 22 (**Meike Diekmann**, **Sebastian Götz**, **Ole Hüter**, **Sabine Keiber**, **Johannes Knorr**, **Anja Krischke**, **Andreas Reiserer**, **Andreas Reuß**, **Sebastian Schott**) and **Kathrin Fischer**, who joined my self-imposed exile. I thank them for the fun but also very productive time and for the shared external lunches.

- **Christoph Schwarz** and **Andreas Steinbacher** for keeping every piece of hardware and software running, especially the VI-Pool and the office computers. **Philipp Rudolf** for setting up and administrating the shared reference database.

- **Florian Kanal**, **Dr. Juliane Köhler**, **Dr. Tatjana Quast**, **Stefan Rützel** and **Christoph Stolzenberger** for spending coffee breaks with me during stressful days. I also thank **Juliane** and **Stefan** for looking after the coffee machines.

- The **Deutsche Forschungsgemeinschaft** for financial help within the research unit "FOR 1809 (Lichtinduzierte Dynamik in molekularen Aggregaten)".

- The **Wilhelm und Else Heraeus-Stiftung** for enabling annual visits of the spring meeting of the German physical society DPG.

- Additionally, I would like to thank every previously unmentioned employee and colleague within the "**Lehrstuhl für Physikalische Chemie I**". I really enjoyed the time spent with all of you.

- My friends and partners-in-crime since the first days of my academic studies in Würzburg: **Matthias Bruhnke**, **Philipp Erler**, **Daniel Neumann** and **Dr. Franz Schilling**. Without you guys the last nine years would have been much more boring and less productive.

- Lastly, I thank my parents **Rita** and **Horst**, my family, and all my friends for the continuous moral support and encouragement to find my own path in life.